Coastal and shelf sea hydro-morphodynamic modelling using process-based and data-based techniques

Mohammad Reza Hashemi

School of Ocean Sciences

Bangor University

This dissertation is submitted for the degree of

Doctor of Philosophy

College of Natural Sciences

2014

Abstract

Recent advances in computer technology and high performance computing have led to exceptional contributions in our understanding of the natural environment. Ocean models, in particular, can simulate hypothetical future scenarios when/where observed data are not available, usually, with less cost. Further, ocean modelling is the only tool which enables scientists to evaluate their conceptual models or test their hypotheses in a complex nonlinear ocean system. Nevertheless, the development of complex numerical models should always be accompanied and supported by sufficient observational data in order to set input parameters, select appropriate model physics, and validate model outputs.

This dissertation, which is presented as a collection of peer-reviewed published journal papers, attempts to answer a number of research questions regarding the hydrodynamics/morphodynamics of the northwest European shelf seas, using numerical modelling at various scales from coastal to shelf-seas.

The first part of the dissertation concerns ocean energy, where wave and tidal energy resource assessment are considered. Some knowledge gaps in wave energy studies such as shortcomings of the existing data bases (e.g. the Atlas of UK Marine Renewable Energy Resources) are introduced; then, using a higher resolution model with improved physics, spatial and temporal variability of the resource, correlation of the wave energy resource with the climatic indices as a potential way to understand the future variability , and effect of tides on shelf-scale resource assessment using a simplified method, and also coupled wave-tide modelling are presented. Next, some research questions regarding tidal energy resources at two sites are mentioned: at Orkney - where the European Marine Energy Centre was established - the vertical variability, asymmetry, turbulence, and effect of wind generated currents using a 3-D ocean model are examined; at Skerries, Anglesey – where a tidal-stream array is planned – the effect of waves on the tidal energy resource is investigated, and shown to have significant influence during winter months.

The second part of the dissertation deals with morphodynamic modelling at coastal and shelf scales. Morphodynamic modelling in presence of rotary currents (which are the origin of the formation/maintenance of many offshore sandbanks) is examined using a suite of numerical models, and a semi-analytical technique developed to estimate the strength of secondary flows. Then, morphodynamic modelling of beach profiles using process-based (i.e. a cascade of wave, tide, sediment transport and bed level change models) and data-based (i.e. artificial neural network) techniques is presented; the performance and advantages/disadvantages of these approaches are discussed based on a case study in the Irish Sea. The effect of ocean energy extraction on dynamics of sandbanks, and coastal morphology, is a new research topic of interest which connects the first and second part of this research, and is considered in prospective future research.

In the final part of the dissertation, coupled morphodynamic and hydrodynamic modelling, and integrated modelling approach are discussed. The coupled wave-tide model of the NW European shelf seas as a first step to develop an integrated modelling system for this region is introduced. The advantages of the coupled model (e.g. improved accuracy in regions where the wave-tide interactions are high) are presented while the potential issues are discussed: computational cost, increased uncertainty, and lack of appropriate observations. Further research is underway to apply this model in morphodynamic simulations. In this respect, prospective future research direction are briefly introduced.

I would like to dedicate this thesis to my parents

Declaration and Consent

Details of the Work

I hereby agree to deposit the following item in the digital repository maintained by Bangor University and/or in any other repository authorized for use by Bangor University.

Author Name: ………………………………………………………………………………...

Title: ……………………………………………………………………...……………………..

Supervisor/Department: ………………………………………………………………………

Funding body (if any): …………………………………………………………………………

Qualification/Degree obtained: ……………………………………………………………..

This item is a product of my own research endeavours and is covered by the agreement below in which the item is referred to as "the Work". It is identical in content to that deposited in the Library, subject to point 4 below.

Non-exclusive Rights

Rights granted to the digital repository through this agreement are entirely non-exclusive. I am free to publish the Work in its present version or future versions elsewhere.

I agree that Bangor University may electronically store, copy or translate the Work to any approved medium or format for the purpose of future preservation and accessibility. Bangor University is not under any obligation to reproduce or display the Work in the same formats or resolutions in which it was originally deposited.

Bangor University Digital Repository

I understand that work deposited in the digital repository will be accessible to a wide variety of people and institutions, including automated agents and search engines via the World Wide Web.

I understand that once the Work is deposited, the item and its metadata may be incorporated into public access catalogues or services, national databases of electronic theses and dissertations such as the British Library's EThOS or any service provided by the National Library of Wales.

I understand that the Work may be made available via the National Library of Wales Online Electronic Theses Service under the declared terms and conditions of use (http://www.llgc.org.uk/index.php?id=4676). I agree that as part of this service the National Library of Wales may electronically store, copy or convert the Work to any approved medium or format for the purpose of future preservation and accessibility. The National Library of Wales is not under any obligation to reproduce or display the Work in the same formats or resolutions in which it was originally deposited.

<u>Statement 1</u>:

This work has not previously been accepted in substance for any degree and is not being concurrently submitted in candidature for any degree unless as agreed by the University for approved dual awards.

Signed .... (candidate)

Date ....

<u>Statement 2</u>:

This thesis is the result of my own investigations, except where otherwise stated. Where correction services have been used, the extent and nature of the correction is clearly marked in a footnote(s).

All other sources are acknowledged by footnotes and/or a bibliography.

Signed .... (candidate)

Date ....

<u>Statement 3</u>:

I hereby give consent for my thesis, if accepted, to be available for photocopying, for inter-library loan and for electronic repositories, and for the title and summary to be made available to outside organisations.

Signed .... (candidate)

Date ....

NB: Candidates on whose behalf a bar on access has been approved by the Academic Registry should use the following version of **Statement 3:**

<u>Statement 3 (bar)</u>:

I hereby give consent for my thesis, if accepted, to be available for photocopying, for inter-library loans and for electronic repositories after expiry of a bar on access.

Signed .... (candidate)

Date ....

Statement 4:

Choose **one** of the following options

a) I agree to deposit an electronic copy of my thesis (the Work) in the Bangor University (BU) Institutional Digital Repository, the British Library ETHOS system, and/or in any other repository authorized for use by Bangor University and where necessary have gained the required permissions for the use of third party material.	
b) I agree to deposit an electronic copy of my thesis (the Work) in the Bangor University (BU) Institutional Digital Repository, the British Library ETHOS system, and/or in any other repository authorized for use by Bangor University when the approved **bar on access** has been lifted.	
c) I agree to submit my thesis (the Work) electronically via Bangor University's e-submission system, however I **opt-out** of the electronic deposit to the Bangor University (BU) Institutional Digital Repository, the British Library ETHOS system, and/or in any other repository authorized for use by Bangor University, due to lack of permissions for use of third party material.	

Options B should only be used if a bar on access has been approved by the University.

In addition to the above I also agree to the following:

1. That I am the author or have the authority of the author(s) to make this agreement and do hereby give Bangor University the right to make available the Work in the way described above.

2. That the electronic copy of the Work deposited in the digital repository and covered by this agreement, is identical in content to the paper copy of the Work deposited in the Bangor University Library, subject to point 4 below.

3. That I have exercised reasonable care to ensure that the Work is original and, to the best of my knowledge, does not breach any laws – including those relating to defamation, libel and copyright.

4. That I have, in instances where the intellectual property of other authors or copyright holders is included in the Work, and where appropriate, gained explicit permission for the inclusion of that material in the Work, and in the electronic form of the Work as accessed through the open access digital repository, *or* that I have identified and removed that material for which adequate and appropriate permission has not been obtained and which will be inaccessible via the digital repository.

5. That Bangor University does not hold any obligation to take legal action on behalf of the Depositor, or other rights holders, in the event of a breach of intellectual property rights, or any other right, in the material deposited.

6. That I will indemnify and keep indemnified Bangor University and the National Library of Wales from and against any loss, liability, claim or damage, including without limitation any related legal fees and court costs (on a full indemnity bases), related to any breach by myself of any term of this agreement.

Signature: …………………………………………………… Date : ……………………………………………

Statement 5:

Referring to Bangor University's "*regulations for the award of the degree of PhD by published works*'", I declare that :

- The submission as a whole is not substantially the same as any that I have previously made or is currently making, whether in published or unpublished form, for a degree, diploma, or similar qualification at any university or similar institution.

- No part of the works submitted has previously been submitted for another qualification

- Until the outcome of the current application to the University is known, the works submitted will not be submitted for any such qualification at another university or similar institution.

  Signature: .... Date: ....

Acknowledgements

Dr Simon P. Neill has contributed to all published works. The majority of the research presented in this thesis would have not existed without his collaboration. It has been a great pleasure for me to continuously work with him since 2006 - my first visit to the School of Ocean Sciences of Bangor University. I would like to thank him for his continues support, guidance, encouragement, and also advising me in writing of this thesis.

I am also very grateful to Prof. Alan J. Elliott for his contribution and support. He was the first one who introduced me to the ocean modelling in realistic conditions and was the reason that I came to Bangor University.

I must thank Prof. Alan G. Davies for his help. His expertise in wave-current interaction, sediment transport, and ocean modelling along with his support has been a great asset for my research. I am in his debt for having always a door open for discussions, sharing his research, and his comments.

I would like to thank Prof. Colin Jago, Dean of College of Natural Sciences, Dr Lewis LeVay, Director of CAMS, and Prof. Chris Richardson, Head of School of Ocean Sciences of Bangor University, for their support and encouragement - without them this accomplishment would not be possible.

I would like to express my appreciation and thanks to my colleagues in School of Ocean Sciences and CAMS, in particular, Prof. David Bowers for his advices, inspirations and feedbacks, Dr Peter Robins and Dr Matt Lewis for sharing their research and their fruitful discussions in all aspects of ocean modelling, Gwyn Roberts and Graham Worley for their technical computer assistance, and Dr John King for his inputs and support. Also, thanks to Dr Ade Fewing for his technical assistance from HPC Wales.

Contents

Nomenclature

Symbol	Description
$\mathbf{c}_g$	Wave group velocity.
C_p	Power coefficient: $C_p = E_k^p / E_k^t$.
E	Wave spectral energy density.
E_k^t	Theoretical tidal energy.
E_k^p	Practical tidal energy.
k	Wave number.
N	Wave action density function.
p	Bed porosity.
P	Wave power or flux of wave energy.
$\mathbf{q}$	Total sediment transport rate (bedload and suspended load); $\mathbf{q} = (q_x, q_y)$.
$\mathbf{Q}$	Various source and sink terms in the wave action conservation energy equation.
T	Period of a tidal cycle.
T_w	Wave period.
U	Current velocity;
u_c	Depth-averaged current velocity; $u_c = \sqrt{u^2 + v^2}$.
z_b	Bed level
θ	Angle of propagation for waves.
κ	Flow field curvature; $\kappa = 1/R$, where R is the radius of curvature.
σ	Wave angular frequency, $\sigma = 2\pi/T_w$.
τ_{cri}	Critical bed shear stress.
τ_c	Current induced bed shear stress.
τ_w	Wave induced bed shear stress.
τ_m	Mean combined wave-current induced bed shear stress.

Chapter 1

Introduction

According to Bangor University's "*regulations for the award of the degree of PhD by published works'*", a candidate should submit his/her published works along with a critical review [1]. The critical review presented here places each work in the context of the existing literature, discusses its contribution, and also demonstrates the coherence and relationship of the published works as a whole in a wider context.

The published works for this submission consist of the eight articles listed in Table 1.1, which have been published, in press, or accepted in peer reviewed journals. Further, other relevant research of the candidate is mentioned in the critical review, but not included in this table or submission.

The published works generally concern the application of computational methods in ocean sciences, in particular, ocean physics. Therefore, an introduction about the philosophy of numerical modelling in ocean sciences and its relation to observational techniques is given first. An overview of the critical review is presented at the end of this chapter.

---

[1] 5,000-10,000 words

Table 1.1 List of the published works

Chapter	**Name**	**Publication details**	Theme
Chapter 2	P-I	Hashemi, M. R. and Neill, S. P. (2014). The role of tides in shelf-scale simulations of the wave energy resource. *Renewable Energy*, 69. 300-310.	Hydrodynamic modelling; ocean energy
Chapter 2	P-II	Neill, S. P. and Hashemi, M. R. (2013). Wave power variability over the northwest European shelf seas. *Applied Energy*, 106:31–46.	
Chapter 2	P-III	Neill, S. P., Hashemi, M. R., and Lewis, M. J. (2014). The role of tidal asymmetry in characterizing the tidal energy resource of Orkney. *Renewable Energy*, 68:337–350.	
Chapter 2	P-III-A	Hashemi, M. R., Neill, S. P., Robins, P. E., Davies, A. G., and Lewis, M. J (2015). Effect of waves on the tidal energy resource at a planned tidal stream array. *Renewable Energy*, 75. 626–639.	
Chapter 3	P-IV	Neill, S. P., Hashemi, M. R., and Elliott, A. J. (2007). An enhanced depth-averaged tidal model for morphological studies in the presence of rotary currents. *Continental shelf research*, 27(1):82–102.	Morphodynamic modelling
Chapter 3	P-V	Neill, S. P., Elliott, A. J., and Hashemi, M. R. (2008). A model of inter-annual variability in beach levels. *Continental Shelf Research*, 28(14):1769–1781.	
Chapter 3	P-VI	Hashemi, M., Ghadampour, Z., and Neill, S. (2010). Using an artificial neural network to model seasonal changes in beach profiles. *Ocean Engineering*, 37(14):1345–1356.	
Chapter 4	P-VII	Hashemi, M. R., Neill, S. P., and Davies, A. G. (2014). A coupled wave-tide model for NW European shelf seas. *Geophysical and Astrophysical Fluid Dynamics*. in press. DOI:10.1080/03091929.2014.944909	Coupled models

1.1 Computational versus observational methods in ocean sciences

Observational techniques such as in-situ measurement and remote sensing provide the most reliable sources for understanding the processes in the oceanic environment, and more generally in physics. Many important laws of physics such as Newton's Law of motion have originated as a result of direct observation. Nevertheless, observational methods have a number of limitations: a) they cannot be used in hypothetical 'future' scenarios (e.g. what impact a tidal barrage would have on sea-level?), b) they are limited to the period when the observed data are available (e.g. what was the sea state and tide 1000 years ago?), c) they cannot be implemented in forecasting (e.g. what is the wave height at Holyhead Port tomorrow at 12:00?), and d) for full temporal-spatial coverage of a process at a region, they are not feasible in terms of cost and/or time (e.g. a high resolution map of the tidal energy resources for the Irish Sea). Computational methods not only help overcome these shortcomings, but they are the only tool which enable scientists to evaluate their conceptual models or test their hypotheses in a complex ocean system.

Recent advances in computer technology and high performance computing have made exceptional contributions in understanding the natural environment. For instance, computational physicists have been able to simulate the formation and evolution of the galaxies and explain the shape of the universe - which compares well with the observations - using numerical modelling, something impossible not long ago (Springel et al., 2005).

However, the development of complex coupled numerical models should be accompanied and supported by enough observations in order to set input parameters, to select proper model physics (e.g. the best sediment transport formula in a morphodynamic model), and to validate model outputs. Therefore, a mixture of observation and modelling is the best approach in ocean sciences (Simpson and Sharples, 2012).

1.2   Structure of the critical review

In brief, Chapters 2 and 3 concentrate on hydrodynamic and morphodynamic modelling, respectively, in the UK shelf seas. Then, Chapter 4 reviews the recent attempts to use coupled modelling systems, where many processes including hydrodynamics and morphodynamics can be simulated in a unified framework.

Chapter 2 is dedicated to ocean - tidal and wave - energy research in the UK shelf seas. Some gaps in the current literature about wave power resource assessment are discussed initially, some of which are addressed in Papers **P-I** and **P-II**. Then, a review of tidal-stream energy is presented in relation to **P-III**, and **P-III-A**. Although the first and the second section of Chapter 2 deal with wave and tidal renewable energy, respectively, the interaction of waves and tides is one of the main research topics considered in this chapter. Therefore, tidal modelling was implemented in a published work concerning the wave energy, and similarly, wave modelling was a part of another work concerning tidal-stream energy.

Chapter 3 covers the critical review of earlier published works with regard to sediment transport and morphodynamic modelling in the Irish Sea. Since marine sediments are transported by the combined action of currents and waves, hydrodynamic modelling is still a fundamental element of the research in this area. An introduction about data-based versus process-based models is presented. Then, **P-IV**, which applies a hydrodynamic and sediment transport model to simulate the formation of sand banks in the presence of rotary currents, is reviewed. **P-V** uses a similar approach to predict beach profile changes in coastal zones where the longshore transport is mainly responsible for morphodynamic changes. Finally, **P-VI**, which applies an artificial neural network model for morphodynamic modelling of the nearshore zone, is reviewed in this section.

Coupled numerical models - which are able to include hydrodynamic as well as morphodynamic processes - are considered in Chapter 4, in relation to **P-VII**. This chapter attempts to discuss the advantages of using this approach while examining its potential drawbacks such as computational cost, validation, and uncertainty. Further, it briefly introduces prospective future research direction.

Chapter 2

Numerical modelling in ocean energy research

2.1 Introduction

Ocean renewable energy is a vast untapped resource which has the potential to supply the world's demand for electricity (Bahaj, 2011). Due to the many advantages of this resource - high security and lower environmental impact compared with non-renewable resources- many countries are investing in ocean tidal/wave energy development alongside other more established forms of renewable energy such as offshore wind or low carbon energy such as nuclear. The UK shelf seas dissipate an estimated 10% of global tidal energy (0.25TW), and are considered one of the best tidal energy resources in the world (Egbert and Ray, 2000). The UK is leading many tidal energy studies and projects, including the EMEC [1] test centre in Orkney.

Numerical modelling has a key role in ocean renewable energy studies at various scales and stages of a project, from the hydrodynamic design of devices, through to resource quantification, and environmental impact assessment. In particular, ocean modelling is the best, and sometimes the only, method with which to address several "what if" questions arising from design scenarios in real case studies (Xia et al., 2010). Nevertheless, numerical mod-

---

[1]European Marine Energy Centre

els still face various challenges in this area. For instance, traditional ocean models have not been developed to fully incorporate the realistic effects of ocean renewable energy devices and simulate the feedback between energy extraction and the resource. The scale of fluid-structure-foundation (bed sediment, local scouring) interaction of a Tidal Energy Convertor (TEC) is still considered small (i.e. sub-grid scale) when compared to oceanic scales (Neill et al., 2012). Consequently, there is a gap between high resolution computational fluid dynamic (CFD) modelling at device scale (Mason-Jones et al., 2012) and regional scale ocean modelling, although both approaches share the same fluid dynamic and numerical modelling principles (Sun et al., 2008). Further, many observations regarding the interaction of a TEC with the ocean environment are based on laboratory studies (e.g. Batten et al. (2007)), which do not take into account realistic conditions including background turbulence (Thyng et al., 2013), the presence of oblique waves, and wave-current interaction. Therefore, more research is needed, firstly to understand the interaction of a TEC with realistic ocean environments, and secondly to implement such interactions within ocean models.

The existing literature regarding applications of ocean models in renewable energy research can be divided into 4 categories: theoretical/practical resource assessment, impacts of renewable devices on the environment, characterising the environmental conditions of renewable energy devices (e.g loading), and array optimisation on a local or a regional scale (e.g. Neill et al. (2014a)). The published works which have been considered in this review concern the first category: resource assessment.

2.2   Wave power

Papers **P-I** and **P-II** attempt to address some issues related to the quantification of the wave resources over the NW European shelf seas - one of the most attractive regions in the world for the development of wave energy projects. In a realistic sea state, where the directional-spectral-energy-density function, $E(\mathbf{x}, t, \sigma, \theta)$ represents the wave energy, the theoretical

wave power or flux of wave energy, P, is evaluated as follows:

$$P(\mathbf{x},t) = \int \int \mathbf{c}_g(\mathbf{x},t,\sigma,\theta) E d\sigma, d\theta \qquad (2.1)$$

where $\mathbf{c}_g$ is the group velocity (see list of symbols at Page viii), and can be quantified through spectral models. The exploitable/practical wave energy resource is then the amount of wave energy that is exploitable by a wave energy convertor; hence, it is dependent on a particular device technology.

Spectral wave models - such as SWAN- solve the evolution of the directional spectrum of the wave action,[2] $N = E(\sigma,\theta)/(\rho g \sigma)$. The balance equation for spectral wave action can be written as:

$$\frac{\partial N}{\partial t} + (\mathbf{c}_g + \vec{u_c}) \cdot \mathbf{grad}_{\vec{x},\vec{k}}(N) = \mathbf{Q} \qquad (2.2)$$

where $\mathbf{Q}$ represents sources/sinks of energy: wind energy input, white-capping, bottom friction, depth-induced wave breaking, non-linear wave-wave quadruplet and triad interactions. The left hand side of the above equation shows the total rate of change of N (local and convective derivatives).

2.2.1 Effect of tides on the wave power resource

Waves and tides - or currents in a wider context - interact with each other; in theory, wave energy resources should be affected by tides and vice versa. Horizontal and vertical tides (i.e. tidal currents and water level variations) alter waves through the following mechanisms:

- wave period by the Doppler effect

- wave group velocity by current field and water depth variations

- wave kinematics (e.g. refraction) as a result of change in the wave properties noted above

---

[2]Wave action density, rather than wave spectral density, is used as the state variable in these models, since it is conserved in the presence of ambient currents (Benoit et al., 1996; Booij et al., 1999).

Spectral models like SWAN have implemented the ambient hydrodynamic field in their formulations and are able to simulate the effect of tides on waves: 1-way/off-line coupling. Nevertheless, until recently, the effects of tides on wave energy resources have been ignored in large to local scale studies which have been based on the uncoupled wave models [e.g. global (Arinaga and Cheung, 2012), NW European shelf seas (Paper **P-II**), EU (Pontes, 1998), UK (ABPmer, 2008), Australia (Hughes and Heap, 2010), and Mediterranean (Liberti et al., 2013)]. In contrast, in observation-based wave resource assessments, based on satellite altimetry data or wave buoys, the effect of ambient currents on the wave signal is implicitly included; however, it is still difficult to separate the effect of tides from a wave signal, and investigate how the tide has contributed to the net wave energy resource. For instance, similar wind events can happen at different stages of the tide (e.g. spring, neap, flood, ebb), and the effect of tides during such events will vary. Besides, due to high inter-annual, inter-seasonal, and spatial variability of the wave resource, it is not usually feasible to characterize it by observations alone.

Paper **P-I** assesses the effect of wave-tide interactions on the wave resources of the NW European shelf seas - a region where tides and waves are concurrently strong and where many wave/tidal energy projects are under development. Two other researchers have also investigated the same effect on the wave resources of Orkney (Saruwatari et al., 2013) and the Adriatic Sea (Barbariol et al., 2013). Saruwatari et al. (2013) implemented the SWAN wave model and MOHID Water Modelling System (MARTINS et al., 2001) for computation of the tidal currents and elevations. They reported a very significant impact of tides on the wave properties. Barbariol et al. (2013) implemented the same modelling system (ROMS+SWAN) as in Paper **P-I**, and concluded that wave resource estimation can alter by up to 10% due to wave-current interaction effects. Paper **P-I** has two main contributions: it proposes a simplified method, based on linear wave theory, to quickly estimate the effect of tides on wave power, and it quantifies the impact in the NW European shelf seas, as a strategic case study. However, further research was necessary to improve the results presented in Paper **P-I**: firstly, the SWAN model was not nested within a larger model; hence, the model results were not accurate near the boundaries; secondly, the model coupling was

1-way/offline and the model performance could be improved by the 2-way coupling technique. Paper **P-VI**, which is discussed in Chapter 3, addresses both issues. Some research questions and highlights of Paper **P-I** are summarised as follows:

Research questions of Paper **P-I**

- Why should the effect of tides be considered in wave power estimations?

- Is there a quick way to estimate the order of magnitude of this effect at a tidal-stream site, without resorting to expensive modelling?

- Which component of tides - tidal depth variations or tidal currents - has the greatest impact on wave power estimations?

- What type of waves - low or high frequency - are likely to be more affected by tides?

- In which regions of the NW European shelf seas should this effect be considered in more detail?

- To what extent can a shelf-scale study determine the effect of tides on wave power estimations?

Highlights of Paper **P-I**

⋄ A simplified/analytical method based on linear wave theory is presented, which can be used to give a rapid estimate of the impact of tides on the wave power estimation at a region using basic wave and tidal information.

⋄ The impact of tides on the wave energy resources can exceed 10% in some regions of the NW European shelf seas.

⋄ The effect of tidal currents generally exceeds the effect of tidal water depth variations.

⋄ The effect of tides is greater in low to medium wave energy sites.

⋄ The effect of tides is significant in high wave energy sites with strong tides.

2.2.2   Inter-annual and inter-seasonal variability

Wave power, which is generated by the wind shear stress, is highly unpredictable in contrast to the regularity of tidal power. It has a high inter-seasonal, inter-annual and even long term decadal temporal variability (e.g. Reguero et al. (2013)). This uncertainty in the wave resource is considered as a major drawback for investment in the wave energy sector (Guanche et al., 2014; Mackay et al., 2010). In addition to the temporal variability, wave parameters may vary considerably within a region of interest - unlike wind energy - as a result of several mechanisms: refraction, diffraction, and sinks of wave energy (e.g. bed friction). Consequently, the wave resource of a site cannot be quantified by a single wave-buoy deployment over a year, or using available coarse resolution wave data products: Atlas of UK Marine Renewable Energy Resources (MRES) has a resolution of $1/6^o \times 1/9^o$ for the wave energy map (ABPmer, 2008).

Paper **P-II** quantifies the inter-annual and inter-seasonal variability as well as the uncertainty of the wave resources over the NW European shelf seas - a region where many wave projects are under study/development. It also improves the spatial resolution of the resource assessment (i.e. $1/24^o$, around 4km) by virtue of high performance computing. Presentation of resource maps along with the uncertainty maps is a novel and useful methodology in Paper **P-II** compared with similar studies. The inter-annual and/or inter-seasonal variability of the wave energy resources has been investigated for other regions of the world: Lanzarote, Spain (Sierra et al., 2013), Persian Gulf (Kamranzad et al., 2013), Orkney (Neill et al., 2014b), and the French Coasts (Gonçalves et al., 2014).

Further research can be conducted to improve the results published in Paper **P-II**. For instance, Bromirski et al. (2013) reported an upward long term decadal trend in the wave power and the significant wave height across the North Pacific during the period 1948-2008. Therefore, the wave power needs to be simulated for a much longer period (30 years) to examine such inter-decadal trends. Also, an unstructured mesh, instead of the applied regular grid, can be implemented to improve the model results near the coasts (Hope et al., 2013; Zijlema, 2010) - where the first generation of wave devices are being deployed.

Paper **P-II** demonstrated a strong correlation between the wave power and the North

Atlantic Oscillation index, which is a source of the inter-annual variability in the North Atlantic climate (Hurrell, 1995; Ruprich-Robert and Cassou, 2014). This opens another discussion: whether the wave power will change in the future, in particular, in relation to climate change. Reeve et al. (2011) showed a small reduction - less than 3% - at the Wave Hub site off the coast of Cornwall, UK from 2061 to 2100. Although a 3% change might have considerable implications in financial terms for a project, the natural inter-annual variability and uncertainty in wave models are still higher than these values. Some research questions and highlights of Paper **P-II** are summarised as follows:

Research questions of Paper **P-II**

- ✐ How accurate is the Atlas of UK Marine Renewable Energy Resources - given its resolution and the wave modelling methodology (i.e. second generation wave model)?

- ✐ Since wave developers may use the annual/seasonal mean values for the wave power development, can we quantify the uncertainties of this method?

- ✐ Is uncertainty in the wave power resource significantly variable for each season?

- ✐ Is uncertainty of the wave power resource considerably variable for each region in the NW European shelf seas?

- ✐ Is there a method to estimate the wave power variability in the future (e.g. as a consequence of climate change)?

Highlights of Paper **P-II**

- ◇ The wave climate of the NW European shelf seas was simulated over a 7 year period using a high resolution 3rd-generation wave model.

- ◇ The spatial/temporal patterns of uncertainties, in estimating the wave power resource, were quantified.

- ◇ The 2nd generation wave model which was used to compile the Atlas of UK Marine Renewable Energy Resources may have overestimated wave power.

◇ Uncertainty is considerably greater over winter months.

◇ There is a positive correlation between the winter wave power and the NAO (North Atlantic Oscillation) index; therefore, the variability of the NAO in the future can indicate the variability of the wave power (e.g. due to climate change). Nevertheless, there is a debate in the literature about how the NAO will vary as a consequence of climate change.

2.3   Tidal power

2.3.1   Introduction to tides in the northwest European shelf seas

The generation and propagation of tidal waves have been studied for centuries, and are relatively well understood concepts in oceanography (Pugh, 1996). Gravitational attractions of the Moon and the Sun on the oceans are the origins of tides; the propagation of generated tidal waves is governed by the Earth rotation, friction, and the shape of ocean boundaries (i.e. continental shelves). The principal lunar semi-diurnal tide (known as M_2), which is generated by the Moon, is the main component of the tide in many places including the northwest European shelf seas. Since the Earth and the Moon rotate in the same direction, it takes slightly more than 24 hours (i.e. a lunar day) for the Earth to return to the same position relative to the Moon: 24+1/27.32 hrs $\approx$ 24.88 days or 24 hours and 50 minutes. Referring to Fig. 2.1, the gravitational attraction of the Moon is inversely proportional to the square of the distance and varies over the surface of the Earth; therefore, the strongest attraction - on the side of the Earth facing the Moon - has a period of a lunar day. The side of the Earth away from the Moon experiences the weakest attraction at the same time. Further, the centrifugal acceleration is the same everywhere on the earth, while the gravitational force of the moon varies depending on the distance to the Moon. Consequently, as a result of the imbalance between the centripetal force and gravitational force on these sides (maximum imbalance), two bulges one on either side of the earth are formed - one by the Moon attraction, and the other one by excess centrifugal force - which result in two high tides during a lunar day or
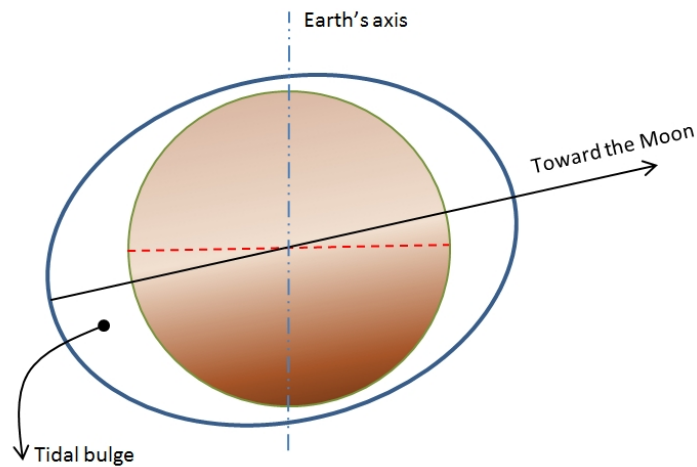
Fig. 2.1 Schematic of semi-diurnal tide generation.

every 12 hours and 25 minutes.

The propagation of the resulting tidal waves in the oceans and continental shelves is primarily affected by the Earth rotation. The dynamics of long waves on a rotating system was originally described by Lord Kelvin. In a rotating reference frame like the Earth, Newton's second Law of motion - which is valid for inertial frame of reference with zero acceleration - cannot be directly applied. By introducing Coriolis as a 'fictitious force', we can use Newton's second Law in the Earth rotating system. In the northern hemisphere, the Coriolis force causes a deflection of the currents towards the right of the direction of motion (e.g. currents toward the pole are deflected to the east). This deflection of flow continues until the flow reaches the right-hand boundary (i.e. coastline) where the build-up of water leads to a pressure gradient. A Kelvin wave propagates as a result of the balance between these two forces. Standing oscillating waves are a special case of interest. When a Kelvin wave enters a basin, it will be reflected at the head of the basin; therefore, from a simplified viewpoint, the tidal wave in a basin can be represented by two Kelvin waves travelling in opposite directions. These waves rotate around a node which is called an amphidrome. The cotidal contour lines radiate outwards from the amphidrome, and tidal amplitude is zero at this node. Considering an idealised rectangular basin and using the above concept, it is

easy to demonstrate why in the northern hemisphere, the direction of the rotation around an amphidrome is anticlockwise.

With regard to the dynamics of tides in the northwest European shelf seas (e.g. Huntley (1980)), the Atlantic semidiurnal anticlockwise Kelvin wave travels toward the north and transfers the tidal energy into the Celtic Sea between Brittany and southern Ireland. Part of this energy propagates into the English Channel and the Irish Sea. The Atlantic Kelvin wave further progresses northwards and deflects toward the east, travels to the North of the Shetland isles, and enters the North Sea. Tides in the North Sea are primarily semidiurnal with two amphidromes in the southern North Sea and a third around the southern tip of Norway. The south travelling wave which moves along the east coast of the UK, generates the the largest amplitudes.

Tides in the northwest European shelf seas provide another forms of ocean energy which is considered here. The existing literature about tidal energy can be classified into tidal-range and tidal-stream research corresponding to vertical and horizontal tides, or potential and kinetic energy of tides, respectively. The theoretical tidal kinetic-energy per unit area, over a tidal cycle is given by:

$$E_k^t = \int_0^T \frac{1}{2} \rho |U|^3 dt \tag{2.3}$$

where T is the period of tide, U is the current velocity, and ρ is the water density. The practical tidal power, which is developed by a generator, depends on the the cross-sectional area of a turbine rotor, A, and the power coefficient, C_p (i.e. efficiency), and is given by:

$$E_k^p = \int_0^T \frac{1}{2} C_p \rho |U|^3 A dt \tag{2.4}$$

The power coefficient for a tidal turbine depends on a specific device, and varies with current speed.

Paper **P-III** concerns tidal-stream modelling at Orkney, where the European Marine Energy Centre (EMEC) was established in 2003 emphasising its unique ocean energy resource. This chapter ends with a section which complements Section 2.2.1 in terms of the impact of

waves on tidal-energy resource.

2.3.2   Turbulence, vertical structure and asymmetry

A TEC - even a tidal-stream array - is very small compared with the grid scale of a typical ocean model. Consequently, neither the spatial variability of hydrodynamic parameters (velocity, turbulence, pressure, etc.) around a TEC nor the interaction of the device with the surrounding hydrodynamic field - and the sea bed - is resolved in such simulations. On the other hand, CFD models which attempt to model a TEC within the flow using appropriate grid scales, cannot accommodate large scale oceanographic circulations and realistic environmental forcings which control the hydrodynamic field at a tidal-stream site.

Paper **P-III** tries to address a part of this knowledge gap by using a more advanced 3-D fine resolution ocean model. It is a common practice to use 2-D depth-averaged models for simulation of tidal currents at tidal-stream sites (e.g. Blunden and Bahaj (2006); Draper et al. (2014); Robins et al. (2014); Serhadlıoğlu et al. (2013)) in which the vertical variability of hydrodynamic parameters is entirely ignored, or parameterised by idealised velocity distributions (e.g. logarithmic). The vertical variability of velocity, for instance, is important in relation to the hub-height of a TEC. Also, the background turbulence, which is caused by bottom boundary layer or surface wind waves, can result in additional fatigue loads on turbine blades. Application of 3-D ocean models can improve the simulation of hydrodynamic fields at tidal-stream sites in these respects. Recently, other researchers have started to employ 3-D models to study the resources or impacts (e.g. on residual flows) of tidal energy sites (Sánchez et al., 2014).

Paper **P-III** also assesses the asymmetry of tidal flows around Orkney and relates this asymmetry to the super-harmonic (i.e. over-tides and compound tides) tidal constituents. This concept can be applied to a much wider extent; since tidal asymmetry can have important financial/technical implications for the development of tidal energy at a site, charts of super-harmonic tidal components can be generated as a quantification of tidal asymmetry around the UK or elsewhere. Some research questions and highlights of Paper **P-III** are summarised as follows:

Research questions of Paper **P-III**

- ℘ Considering the increased modelling cost, what are the advantages of using an advanced 3-D regional ocean models for tidal energy resource assessments, compared with less expensive 2-D depth averaged models?

- ℘ How does tidal asymmetry affect the tidal energy resources?

- ℘ Is there a way to characterise tidal asymmetry without modelling, using super-harmonic tidal components?

- ℘ For a tidal-stream site which has a dominant wind climate, can wind generated currents contribute to the asymmetry of the tidal power?

Highlights of Paper **P-III**

- ◇ A high-resolution 3-D ROMS tidal model of Orkney was developed which quantified the vertical variability of the tidal energy resource, in relation to the hub heights of tidal energy devices as well as turbulence.

- ◇ 3-D ocean models can quantify the background turbulence properties: turbulence kinetic energy, and dissipation. However, due to strong tidal currents in those sites, observed turbulence data are very limited - which are needed to validate model outputs.

- ◇ M_2/M_4 phase relationship can predict the degree of asymmetry for a tidal site.

- ◇ A small asymmetry (e.g. 30 %) in current velocity can lead to significant asymmetry in tidal power (e.g. 100%).

- ◇ For our study site, during periods of spring tides, a strong gale had minimal impact on tidal power asymmetry. However, during periods of neap tides, the relative impact on asymmetry is much greater, with a consistent impact at all considered hub heights.

2.3.3   Impact of waves on the tidal energy resource

The impact of tides on wave power was discussed in Section 2.2.1. This has been comple-
mented recently by further research, **P-III-A**, which was carried out for the reverse scenario
(i.e, the impact of waves on tidal power).

As mentioned before, previous research has shown that wave-current interaction pro-
cesses can change the hydrodynamics of tidal currents through several processes including
wave induced forces and enhanced bottom friction (e.g. Davies et al. (1988); Soulsby et al.
(1993); Wolf and Prandle (1999)); hence, waves can potentially alter the tidal energy re-
source of a site. These effects can be significant for water depths less than 50m (Prandle,
1997), where a majority of the first generation tidal devices are likely to operate. The theory
of Wave Effects on Currents (WEC) has been extensively developed in previous research,
and can be implemented using a range of coupled Ocean-Wave-Sediment Transport mod-
els. In this respect, **P-III-A** has assessed the effect of waves on the tidal energy resources
of the Skerries Marine Current Turbines - or other companies- site. The site is within the
coastal waters of Anglesey, North Wales, which is one of the 'hot spots' for tidal-stream
development, and is likely to be one of the first sites for a commercial tidal array in UK
waters. The results of this study showed that due to the combined effects of wave radia-
tion stresses and enhanced bottom friction, the tidal energy resource can be reduced by up
to 15% and 20% during mean and extreme wave scenarios, respectively. The results were
based on a high-resolution unstructured coupled wave-tide model of the region, which was
developed using the finite element method. Other research, which is based on a 3-D cou-
pled ROMS-SWAN model of an idealised headland, suggests similar effects (Lewis et al.,
2014). Some research questions and highlights of Paper **P-III-A** are summarised as follows:

Research questions of Paper **P-III-A**

    ℘   Is effect of waves on the energy resource of a tidal-stream array significant?

    ℘   Is this effect negative or positive (for a dominant wave climate at a region)?

    ℘   Can wind shear stress considerably alter the distribution or magnitude of this effect?

Highlights of Paper **P-III-A**

    ◇   A simple method to include the effect of waves on tidal currents in the TELEMAC model was introduced.

    ◇   As a result of the combined effects of wave radiation stresses and enhanced bottom friction, the tidal energy resource can be reduced by up to 15% and 20% for mean and extreme winter wave scenarios, respectively, at a relatively exposed tidal stream site.

    ◇   The effect of WCI processes on tidal energy increases as the ratio of wave stress to current stress increases. Therefore, this effect is more significant for lower tidal energy sites which are exposed to strong waves, rather than higher tidal energy sites which are exposed to moderate waves.

    ◇   The wind generated currents, due to wind shear stress, can alter the distribution of this effect.

Chapter 3

Data-based and process-based numerical models in ocean morphodynamic simulations

3.1 Introduction

This chapter reviews three papers regarding morphodynamic modelling. Morphodynamics can be defined as (Cowell et al., 1994): "mutual adjustment of topography and fluid dynamics involving sediment transport". The hydrodynamic field drives the sediment transport, which leads to morphological (bed-level) changes. These changes affect the boundary conditions of the flow field, which in turn causes further changes in sediment transport and morphodynamics. Accordingly, morphodynamic processes are inherently nonlinear due to feedbacks between the flow field, sediments, and the bed level. Understanding the nearshore/offshore morphodynamics is essential in many areas of ocean research: coastal erosion, sand bank dynamics, dredging, marine aggregate extraction, interaction of ocean energy devices with the physical environment (e.g. local scouring), coastal management, navigation, and ocean hydrodynamics. As a fundamental concept of morphodynamics, Exner's law relates the bed level (z_b) changes to the divergence of the sediment transport

rate ($\mathbf{q}$) (Wang et al., 1995):

$$\frac{\partial z_b}{\partial t} = \frac{\nabla.\mathbf{q}(\tau_m, \tau_{cri})}{1-p} \qquad (3.1)$$

where p is the bed porosity, τ_{cri} is the critical bed shear stress, $\mathbf{q}$ is the total sediment transport rate, and τ_m is the mean combined wave-current induced bed shear stress given by,

$$\tau_m = \tau_c \left\{ 1 + 1.2 \left(\frac{\tau_w}{\tau_c + \tau_w} \right)^{3.2} \right\} \qquad (3.2)$$

in which τ_c and τ_w are the current-induced and wave-induced bed shear stresses, respectively. The enhancement of the bed shear stress felt by currents - in the presence of waves - is due to the interaction with the wave boundary layer, and should be included in sediment transport modelling (Soulsby, 1997). Accordingly, since ocean sediments move by the combined action of waves and currents, hydrodynamic modelling is still discussed in this chapter. Paper **P-IV** applies a mathematical technique to enhance the morphodynamic simulations of sandbanks in offshore zones using the POLCOMS [1] ocean model. Paper **P-V** employs a set of hydro-morphodynamic models - including POLCOMS and SWAN - to assess the inter-annual variability of beach profiles for a case study in northern Cardigan Bay, Irish Sea. Using the same beach profile data-set, Paper **P-VI** improves the prediction of beach profile changes by implementing an artificial neural network which is a purely data-based method. As paper **P-VI** implements a fundamentally different approach to morphodynamics, compared with that of Papers **P-V** and **P-IV**, a general introduction about data-based and process-based approaches is provided here.

3.1.1   Data-based versus process-based techniques in ocean sciences

Process-based ocean models describe ocean processes and their interactions in mathematical terms, usually as a system of partial differential equations, and predict them by numerically solving those equations. They also contain parameters whose values represent intrinsic properties of the system (e.g. grain roughness, molecular viscosity, water density)

---

[1]Proudman Oceanographic Laboratory Coastal Ocean Modelling System

which are determined from direct measurement. A majority of ocean and atmosphere circulation models (e.g. ROMS, SWAN, WRF[2]) 'almost' [3] fall into this category where their formulations are derived from the principles of mass, momentum, energy, and tracer conservation. Process-based models are subject to several sources of uncertainty: assumptions and simplifications of the governing equations, discretisation and numerical errors, model input parameters/data, and initial/boundary conditions.

Where uncertainties associated with the processes and their interactions are high (e.g. longshore sediment transport[4]), fundamental mathematical equations which can represent the underlying physical processes are unavailable. Accordingly, empirical or statistical approaches attempt to correlate the variables, usually inputs and outputs, using any mathematical expression, and regardless of the scientific laws which underlie the system (Hsieh and Tang, 1998). Black-box or data-based models, as opposed to white-box/process-based, are other terms used to describe this alternative approach.

Many ocean models comprise a combination of data-based/empirical and process-based components. For instance, in morphodynamic simulations using the COWAST[5], the hydrodynamics of flow is simulated by a process-based model while the sediment transport formulations can be based on empirical relationships.

Another data-based measure to improve a model representation of 'reality' is data assimilation. As oceanographic observations including in-situ and remote-sensing data increases, a large number of techniques have been developed to reduce uncertainties associated with ocean models using inverse modelling (Di Lorenzo et al., 2007; Wunsch, 1996).

If the performance of an ocean model is only evaluated by comparison of the model outputs and observations, empirical-based techniques can outperform process-based models using simpler and even more efficient computations. However - like observational techniques - they cannot be used in hypothetical 'future' scenarios, as discussed later.

---

[2]Weather Research & Forecasting

[3]For instance, some source terms in SWAN, or some turbulence models in ROMS are empirically based.

[4]The widely used method proposed by Kamphuis (1991) is entirely based on a statistical/empirical formula.

[5]Coupled Ocean-Atmosphere-Wave-Sediment Transport modeling system

3.2   Morphodynamic simulation of offshore sandbanks using process-based models

Paper **P-IV** applies a mathematical technique to enhance the morphodynamic simulations around headlands and sandbanks when using depth averaged models. Due to low computational cost and fewer stability issues, 2-D depth averaged hydrodynamic models are still popular in research and industry despite their limitations (Stansby, 2006). However, because of the 3-D spiral (helical) nature of the flow in rotational hydrodynamic fields (i.e. eddies), they cannot fully accommodate secondary flows which are mainly responsible for the convergence of sediments toward the centre of eddies. Early studies in river mechanics attempted to explain/simulate similar processes which resulted in the sediment deposition of inner-banks and erosion of outer-banks of river meanders (Kikkawa et al., 1976). Paper **P-IV** proposed a simplified method to estimate the strength of secondary flows based on the flow curvature (κ), and depth averaged velocities [i.e. $\mathbf{u}_s = f(\mathbf{u}_m, \kappa, \text{other parameters})$]. The central idea of the methodology was to compute the *curvature field* of a 2-D hydrodynamic flow field as follows (Theisel, 1995):

$$\kappa = \frac{u^2 \frac{\partial v}{\partial x} - v^2 \frac{\partial u}{\partial y} + uv \left(\frac{\partial v}{\partial x} - \frac{\partial u}{\partial y} \right)}{(u^2 + v^2)^{3/2}} \tag{3.3}$$

in which u and v are the depth averaged components of velocity. The above relation is easy to implement into models with structured grids (e.g. POLCOMS). Later, Begnudelli et al. (2010) proposed a method applicable to unstructured meshes. Other models such as SISYPHE - the sediment transport module of TELEMAC (Hervouet, 2000) - have also incorporated a procedure to account for secondary flows (Tassi and Villaret, 2014). SISYPHE's method is based on a formula proposed by Engelund (1974). This method was originally developed for river flows, where curvature and friction are the main forces which generate secondary currents. However, the analysis which has been provided in Paper **P-IV** covers other scenarios. For instance, when the Coriolis force is dominant, the strength of the secondary flow is proportional to the Coriolis coefficient rather than flow curvature.

An interesting application of morphodynamic simulations in the presence of a rotary current is the mechanism for the formation of sandbanks. Understanding of sandbank dynamics is important in navigation, dredging, and marine aggregate extraction. Sandbanks, which are often formed and maintained by tidal eddy systems, provide a natural coastal protection due to enhanced dissipation of wave energy. The dynamic involved in the formation and maintenance of sandbanks has been extensively studied in the past literature (e.g. Berthot and Pattiaratchi (2006); Dyer and Huntley (1999); Huthnance (1982a,b); Komarova and Newell (2000)). The methodology which was first implemented in Paper **P-IV** was then used in the study of sandbanks in subsequent research (Neill, 2008; Neill and Scourse, 2009). A notable application is the impact of tidal-stream energy extraction on sandbanks (Neill et al., 2012), which nicely connects the published works of this chapter with the previous chapter. Some research questions and highlights of Paper **P-IV** are summarised as follows:

Research questions of Paper **P-IV**

✐ How can we estimate the strength of secondary flows in a depth averaged model using the main flow field?

✐ Can we quantify the contribution of the flow curvature, bottom friction, Coriolis, and advection in generating the secondary flows?

✐ Can we predict the formation/maintenance of sand banks, in a case study at northern Cardigan Bay, using a simplified method which takes into account secondary flows?

Highlights of Paper **P-IV**

◇ An analytical formula, based on the main flow field, was applied to simulate the secondary flows. The estimated secondary currents were in good agreement with the results from a 3-D POLCOMS model and ADCP data taken through eddies generated around a headland.

◇ The enhanced model produced accumulation of sediment in the region of existing sand banks.

◇ The relative importance of governing factors in generating secondary flows should be estimated first for a region; then, a similar procedure can be implemented to evaluate the strength of secondary currents.

3.3 Morphodynamic simulation of nearshore zone using process-based and data-based techniques

Papers **P-V** and **P-VI** attempt to model beach profile changes as a consequence of storm events. Two likely consequences of climate change, sea-level rise and increased storminess (Beniston et al., 2007), have raised concerns about coastal erosion (Zhang et al., 2004). For instance, the UK Met Office[6], has recently reported the impacts of successive storms: "*From*

---

[6]www.metoffice.gov.uk/climate/uk/

mid-December 2013 to early January 2014, the UK experienced a spell of extreme weather as a succession of major winter storms brought widespread impacts to the UK" which resulted in coastal flooding, erosion and several properties and infrastructure collapsing into the sea. Consequently, it would be very useful (e.g. in coastal management) to develop a tool which can predict the change in beach profiles as a result of a single or successive storm events (Splinter et al., 2014).

It can be argued that understanding the intertidal/surfzone morphodynamics is more complex than that of the offshore zone due to several interrelated processes: depth-induced wave breaking, wave-current interaction, wetting and drying, longshore transport, complex beach geometry (e.g. natural dunes), and human impacts. Therefore, prediction of beach profile change has been considered as a challenge in the past(Roelvink and Brøker, 1993; Wright and Short, 1984) while more success has been reported in recent studies (Karunarathna et al., 2014). The process-based approach involves the implementation of a suite of deterministic models to predict wave, tide, longshore transport, and the resulting changes in bed level. Paper **P-V** applies this approach using SWAN (wave model), POLCOMS (tide model), and a bed level change numerical scheme to simulate inter-annual variability in beach levels over a 7 year period in northern Tremadoc Bay, within northern Cardigan Bay, Irish Sea. Despite success in predicting the beach profiles, some discrepancies were identified which can be associated with the model simplifications such as resolution (which was coarse at the nearshore zone), neglecting cross-shore sediment transport, sediment supplied by rivers (Pranzini et al., 2013), and the effect of the swell waves. Further, the development of a morphodynamic coastal model is a time consuming and computationally expensive task due to the number of models which should be validated separately, the complexity of the sediment transport dynamics in this zone, and the inter-annual variability of the beach profiles which means that many years/decades of simulation are required. Some research questions and highlights of Paper **P-V** are summarised as follows:

Research questions of Paper **P-V**

- ✏ Is a cascade of tide, wave, longshore transport, and morphodynamic models able to predict the response of the beach to storm events in a wave exposed bay?
- ✏ Given the inter-annual variability of the beach profiles, how can we use an expensive wave model - with 3 stages of nesting - for a long period (7 year) simulation?
- ✏ What are the sources of uncertainty in simulating the evolution of beach profiles?

Highlights of Paper **P-V**

- ◇ An innovative wave modelling technique was used to predict waves over a 7 year period.
- ◇ A suite of numerical models was used to simulate the morphological development of a wave exposed bay.
- ◇ Although, the model results had reasonable agreement with the beach profile surveys, the observed magnitude of bed level changes in the bay lagged the model output by 1 year, which can be indicative of external sources of sediment to the domain.

Recent advances in high performance computing are enabling the application of more sophisticated deterministic modelling systems in coastal morphodynamics. For instance, Barnard et al. (2014) used a cascade of nested regional ocean scale (WAVEWATCH III) to nearshore - about 1m - scale (XBeach [7]) models for the prediction of the coastal erosion as a consequence of extreme storm events. They applied this modelling system (CoSMoS)[8] to the Southern California Bight which extended 470 km along the coast. The performance of their model in predicting hydrodynamic field variables such as wave heights and tidal constituents was generally better than that of cross-shore profile evolution. Although using high performance computing and multiple nesting improves some aspects of the model predictions, it cannot resolve the uncertainties associated with model formulation and physics. They reported (Barnard et al., 2014), "The model does show skill in reproducing the general

---

[7]eXtreme Beach
[8]Coastal Storm Modeling System

trends of profile evolution; however, it does not reproduce the smaller-scale morphology (multiple bar profile) that was mapped in the measurements, as the model is not capable of reproducing bar migration".

Therefore, process-based models, despite their advantages, still experience considerable drawbacks in this context including uncertainty, computational cost, and a sophisticated modelling process; data-based approaches can bypass some of these issues. Paper **P-VI** employs the Artificial Neural Network (ANN) method, for the first time, for this application.

Artificial Neural Network is a data-based technique which originated in the field of biology and has been subsequently applied in numerous other fields (Yegnanarayana, 2009) including earth sciences (e.g. Mekanik et al. (2013)) and oceanography (e.g. Ferrarin et al. (2014); Hsieh and Tang (1998); Malekmohamadi et al. (2008)). In a wider context, several branches of artificial intelligence have emerged into geophysical sciences and oceanography: support vector regression for storm surge predictions (Rajasekaran et al., 2008), genetic programming for wave forecasting (Gaur and Deo, 2008), and a number of optimization techniques applicable to ocean energy research (e.g. artificial bee colony optimization; ant colony optimization; differential evolution; evolutionary algorithm; genetic algorithms; greedy randomized adaptive search procedures; genetic tabu search; honey bee mating optimization; see Banos et al. (2011) for more information). The idea of an ANN is based on the architecture of the human brain, which is estimated to have around 10 billion neurons, each connected on average to 10,000 other neurons. It can handle very complex tasks using these units and their connections. Each unit just performs a very simple process. An ANN model is usually 'trained' using 80% of the observed data, and is tested by 20 % of the remaining data. A basic ANN model can easily outperform multiple nonlinear regression methods (Razi and Athappilly, 2005).

The ANN presented in Paper **P-VI** learns the relationship of storm event parameters (wind speed, wave heights, number of successive storms, etc.) with the beach profile changes in the same case study (i.e. Tremadoc Bay, the Irish Sea). The performance of this model is better than that of the process-based model (Paper **P-V**) using less computational effort and a much simpler procedure.

Yet, an ANN model lacks an important capability of deterministic models. It cannot predict a scenario which is outside the scope of its training data. For instance, the combined impact of sea-level rise and successive storms in 100 years, when the conditions may be significantly different from now, cannot be examined by an ANN model which has been trained by historical data. As a future research approach, a combination of processed-based and data-based models may be a useful technique to simulate coastal erosion; a data-based model can be trained by a process-based model for a wider range of scenarios in this case. Some research questions and highlights of Paper **P-VI** are summarised as follows:

Research questions of Paper **P-VI**

- ✐ Is it possible to predict beach profile changes using an ANN method, based on basic climate and ocean data (wind, current and waves)?

- ✐ What is the suitable ANN type (back propagation, radial basis function, etc), and architecture (number of layers and neurons) for this study ?

- ✐ What are the best input variables (wave height, wind speed, wave direction, number of successive storms, etc.) in an ANN model to predict beach profile changes?

- ✐ What are the advantages of using an ANN method in beach profile simulation compared with traditional process-based methods?

- ✐ Is there a major drawback in this approach?

- ✐ What is the accuracy of an ANN model in beach profile predictions?

Highlights of Paper **P-VI**

- ◇ An ANN model was applied to predict seasonal beach profile evolution - 19 stations for a period of 7 years - along a wave exposed bay in the Irish Sea.

- ◇ This study was the first application of an ANN in this area.

- ◇ The correlation matrix method and principal component analysis were employed to select input variables.

- ◇ In terms of the ANN architecture, one hidden layer with 20 neurons, and the hyperbolic tangent sigmoid transfer function led to excellent model performance (MSE=0.0007).

- ◇ The application of the ANN method is limited to the historical training data; it cannot be applied to hypothetical situations - e.g. future coastal constructions - or extreme events which have not been found in the training data.

Chapter 4

Coupled hydro-morphodynamic models - integrated approach

Atmosphere, catchment, river, estuary, continental shelf, and ocean (Cloud to Ocean: C2O) comprise a unified dynamic system with profound interactions. However, in the majority of the existing literature, this unified system has been studied separately, and by scientists from different disciplines (i.e., meteorologists, hydrologists, civil/coastal engineers, and oceanographers). While the interactions of these components are usually ignored or oversimplified in this traditional approach, a number of fundamental challenges arise in attempting to model this system as a unit: scaling issues, computational cost, lack of knowledge and uncertainty regarding the interactions (e.g. ocean-atmosphere; river-estuary), lack of observation data and increasing uncertainty in coupled models (Simpson and Sharples, 2012), and difficulty of understanding the whole system by a scientist who is usually coming from a particular discipline.

Paper **P-VII** can be considered as a first step to develop a coupled unified modelling system for the NW European or the UK shelf seas. The Coupled Ocean-Atmosphere-Wave-Sediment Transport (COAWST) modelling system (Warner et al., 2010), which has been employed in this paper, comprises the ocean model ROMS (Shchepetkin and McWilliams, 2005), the atmospheric model WRF (Skamarock et al., 2005), the wave model SWAN (Booij et al., 1999), and the sediment capabilities of the Community Sediment Transport Model.

The data exchange between these modules is conducted by the Model Coupling Toolkit (Warner et al., 2010). Paper **P-VI** models the interaction of tides and waves using this modelling system, and discusses some of the issues such as increased computational cost: 5 times the cost of decoupled simulations. The coupled model was applied to study wave current interaction effects on the estimation of wave power . The paper addresses some shortcomings of Paper **P-I** (see the last paragraph of Section 2.2.1) by implementing a dynamic boundary forcing and a two way wave-tide interaction methodology. As an interesting contribution, this paper shows a significant improvement (25% [1]) in the model performance, as well as tidal modulation of the wave height and period, compared with a decoupled model. The paper also predicts the combined wave-current induced stresses which are the basis for morphodynamic simulations (Eq. 3.1). Further research is underway to apply this model in morphodynamic simulations. Some research questions and highlights of Paper **P-VII** are summarised as follows:

Research questions of Paper **P-VII**

- ✍ Under what circumstances do we need to use coupled tide-wave models instead of the decoupled models in the NW European shelf seas?

- ✍ What is the performance of the COAWST modelling system as a coupled shelf-sea model for this region?

- ✍ How does the computational cost of a coupled tide-wave model compare with decoupled models?

- ✍ What are the important wave current interaction processes, and how can they be simulated for this region using the COAWST modelling systems?

- ✍ Can we nest a COAWST model of the NW European shelf seas inside a larger North Atlantic SWAN model? How does this affect the results?

- ✍ Do we have sufficient observations to evaluate the performance of the coupled model where the wave current interaction is important?

- ✍ What are the benefits and issues associated with using a coupled tide-wave model?

---

[1]The mean absolute errors were 0.30m and 0.58s for the significant wave height and the mean wave period, respectively, in the decoupled SWAN model, which were reduced to 0.24m and 0.48s, respectively, in the coupled model.

Highlights of Paper **P-VII**

◇ A COAWST model of the NW European shelf seas has been developed, validated extensively for wave/tide, and applied to a number of physical processes.

◇ The COAWST model was about 5 times more computationally expensive than running decoupled ROMS (ocean model) and SWAN (wave model).

◇ The COAWST modelling system has advantages over similar modelling systems: the flexibility to switch on/off a particular wave current interaction process, and the convenient pre/post-processing of input and output data.

◇ The performance of the COAWST model in the prediction of the wave parameters was shown to be improved by 25% in places where wave-current interaction is significant.

◇ Some applications of the model such as the effect of tides in quantifying the wave energy resource, and the effect of waves on the calculation of the bottom stress, which was dominant in parts of the North sea and west of Scotland, during an energetic wave period were presented.

4.1   Research prospects

There are many examples where understanding/predicting the interactions of two or more components of the Earth system (e.g. ocean-atmosphere-catchment-river) is essential in addressing a scientific problem or tackling a societal challenge (Fig. 4.1). Coastal flooding is a good example (Barnard et al., 2014; Zou et al., 2013). The design of coastal flood defence systems is usually based on the prediction of the maximum water level during an extreme event (e.g. 100 years period). Failure to accurately quantify this variable can lead to overtopping of flood defence structures (e.g. dykes), and hence flooding. The maximum water elevation during a storm event is a function of several interrelated processes including tide, storm surge, river flood discharge, and wave height. Accurate representation of the spatiotemporal variability of wind/air pressure by an atmosphere model (e.g. WRF climate model) is necessary for proper prediction of the wave height (e.g. SWAN wave model), and storm surge (e.g. ROMS ocean/coastal model). In the meantime, prediction of water elevation in an estuary not only depends on the estimation of flood discharge coming from the upstream catchment (e.g. SWAT [2] catchment model) , it is also a function of the tidal elevation and storm surge downstream. Accordingly, a cascade of interlinked models from climate to catchment and to the coast, which have been trained/validated using historical data, is an ideal tool for accurate prediction of floods for future scenarios, considering climate change has affected each component of this system.

Apart from the COAWST model, similar efforts have been made recently to develop integrated modelling tools and software. For instance, the Community Surface Dynamics Modeling System (CSDMS) project (Peckham et al., 2013) is a component based approach to develop an integrated modelling system in geoscience using existing 'standalone' modular numerical models. This project aims to develop multi-scale simulations of earth-surface processes, on time scales ranging from individual daily events to millions of years.

The unified modelling system also provides a tool to test some scientific hypotheses which involve the interactions of C2O compartments. For instance, it can be used to test a theory about the ocean-atmosphere boundary layer by simulation of historical storm tracks

---

[2] the Soil Water Analysis Toolbox
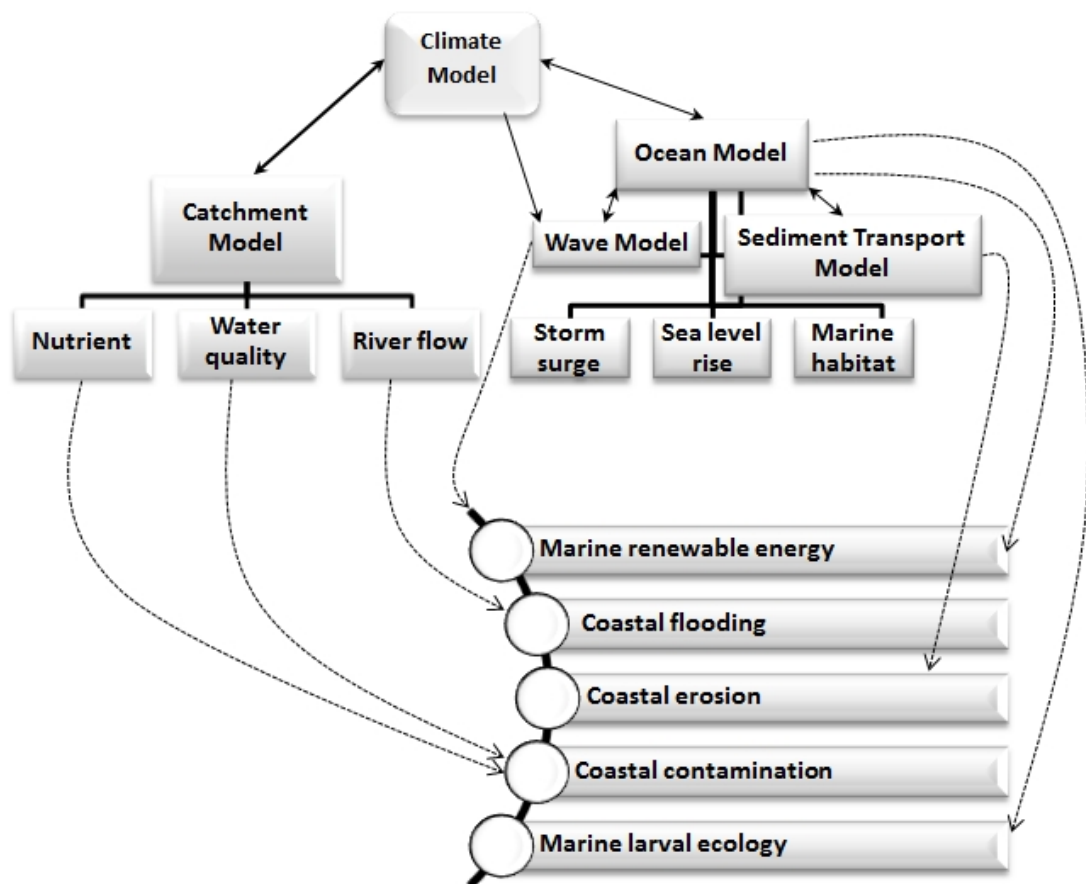
Fig. 4.1 Schematic of the Cloud-to-Ocean (C2O) integrated modelling system

and checking whether that theory has improved the model predictions.

References

ABPmer (2008). The Met Office and Proudman Oceanographic Laboratory; Atlas of UK marine renewable energy resources. Technical report, Department for Business Enterprise & Regulatory Reform.

Arinaga, R. A. and Cheung, K. F. (2012). Atlas of global wave energy from 10 years of reanalysis and hindcast data. *Renewable Energy*, 39(1):49–64.

Bahaj, A. S. (2011). Generating electricity from the oceans. *Renew Sust Energ Rev*, 15:3399–416.

Banos, R., Manzano-Agugliaro, F., Montoya, F., Gil, C., Alcayde, A., and Gómez, J. (2011). Optimization methods applied to renewable and sustainable energy: A review. *Renewable and Sustainable Energy Reviews*, 15(4):1753–1766.

Barbariol, F., Benetazzo, A., Carniel, S., and Sclavo, M. (2013). Improving the assessment of wave energy resources by means of coupled wave-ocean numerical modeling. *Renewable Energy*, 60:462–471.

Barnard, P., van Ormondt, M., Erikson, L., Eshleman, J., Hapke, C., Ruggiero, P., Adams, P., and Foxgrover, A. (2014). Development of the Coastal Storm Modeling System (CoS-MoS) for predicting the impact of storms on high-energy, active-margin coasts. *Natural Hazards*, pages 1–31.

Batten, W., Bahaj, A., Molland, A., and Chaplin, J. (2007). Experimentally validated numerical method for the hydrodynamic design of horizontal axis tidal turbines. *Ocean Engineering*, 34(7):1013–1020.

Begnudelli, L., Valiani, A., and Sanders, B. F. (2010). A balanced treatment of secondary currents, turbulence and dispersion in a depth-integrated hydrodynamic and bed deformation model for channel bends. *Advances in Water Resources*, 33(1):17–33.

Beniston, M., Stephenson, D. B., Christensen, O. B., Ferro, C. A., Frei, C., Goyette, S., Halsnaes, K., Holt, T., Jylhä, K., Koffi, B., et al. (2007). Future extreme events in European climate: an exploration of regional climate model projections. *Climatic change*, 81(1):71–95.

Benoit, M., Marcos, F., and Becq, F. (1996). Development of a third generation shallow-water wave model with unstructured spatial meshing. *Coastal Engineering Proceedings*, 1(25).

Berthot, A. and Pattiaratchi, C. (2006). Mechanisms for the formation of headland-associated linear sandbanks. *Continental shelf research*, 26(8):987–1004.

Blunden, L. S. and Bahaj, A. S. (2006). Initial evaluation of tidal stream energy resources at portland bill, uk. *Renewable Energy*, 31(2):121–132. Cited By (since 1996):45.

Booij, N., Ris, R., and Holthuijsen, L. H. (1999). A third-generation wave model for coastal regions: 1. Model description and validation. *Journal of Geophysical Research: Oceans (1978–2012)*, 104(C4):7649–7666.

Bromirski, P. D., Cayan, D. R., Helly, J., and Wittmann, P. (2013). Wave power variability and trends across the North Pacific. *Journal of Geophysical Research C: Oceans*, 118(12):6329–6348.

Cowell, P., Thom, B., Carter, R., and Woodroffe, C. (1994). *Morphodynamics of coastal evolution*. Cambridge University Press, Cambridge, United Kingdom and New York, NY, USA.

Davies, A., Soulsby, R., and King, H. (1988). A numerical model of the combined wave and current bottom boundary layer. *Journal of Geophysical Research: Oceans (1978–2012)*, 93(C1):491–508.

Di Lorenzo, E., Moore, A. M., Arango, H. G., Cornuelle, B. D., Miller, A. J., Powell, B., Chua, B. S., and Bennett, A. F. (2007). Weak and strong constraint data assimilation in the inverse regional ocean modeling system (ROMS): Development and application for a baroclinic coastal upwelling system. *Ocean Modelling*, 16(3):160–187.

Draper, S., Adcock, T. A. A., Borthwick, A. G. L., and Houlsby, G. T. (2014). Estimate of the tidal stream power resource of the pentland firth. *Renewable Energy*, 63:650–657. Cited By (since 1996):2.

Dyer, K. R. and Huntley, D. A. (1999). The origin, classification and modelling of sand banks and ridges. *Continental Shelf Research*, 19(10):1285–1330.

Egbert, G. and Ray, R. (2000). Significant dissipation of tidal energy in the deep ocean inferred from satellite altimeter data. *Nature*, 405(6788):775–778.

Engelund, F. (1974). Flow and bed topography in channel bends. *Journal of the Hydraulics Division*, 100(11):1631–1648.

Ferrarin, C., Zaggia, L., Paschini, E., Scirocco, T., Lorenzetti, G., Bajo, M., Penna, P., Francavilla, M., D'Adamo, R., and Guerzoni, S. (2014). Hydrological regime and renewal capacity of the micro-tidal Lesina Lagoon, Italy. *Estuaries and Coasts*, 37(1):79–93.

Gaur, S. and Deo, M. (2008). Real-time wave forecasting using genetic programming. *Ocean Engineering*, 35(11):1166–1172.

Gonçalves, M., Martinho, P., and Guedes Soares, C. (2014). Wave energy conditions in the western French coast. *Renewable Energy*, 62:155–163. Cited By (since 1996):4.

Guanche, R., de Andrés, A. D., Simal, P. D., Vidal, C., and Losada, I. J. (2014). Uncertainty analysis of wave energy farms financial indicators. *Renewable Energy*, 68:570–580.

Hervouet, J.-M. (2000). TELEMAC modelling system: an overview. *Hydrological Processes*, 14(13):2209–2210.

Hope, M. E., Westerink, J. J., Kennedy, A. B., Kerr, P., Dietrich, J., Dawson, C., Bender, C. J., Smith, J., Jensen, R. E., Zijlema, M., et al. (2013). Hindcast and validation of hurricane ike (2008) waves, forerunner, and storm surge. *Journal of Geophysical Research: Oceans*, 118(9):4424–4460.

Hsieh, W. W. and Tang, B. (1998). Applying neural network models to prediction and data analysis in meteorology and oceanography.

Hughes, M. G. and Heap, A. D. (2010). National-scale wave energy resource assessment for Australia. *Renewable Energy*, 35(8):1783–1791.

Huntley, D. (1980). Tides on the north-west european continental shelf. *Elsevier Oceanography Series*, 24:301–351.

Hurrell, J. W. (1995). Decadal trends in the north atlantic oscillation: regional temperatures and precipitation. *Science*, 269(5224):676–679.

Huthnance, J. (1982a). On the formation of sand banks of finite extent. *Estuarine, Coastal and Shelf Science*, 15(3):277–299.

Huthnance, J. M. (1982b). On one mechanism forming linear sand banks. *Estuarine, Coastal and Shelf Science*, 14(1):79–99.

Kamphuis, J. W. (1991). Alongshore sediment transport rate. *Journal of Waterway, Port, Coastal, and Ocean Engineering*, 117(6):624–640.

Kamranzad, B., Etemad-Shahidi, A., and Chegini, V. (2013). Assessment of wave energy variation in the Persian Gulf. *Ocean Engineering*, 70:72–80. Cited By (since 1996):1.

Karunarathna, H., Pender, D., Ranasinghe, R., Short, A. D., and Reeve, D. E. (2014). The effects of storm clustering on beach profile variability. *Marine Geology*, 348:103–112.

Kikkawa, H., Kitagawa, A., and Ikeda, S. (1976). Flow and bed topography in curved open channels. *Journal of the Hydraulics Division*, 102(9):1327–1342.

Komarova, N. L. and Newell, A. C. (2000). Nonlinear dynamics of sand banks and sand waves. *Journal of Fluid Mechanics*, 415:285–321.

Lewis, M., Neill, S. P., and Hashemi, M. R. (2014). Realistic wave conditions and their influence on quantifying the tidal stream energy resource. *Applied Energy*. in press, DOI: 10.1016/j.apenergy.2014.09.061.

Liberti, L., Carillo, A., and Sannino, G. (2013). Wave energy resource assessment in the Mediterranean, the Italian perspective. *Renewable Energy*, 50:938–949.

Mackay, E. B. L., Bahaj, A. S., and Challenor, P. G. (2010). Uncertainty in wave energy resource assessment. part 2: Variability and predictability. *Renewable Energy*, 35(8):1809–1819. Cited By (since 1996):15.

Malekmohamadi, I., Ghiassi, R., and Yazdanpanah, M. (2008). Wave hindcasting by coupling numerical model and artificial neural networks. *Ocean Engineering*, 35(3):417–425.

MARTINS, F., LEITÃO, P., SILVA, A., and NEVES, R. (2001). 3D modelling in the Sado estuary using a new generic vertical discretization approach. *Oceanologica Acta*, 24:51–62.

Mason-Jones, A., O'Doherty, D. M., Morris, C. E., O'Doherty, T., Byrne, C., Prickett, P. W., Grosvenor, R. I., Owen, I., Tedds, S., and Poole, R. (2012). Non-dimensional scaling of tidal stream turbines. *Energy*, 44(1):820–829.

Mekanik, F., Imteaz, M., Gato-Trinidad, S., and Elmahdi, A. (2013). Multiple regression and Artificial Neural Network for long-term rainfall forecasting using large scale climate modes. *Journal of Hydrology*, 503:11–21.

Neill, S. P. (2008). The role of Coriolis in sandbank formation due to a headland/island system. *Estuarine, Coastal and Shelf Science*, 79(3):419–428.

Neill, S. P., Hashemi, M. R., and Lewis, M. J. (2014a). Optimal phasing of the european tidal stream resource using the greedy algorithm with penalty function. *Energy*.

Neill, S. P., Jordan, J. R., and Couch, S. J. (2012). Impact of tidal energy converter (TEC) arrays on the dynamics of headland sand banks. *Renewable Energy*, 37(1):387–397.

Neill, S. P., Lewis, M. J., Hashemi, M. R., Slater, E., Lawrence, J., and Spall, S. A. (2014b). Inter-annual and inter-seasonal variability of the orkney wave power resource. *Applied Energy*, 132:339–348.

Neill, S. P. and Scourse, J. D. (2009). The formation of headland/island sandbanks. *Continental Shelf Research*, 29(18):2167–2177.

Peckham, S. D., Hutton, E. W., and Norris, B. (2013). A component-based approach to integrated modeling in the geosciences: The design of csdms. *Computers & Geosciences*, 53:3–12.

Pontes, M. (1998). Assessing the European wave energy resource. *Journal of Offshore Mechanics and Arctic Engineering*, 120(4):226–231.

Prandle, D. (1997). The influence of bed friction and vertical eddy viscosity on tidal propagation. *Continental Shelf Research*, 17(11):1367–1374.

Pranzini, E., Rosas, V., Jackson, N. L., and Nordstrom, K. F. (2013). Beach changes from sediment delivered by streams to pocket beaches during a major flood. *Geomorphology*, 199:36–47.

Pugh, D. T. (1996). *Tides, surges and mean sea-level (reprinted with corrections)*. John Wiley & Sons Ltd.

Rajasekaran, S., Gayathri, S., and Lee, T.-L. (2008). Support vector regression methodology for storm surge predictions. *Ocean Engineering*, 35(16):1578–1587.

Razi, M. A. and Athappilly, K. (2005). A comparative predictive analysis of neural networks (NNs), nonlinear regression and classification and regression tree (CART) models. *Expert Systems with Applications*, 29(1):65–74.

Reeve, D. E., Chen, Y., Pan, S., Magar, V., Simmonds, D. J., and Zacharioudaki, A. (2011). An investigation of the impacts of climate change on wave energy generation: The WAVE HUB, CORNWALL, UK. *Renewable Energy*, 36(9):2404–2413. Cited By (since 1996):8.

Reguero, B., Méndez, F., and Losada, I. (2013). Variability of multivariate wave climate in Latin America and the Caribbean. *Global and Planetary Change*, 100:70–84.

Robins, P. E., Neill, S. P., and Lewis, M. J. (2014). Impact of tidal-stream arrays in relation to the natural variability of sedimentary processes. *Renewable Energy*, 72:311–321.

Roelvink, J. and Brøker, I. (1993). Cross-shore profile models. *Coastal Engineering*, 21(1):163–191.

Ruprich-Robert, Y. and Cassou, C. (2014). Combined influences of seasonal east atlantic pattern and north atlantic oscillation to excite atlantic multidecadal variability in a climate model. *Climate Dynamics*. Article in Press.

Saruwatari, A., Ingram, D. M., and Cradden, L. (2013). Wave–current interaction effects on marine energy converters. *Ocean Engineering*, 73:106–118.

Serhadlıoğlu, S., Adcock, T. A., Houlsby, G. T., Draper, S., and Borthwick, A. G. (2013). Tidal stream energy resource assessment of the Anglesey Skerries. *International Journal of Marine Energy*, 3:e98–e111.

Shchepetkin, A. F. and McWilliams, J. C. (2005). The regional oceanic modeling system (ROMS): a split-explicit, free-surface, topography-following-coordinate oceanic model. *Ocean Modelling*, 9(4):347–404.

Sierra, J. P., González-Marco, D., Sospedra, J., Gironella, X., Mösso, C., and Sánchez-Arcilla, A. (2013). Wave energy resource assessment in Lanzarote (Spain). *Renewable Energy*, 55:480–489. Cited By (since 1996):6.

Simpson, J. H. and Sharples, J. (2012). *Introduction to the physical and biological oceanography of shelf seas*. Cambridge University Press.

Skamarock, W. C., Klemp, J. B., Dudhia, J., Gill, D. O., Barker, D. M., Wang, W., and Powers, J. G. (2005). A description of the advanced research WRF version 2. Technical report, DTIC Document.

Sánchez, M., Carballo, R., Ramos, V., and Iglesias, G. (2014). Tidal stream energy impact on the transient and residual flow in an estuary: A 3D analysis. *Applied Energy*, 116:167–177. Cited By (since 1996):1.

Soulsby, R. (1997). *Dynamics of marine sands: a manual for practical applications*. Thomas Telford.

Soulsby, R., Hamm, L., Klopman, G., Myrhaug, D., Simons, R., and Thomas, G. (1993). Wave-current interaction within and outside the bottom boundary layer. *Coastal engineering*, 21(1):41–69.

Splinter, K. D., Carley, J. T., Golshani, A., and Tomlinson, R. (2014). A relationship to describe the cumulative impact of storm clusters on beach erosion. *Coastal Engineering*, 83(0):49 – 55.

Springel, V., White, S. D., Jenkins, A., Frenk, C. S., Yoshida, N., Gao, L., Navarro, J., Thacker, R., Croton, D., Helly, J., et al. (2005). Simulations of the formation, evolution and clustering of galaxies and quasars. NATURE, 435(7042):629–636.

Stansby, P. K. (2006). Limitations of depth-averaged modeling for shallow wakes. *Journal of Hydraulic Engineering*, 132(7):737–740.

Sun, X., Chick, J., and Bryden, I. (2008). Laboratory-scale simulation of energy extraction from tidal currents. *Renewable Energy*, 33(6):1267–1274.

Tassi, P. and Villaret, C. (2014). Sisyphe v6.3 user's manual. Technical report, EDF R & D.

Theisel, H. (1995). Vector field curvature and applications. *Doktorarbeit, FB Informatik, Universit at Rostock*.

Thyng, K. M., Riley, J. J., and Thomson, J. (2013). Inference of turbulence parameters from a ROMS simulation using the $k\varepsilon$ closure scheme. *Ocean Modelling*, 72:104–118.

Wang, Z., Louters, T., and De Vriend, H. (1995). Morphodynamic modelling for a tidal inlet in the Wadden Sea. *Marine Geology*, 126(1):289–300.

Warner, J. C., Armstrong, B., He, R., and Zambon, J. B. (2010). Development of a coupled ocean–atmosphere–wave–sediment transport (COAWST) modeling system. *Ocean modelling*, 35(3):230–244.

Wolf, J. and Prandle, D. (1999). Some observations of wave–current interaction. *Coastal Engineering*, 37(3):471–485.

Wright, L. and Short, A. D. (1984). Morphodynamic variability of surf zones and beaches: a synthesis. *Marine geology*, 56(1):93–118.

Wunsch, C. (1996). *The ocean circulation inverse problem*. Cambridge University Press.

Xia, J., Falconer, R. A., and Lin, B. (2010). Impact of different tidal renewable energy projects on the hydrodynamic processes in the Severn Estuary, UK. *Ocean Modelling*, 32(1):86–104.

Yegnanarayana, B. (2009). *Artificial neural networks*. PHI Learning Pvt. Ltd.

Zhang, K., Douglas, B. C., and Leatherman, S. P. (2004). Global warming and coastal erosion. *Climatic Change*, 64(1-2):41–58.

Zijlema, M. (2010). Computation of wind-wave spectra in coastal waters with SWAN on unstructured grids. *Coastal Engineering*, 57(3):267–277.

Zou, Q.-P., Chen, Y., Cluckie, I., Hewston, R., Pan, S., Peng, Z., and Reeve, D. (2013). Ensemble prediction of coastal flood risk arising from overtopping by linking meteorological, ocean, coastal and surf zone models. *Quarterly Journal of the Royal Meteorological Society*, 139(671):298–313.

Published works

.1 Published work P-I
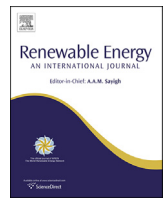
The role of tides in shelf-scale simulations of the wave energy resource

M. Reza Hashemi*, Simon P. Neill

School of Ocean Sciences, Bangor University, Menai Bridge, Bangor LL59 5AB, UK

A B S T R A C T

Many regions throughout the world that are suitable for exploitation of the wave energy resource also experience large tidal ranges and associated strong tidal flows. However, tidal effects are not included in the majority of modelling studies which quantify the wave energy resource. This research attempts to quantify the impact of tides on the wave energy resource of the northwest European shelf seas, a region with a significant wave energy resource, and where many wave energy projects are under development. Results of analysis based on linear wave theory, and the application of a non-linear coupled wave-tide model (SWAN–ROMS), suggest that the impact of tides is significant, and can exceed 10% in some regions of strong tidal currents (e.g. headlands). Results also show that the effect of tidal currents on the wave resource is much greater than the contribution of variations in tidal water depth, and that regions which experience lower wave energy (and hence shorter wave periods) are more affected by tides than high wave energy regions. While this research provides general guidelines on the scale of the impact in regions of strong tidal flow, high resolution site-specific coupled wave-tide models are necessary for more detailed analysis.

© 2014 Elsevier Ltd. All rights reserved.

1. Introduction

To aid sustainable development, it is essential that we deliver a secure source of energy services, with minimal environmental impact [1]. To address this, many countries are investing in renewable energy technologies, including bioenergy, solar, geothermal, hydropower, wind, and ocean energy. In relation to the latter, the ocean is a vast and largely untapped energy resource which has the potential to provide all of our electricity demand [2]. The global wave power resource has been estimated as around 2.1 TW [3], and tidal as around 2.5 TW [4]. Although tidal range power stations like La Rance have been operating since the 1960s, and other large schemes have been built or are under construction in South Korea, there are concerns about the environmental impacts of exploiting tidal range [5,6]. Therefore, recent government investment, and so most research and development, has tended to focus on tidal stream (tidal energy convertor, TEC) and wave (wave energy convertor, WEC) devices and arrays [7].

There are many regions throughout the world which concurrently experience a high wave and a high tidal energy resource. These regions include the northwest European shelf seas, the Gulf of Alaska, New Zealand, northwest Australia, and the Atlantic seaboard of Argentina. Due to wave-tidal interactions, special consideration needs to be given to energy schemes developed in such regions. In particular, resource assessments of such regions should account for the way that one marine resource (e.g. waves) modulates other marine resources (e.g. tides) at a variety of timescales from semi-diurnal, spring-neap, to seasonal.

The northwest European shelf seas are one of the most attractive regions in the world for the development of wave energy projects. The climate (and hence wind) of the northwest European shelf is dominated by the atmospheric polar front. The instability of this front causes depressions to form, tracking across the north Atlantic and following a preferred route which passes between Iceland and Scotland [8]. Additionally, the strengths of tidal currents as well as tidal range are very high in many regions of the northwest European shelf seas, particularly around the UK and in the English Channel. For instance, with a mean spring tidal range of 12.2 m, and a mean neap range of 6.0 m at Avonmouth, the Bristol Channel has one of the highest tidal ranges in the world [9]. Consequently, many tidal projects are under development in parallel with wave energy projects across the northwest European shelf seas (Fig. 1).

Although the tide can significantly alter wave properties through various wave-current interaction mechanisms [10–13],

* Corresponding author.
   E-mail address: r.hashemi@bangor.ac.uk (M.R. Hashemi).

such interactions are not routinely considered in the majority of wave energy resource assessments that are based on numerical modelling [14,15]. It has been demonstrated that neglecting tidal effects could lead to significant errors in regions which experience low wave energy [16] or high wave energy [17,18].

By virtue of recent advances in marine hydrodynamic modelling and high performance computing, it is now becoming increasingly feasible to develop coupled wave-current models of a region to examine wave-tide interactions (e.g. Refs. [19,17]).

In the present study, the impact of the tide on the wave energy resource of the northwest European shelf seas is investigated using a coupled SWAN–ROMS wave-tidal model. Further, a simplified analysis based on linear wave theory is presented, which can be used to give a rapid estimate of the impact at a region, based on basic wave and tidal information.

2. Methods

A simple analysis of the effect of the tide on wave power is presented first. The details of the coupled wave-tide model will be presented consequently.

2.1. Effect of tide on wave energy; idealised cases

Quantifying how the tide affects the wave power resource for simple idealised domains helps us understand these inter-related processes, and enables us to estimate the order of magnitude of the associated error. Such an idealised study also provides us with an idea about which regimes will be most affected by wave/tide interaction, in terms of water depth, tidal regime, and wave exposure.

Many wave models are based on the assumptions of linear wave theory. Therefore, a simple case with an analytical solution based on linear wave theory is a good starting place. We assume that a regular wave with a wave period T and wave height H is propagating in constant water depth h. Based on the Airy wave theory, the average energy flux per unit width over a wave period is given by

$$P = \int_0^T \int_{-h}^{\eta} p_D u \, dz \, dt = \frac{1}{8}\rho g H^2 C\left\{\frac{1}{2}\left(1 + \frac{2kh}{\sinh 2\,kh}\right)\right\} = EC_g,$$

(1)

$$C_g = C\left\{\frac{1}{2}\left(1 + \frac{2kh}{\sinh 2\,kh}\right)\right\}$$
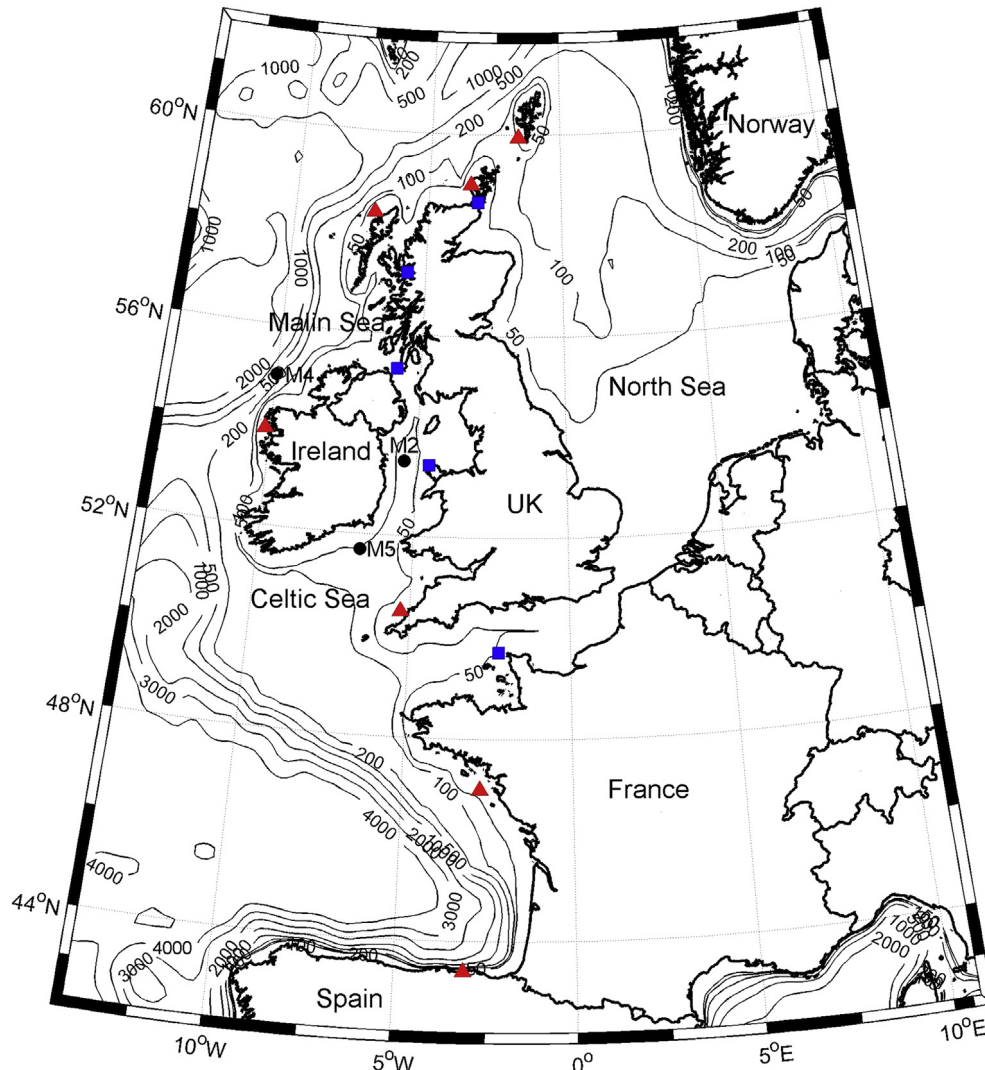
Fig. 1. Overview of the study region, including examples of wave and tidal energy projects (blue squares = tidal sites, red triangles = wave sites). Further details of these sites are provided in Table 1. Also shown are bathymetry contours (in metres relative to mean sea level), and the three wave buoys (M2, M4, M5) used for model validation. (For interpretation of the references to colour in this figure legend, the reader is referred to the web version of this article.)

where p_D is the dynamic pressure and u is the horizontal velocity. As this equation suggests, the group velocity C_g is dependent on the wave celerity C, wave number k, and water depth; all of which are related to tidal elevation particularly in shallower waters. Further, although the wave number is not affected by the ambient current for this idealised case, the wave period and consequently the wave celerity are affected by tidal currents.

Since the tidal period is much greater than the wave period, it is reasonable to assume quasi-steady state at each time slice. Airy wave theory is applicable for a specific tidal elevation and ambient tidal current. Consequently, the tidally-modulated wave properties as well as wave power, can be evaluated exactly using linear wave theory. For instance, the water depth and the ambient tidal currents for the principal semi-diurnal lunar (M_2) tide can be computed by simple harmonic equations.[1] To compute the wave power in the presence of a tide, the wave number is firstly determined by solving the dispersion equation,

$$\omega'^2 = \left(\omega^* - U^t k^*\right)^2 = gk^* \tanh k^* h \tag{2}$$

where $\omega' = 2\pi/T'$ and $\omega^* = 2\pi/T^*$ are the relative and absolute angular wave frequencies, respectively, corresponding to relative (T') and absolute (T^*) wave periods. T' can be observed in a coordinate system moving with the same velocity as the ambient current, and is the same as the wave period in the absence of tidal currents. k^* is the wave number affected by the tide. The modified wave celerity and the group wave celerity can be computed next,

$$C^* = U_0^t + \sqrt{\frac{g}{k^*} \tanh k^* h} \tag{3}$$

$$C_g^* = C^* \left\{ \frac{1}{2} \left(1 + \frac{2k^* h}{\sinh 2k^* h} \right) \right\} \tag{4}$$

The significance of including tidal effects when estimating the wave power resource can be quantified by comparing $P^* = EC_g^*$ and $P = EC_g$. Even for this idealised case, the effect of the tide on wave power is a function of five independent variables: the water depth relative to mean sea level, the wave period, the amplitudes of tidal elevation and velocity, and the phase relationship between the tidal elevations and the tidal currents.

To estimate this effect, these variables were modified according to the tide and wave climate of the Bristol Channel: a region of particular interest for tide-wave interactions and renewable energy extraction [20,21]. It should be noted that since this section is based on linear wave theory, the results will not be accurate for very shallow water or for very large and steep waves. Nevertheless, the results clearly demonstrate the order of magnitude of the error and the sensitivity of each variable. The tidal variables and the bathymetry were altered according to the ranges of values presented in Table 2.

Fig. 2 shows the effect of the tide on estimates of the wave power resource. The initial water depth and tidal amplitude have been normalised by the wave period consistent with similar graphs based on the linear wave theory [22]. Nevertheless, the results are sensitive to the wave period, as discussed later, and the graphs have been plotted for a sample period of 8 s. As Fig. 2 shows, the error can be as great as 20% for strong tidal currents in shallow waters (i.e. 4 m tidal range, 1.5 m/s currents, and 15 m water depth). If the

Table 1
Examples of wave and tidal energy projects across the northwest European shelf seas.

Project name	Technology	Project type[a]
BIMEP – Biscay Marine Energy Platform	Wave	Test site
SEMREV – wave energy test site	Wave	Test site
Wave hub	Wave	Test site
Alderney – OpenHydro	Tidal	Commercial
Aegir (Shetland) – Pelamis	Wave	Commercial
EMEC wave test site	Wave	Test site
Pentland Firth – MeyGen	Tidal	Commercial
Bernera (Lewis) – Pelamis	Wave	Commercial
Kyle Rhea – Seagen	Tidal	Commercial
Mull of Kintyre – Nautricity/Argyll Tidal	Tidal	Commercial
Skerries (Anglesey) – MCT/Siemens	Tidal	Commercial
Achill (Ireland) – Westwave NER300	Wave	Test site

[a] Sources of data:www.sowfia.hidromod.com, www.en.openei.org/wiki/Marine_and_Hydrokinetic_Technology_Database, www.thecrownestate.co.uk, www.openhydro.com, www.marineturbines.com, www.pelamiswave.com.

currents are negligible (Fig. 2a), tidal effects are not significant for regions deeper than 50 m. It is clear that for cases where ambient currents are included, the contour lines approach horizontal lines in deep waters. Therefore, the impact of tides on wave power in deep water depends mainly on the tidal current for these idealised cases as we would expect. Further, the impact of currents is generally more significant compared with tidal elevation.

The results in Fig. 2 are based on the assumption of a progressive tidal wave, where there is no phase lag between the currents and elevations. Further analysis showed that the results are not significantly sensitive to the phase lag between the currents and elevations.

It should be noted that the idealised study is based on several assumptions and simplifications which should be considered when interpreting the results. For instance, the wave energy flux is the product of the group velocity (C_g) and the wave energy ($E = (1/2)\rho g H^2$). Tides not only affect the group velocity, but they also affect the wave heights (modulation), and consequently wave energy. Saruwatari et al. [18], in a case study around Orkney using the SWAN wave model, showed that the relative direction of a wave field and a current field directly affects the wave height, and consequently the wave energy. Since tidal currents change direction over a tidal cycle, the 1-D assumption includes the effect of currents which are opposing or following waves on the group velocity. However, in the case where there is an oblique angle between currents and waves, more sophisticated numerical models which solve the evolution of the wave action density (e.g. SWAN) should be applied. These models can also simulate the effect of tides on the wave height. For simplicity, these processes have not been considered in the above analysis, which is based on linear wave theory. Even in this simplified case, it was shown that the effect of the tide on wave power will be significant in shallow waters in the presence of a strong tide. More detailed numerical modelling is necessary to examine the effect of tides on the wave power, as provided in the following sections.

2.2. Study area

With an annual mean wave power that exceeds 120 kW/m in some areas, the northwest European shelf seas are one of the most

---

[1] $h = h_o + \eta(t) = h_o + a_{M_2}^h \sin((2\pi/T_{M_2})t + \Omega_h)$ and $U = a_{M_2}^v \sin((2\pi/T_{M_2})t + \Omega_v)$, where a is the amplitude, Ω is the phase of the tide, and h_o is the water depth relative to mean sea level.

Table 2
Selected variables for sensitivity analysis.

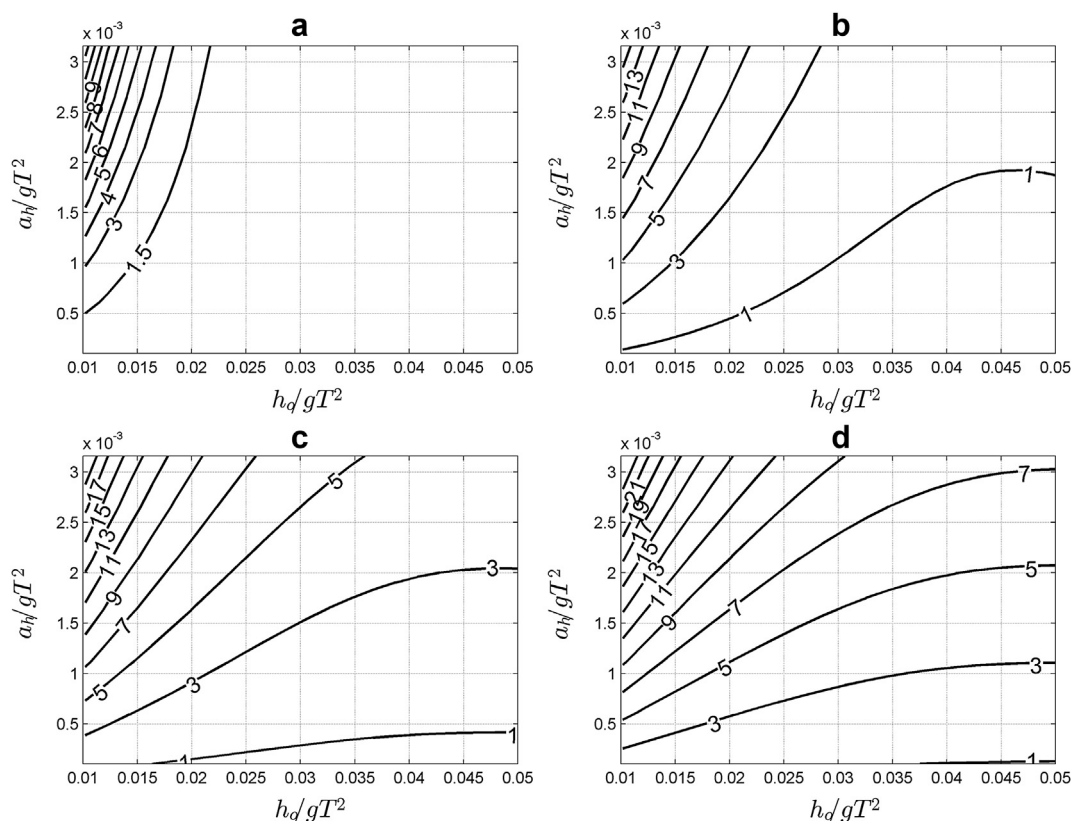| Variable	h_o (m)	$a_{M_2}^h$ (m)	$a_{M_2}^v$ (m/s)	$\Omega_h - \Omega_v$
Min	15	0	0	0
Max	50	4	1.5	$\pi/2$

Fig. 2. Percentage effect of tides on wave power estimate for a range of tidal currents and idealised regular waves. The contour lines represent the absolute relative difference of the wave power in the presence and absence of tide over a wave period. a: No current; b: Maximum current speed = 0.5 m/s; c: Maximum current speed = 1.0 m/s; d: Maximum current speed = 1.5 m/s.

energetic wave regions in the world [15,23], and so have been selected as the focus of this study. Fig. 1 shows the extent and the bathymetry of the study region. The majority of this area is shallower than 200 m, with the exception of the deeper (>500 m) Norwegian Trench in the North Sea. The wave climates in the Celtic Sea, Malin Sea and northern North Sea are dominated by waves propagating from the Atlantic Ocean. The Danish Peninsula and Norway are exposed to waves generated in the North Sea, which has sufficient fetch to generate relatively high waves as a result of westerly or northerly winds. Referring to Fig. 1, many sites throughout the northwest European shelf seas are under active development for the deployment of a diverse range of wave and tidal energy technologies. Some of the operational wave sites are listed in Table 1 and exposed to significant tidal currents (e.g. Aegir (Shetland), EMEC wave test site (Orkney), and Achill (Ireland)).

2.3. Modelling period

Neill and Hashemi [15] recently investigated interannual and interseasonal variability of the wave power over the same study area. Fig. 3 shows the monthly variability of the wave resource during 2005–2011. From this figure, January 2005, December 2006, and December 2011, with average monthly wave powers of 74 kW/m and 85 kW/m, and 77 kW/m respectively, are the most energetic months. Further, Fig. 3 confirms that the likelihood of average wave power exceeding 74 kW/m is less than 5% for both of the months. Therefore, January 2005 was considered as representative of a highly energetic month, and so the numerical modelling of tides, waves, and their interactions, was performed for this period. Due to the spatial variability of wave power, areas with extremely high waves (more than 10 m) and, in contrast, very low and even

negligible wave power, can be examined within this time period, to assess the impact of the tide in both low and high wave energy environments.

2.4. Numerical models

2.4.1. Tidal model

Tides were simulated using ROMS (Regional Ocean Modelling System), a free-surface, terrain-following, primitive equations
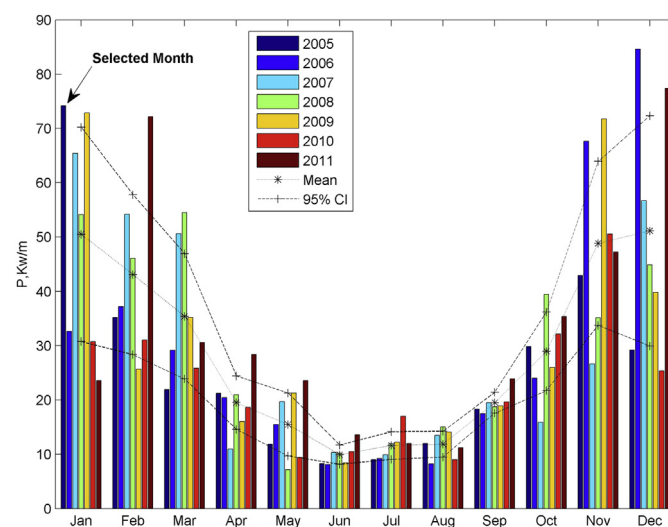
Fig. 3. Variability of monthly mean wave power, averaged over the domain, during 2005–2011 [15].
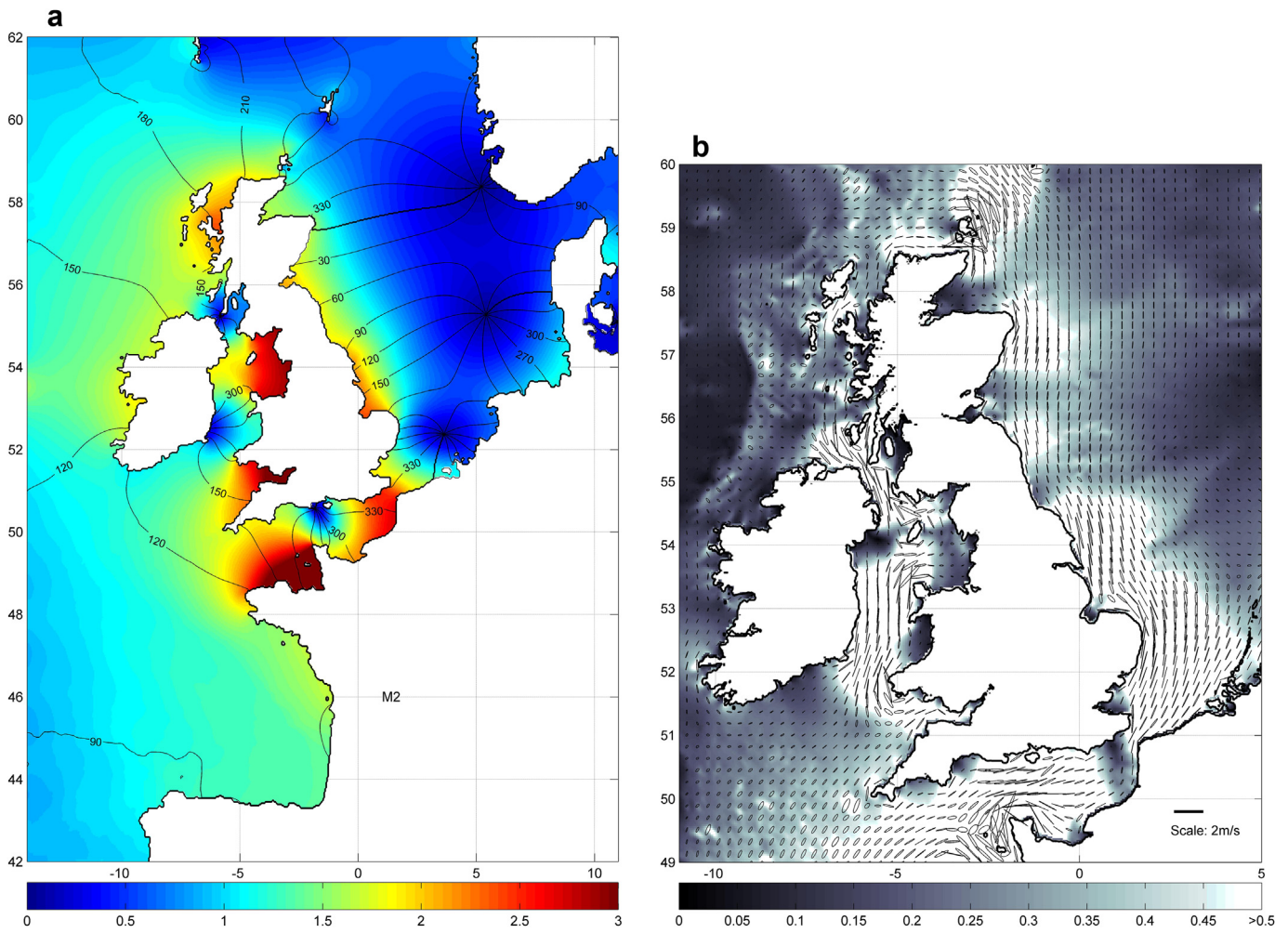
Fig. 4. Computed M_2 cotidal chart and current ellipses based on tidal analysis of the ROMS model output. The high tidal range and current speed in the Bristol channel and in the English channel are mainly due to strong M_2 tidal currents. a:M_2 cotidal; b: M_2 current ellipses. The colour scales show amplitudes in metres and m/s respectively. (For interpretation of the references to colour in this figure legend, the reader is referred to the web version of this article.)

ocean model. The hydrodynamics of ROMS are based on the Reynolds-averaged Navier–Stokes equations, with the hydrostatic and Boussinesq assumptions. The numerical algorithm of ROMS has been described in Shchepetkin and McWilliams [24,25]. ROMS has been widely applied to a range of scales in shelf sea modelling for barotropic and baroclinic tides [26–28]. The ROMS code is highly flexible, and can be compiled assuming a diverse range of physics and solution algorithms, applied to the momentum equations, horizontal and vertical advection, pressure gradient, turbulence,

Table 3
Validation of ROMS model (m) with tidal gauge data (o). The amplitudes (a, metres) and phases (Ω, degrees) of the M_2 and S_2 tidal constituents are compared with measured data at several tidal gauges.

Station	Coordinate	$a^o_{M_2}$	$a^m_{M_2}$	$\Omega^o_{M_2}$	$\Omega^m_{M_2}$	$a^o_{S_2}$	$a^m_{S_2}$	$\Omega^o_{S_2}$	$\Omega^m_{S_2}$
Mumbles	−3.97 51.57	3.18	2.97	171	167	1.12	1.25	221	229
St Marys	−6.32 49.93	1.75	1.72	132	131	0.60	0.63	174	191
Holyhead	−4.62 53.51	1.80	1.92	292	279	0.59	0.66	329	331
Aberdeen	−2.67 57.15	1.30	1.62	25	9	0.44	0.55	63	56
Dover	−1.32 51.07	2.27	2.29	331	331	0.70	0.71	23	42
Galway	−9.04 53.27	1.54	1.86	140	130	0.56	0.66	173	160
Pointe de Grave	−1.07 45.56	1.58	1.55	138	122	0.52	0.59	174	154
Brest	−4.50 48.38	2.05	2.07	138	138	0.75	0.77	178	177
Mean absolute error		0.13		8		0.07		11	

open boundary forcing, sediment transport, and wave-current interactions [19].

The ROMS model domain extended from 14° W to 11° E, and from 42° N to 62° N (Fig. 1). The domain was discretised with a horizontal curvilinear grid, with a longitudinal resolution of 1/24° and variable latitudinal mesh size to ensure an approximately uniform cell aspect ratio. The model bathymetry is based on the ETOPO (www.ngdc.noaa.gov/mgg/global) global bathymetric data set. The vertical grid consists of 11 layers distributed according to the ROMS terrain-following coordinate system. The open boundaries of the model were forced by tidal elevation (Chapman boundary condition) and tidal velocities (Flather boundary condition), generated by 10 tidal constituents (M_2, S_2, N_2, K_2, K_1, O_1, P_1, Q_1, M_f, M_m) obtained from TPXO7 global tide data with 1/4° resolution ([29]; volkov.oce.orst.edu/tides/).

ROMS compilation settings (cpp flags) which customise the physics of the model for a specific application were: quadratic bottom friction (0.003 non-dimensional drag coefficient), SWAN coupling option, horizontal and vertical mixing of momentum, the generic length scale turbulence closure model tuned to $k-\varepsilon$ ($p = 3$, $m = 1.5$, and $n = -1$; see Warner et al. [30] for more details). It should be noted that for studies where the effect of the waves on tides in shallow waters are considered, the nearshore compilation option of ROMS, which accommodates the bottom
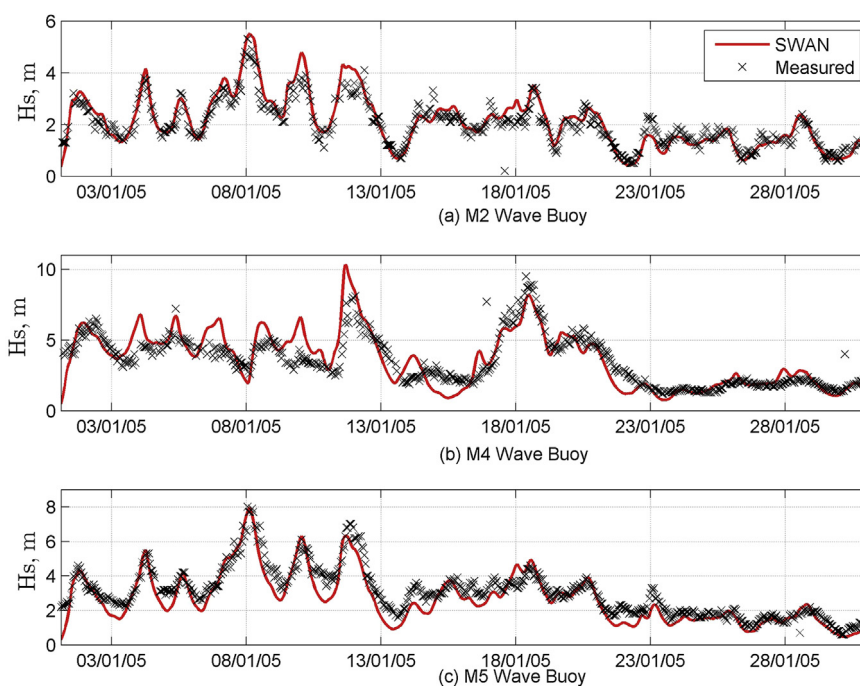
Fig. 5. Validation of SWAN wave model throughout January 2005 at several wave buoys; M2: 53.4800N 05.4250W; M4: 54.9982N 09.992154W; M5: 51.6891N 06.7010W. See Fig. 1 for location of wave buoys. The relative errors are 0.23 m, 0.70, and 0.47 m for M2, M4, and M5 respectively.

friction and radiation stresses generated by waves, should also be included.

2.4.2. Wave model

SWAN (Simulating WAves Nearshore) was used for the wave modelling. SWAN is a third-generation numerical wave model which computes random waves from deep waters to the surf zone and coastal regions. The basic scientific philosophy of SWAN is identical to that of WAM cycle 3, which considers problems at

oceanic scales. SWAN is based on the Eulerian formulation of the discrete spectral balance of action density, and accounts for refractive propagation over arbitrary bathymetry and ambient current fields. Several processes including wind generation, whitecapping, quadruplet wave–wave interactions, and bottom dissipation are represented explicitly in the SWAN source terms [31].

SWAN was applied to the same curvilinear grid and bathymetry as the ROMS model. Wind forcing was provided by European
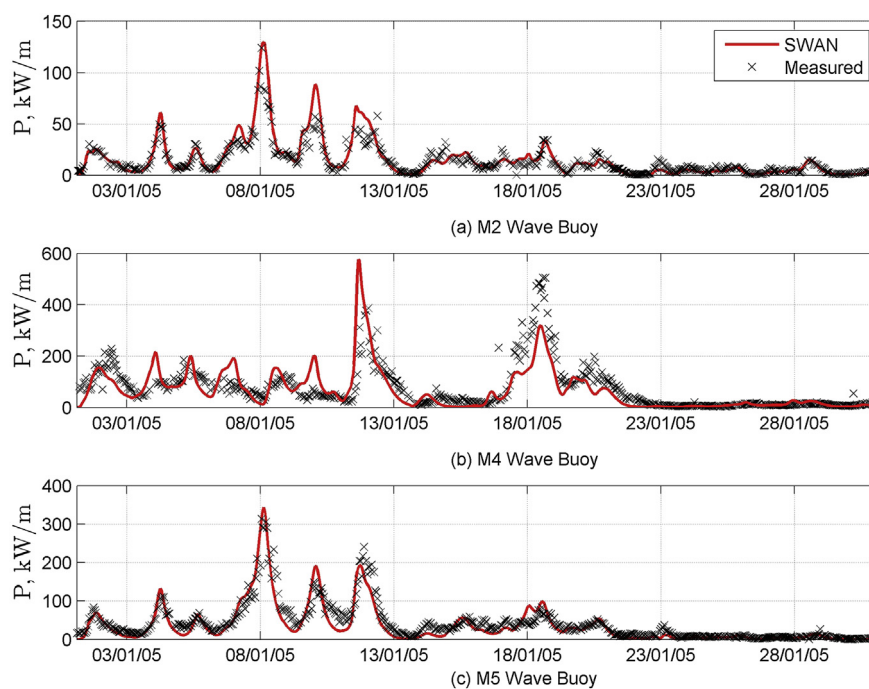
Fig. 6. Comparison of the SWAN model results and estimated wave power at selected wave buoys used for validation, January 2005. See Fig. 1 for locations of the wave buoys.
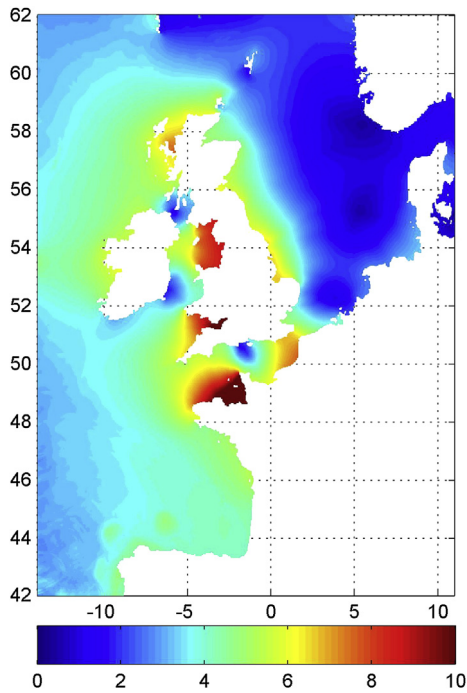
Fig. 7. Simulated tidal range (m) over the study region during January 2005.

Centre for Medium-Range Weather Forecasts (ECMWF; www. ecmwf.int). ERA (Interim reanalysis) full resolution data was used, which is available 3-hourly at a spatial resolution of 0.75°. This wind data is based on model simulations, with data assimilation. SWAN was run in third-generation mode, with Komen linear wave growth and whitecapping, and quadruplet wave–wave

interactions. Due to the scale of our study, neglecting bottom friction did not make a significant difference on the results.

2.5. Model coupling

The effect of tides on waves can be modelled at various levels of complexity. SWAN and ROMS have been fully coupled in previous studies, using the Model Coupling Toolkit (MCT) [19,32]. In a coupled SWAN–ROMS simulation, it is possible to control the detailed interaction between the models via importing and exporting variables, and ROMS compiler options. In the fully coupled model, the wave parameters which affect the current (wave height, wave direction, wave length, wave period, bottom orbital velocity, and radiation stresses) will be exported to the ocean model in each coupling time interval, while the hydrodynamic parameters (water depth, current velocity, and friction) will be exported from the ocean model to the wave model. If the effect of waves on tides is ignored, SWAN can read the current field and water level data from a data file which has already been generated by ROMS or any other hydrodynamic model. This approach (one-way coupling) has much lower computational cost for studies which are more focussed on simulating accurate wave climates.

3. Results and discussion

3.1. Model validation

A tidal model can be validated against tide gauge data at particular locations. However, a more comprehensive approach is to perform tidal analysis for the entire computational domain and compare the resulting cotidal charts with well established cotidal charts of the region. Fig. 4 shows the M_2 cotidal chart and current ellipses of the northwest European shelf seas based on the model results, which is in good agreement with those available in the

(a) Average current speed

(b) Maximum current speed
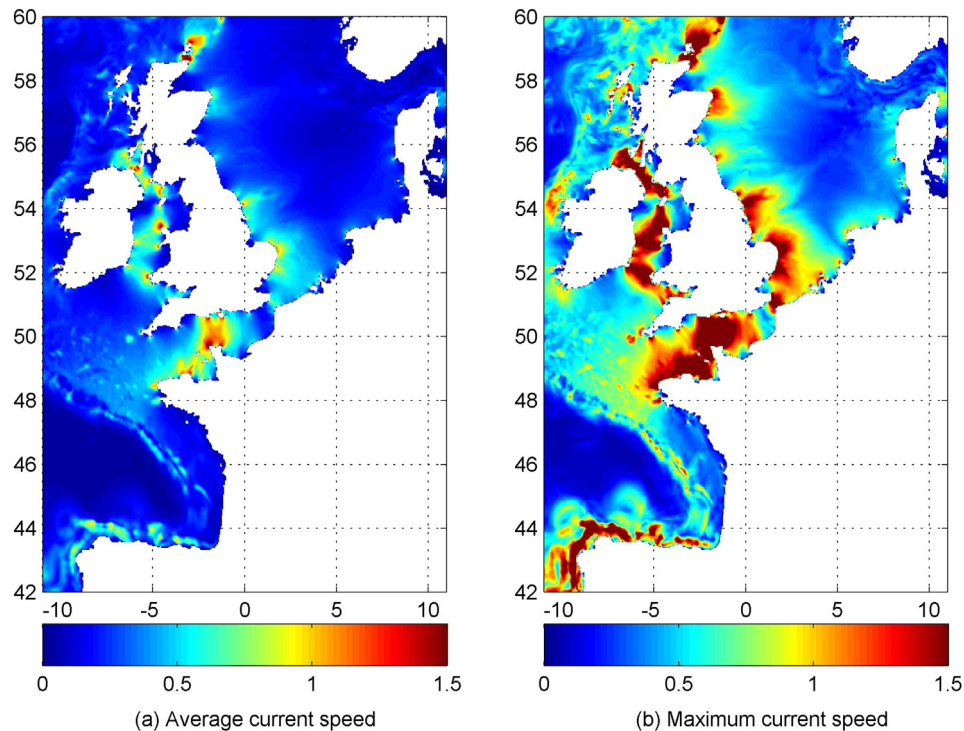
Fig. 8. Tidal current regime over the northwest European shelf seas. The colour scale show velocity in m/s. (For interpretation of the references to colour in this figure legend, the reader is referred to the web version of this article.)
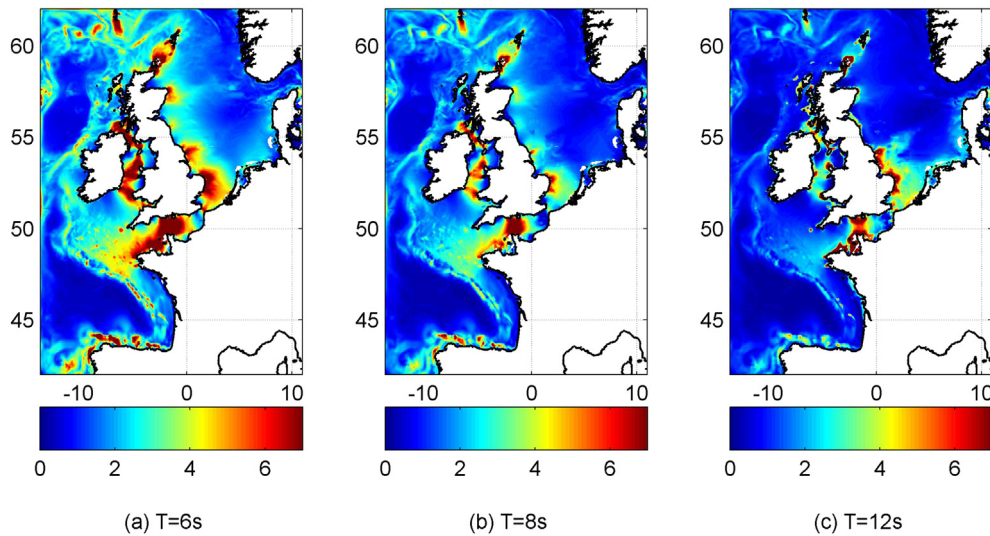
Fig. 9. Percentage estimated impact of the tide for different uniform wave periods over the region using the simplified method presented in Section 2.1.

literature (e.g. Ref. [33]). The M_2 semi-diurnal tide is responsible for the majority of tidal energy in this region, and so is presented as a sample. Also, Table 3 shows the validation of the ROMS model at a number of tide gauge stations distributed throughout the domain, with typical mean absolute error of 10 cm and 10° for amplitude and phase, respectively.

In terms of wave model validation, the SWAN model of the northwest European shelf seas has been validated in detail in a previous study [15] which was based on the same configuration as the present model. Nevertheless, a brief validation of SWAN against additional wave buoy data is presented here. Fig. 5 demonstrates the good agreement of the computed and observed wave heights at

Fig. 10. Spatial distribution of mean wave period (s) during January 2005.

selected wave buoys (see Fig. 1) for January 2005 with mean absolute errors of 23 cm–70 cm. In addition, wave power can be estimated using the observed significant wave height H_{mo} and the wave energy period (T_e) using [7],

$$P = \frac{\rho g^2}{64\pi} H_{mo}^2 T_e \tag{5}$$

The estimated wave power at each of the wave buoys has been compared with those computed by the SWAN model in Fig. 6 and demonstrates convincing agreement. The performance of the model is slightly better in M2 and M5 compared M4 which is closer to the western boundary. Moreover, part of the discrepancies at M4 wave buoy can be related to its malfunctioning which has been reported elsewhere [21].

3.2. Impact of tides on wave power

3.2.1. Simple estimate based on the tidal regime

Although the best way to quantify the effect of tides on wave power is through high resolution coupled wave-current models, this method is time consuming and computationally expensive. Therefore, an approximate and quick estimate could be useful in many practical circumstances, and could determine whether it is worth investing in a more expensive detailed modelling study for a particular location. As discussed in Section 2.1, linear wave theory can give an estimate of the potential effect of tides on wave power assessment using basic tidal and wave information, such as tidal amplitude, current speed, and wave period. Based on this simplified method, an estimate of the effect of tide on wave resources can be computed easily without extensive time consuming coupled wave-tide modelling. This is particularly useful in the early stages of a project study.

To compute the effect of tides on the wave resource estimation, based on this method, tidal parameters which represent the tidal regime throughout the domain were extracted from the ROMS model results. Fig. 7 and Fig. 8 show the spatial distribution of tidal range and current speed (maximum and average) during January 2005. The potential effect of tides on the wave energy resource can be estimated by combining these variables with the bathymetry of the region (Fig. 1) and applying the simplified method described in Section 2.1. The estimated effect of tides on wave power estimation for a sample range of mean wave periods is depicted in Fig. 9. This
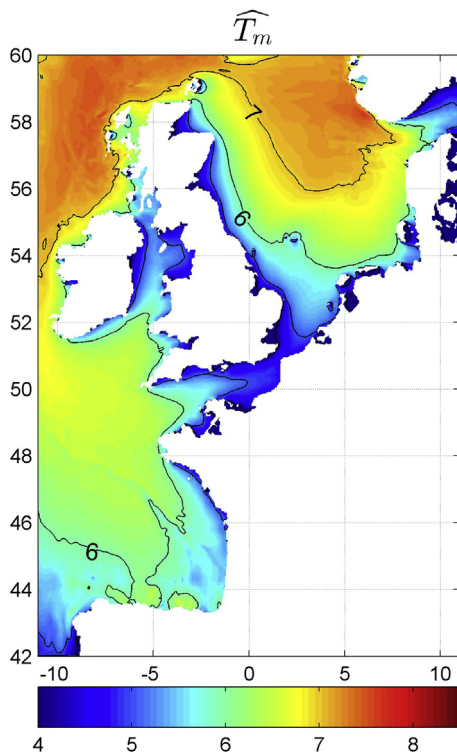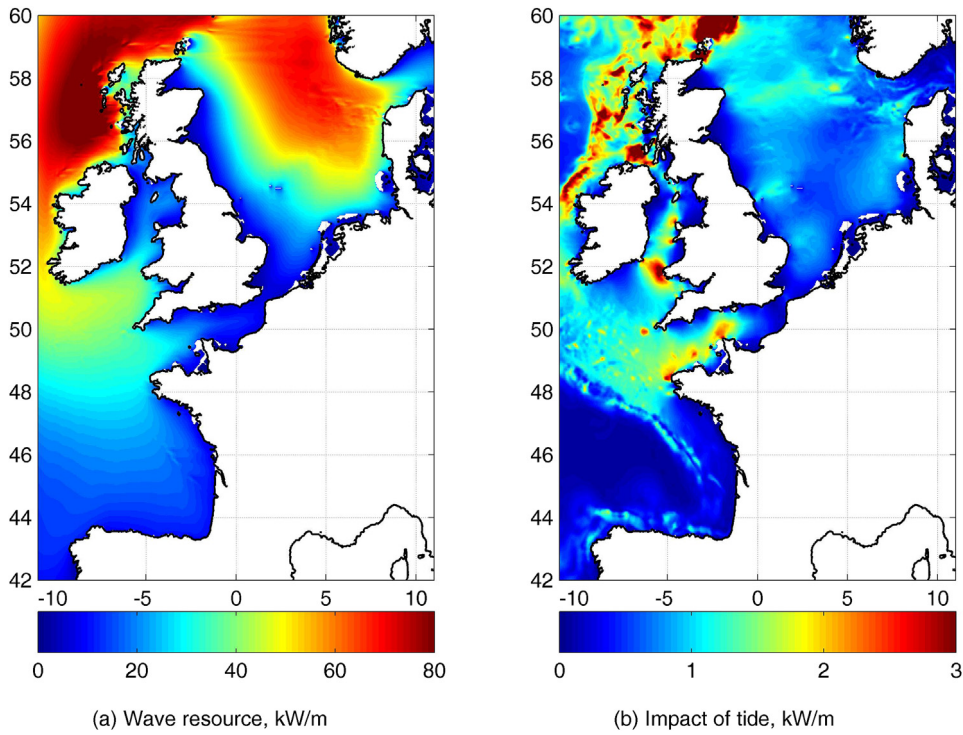
(a) Wave resource, kW/m

(b) Impact of tide, kW/m

Fig. 11. Distribution of the estimated effect of tides on the wave power resource.

effect has been computed as the relative difference in the estimated wave power with and without inclusion of tides. Referring to Fig. 10, which shows the spatial variation of the mean wave period during January 2005, the most common wave periods have been

selected for this analysis. According to Fig. 9, the effect of the tide on wave power estimation decreases with wave period. Since the wave period is generally proportional to the wave height, more energetic regions therefore experience lower impact. In contrast, less energetic regions with lower wave periods are likely to be affected more
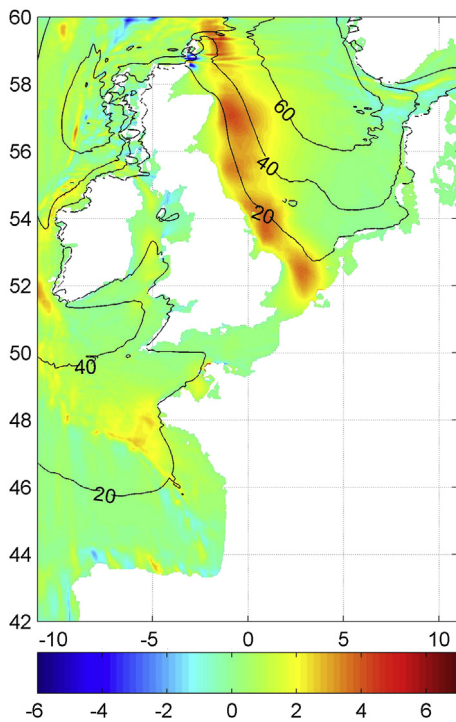
Fig. 12. Computed effect of tides on the wave power resource using SWAN−ROMS coupled model. The contour lines represent the January 2005 mean wave energy resource, and the colour scale is the magnitude of the effect, kW/m. (For interpretation of the references to colour in this figure legend, the reader is referred to the web version of this article.)
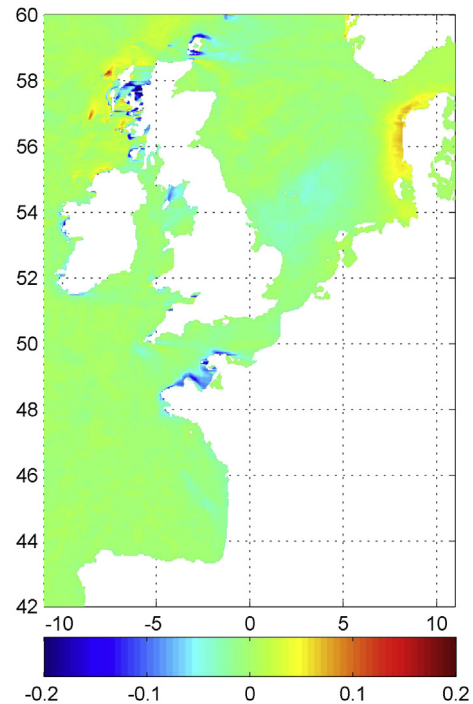
Fig. 13. The computed effect of tidal water depth (neglecting currents) on the wave power resource estimation using the SWAN−ROMS coupled model, kW/m. The magnitude is negligible compared with the impact of tidal currents (i.e. Fig. 12).

by the tide. This is consistent with results of previous studies which reported significant effect of the tides in relatively low energy regions such as the Adriatic Sea [16]. Nevertheless, even for large wave periods, the magnitude of the effect in strong tidal current regions exceeds 8 kW/m, which will have a significant impact on the net power generated over the life cycle of a wave energy project. The magnitude, rather than the percentage of this effect is depicted in Fig. 11. As expected, wave sites which are located in strong tidal currents such as the Pembrokeshire coast, Orkney, the northwest coast of France, and the west coast of Ireland could be affected significantly. These results are generally consistent with those based on the SWAN–ROMS coupled model, discussed in the following section.

3.2.2. Evaluation of the impact of tides using the SWAN–ROMS coupled model

The effect of tides on the wave resource of the northwest European shelf seas can be computed by contrasting SWAN model results (without tidal effects) and SWAN–ROMS coupled model results. Fig. 12 shows the results of the average impact on wave power during January 2005 (contour lines denote the mean wave power in this figure). Since some regions have negligible mean wave power, presenting the results as the percentage of the wave resource is in some ways misleading. The mean wave power over the entire model domain during January 2005 is 74 kW/m. Consequently, the impact is as high as 10% in regions of strong tidal flow. The order of magnitude of this impact is consistent with the simplified method that was applied in the previous section. Regions of particular interest which are significantly affected by tides are the west coast of Scotland, Orkney, the west coast of Ireland, the Pembrokeshire coast (UK), the northwest coast of France, and the north coast of Spain. In contrast to the analysis of the previous section, the east coast of the UK experiences a significant impact. The low energy environment of this region is mainly responsible for this impact since shorter wave periods are more strongly affected by tidal currents (Fig. 9). Further, because of the sheltering effect of the UK, the nature of wave generation and transformation, including the relative directions of tides and waves direction, is more complex and nonlinear in such sheltered regions, compared with more exposed areas. These processes have not been included in the simplified analysis presented before. Nevertheless, the simplified approach can give an order of magnitude of the effect with minimal effort.

In the majority of cases, the result of ignoring tides when simulating waves is an underestimate of the wave energy resource (positive values), while in regions like the west coast of Scotland an overestimate of the wave resource is likely, if tidal effects are neglected. In addition, it is interesting to note that the effect of variations in tidal water depths is much less than that of the current speed. As shown in Fig. 13, this effect is negligible for this scale of study. This is consistent with results reported in Fig. 2a which shows a very low impact due to variations in tidal water level in deeper waters. It should be noted that further analysis at a specific site location with a high resolution model may not lead to same conclusion due to nonlinearity of combined wave and tidal processes.

3.3. Further discussion

Direct measurement of wave properties in the presence of tides over relatively long time periods (including high energy and low energy months) is a very reliable method for accurate resource assessment at a site. Although the effect of tides on the wave signal is included implicitly in wave measurements, it is still difficult to filter the impact of tides from a wave signal, and investigate how the tide has contributed to the net wave resource. Further, similar wave events can happen at different stages of the tide (e.g. spring, neap, flood, ebb), and the impact of tides during such events will differ. Given the stochastic nature of waves, when the impact of tides on waves is expected to be significant, modelling studies are particularly useful for future scenarios when a wave event can occur at various stages of the tide. While the two methods presented here are samples of simple and more complex approaches, other methods with different degrees of complexity can be applied, depending on the stage of development and level of investment at a specific site. For instance, more complex wave-current formulations can be incorporated in ROMS. As mentioned before, the model computational grid, the resolution of the inputs, and validation data, are major factors in resolving these processes.

4. Conclusion

Our simple, yet rigorous, numerical study demonstrates that tides have a significant impact on the simulated wave energy resource. The magnitude of the impact exceeds 10% of the resource (around 8 kW/m in some regions such as Orkney (Scotland) and the west coast of Ireland) in high tidal current regions. While many sites are under development for wave energy extraction, particular care should be taken in areas such as the west coast of Scotland, Orkney, the west coast of Ireland, Pembrokeshire coast (UK), the northwest coast of France, and the north coast of Spain. It should be noted that the "mean" impact when considered over the entire northwest European shelf seas is almost negligible, while the impact is highly significant in some regions.

Results show that the effect of tidal currents on wave power is much greater than the effect of tidal elevations at the scale of our study. We have also demonstrated that the magnitude of the impact decreases with the wave period. Therefore, low to medium wave energy sites will be more affected by tides compared with high energy sites where the wave period will be higher. Nevertheless, the impact is still significant in high energy sites such as waters to the west of Scotland.

The simplified method which was developed here, based on linear wave theory, can provide a rapid estimate of the effect of tides on the wave energy resource. However, more detailed assessment using rigorous coupled wave-current modelling is recommended for complex regions during later stages of project development.

Due to the scale of this study, and limitations in model resolution, it was not possible to include detailed shallow water processes in the wave-current interaction modelling. Therefore, detailed high resolution models for specific sites could lead to a more accurate estimate of the impact.

While this study focused on the impact of the tide on the wave energy resource, the impact of waves on the tidal energy resource can also be studied using the ROMS-SWAN coupled model at shelf scale. The inclusion of shallow water wave-current interactions at this scale will be challenging, due to the high computational costs associated with required model resolution.

## References

[1] IPCC. Renewable Energy Sources and Climate Change Mitigation. Cambridge, United Kingdom and New York: Cambridge University Press; 2011.

[2] Pelc R, Fujita R. Renewable energy from the ocean. Mar Policy 2002;26:471–9.

[3] Gunn K, Stock-Williams C. Quantifying the global wave power resource. Renew Energy 2012;44:296–304.

[4] Egbert GD, Ray RD. Semi-diurnal and diurnal tidal dissipation from TOPEX/Poseidon altimetry. Geophys Res Lett 2003;30:1907. http://dx.doi.org/10.1029/2003GL017676.

[5] Gosscustard J, Warwick R, Kirby R, McGrorty S, Clarke R, Pearson B, et al. Towards predicting wading bird densities from predicted prey densities in a post-barrage Severn Estuary. J Appl Ecol 1991;28:1004–26.

[6] Ward SL, Green JAM, Pelling HE. Tides, sea-level rise and tidal power extraction on the European shelf. Ocean Dyn 2012;62:1153–67.

[7] Bahaj AS. Generating electricity from the oceans. Renew Sustain Energy Rev 2011;15:3399–416.

[8] Hulme M, Barrow E. Climates of the British Isles. London and New York: Routledge; 1997.

[9] Hashemi MR, Abedini MJ, Neill SP, Malekzadeh P. Tidal and surge modelling using differential quadrature: a case study in the Bristol Channel. Coast Eng 2008;55:811–9.

[10] Mellor GL. The depth-dependent current and wave interaction equations: a revision. J Phys Oceanogr 2008;38:2587–96.

[11] Guillou N, Chapalain G. Modeling the tide-induced modulation of wave height in the outer seine estuary. J Coast Res 2012;28:613–23.

[12] Brown JM, Davies AG. Methods for medium-term prediction of the net sediment transport by waves and currents in complex coastal regions. Cont Shelf Res 2009;29:1502–14.

[13] João Teles M, . Pires-Silva AA, Benoit M. Numerical modelling of wave current interactions at a local scale. Ocean Model; 2013.

[14] ABPmer. The met Office and Proudman Oceanographic Laboratory; Atlas of UK marine renewable energy resources. Technical Report. Department for Business Enterprise & Regulatory Reform; 2008.

[15] Neill SP, Hashemi MR. Wave power variability over the northwest European shelf seas. Appl Energy 2013;106:31–46.

[16] Barbariol F, Benetazzo A, Carniel S, Sclavo M. Improving the assessment of wave energy resources by means of coupled wave-ocean numerical modeling. Renew Energy 2013;60:462–71.

[17] M. Hashemi, S. Neill, A. Davies. A numerical study of wave and current fields around Ramsey island – tidal energy resource assessment, in: XIXth TELEMAC-MASCARET User Conference, Oxford, United Kingdom.

[18] Saruwatari A, Ingram DM, Cradden L. Wave–current interaction effects on marine energy converters. Ocean Eng 2013;73:106–18.

[19] Warner JC, Armstrong B, He R, Zambon JB. Development of a coupled ocean–atmosphere–wave–sediment transport (COAWST) modeling system. Ocean Model 2010;35:230–44.

[20] Jones B. A numerical study of wave refraction in shallow tidal waters, Estuarine. Coast Shelf Sci 2000;51:331–47.

[21] Elliott AJ, Neill SP. Simulating storm waves in the Irish Sea. Proc ICE-Maritime Eng 2007;160:57–64.

[22] Dean RG, Dalrymple RA. Water wave mechanics for engineers and scientists; 1991.

[23] Clément A, McCullen P, Falcão A, Fiorentino A, Gardner F, Hammarlund K, et al. Wave energy in europe: current status and perspectives. Renew Sustain Energy Rev 2002;6:405–31.

[24] Shchepetkin AF, McWilliams JC. The regional oceanic modeling system (roms): a split-explicit, free-surface, topography-following-coordinate oceanic model. Ocean Model 2005;9:347–404.

[25] Shchepetkin AF, McWilliams JC. Correction and commentary for "ocean forecasting in terrain-following coordinates: formulation and skill assessment of the regional ocean modeling system" by Haidvogel et al., J. Comp. Phys. 227, pp. 3595–3624. J Comp Physiol 2009;228:8985–9000.

[26] Haidvogel DB, Arango H, Budgell W, Cornuelle B, Curchitser E, Di Lorenzo E, et al. Ocean forecasting in terrain-following coordinates: formulation and skill assessment of the regional ocean modeling system. J Comp Physiol 2008;227:3595–624.

[27] MacCready P, Banas NS, Hickey BM, Dever EP, Liu Y. A model study of tide-and wind-induced mixing in the Columbia River estuary and plume. Cont Shelf Res 2009;29:278–91.

[28] Di Lorenzo E, Moore AM, Arango HG, Cornuelle BD, Miller AJ, Powell B, et al. Weak and strong constraint data assimilation in the inverse regional ocean modeling system (ROMS): development and application for a baroclinic coastal upwelling system. Ocean Model 2007;16:160–87.

[29] Egbert GD, Erofeeva SY. Efficient inverse modeling of barotropic ocean tides. J Atmos Ocean Technol 2002;19:183–204.

[30] Warner JC, Sherwood CR, Arango HG, Signell RP. Performance of four turbulence closure models implemented using a generic length scale method. Ocean Model 2005;8:81–113.

[31] Booij N, Ris R, Holthuijsen LH. A third-generation wave model for coastal regions: 1. Model description and validation. J Geophys Res Oceans (1978–2012) 1999;104:7649–66.

[32] Warner JC, Sherwood CR, Signell RP, Harris CK, Arango HG. Development of a three-dimensional, regional, coupled wave, current, and sediment-transport model. Comput Geosci 2008;34:1284–306.

[33] Neill SP, Scourse JD, Uehara K. Evolution of bed shear stress distribution over the northwest European shelf seas during the last 12,000 years. Ocean Dyn 2010;60:1139–56.

List of symbols

a^h, a^v: amplitudes of the water elevation and velocity for a harmonic tide

C, C^*: wave celerity in the absence and presence of currents, respectively

C_g, C_g^*: group velocity in the absence and presence of currents, respectively

E: wave energy, $\Omega_{M_2}^m$

h: water depth (dependent on tide)

h_o: bathymetry (water depth at mean sea level; constant)

H_{mo}: significant wave height

k, k^*: wave number in the absence and presence of tides, respectively

p_D: dynamic pressure resulting from a linear wave

P_m: computed wave energy flux per unit wave (power) based on the SWAN–ROMS coupled model.

P, P^*: average energy flux per unit wave in the absence and presence of tides, respectively

T_{M_2}: period of M_2 tide, 12.42 h

T_e: wave energy period

u: wave induced velocity in the linear wave theory

U: tide induced velocity in a harmonic tide

Ω_h, Ω_v: phases of water depth and velocity in a simple harmonic tide

ω, T: relative angular wave frequency and relative wave period for a linear wave

ω^*, T^*: absolute angular wave frequency and absolute wave period for a linear wave

.2   Published work P-II
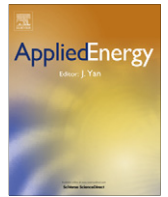
Wave power variability over the northwest European shelf seas

Simon P. Neill *, M. Reza Hashemi

School of Ocean Sciences, Bangor University, Menai Bridge, UK

HIGHLIGHTS

► We simulate the wave climate of the NW European shelf seas over a 7 year period.
► We apply a high resolution 3rd-generation wave model.
► We quantify spatial patterns of uncertainties in estimating the wave power resource.
► Uncertainty is considerably greater over winter months.
► There is a positive correlation between winter wave power and the NAO.

ARTICLE INFO

ABSTRACT

Regional assessments of the wave energy resource tend to focus on averaged quantities, and so provide potential developers with no sense of temporal variability beyond seasonal means. In particular, such assessments give no indication of inter-annual variability – something that is critical for determining the potential of a region for wave energy convertor (WEC) technology. Here, we apply the third-generation wave model SWAN (Simulating Waves Nearshore) at high resolution to assess the wave resource of the northwest European shelf seas, an area where many wave energy test sites exist, and where many wave energy projects are under development. The model is applied to 7 years of wind forcing (2005–2011), a time period which witnessed considerable extremes in the variability of the wind (and hence wave) climate, as evidenced by the variability of the North Atlantic Oscillation (NAO). Our simulations demonstrate that there is much greater uncertainty in the NW European shelf wave resource during October–March, in contrast to the period April–September. In the more energetic regions of the NW European shelf seas, e.g. to the northwest of Scotland, the uncertainty was considerably greater. The winter NW European shelf wave power resource correlated well with the NAO. Therefore, provided trends in the NAO can be identified over the coming decades, it may be possible to estimate how the European wave resource will similarly vary over this time period. Finally, the magnitude of wave power estimated by this study is around 10% lower than a resource which is used extensively by the wave energy sector – the Atlas of UK Marine Renewable Energy Resources. Although this can partly be explained by different time periods analysed for each study, our application of a third-generation wave model at high spatial and spectral resolution significantly improves the representation of the physical processes, particularly the non-linear wave-wave interactions.

© 2013 Elsevier Ltd. All rights reserved.

1. Introduction

To reduce greenhouse gas emissions and aid sustainable development, there is an urgent need to support our electricity generating capacity through the development of low carbon technologies, particularly those generated from renewable sources [1]. The ocean is a vast and largely untapped energy resource – wave energy alone has been estimated as around 2 TW globally [2]. A significant portion of this wave energy could be exploited by a range of wave energy converter (WEC) technologies [3], and so wave energy has been highlighted as a key contributor to the future global energy mix. However, progress from full-scale testing to commercialisation of wave energy projects has been relatively slow, partly due to the financial risks associated with uncertainty in quantifying the wave energy resource at a variety of timescales. This is in direct contrast to assessment of the tidal energy resource – tidal currents are largely driven by astronomical forces, and so can be accurately predicted over long time scales [4]. Beyond seasonal trends, waves are largely stochastic, and so it is difficult to quantify the long-term wave resource for a region at a variety of timescales. With likely future changes in the wave energy resource due to climate change [5–7], this uncertainty in resource assessment will increase for proposed future large-scale WEC array scenarios that have been identified in marine energy roadmaps (e.g. [8]).

* Corresponding author.
  E-mail address: s.p.neill@bangor.ac.uk (S.P. Neill).

One of the most popular data sources used by developers for quantifying the UK wave energy resource is the Atlas of UK Marine Renewable Energy Resources [9]. Similar wave resource assessments have been made for Europe [3], the Black Sea [10], the Baltic Sea [11], the Canary Islands [12], Australia [13], China [14], the United States [15], and globally [2]. Regardless of the accuracy of such studies in terms of data quality and availability, and the spatial, temporal, and spectral resolution of the underlying wave models, most assessments provide potential developers with only averaged quantities such as the annual mean significant wave height and wave power, and give no indication of temporal variability beyond seasonal means [16]. Of the few studies which do analyse how the temporal distribution of wave energy resource at seasonal and inter-annual scale affects site selection, Cornett [17] analysed variability of the global resource at a relatively coarse (1.25° × 1°) model resolution, and Liberti et al. [18] provide a study of wave variability for the Mediterranean. Akpinar and Komurcu [10] provide a thorough resource assessment for the Black Sea, examining monthly, seasonal, and annual distributions of wave height and wave power. However, most studies give no indication of the inter-annual variability of the wave resource, something that is critical for even a superficial assessment of the wave energy potential of a region. Further, the suitability of a particular location cannot be matched to a particular WEC technology [19], since these resource assessments provide no information on the spectral properties of the waves. Rather, relatively expensive high-resolution nested model studies [20], or expensive *in situ* monitoring programmes [21], are required to make even an initial assessment of the wave energy potential of a region. The present research aims to address such issues by providing a thorough assessment of the wave energy potential of the NW European shelf seas, a region where many wave energy projects are under development. In particular, this study focusses on temporal variation of the wave resource over seasonal and inter-annual timescales, and assesses the spectral properties of the waves for a range of contrasting locations.

2. Study region

The NW European shelf sea has been selected for this study as it is one of the most energetic shelf sea regions in the world [2,22]. Due to its large wave energy resource, and the prominence of European nations (particularly the UK) in developing wave energy technologies [3], many wave energy test sites exist, and many wave energy projects are under development throughout this region, with selected sites shown on Fig. 1, and further details provided in Table 1. These eight locations form the basis of the detailed site-specific resource assessment in Section 4.2, and further details of the sites can be found in Bahaj [1], Reeve et al. [6], Mouslim et al. [23], Beels et al. [24] and Aquamarine Power [25]. These sites are located in regions of considerable variations in water depths and wave exposures, and so enable a contrast in wave properties to be made for a wide range of environments. In addition to being a suitable region for exploitation of the wave energy resource, the oceanography of the northwest European shelf seas is well documented, and extensive datasets are available, including wave buoy data, to validate models of the region. Further, since many countries have coastlines bordering the NW European shelf seas, this increases the relevance, and hence impact, of this study.

The NW European shelf seas, located on the northeastern margin of the North Atlantic, are generally shallower than 200 m (Fig. 1). The Celtic Sea, Malin Sea and northern North Sea are exposed to Atlantic waters, with water depths in the range 100–200 m, with the exception of the deeper (600 m) Norwegian Trench in the northeastern North Sea. The Celtic Sea borders the Irish Sea to the north, a semi-enclosed water body. To the east of

the Celtic Sea, the English Channel connects to the southern North Sea; and to the south of the Celtic Sea lies the Bay of Biscay.

The climate of the NW European shelf is dominated by the atmospheric polar front [26]. The instability of this front causes depressions to form, tracking across the North Atlantic and following a preferred route which passes between Iceland and Scotland. There is considerable variation in the wind climate around the NW European shelf seas, but the strongest winds generally emanate from the west and south, and the mean winds from the southwest [27]. Wind speeds tend to be highest to the northwest of the British Isles (closest to the depression tracks), decreasing towards the south and east. An annual cycle of higher wind speeds in winter and lower speeds in summer reflects the seasonally varying strength of the large-scale atmospheric circulation [26]. The strong background flow leads to high mean wave energy over the shelf seas and the variability results in a wave climate with considerable extremes [28]. Considerable interannual variability in the synoptic-scale circulation over the Atlantic is described by the North Atlantic Oscillation (NAO) index [29], and a previous study has demonstrated that there is a positive correlation between the NAO and the mean wave power for an area off the north coast of Scotland [30]. In regions of the shelf seas exposed to the Atlantic, the orbital velocity of the longer-period (swell) waves penetrates to the sea bed [31]. Where fetch length is sufficient, the wave distribution over the shelf seas broadly maps to the wind distribution [28]. Due to the dominant southwesterly wind direction, many regions of the NW European shelf seas are relatively sheltered from wind effects and hence experience relatively low wave energy, particularly the western seaboard of the North Sea (sheltered by the UK land mass) and the northern half of the Irish Sea (sheltered by Ireland).

3. Methods

3.1. Wave model

The third-generation spectral wave model SWAN (Simulating Waves Nearshore) was used to simulate wave climates over the North Atlantic, including the NW European shelf seas. SWAN is an Eulerian formulation of the discrete wave action balance equation [32]. The model is spectrally discrete in frequencies and directions, and the kinematic behaviour of the waves is described by the linear theory of gravity waves. SWAN accounts for wave generation by wind, non-linear wave-wave interactions, white-capping, and the shallow water effects of bottom friction, refraction, shoaling, and depth-induced wave breaking.

The evolution of the action density N is governed by the wave action balance equation which, in spherical coordinates, is [32]

$$\frac{\partial N}{\partial t} + \frac{\partial c_\lambda N}{\partial \lambda} + \frac{\partial c_\phi N}{\partial \phi} + \frac{\partial c_\sigma N}{\partial \sigma} + \frac{\partial c_\theta N}{\partial \theta} = \frac{S_{tot}}{\sigma} \tag{1}$$

where c_λ and c_ϕ are the propagation velocities in the longitude (λ) and latitude (ϕ) directions, σ is frequency, θ is wave direction, and S_{tot} represents the source terms, i.e. generation, dissipation, and non-linear wave-wave interactions. For this application, the wave energy spectrum at each grid point was divided into 40 discrete frequency bins and 45 discrete direction bins for both scales of model simulation (North Atlantic and NW European shelf seas – see Section 3.3). The lowest modelled frequency was 0.05 s^{-1} (period T = 20 s), and the highest frequency resolved by the model was 2 s^{-1} (T = 0.5 s). Outside of this range, the wave spectrum was imposed, hence the effects of lower and higher frequencies are included in the simulations [33].

Version 40.85 of SWAN was run in third-generation mode, with Komen linear wave growth and whitecapping, and quadruplet
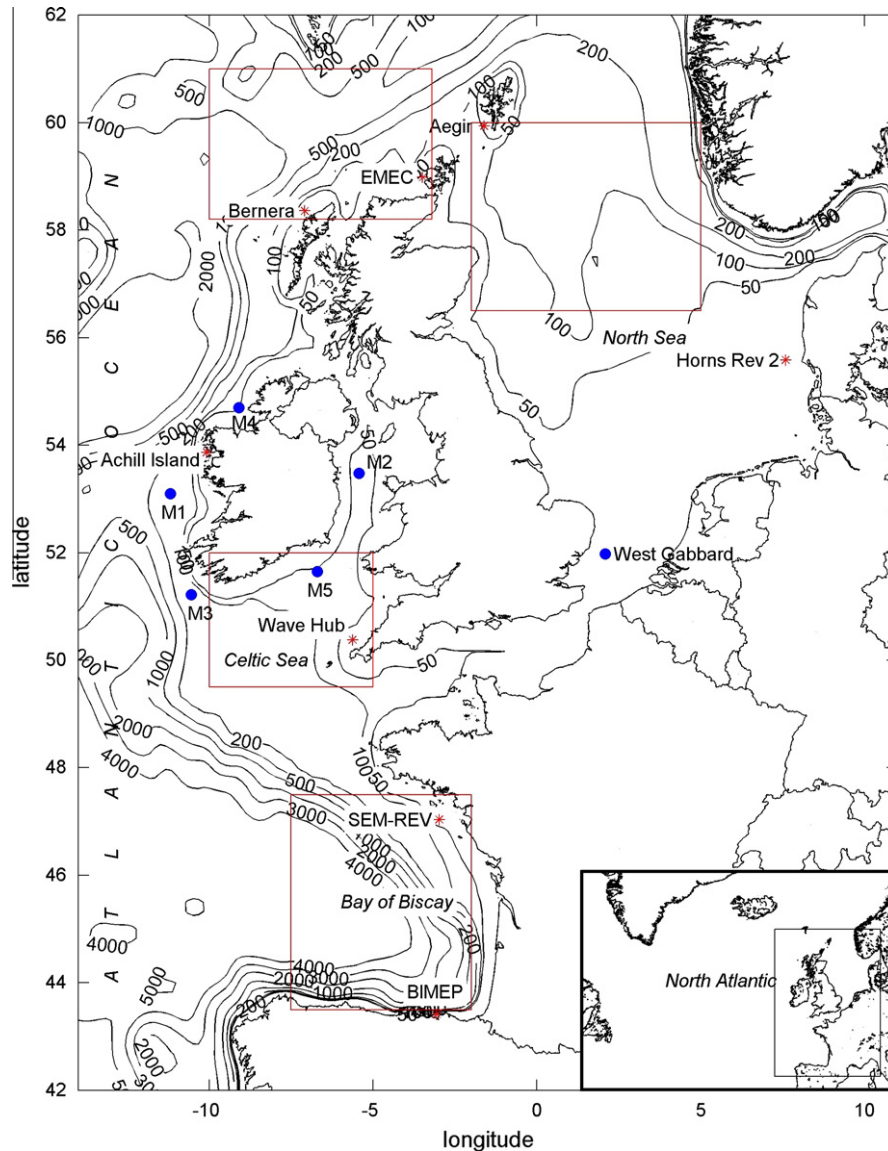
Fig. 1. Locations of selected wave energy projects and test sites distributed around the NW European shelf seas in regions of contrasting exposure, water depths, and wave climates. Blue circles (labelled) are the wave buoys used for model validation (further details are provided in Table 2), and the boxed regions are the areas used for regional comparisons (Biscay, Celtic, North Scotland and North Sea). Contours show water depth in metres relative to mean sea level. The inset which covers the entire North Atlantic shows the limits of the $1/6° \times 1/6°$ (outer) wave model which was run initially to generate boundary conditions for the $1/24° \times 1/24°$ (inner) nested wave model. (For interpretation of the references to colour in this figure legend, the reader is referred to the web version of this article.)

wave-wave interactions. Due to the scale of the simulations, bottom friction, depth-induced wave breaking, and triads were turned off. SWAN default formulations and coefficients were used for all of the physical processes.

3.2. Data sources

3.2.1. Bathymetry

GEBCO (General Bathymetric Chart of the Oceans) gridded bathymetry data was obtained from the British Oceanographic Data Centre (BODC) at a resolution of 30 arc-seconds in both latitude and longitude. This data was bi-linearly interpolated to the desired resolution of the computational domain (Section 3.3).

3.2.2. Wind data

Gridded wind data was provided by Met Éireann (the Irish Meteorological Service) using their operational HIRLAM (High Resolution Limited Area Model) version 7.2 forecast model

Table 1
Locations of wave energy projects and test sites used for detailed analysis.

Project	Lat	Long
BIMEP (Spain) – Biscay Marine Energy Platform	43.42	−3.07
SEM-REV (France) – wave energy test site	47.04	−2.98
Wave Hub (England)	50.38	−5.63
Horns Rev 2 (Denmark) – wind farm	55.58	7.59
Aegir (Shetland) – Pelamis	59.94	−1.62
EMEC (Orkney)	58.98	−3.49
Bernera (Scotland) – Pelamis	58.36	−7.09
Achill Island (Ireland) – Aquamarine Power	53.87	−10.08

(www.hirlam.org). The grid resolution of the model is $0.1° \times 0.1°$, with 60 vertical levels, and the resolution of the interpolated output wind data is $0.5° \times 0.5°$, extending from 60°W to 15°E, and from 40°N to 70°N. Data was available 3-hourly from January 2005 to December 2011.

Table 2
Model performance for Hs and Tp at various locations around the NW European shelf seas. Results are generally reported for an entire year of data and, in addition, results are reported seasonally for the M1 wave buoy to demonstrate temporal differences in model/data comparison.

Reference	Water depth (m)	Lat	Long	Hs			Tp		
				RMSE (m)	SI	Bias (m)	RMSE (s)	SI	Bias (s)
M1-2005	124	53.10	−11.19	0.50	0.17	−0.22	1.10	0.15	−0.42
M1 – D-J-F 2005				0.65	0.22	−0.36	1.25	0.18	−0.79
M1 – M-A-M 2005				0.47	0.16	−0.19	1.06	0.15	−0.28
M1 – J-J-A 2005				0.33	0.11	−0.15	0.95	0.14	−0.23
M1 – S-O-N 2005				0.53	0.18	−0.19	0.97	0.14	−0.40
M2-2005	73	53.48	−5.43	0.31	0.26	−0.16	0.82	0.19	0.53
M3-2005	126	51.22	−10.55	0.51	0.18	−0.24	1.17	0.17	−0.40
M4-2005	50	54.70	−9.09	0.62	0.26	0.17	1.06	0.16	−0.18
M5-2005	65	51.65	−6.70	0.59	0.36	0.39	0.94	0.18	0.21
W Gabbard – 2007	34	51.98	2.08	0.28	0.25	−0.09	1.14	0.21	−0.64

3.2.3. Wave data

Data from five wave buoys was obtained from the Irish Marine Institute, and data from an additional wave buoy operated by Cefas (Centre for Environment, Fisheries and Aquaculture Science) was obtained from BODC to provide validation for the North Sea. These wave buoys are located in a range of water depths and wave exposures (Table 2), and so provide a rigorous validation test over a range of environments. Data of significant wave height (Hs) and peak wave period (Tp) was available hourly throughout 2005 for the Irish Marine Institute wave buoys, and half-hourly throughout 2007 for the Cefas wave buoy.

3.3. Implementation of the wave model

The wave model was applied initially to a region which included the entire North Atlantic at a grid resolution of $1/6° \times 1/6°$, extending from 60°W to 15°E, and from 40°N to 70°N (i.e. the same domain covered by the gridded wind data) (see the inset on Fig. 1). Two-dimensional (2D) wave spectra were output hourly from this coarse outer grid simulation and interpolated to the boundary of an inner nested high resolution model of the NW European shelf seas. This inner nested region had a grid resolution of $1/24° \times 1/24°$, extending from 14°W to 11°E, and from 42°N to 62°N. After running the coarser outer model of the North Atlantic, this inner nested simulation was run without feedback to the outer nest, i.e. the nesting process was one-way. Variables were output every 3 h from this nested simulation at every grid point. One-dimensional (1D) and 2D wave spectra were also output at various locations where the spectral properties of waves were to be examined (Table 1). The period 2005–2011 was simulated, corresponding to the period of the available wind data. It took approximately 35,000 CPU hours to perform all of the model simulations, using 96 cores of a 2072 core system, based on Intel Xeon processors.

To demonstrate that the selected years of simulation (2005–2011) were representative of temporal variability over the study region, we made use of the ERA-Interim dataset (available 6-hourly at a grid resolution of $1.5° \times 1.5°$) over the North Atlantic, a dataset that has been successfully applied in previous studies of wave energy flux [34]. The ERA-Interim data were used to calculate the mean value of Hs^2 (a proxy for wave energy) over the North Atlantic (from 60°W to 15°E, and from 40°N to 70°N) every 6 h from 1979 to 2011. The statistical properties of $\overline{Hs^2}$ were then calculated for different time periods to check for stationarity in the data. The mean $\bar{x} = 9.93$ m^2 and standard deviation $s = 7.02$ m^2 were calculated for the time period 1979–2004. The corresponding values for the time period 1979–2011 (i.e. extending the analysis to incorporate our modelled time period) were $\bar{x} = 9.99$ m^2 and $s = 6.98$ m^2, i.e. differences of around 0.6% from the time period 1979 to 2004. Finally, $\bar{x} = 10.21$ m^2 and $s = 6.82$ m^2 were calculated for the time period 2005–2011, differences of around 2% from the

calculations for the 1979 to 2011 time period. Since these differences in statistical properties between each of the time periods was very small, our modelled time period (2005–2011) can be regarded as a representative sample of the wave power.

3.4. Model validation

The model was validated throughout 2005 using hourly time series of Hs and Tp from five wave buoys, and throughout 2007 for an additional (half-hourly) wave buoy located in the North Sea (Table 2). Good agreement was obtained for Hs (Fig. 2), with an average root mean square error (RMSE) of 0.47 m across all wave buoys (Table 2). Also reported on the table are the scatter index SI (RMSE normalised by the mean of the observations), and bias (mean error, calculated as model results minus observations). The SI for Hs was generally less than 0.25, with a peak value of 0.36 at the M5 buoy in the southern Irish Sea. The calculations of bias indicate that there was no systematic error in modelled Hs, with a mean value across all six wave buoys of −0.03 m. To assess the temporal variability in model performance, we also report seasonal values of RMSE, SI and bias for the M1 buoy (Table 2). Although we do find slightly larger RMSE (and SI) during autumn and winter months, these increased values are consistent with the increased uncertainty in wave power which occurs over these months (Section 4.1). There was considerably more variability in Tp at all of the validation locations (Fig. 3), but the model was generally in good agreement with the data, successfully reproducing variability at seasonal and sub-seasonal timescales. The average RMSE for Tp was 1.04 s across all sites (Table 2), but the values of SI were generally lower than the corresponding SI for Hs. Again, there was no particular bias in the modelled Tp, and there were increased errors during winter months, consistent with increased uncertainty in wave power during these more energetic periods.

4. Results

4.1. Wave power

Much of the subsequent analysis is based on wave power, which was calculated using linear wave theory. For a sinusoidal wave, the total (potential plus kinetic) time-averaged energy per unit horizontal area is

$$E = \frac{1}{8}\rho g H^2 \qquad (2)$$

Since $H = \sqrt{2}Hs/2$, then wave energy

$$E = \frac{1}{16}\rho g Hs^2 \qquad (3)$$

Wave energy is transported at the group velocity, c_g, and so the wave energy flux, or wave power P, can be calculated using
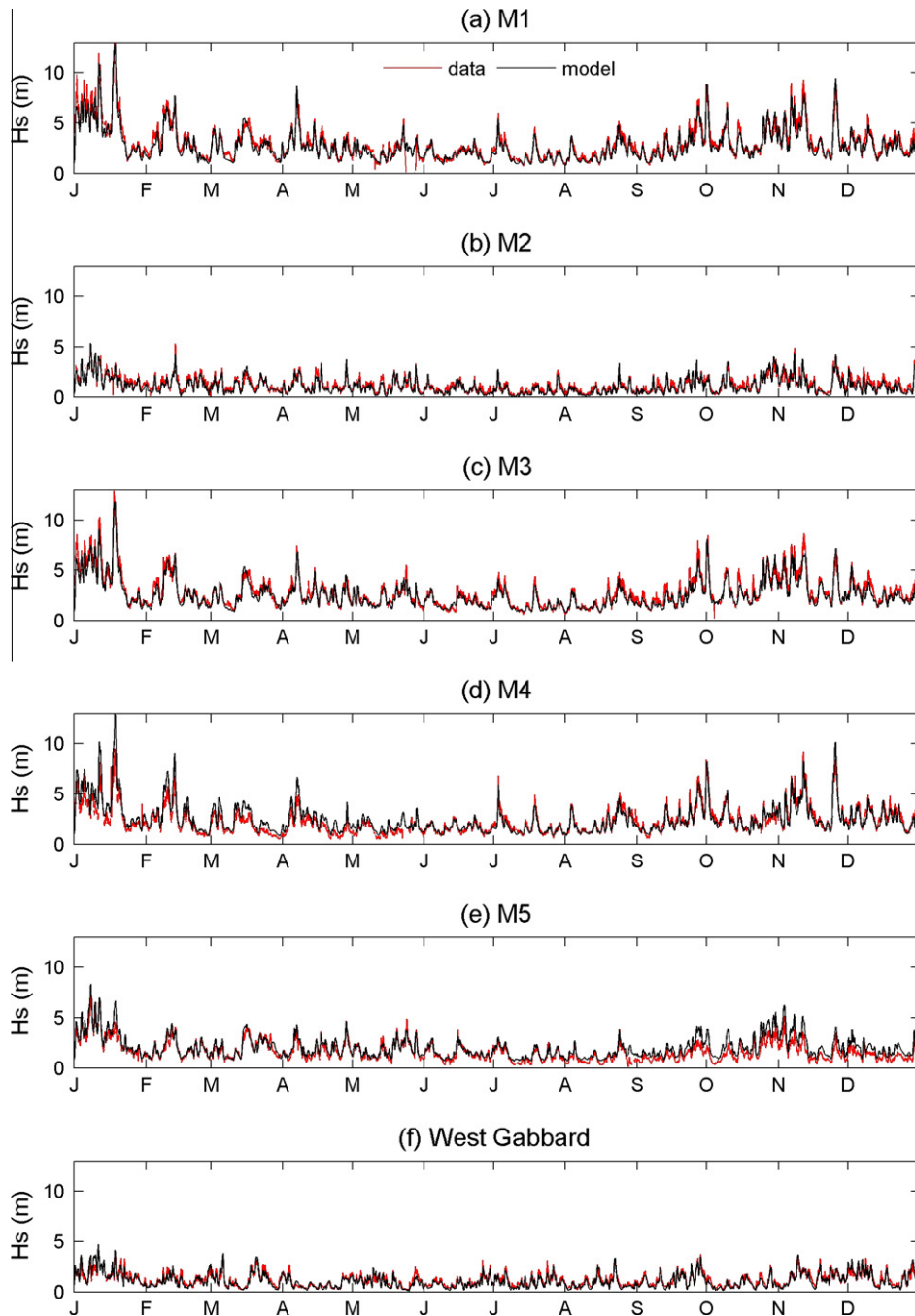
Fig. 2. Comparison of observed and modelled significant wave height for six locations distributed around the NW European shelf seas.

$$P = \frac{1}{16}\rho g Hs^2 c_g \qquad (4)$$

Results of the monthly mean wave power for a typical year (2007) are given in Fig. 4. It is difficult to define what a typical year actually is, but 2007 was typical in that wave power was greatest during the winter months (December–January–February), and at a minimum during the summer months (June–July–August). How-ever, several anomalies exist, typical of multi-year/multi-seasonal datasets. For example, wave power during March (a spring month) was greater than February (a winter month). It is also interesting to note the differences in the geographic distribution of wave power between the peak months of January, February, March and Decem-ber. In January and March, peak wave power was located to the northwest of Scotland and Ireland. In contrast, the wave power

in February was more focussed on the Celtic Sea and Bay of Biscay, while during December this distribution extended further north than the February distribution to encompass the west coast of Ireland. However, the objective of this paper is not to discuss any particular year in detail, but to examine inter-seasonal and inter-annual variability. It is therefore more useful to consider season-ally- and annually-averaged quantities.

The seasonal and annual distribution of wave power is summa-rised qualitatively in Fig. 5. With the exception of 2010, the wave resource was greatest in the winter months (December–January–February), and tended to be concentrated in waters exposed to the North Atlantic, particularly the northwest of Scotland and Ireland, and the west coast of Ireland, occasionally extending into the Celtic Sea and Bay of Biscay. With very few exceptions, the
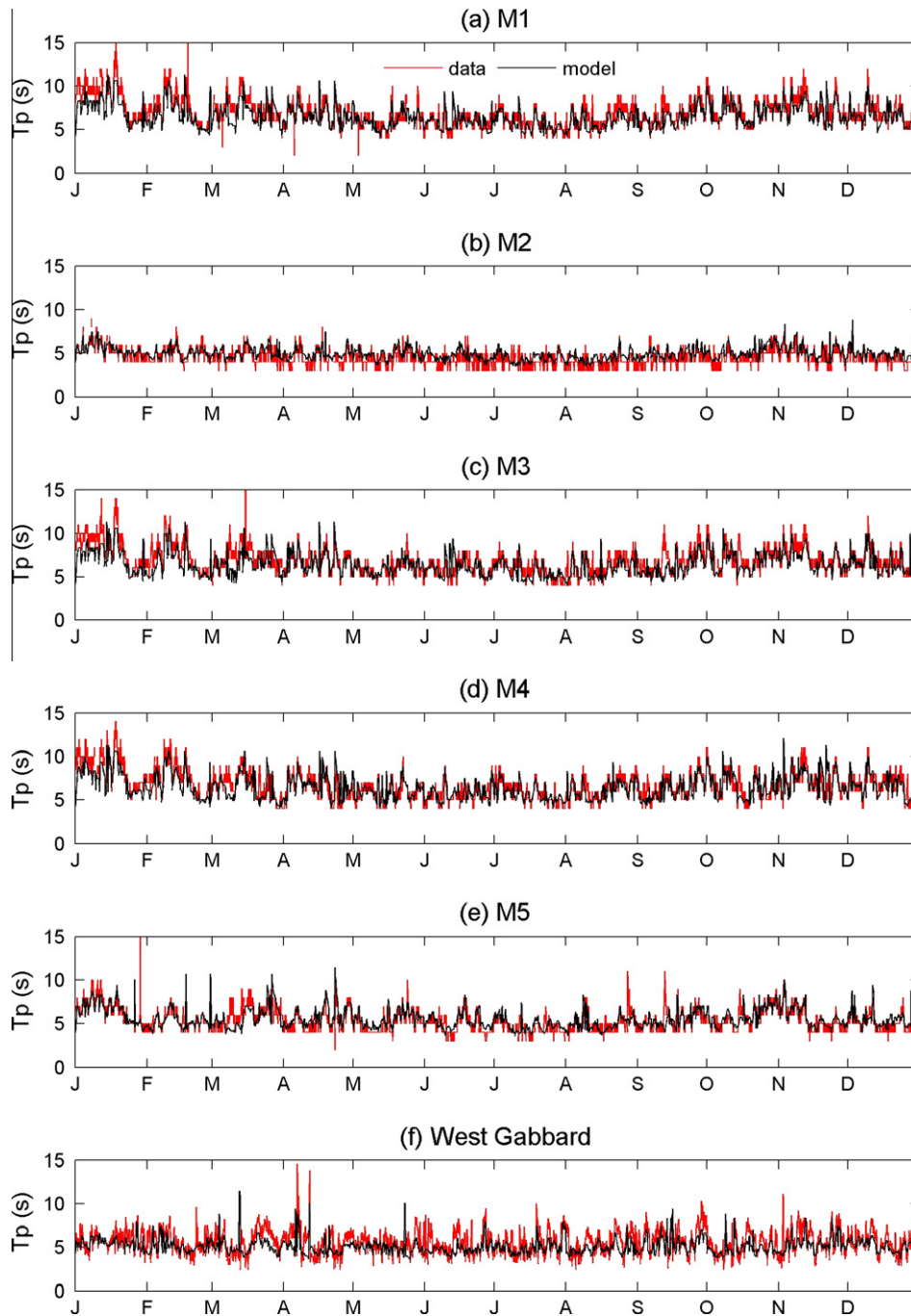
Fig. 3. Comparison of observed and modelled peak wave period for six locations distributed around the NW European shelf seas.

Autumn (September–October–November) resource was greater than the Spring (March–April–May) resource, and wave power was always at a minimum during the summer months (June–July–August). There was considerable variation between years, with 2010 being the least energetic year, and 2011 being the most energetic year.

To quantify the above results, the mean wave power was calculated over the NW European shelf seas for each season (Fig. 6). Averages, based on all of the data, provide a context (Table 3). Generally, wave power over the NW European shelf seas was around 48 kW/m in the winter, reducing to 11 kW/m in the summer. There were considerable extremes in the winter wave power, ranging from 29 kW/m in 2010 to 59 kW/m in 2007. Indeed, in 2010 the

autumn wave power (34 kW/m) actually exceeded the winter wave power. However, when averaged over the whole year, there is significantly less variability of the wave resource – the annual mean wave power ranged from 23 to 33 kW/m over the NW European shelf seas, compared to a mean for all simulated years of 29 kW/m. The annual fluctuation of wave power over the NW European shelf seas is shown on Fig. 7, including 90% confidence intervals calculated using all 7 years of model output. There is clearly much greater uncertainty over the winter months, plus early spring (March) and mid to late autumn (October and November), compared to the less variable April–September period. The uncertainty from October–March is ±3.9 kW/m (compared to an October–March mean wave power of 43 kW/m), in contrast to an
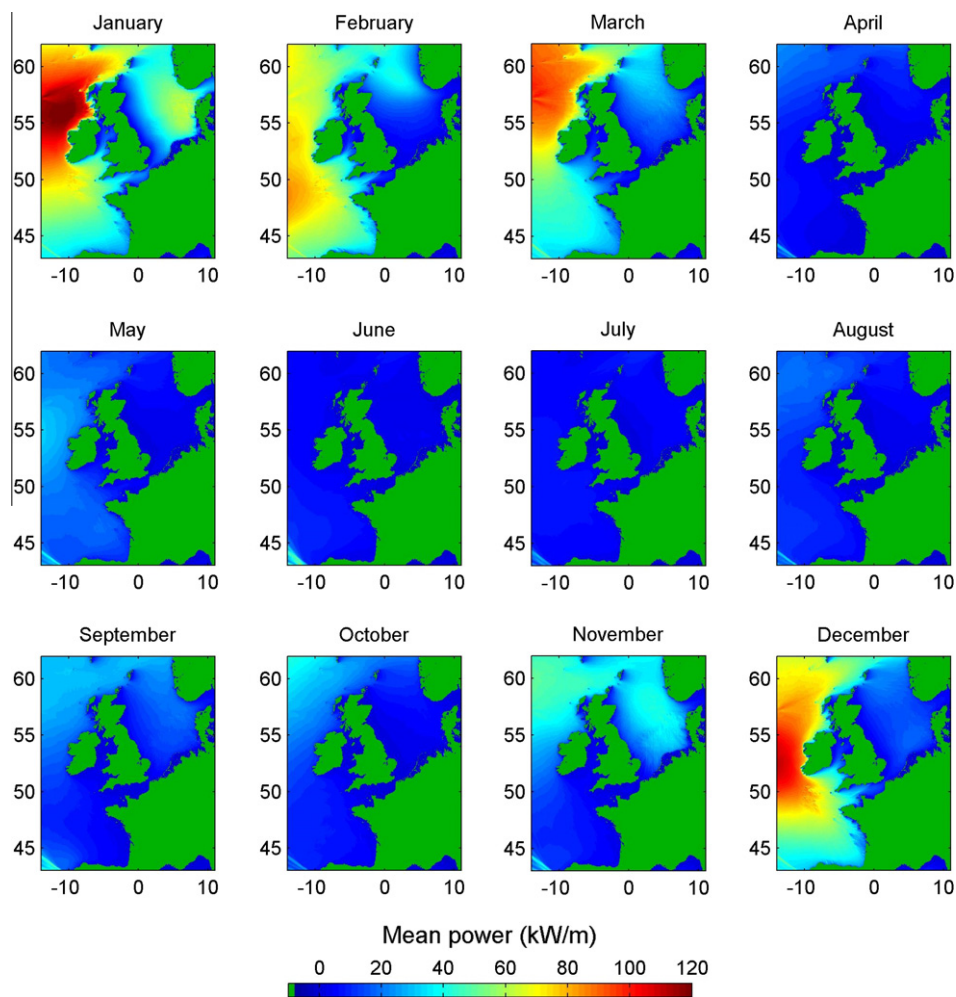
Fig. 4. Spatial distribution of mean monthly wave power throughout 2007.

April–September uncertainty of ±1.4 kW/m (compared to an April–September mean of 15 kW/m). It is therefore important to consider whether electricity supply for a region needs to be matched to demand in either winter (e.g. for heating) or summer (e.g. for cooling). If wave power is to be relied on as a key contributor to the future energy mix for Europe from October–March, there is considerable risk in the reliability (i.e. predictability) of the resource during this period, particularly on a month-by-month basis.

From Fig. 5, it is clear that there are significant regional variations in the European wave power resource, and these have not been accounted for in the shelf-scale analysis presented above. Four contrasting shelf sea regions were therefore selected, representing a spatial contrast in the wave resource. These four regions (Biscay, Celtic, North Scotland and North Sea) are shown on Fig. 1. The mean wave power was calculated over each of these shelf sea regions for each year and for each season (Fig. 8). Again, seasonal/annual averages calculated for all years for each of these regions (Table 3) provide a context. As expected from the previous analysis, the north of Scotland contains the greatest wave resource with a typical annual mean of 44 kW/m, almost double the next highest region (Celtic at 26 kW/m). In terms of seasonal variability between these regions, it is useful to examine uncertainty over the time period October–March (Fig. 9), when the shelf-scale variability was greatest, and corresponding to the time when wave power is at its peak. To the north of Scotland, the October–March uncertainty in wave power was ±10.7 kW/m (compared to an October–March mean wave power of 68 kW/m), in contrast to an April–September uncertainty of

± 2.7 kW/m (compared to an April–September mean wave power of 21 kW/m). It is also interesting to note the high uncertainty in October to the north of Scotland (±15.8 kW/m, compared to a mean October wave power resource of 51 kW/m), since this high October uncertainty is unique over the four regions examined in detail. To examine the spatial distribution of wave power variability in more detail, seasonal and annual means, uncertainty, and uncertainty expressed as a percentage of the mean wave power, were calculated for the entire model domain (Fig. 10). Although the regions to the northwest of Scotland and west of Ireland are associated with the highest uncertainty, particularly during winter months, various other regions have a high uncertainty when expressed as a percentage of the mean wave power. The spatial distribution of this quantity tends to change seasonally, and so is not fully reflected in the annual percentage uncertainty. For example, during March–April–May, there is a high percentage uncertainty in the western part of the North Sea, with low percentage uncertainty in the Irish Sea. In June–July–August, this pattern is reversed with low percentage uncertainty in the western North Sea, and high percentage uncertainty in the Irish Sea. Although these regions are associated with some of the most reliable wave resources throughout the year, the wave power in these regions is relatively low.

4.2. Wave spectra

Knowledge of the spectral properties of waves is important when attempting to match a WEC technology with the wave
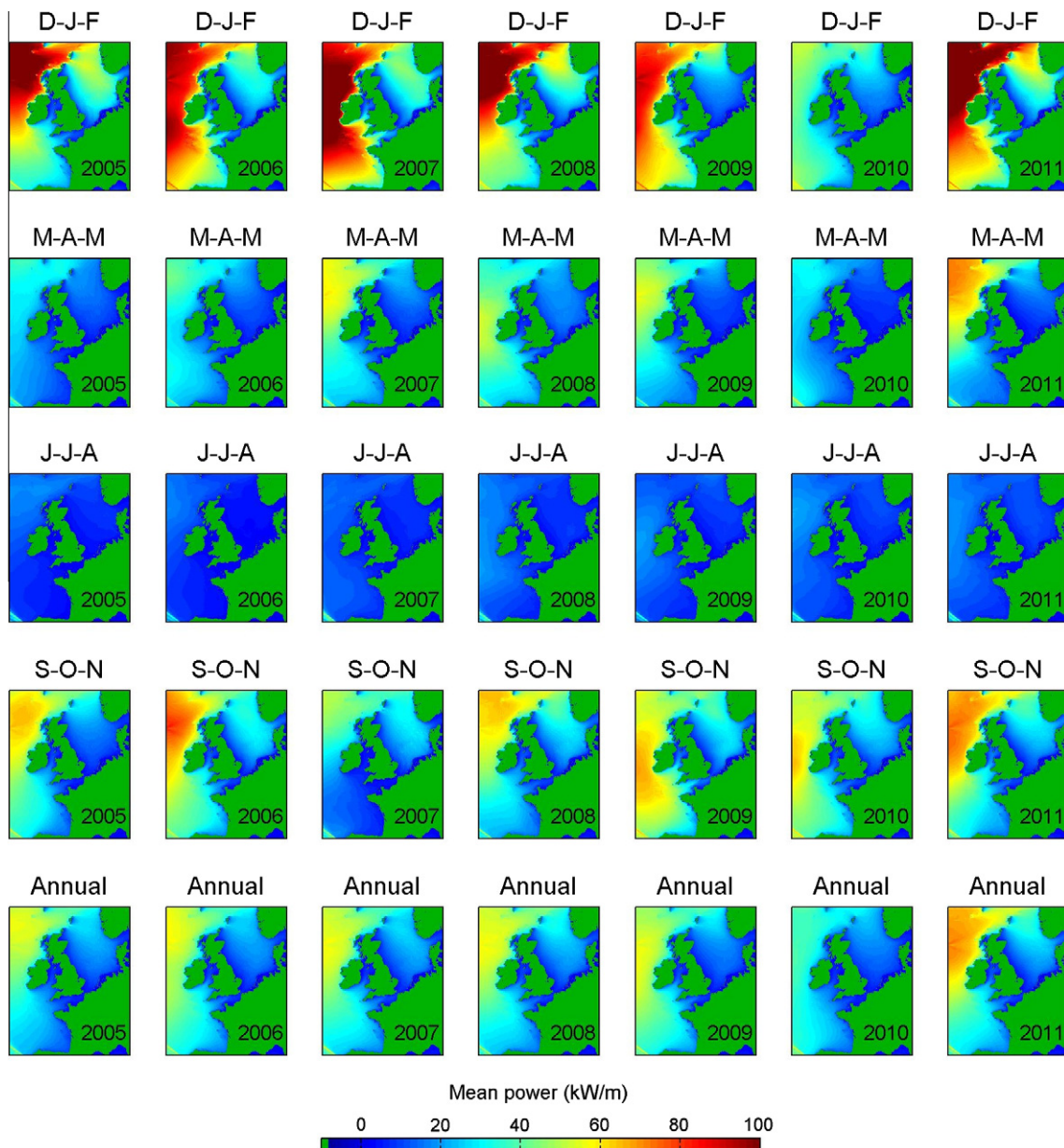
Fig. 5. Spatial distribution of seasonal and annual mean wave power for all simulated years.

climate at a particular location. Therefore, wave spectra were output from the model every 3 h for the eight locations listed in Table 1, and used to calculate annual and seasonal means for each year of simulation. To give us confidence in the simulated wave spectra, we qualitatively compared outputs of the one-dimensional (1D) and 2D wave spectra with data available for the Wave Hub site [35]. Comparing over a range of conditions with varying complexity (e.g. swell-dominated and bi-modal spectra), the 1D and 2D spectra produced by the model compared well with the observations, in terms of frequency, direction, and the magnitude of spectral density. The annual mean (1D) wave spectra for the eight locations are shown in Fig. 11. Clearly, Aegir, Bernera and Achill Island are the most energetic sites, located to the west of Ireland and northwest of Scotland, where peak wave power tends to occur over the NW European shelf seas (Fig. 5). Fig. 11 reflects the low wave energy which occurred in 2010 (largely due to a quiescent winter), and demonstrates the range of inter-annual variability. In Bernera, for example, a peak spectral density of 5.4 m² s (averaged over a year) occurred in 2011, yet in the previous year (2010) the peak

was only 2.2 m² s. The winter (December–January–February) mean 1D wave spectra (Fig. 12) follow a similar trend. It is interesting to note that the peak wave frequency does not vary considerably from year-to-year, regardless of whether the mean is calculated over the entire year, or only over winter months. Table 4 shows the peak wave period at each location for each year of simulation, listed as both the annual and winter mean. In some years, and for some locations, e.g. Wave Hub in 2010, the annual mean of the peak wave period (Tp = 9.6 s) actually exceeded the winter mean (Tp = 6.6 s), indicating the importance of swell waves throughout the year. However, 2010 was an exceptionally quiescent winter in terms of the wave power resource (Fig. 5).

Typical annual mean 2D wave spectra are shown in Fig. 13, demonstrating variability in the directionality of wave energy between locations. Generally, the peak direction is aligned with the predominant wind (and hence wave) direction, reflecting both the geographic location with respect to the larger-scale North Atlantic climate system, and wave refraction in intermediate water depths. For example, there are very clear refraction effects over the
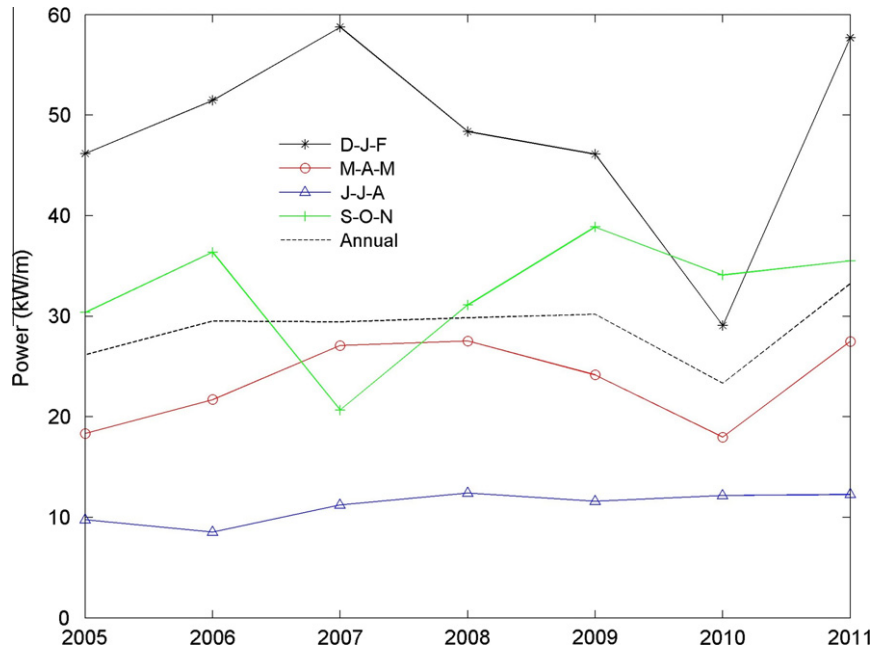
Fig. 6. Seasonal and annual mean wave power over the NW European shelf seas calculated for each simulated year.

Table 3
Calculated wave power (in kW/m) from 2005 to 2011 for regions of the NW European shelf seas: seasonal and annual means, plus 90% confidence intervals.

Region	Mean wave power				
	Winter	Spring	Summer	Autumn	Annual
Entire shelf seas	48.2 ± 7.3	23.5 ± 3.1	11.1 ± 1.1	32.4 ± 4.4	28.8 ± 2.3
Biscay	39.8 ± 7.1	18.2 ± 3.3	7.5 ± 1.5	23.9 ± 6.3	22.3 ± 2.3
Celtic	46.0 ± 11.4	20.1 ± 3.8	9.3 ± 2.1	28.4 ± 8.1	25.9 ± 3.4
N Scotland	76.6 ± 15.2	37.3 ± 7.8	13.4 ± 1.1	50.5 ± 5.6	44.4 ± 5.8
N Sea	36.9 ± 6.2	16.2 ± 2.0	8.4 ± 1.4	27.9 ± 2.2	22.4 ± 2.1

relatively shallow shelf at BIMEP and Wave Hub, but the sites to the west of Ireland and northwest Scotland (e.g. Bernera and Achill

Island) are relatively unaffected by refraction, since there is a very narrow shelf between these sites and the long period waves propagating from the North Atlantic. It is also interesting to note from Fig. 13 that at Horns Rev 2, although the wave resource is relatively low, the spectral peak is strongly bi-modal, reflecting the different modes of wave climate that are responsible for generating most of the wave energy at this site. Also reported on Fig. 13 is mean directional spread. Directional spread provides a measure of dispersion around the mean wave direction, and is defined as the standard deviation of the wave direction distribution, or directional standard deviation. The directional spread across the sties ranges from 21.3° (BIMEP) to 29.7° (Aegir). These values demonstrate that whereas the peak wave direction is generally narrowly defined at each of the locations, there is a significant quantity of wave energy distributed over a much larger range of directions, particularly at
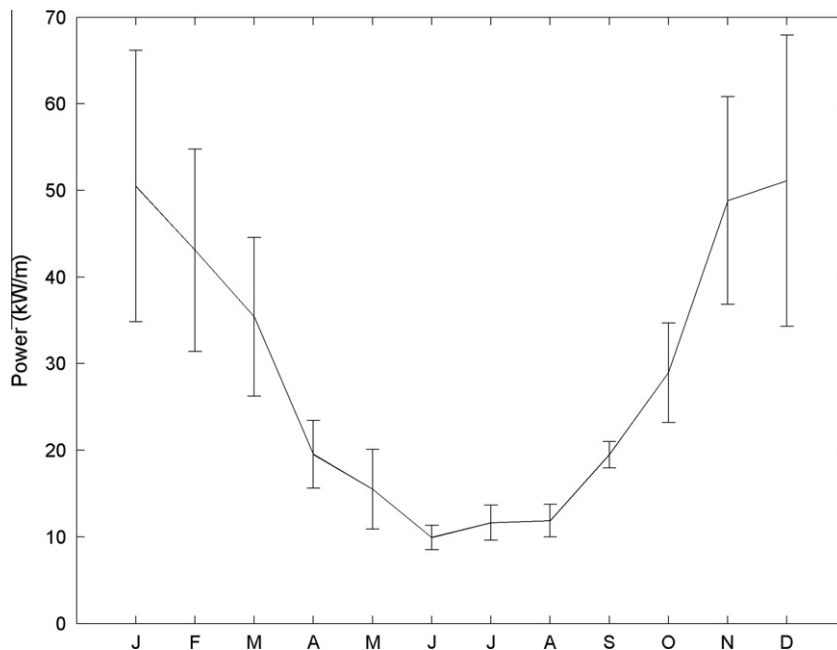
Fig. 7. Annual cycle of monthly mean wave power over the NW European shelf seas. Error bars show the 90% confidence intervals.
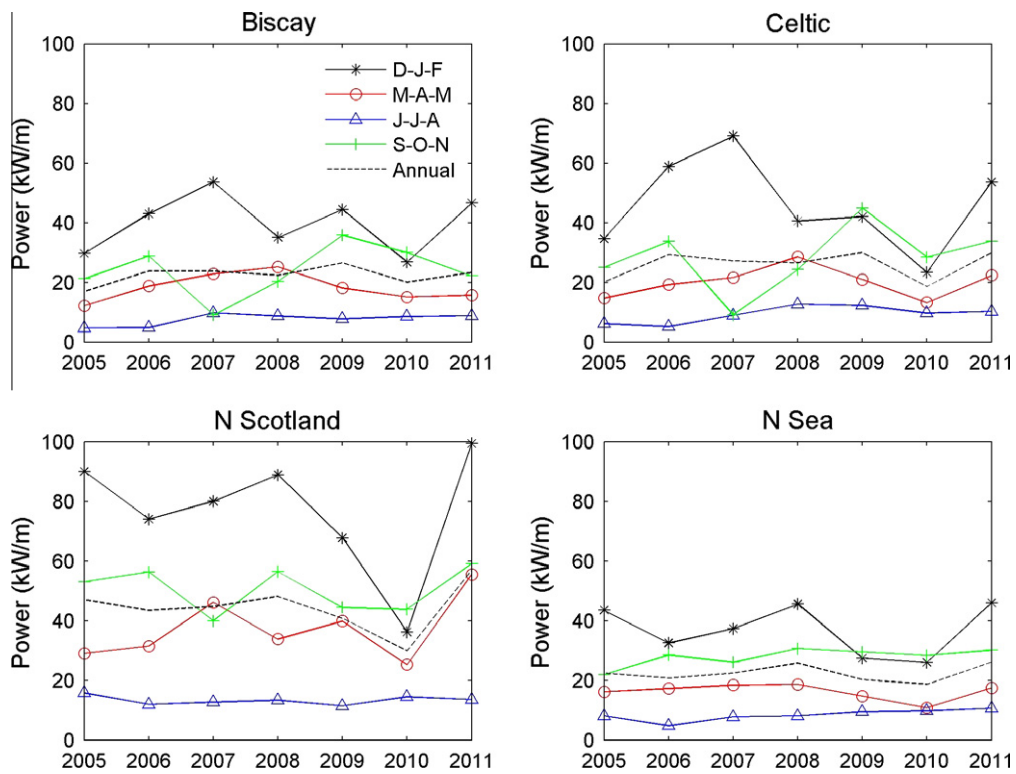
Fig. 8. Seasonal and annual mean wave power over regions of the NW European shelf seas calculated for each simulated year.
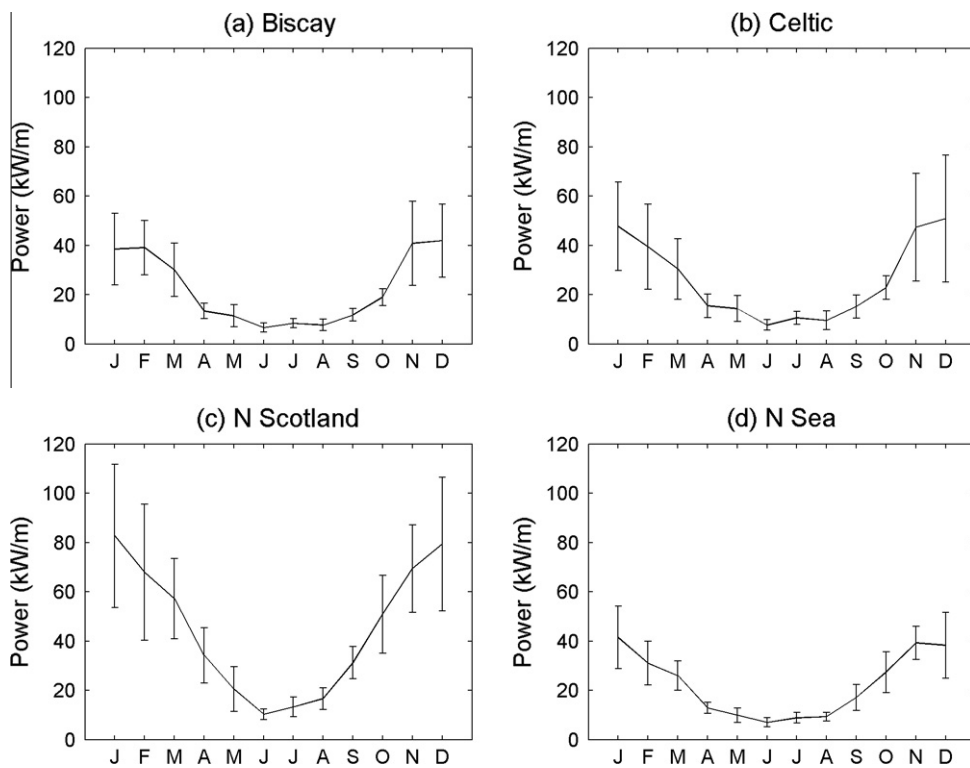
Fig. 9. Annual cycle of monthly mean wave power over regions of the NW European shelf seas. Error bars show the 90% confidence intervals.

the more exposed sites. Knowledge of this statistic enables developers to select devices appropriate to the expected spread of wave energy, and provides a more realistic assessment of how wave power propagates in relation to the mean wave direction [2].

5. Discussion

As expected, the largest wave power resource occurred during winter months December–January–February (48 kW/m averaged
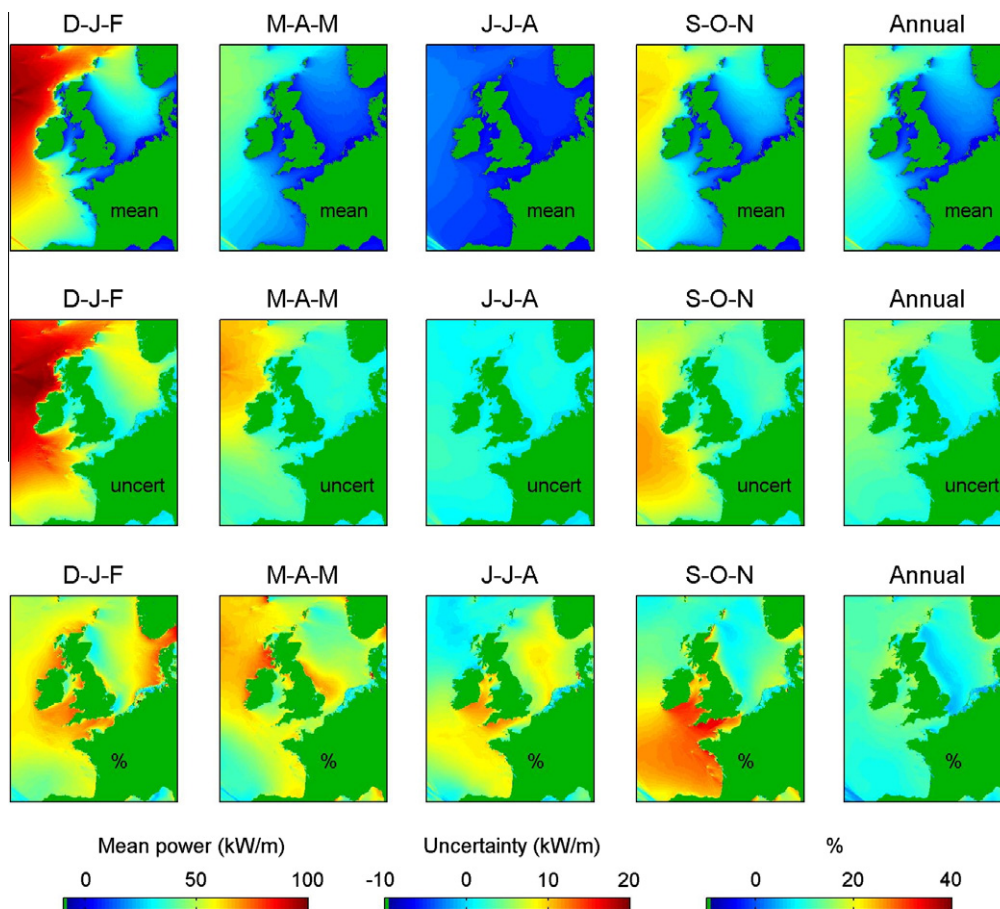
Fig. 10. Seasonal and annual distribution of mean wave power, wave power uncertainty (90% confidence), and uncertainty expressed as a percentage of mean wave power.

over the NW European shelf seas for all years), with a minimum during the summer months June–July–August (11 kW/m). Further, the wave resource during the autumn months September–October–November (32 kW/m) was considerably greater than the spring (March–April–May) resource (24 kW/m). Although the uncertainty in annual wave power over the shelf seas was relatively small (±2.3 kW/m, relative to an annual mean of 29 kW/m), the uncertainty was much greater during winter months (±7.3 kW/m, relative to a winter mean of 48 kW/m). There was considerably less uncertainty in wave power over the summer months (±1.1 kW/m, relative to a summer mean of 11 kW/m). Since swell waves are still present during summer months, and wave power is still appreciable in some regions of the NW European shelf seas during summer, this has relevance to the reliability of the wave resource in providing electricity for cooling during the summer, an issue which is likely to be exacerbated in the future under a changing climate [36]. In general, the results of this study show that uncertainty in the wave resource is relatively high during October–March, and relatively low during April–September. Further, in more energetic regions of the NW European shelf seas (e.g. to the northwest of Scotland), the uncertainty is much greater (±15.2 kW/m over the winter months, compared to a winter mean of 77 kW/m). A previous study of this region to the north of Scotland, based on analysis of a single point of a relatively coarse wave model, indicated that inter-annual variability of wave energy yield (for a Pelamis device) was around 360–720 kW in the winter, reducing to around 90–330 kW in summer [30]. The Bay of Biscay and the northern part of the North Sea, although not particularly energetic regions with typical annual mean wave powers of around

22 kW/m, have relatively low uncertainties (around ±2 kW/m), and so could provide a reliable source of wave energy for a device/array which is tuned to the appropriate wave frequencies.

5.1. The North Atlantic Oscillation

The North Atlantic Oscillation (NAO) is a large-scale mode of natural climate variability that has important impacts on the climate of northern Europe [37]. Although the NAO can be calculated throughout the year, it is during the winter months that it is particularly dominant, corresponding to the months when wave power generally peaks over the NW European shelf seas (Fig. 7). To help explain the inter-annual variability of the NW European shelf sea wave resource, the December–January–February (DJF) mean wave power over the shelf seas was plotted against the DJF NAO, using data available from the Climatic Research Unit at the University of East Anglia. There is a large range of the NAO over our modelled time period, ranging from −3.1 (generally anticyclonic) to +1.8 (mostly strong westerlies), representing a considerable range of climatic conditions with which to test the relationship between wave power and the NAO. There is good agreement (coefficient of determination $r^2 = 0.69$) between wave power and the NAO (Fig. 14), and the positive gradient indicates that winter wave power will be relatively high (e.g. >60 kW/m) over the NW European shelf seas for strongly positive DJF NAO years, and the winter wave power will be relatively low (e.g. <30 kW/m) for strongly negative DJF NAO years. Therefore, in support of other research which has correlated wave power with the NAO [30], this study demonstrates that the NAO is a useful tool
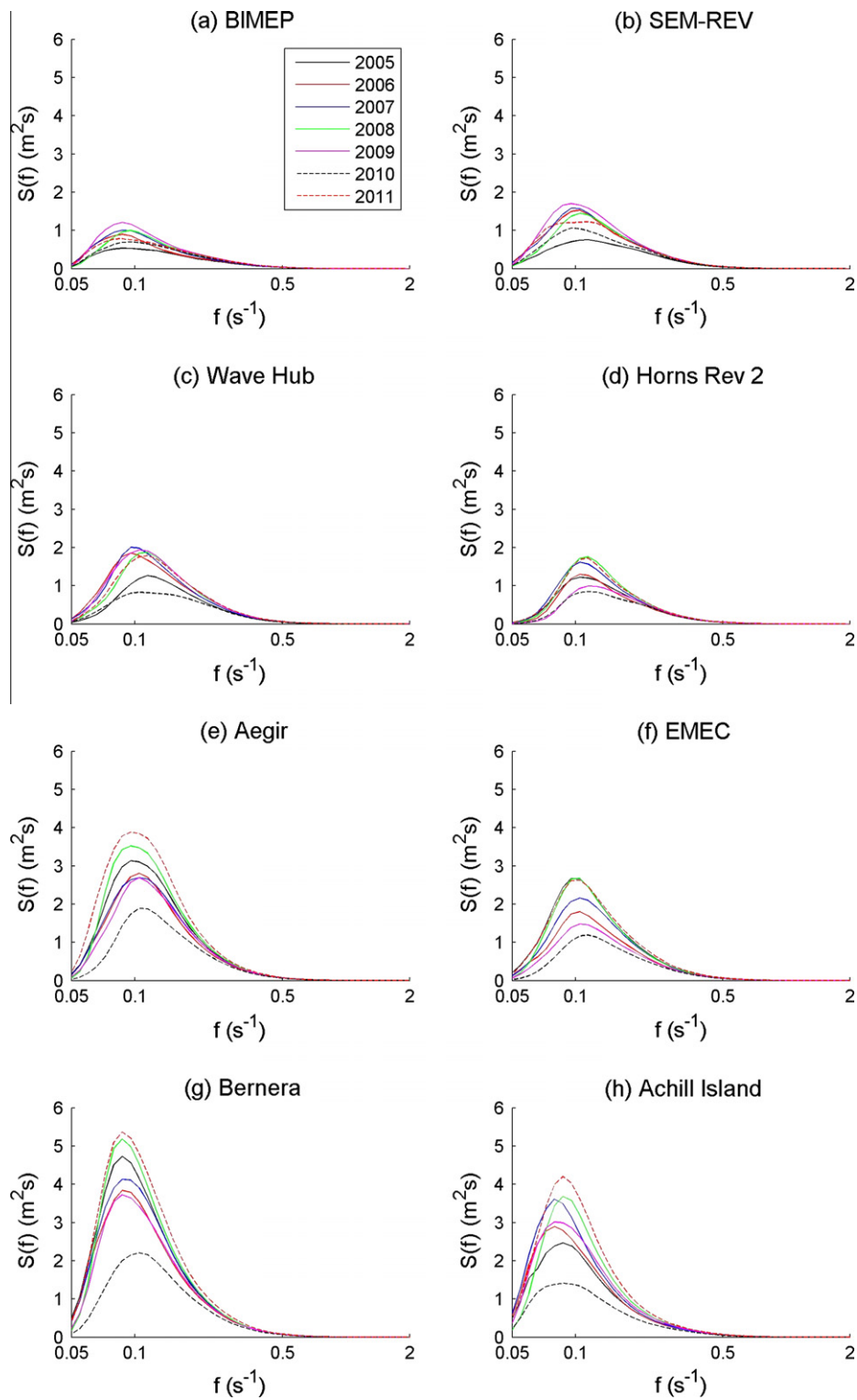
Fig. 11. One-dimensional annual mean wave spectra for eight locations distributed around the NW European shelf seas.

to determine how the winter NW European shelf wave energy resource will vary over the coming decades, provided trends in the NAO can be identified with any certainty. Although annual forecasts of the NAO are not reliable due to the high uncertainty associated with global circulation model predictions, it is a useful indice for predicting variability over longer time periods (e.g. multi-annual to multi-decadal) [38].

5.2. Comparison with the Atlas of UK Marine Renewable Energy Resources

How do our results compare with those presented in the Atlas of UK Marine Renewable Energy Resources [9] – a resource which is used extensively by the wave energy sector? The Atlas is restricted to the UK continental shelf and channel islands territorial
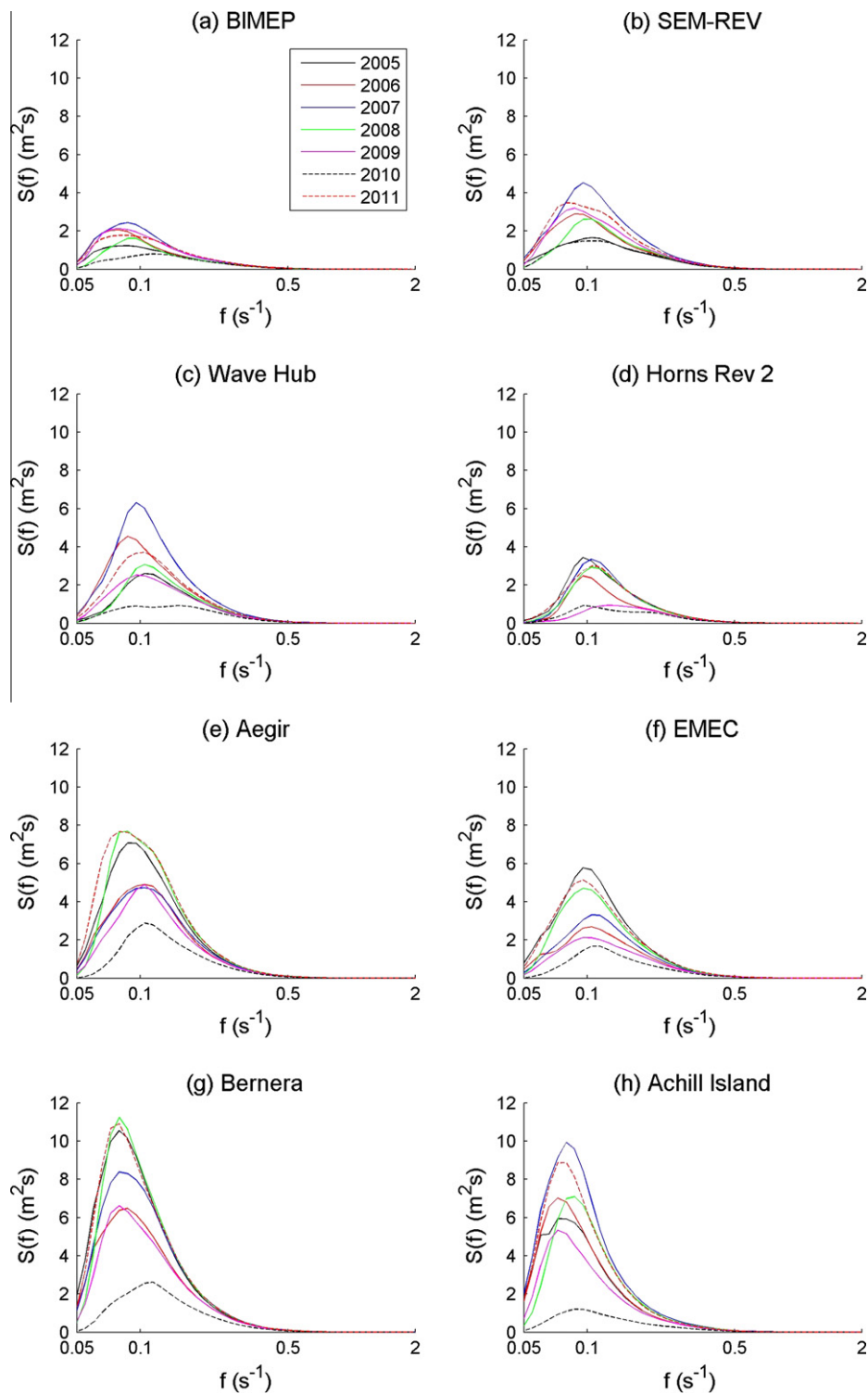
Fig. 12. One-dimensional winter (December–January–February) mean wave spectra for eight locations distributed around the NW European shelf seas.

sea limits, whereas our study covers the entire NW European shelf seas. However, if we interpolate our high-resolution gridded model outputs to the data points covered by the Atlas, we can compare the annual mean wave power estimated by the two studies. Since we have simulated different dates (January 2005–December 2011) than those dates analysed to produce the Atlas (June 2000–May 2007), it is appropriate to normalise the results of each study by the wave power averaged over all of the data points covered by the Atlas. The normalised comparison falls closely to the line of

equality (Fig. 15), and so the two studies are comparable. However, when comparing non-normalised outputs between the two studies, we found that the mean annual wave power from our study is around 10% lower than that estimated by the Atlas. This can partly be explained by variability of the wind (and hence wave) climates over the different time periods used for the two studies. For example, the mean DJF NAO used for the Atlas was +0.21, compared to −0.32 used for this study. Based on the equation describing the line of best fit on Fig. 14, this could account for around 10%

Table 4
Inter-annual variability of peak wave period Tp (s) at each of eight wave energy project locations averaged over winter months (December–January–February), and over the entire year. Values in each cell of the table are given as $w(a)$: w = winter mean, a = annual mean.

Project	Peak wave period Tp (s)						
	2005	2006	2007	2008	2009	2010	2011
BIMEP	11.5(11.5)	12.6(11.5)	11.5(11.5)	10.5(10.5)	12.6(11.5)	8.7(10.5)	12.6(11.5)
SEM-REV	9.6(8.7)	11.5(9.6)	10.5(10.5)	9.6(9.6)	11.5(10.5)	9.6(10.5)	12.6(8.7)
Wave Hub	9.6(8.7)	11.5(10.5)	10.5(10.5)	9.6(8.7)	10.5(9.6)	6.6(9.6)	9.6(8.7)
Horns Rev 2	10.5(9.6)	10.5(9.6)	9.6(9.6)	9.6(8.7)	8.0(8.7)	10.5(8.7)	9.6(8.7)
Aegir	11.5(10.5)	9.6(9.6)	9.6(9.6)	11.5(10.5)	9.6(9.6)	9.6(9.6)	12.6(10.5)
EMEC	10.5(10.5)	9.6(9.6)	9.6(9.6)	10.5(9.6)	10.5(9.6)	8.7(8.7)	10.5(9.6)
Bernera	12.6(11.5)	11.5(11.5)	12.6(11.5)	12.6(11.5)	12.6(11.5)	8.7(9.6)	12.6(11.5)
Achill Island	13.8(11.5)	13.8(12.6)	12.6(12.6)	11.5(11.5)	13.8(12.6)	11.5(11.5)	12.6(11.5)
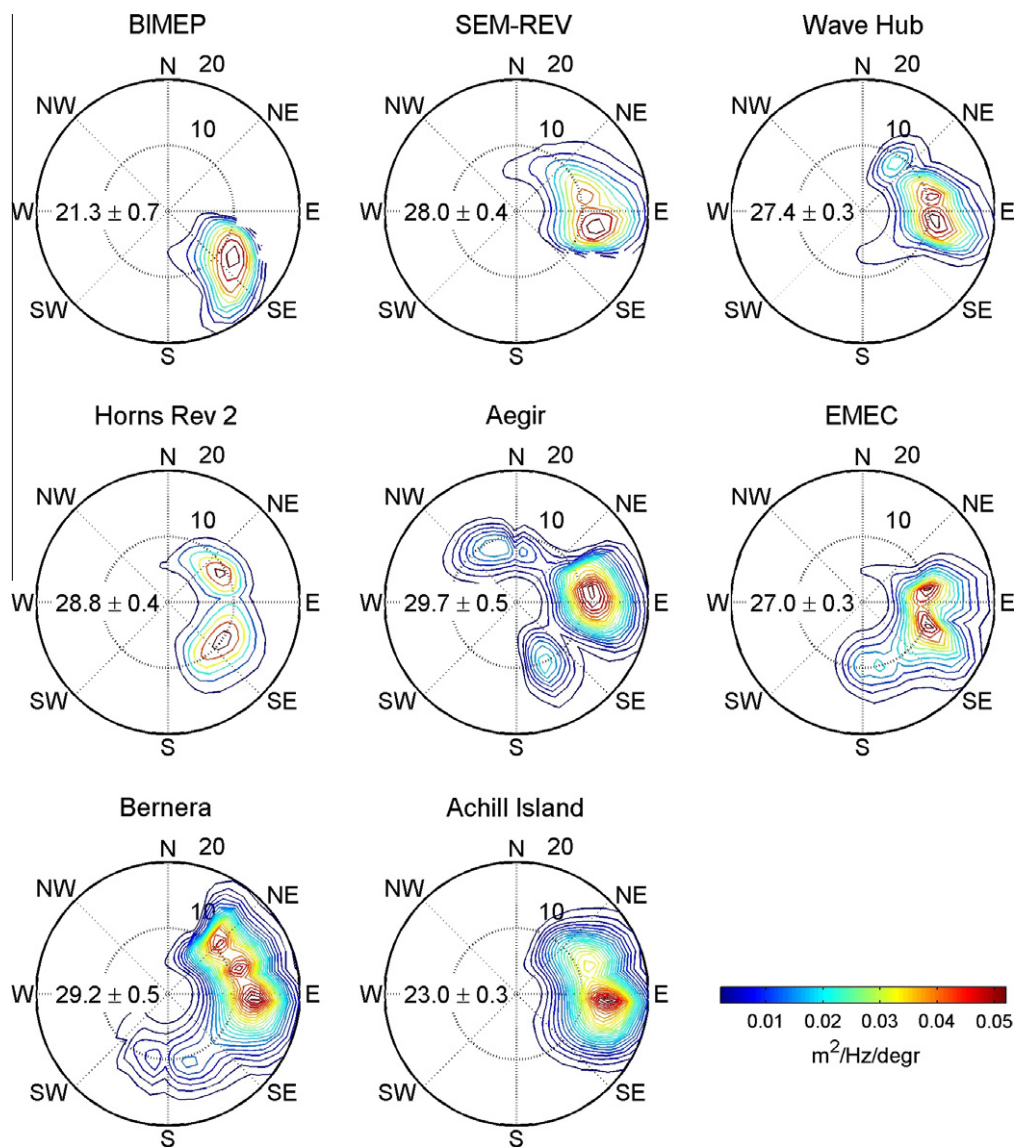
Fig. 13. Annual mean two-dimensional wave spectra (calculated for period 2005–2011) for eight locations distributed around the NW European shelf seas. The radial coordinate is wave period(s), and contours are variance densities in m²/Hz/°. The numbers on each plot are the mean directional spreading (in degrees), including the 90% confidence intervals.

discrepancy during the winter months. Further, there were considerable discrepancies between model configurations used in each of the two studies. There are differences in spatial resolution (1/24° × 1/24° in our study, compared to 1/6° × 1/9° for the Atlas), frequency resolution (40 frequency bins in our study, compared to 13 frequency bins for the Atlas), and directional resolution (45 discrete direction bins for our study, compared to 16 direction bins for the Atlas). However, perhaps more fundamental is the choice of wave model. The Atlas is based on analysis of outputs from a second-generation wave model, whereas our study uses a
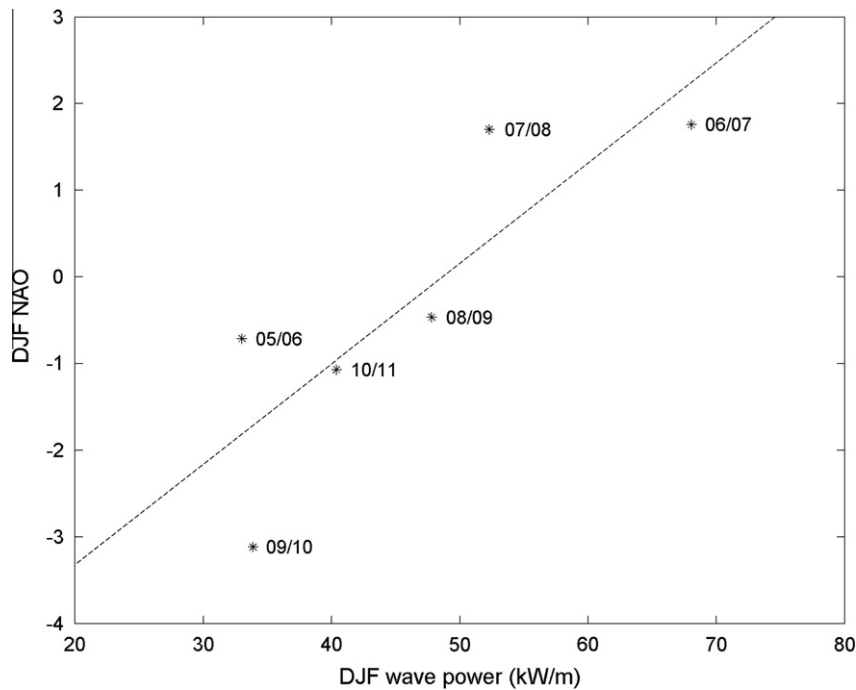
Fig. 14. Mean winter (December–January–February) wave power averaged over the NW European shelf seas plotted against the DJF NAO. The dashed line is the least squares line of best fit ($r^2 = 0.69$).
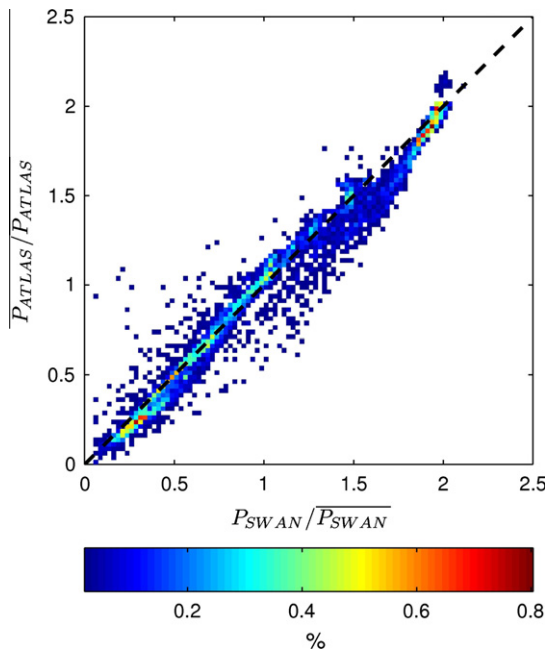

Fig. 15. Comparison of annual mean wave power estimated by this study and the UK Atlas of Marine Renewable Energy Resources plotted as percentage probability. Since a different time period was used for each resource assessment, wave power at each data point has been normalised by the spatial mean. The equality line at 45° is shown as a dashed line.

third-generation wave model. One of the key differences between a 2nd and 3rd generation wave model is more accurate representation of non-linear wave-wave interactions. In particular, 3rd generation wave models explicitly calculate quadruplet wave-wave interactions, rather than parameterising such non-linear process [32]. Quadruplet wave-wave interactions redistribute a significant fraction of the wind input from the mid-range frequencies to lower frequencies, and a smaller fraction to higher frequencies [33], the energy of which is then dissipated by other physical process which have improved representation in 3rd generation wave models, e.g. white-capping. Our results therefore indicate that the 2nd generation wave model which was used to compile the Atlas of UK Marine Renewable Energy Resources may have over-estimated wave power. It is interesting to note that in the same year that the Atlas was published (2008), the UK Met Office implemented a third-generation wave model (WAVEWATCH III) as a replacement for the Met Office second-generation operational wave model.

6. Conclusions

Our high resolution third-generation SWAN wave model simulations, applied to 7 years of wind forcing, provide a realistic assessment of the NW European wave resource. We have examined inter-annual and inter-seasonal variability, and compared the wave power resource for contrasting regions of the NW European shelf seas. This thorough assessment, including the analysis of wave spectra for sites where wave energy projects are under development, quantifies variability of the NW European wave resource, and so provides potential developers with statistics relevant to matching each site to the most appropriate wave energy converter (WEC) technology.

Our analysis demonstrates that there is considerably more uncertainty in the wave resource from October to March, in contrast to the lower April–September uncertainty. The strong correlation between wave power over the winter months and large-scale modes of natural climate variability demonstrates that the North Atlantic Oscillation (NAO) is a good indicator of the NW European shelf sea winter wave power resource, provided that trends in the NAO can be identified with any certainty over the coming decades.

Model studies like this can generally be improved by increasing model resolution. However, our spatial resolution of $1/24° \times 1/24°$ over the entire NW European shelf seas already represents a

significant advancement on previous resource assessments which include parts of the study region, since these models had spatial resolutions of $1/6° \times 1/9°$ [9], and $1/5° \times 1/5°$ [6]. Finally, our use of the third-generation wave model SWAN, compared to a previous resource assessment of a large part of the study region which was based on analysing outputs from a second-generation wave model, has improved the representation of the physical processes, particularly non-linear wave-wave interactions. We believe that considering the advances in computing power, availability of wind data, and the urgency with which we must move towards generating electricity from low carbon technologies, it is timely to produce an updated high-resolution atlas of the NW European shelf sea wave energy resource, and this research represents a first step towards creating such a resource.

Acknowledgements

References

[1] Bahaj AS. Generating electricity from the oceans. Renew Sust Energy Rev 2011;15:3399–416.
[2] Gunn K, Stock-Williams C. Quantifying the global wave power resource. Renew Energy 2012;44:296–304.
[3] Clément A, McCullen P, Falcão A, Fiorentino A, Gardner F, Hammarlund K, et al. Wave energy in Europe: current status and perspectives. Renew Sust Energy Rev 2002;6:405–31.
[4] Bryden IG, Melville GT. Choosing and evaluating sites for tidal current development. Proc Inst Mech Eng Part A: J Power Energy 2004;218:567–77.
[5] Carretero JC, Gomez M, Lozano I, de Elvira AR, Serrano O, Iden K, et al. Changing waves and storms in the northeast Atlantic? Bull Amer Meteorol Soc 1998;79:741–60.
[6] Reeve DE, Chen Y, Pan S, Magar V, Simmonds DJ, et al. An investigation of the impacts of climate change on wave energy generation: the Wave Hub, Cornwall, UK. Renew Energy 2011;36:2404–13.
[7] Charles E, Idier D, Delecluse P, Déqué M, Le Cozannet G. Climate change impact on waves in the Bay of Biscay, France. Ocean Dynam 2012;62:831–48.
[8] Jeffrey H, Sedgwick J. ORECCA European offshore renewable energy roadmap. Published by the ORECCA Coordinated Action Project, University of Edinburgh; 2011.
[9] ABPmer, The Met Office, Proudman Oceanographic Laboratory. Atlas of UK marine renewable energy resources. Tech. rep., Department for Business Enterprise & Regulatory Reform; 2008.
[10] Akpinar A, Komurcu MI. Assessment of wave energy resource of the Black sea based on 15-year numerical hindcast data. Appl Energy 2013;101:502–12.

[11] Bernhoff H, Sjostedt E, Leijon M. Wave energy resources in sheltered sea areas: a case study of the Baltic Sea. Renew Energy 2006;31:2164–70.
[12] Iglesias G, Carballo R. Wave resource in El Hierro – an island towards energy self-sufficiency. Renew Energy 2011;36:689–98.
[13] Hughes MG, Heap AD. National-scale wave energy resource assessment for Australia. Renew Energy 2010;35:1783–91.
[14] Zheng CW, Zhuang H, Li X, Li XQ. Wind energy and wave energy resources assessment in the East China Sea and South China Sea. Sci China – Technol Sci 2012;55:163–73.
[15] EPRI. Mapping and assessment of the United States ocean wave energy resource. Technical report 1024637, Electrical Power Research Institute, Palo Alto, CA; 2011.
[16] Cooper WS, Hinton CL, Ashton N, Saulter A, Morgan C, Proctor R, et al. An introduction to the UK marine renewable atlas. Proc Inst Civil Eng – Marit Eng 2006;159:1–7.
[17] Cornett AM. A global wave energy resource assessment. In: Proceedings of the 18th ISOPE conference, Vancouver, BC, Canada; 2008. p. 1–9.
[18] Liberti L, Carillo A, Sannino G. Wave energy resource assessment in the Mediterranean, the Italian perspective. Renew Energy 2013;50:938–49.
[19] Izadparast AH, Niedzwecki JM. Estimating the potential of ocean wave power resources. Ocean Eng 2011;38:177–85.
[20] Iglesias G, Carballo R. Wave resource characterization and WEC selection a comprehensive methodology applied to NW Spain. In: Proceedings of the 9th European wave and tidal energy conference, Southampton, UK; 2011. p. 1–8.
[21] Kofoed JP, Frigaard P, Friis-Madsen E, Chr. Srensen H. Prototype testing of the wave energy converter wave dragon. Renew Energy 2006;31:181–9.
[22] Neill SP, Scourse JD, Bigg GR, Uehara K. Changes in wave climate over the northwest European shelf seas during the last 12,000 years. J Geophys Res – Oceans 2009;114:C06015.
[23] Mouslim H, Babarit A, Clément A, Borgarino B. Development of the French wave energy test site SEM-REV. In: Proceedings of the 8th European wave and tidal energy conference, Uppsala, Sweden; 2009. p. 31–5.
[24] Beels C, Henriques JCC, de Rouck J, Pontes MT, de Backer G, Verhaeghe, H. Wave energy resource in the North Sea. In: Proceedings of the 7th European wave and tidal energy conference, Porto, Portugal; 2007. p. 1–10.
[25] http://www.aquamarinepower.com/projects/west-coast-ireland; 2012 [accessed 06.09.12].
[26] Palutikof J, Holt T, Skellern A. Wind: resources and hazard. In: Hulme M, Barrow E, editors. Climates of the British Isles. London: Routledge; 1997. p. 220–42.
[27] Barrow E, Hulme M. Describing the surface climate of the British Isles. In: Hulme M, Barrow E, editors. Climates of the British Isles. London: Routledge; 1997. p. 33–62.
[28] Draper L. Wave climatology of the UK continental shelf. In: Banner FT, Collins MB, Massie KS, editors. The north-west European shelf seas: the sea bed and the sea in motion. II. Physical and chemical oceanography, and physical resources. Elsevier; 1980. p. 353–68.
[29] Hurrell JW. Decadal trends in the North-Atlantic Oscillation – regional temperatures and precipitation. Science 1995;269:676–9.
[30] Mackay EBL, Bahaj AS, Challenor PG. Uncertainty in wave energy resource assessment. Part 2: Variability and predictability. Renew Energy 2010;35:1809–19.
[31] Neill SP, Scourse J, Uehara K. Evolution of bed shear stress distribution over the northwest European shelf seas during the last 12,000 years. Ocean Dynam 2010;60:1139–56.
[32] Booij N, Ris RC, Holthuijsen LH. A third-generation wave model for coastal regions – 1. Model description and validation. J Geophys Res 1999;104: 7649–66.
[33] Holthuijsen LH. Waves in oceanic and coastal waters. Cambridge University Press; 2009.
[34] Pinson P, Reikard G, Bidlot JR. Probabilistic forecasting of the wave energy flux. Appl Energy 2012;93:364–70.
[35] Saulnier JB, Maisondieu C, Ashton I, Smith GH. Refined sea state analysis from an array of four identical directional buoys deployed off the Northern Cornish coast (UK). Appl Ocean Res 2012;37:1–21.
[36] Meehl GA, Tebaldi C. More intense, more frequent, and longer lasting heat waves in the 21st century. Science 2004;305:994–7.
[37] Trigo RM, Osborn TJ, Corte-Real JM. The North Atlantic Oscillation influence on Europe: climate impacts and associated physical mechanisms. Clim Res 2002; 20:9–17.
[38] Bojariu R, Gimeno L. Predictability and numerical modelling of the North Atlantic Oscillation. Earth-Sci Rev 2003;63:145–68.

.3 Published work P-III
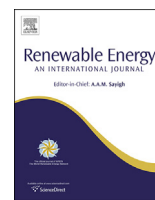
The role of tidal asymmetry in characterizing the tidal energy resource of Orkney

Simon P. Neill*, M. Reza Hashemi, Matt J. Lewis

School of Ocean Sciences, Bangor University, Menai Bridge, UK

ARTICLE INFO

ABSTRACT

When selecting sites for marine renewable energy projects, there are a wide range of economical and practical constraints to be considered, from the magnitude of the resource through to proximity of grid connections. One factor that is not routinely considered in tidal energy site selection, yet which has an important role in quantifying the resource, is tidal asymmetry, i.e. variations between the flood and ebb phases of the tidal cycle. Here, we present theory and develop a high-resolution three-dimensional ROMS tidal model of Orkney to examine net power output for a range of sites along an energetic channel with varying degrees of tidal asymmetry. Since power output is related to velocity cubed, even small asymmetries in velocity lead to substantial asymmetries in power output. We also use the 3D model to assess how tidal asymmetry changes with height above the bed, i.e. representing different device hub heights, how asymmetry affects turbulence properties, and how asymmetry is influenced by wind-driven currents. Finally, although there is minimal potential for tidal phasing over our study site, we demonstrate that regions of opposing flood- versus ebb-dominant asymmetry occurring over short spatial scales can be aggregated to provide balanced power generation over the tidal cycle.

© 2014 Elsevier Ltd. All rights reserved.

1. Introduction

Site selection for tidal energy projects is not simply a case of identifying sites with an appropriately large peak tidal current [1]. Rather, it is important to consider how the resource varies over a variety of time scales, from seasonal, to lunar, to semi-diurnal, and down to turbulent time scales [2]. It is also important to consider whether tidal energy extraction will significantly impact on the resource [3,4], and associated coastal processes such as sediment transport and morphodynamics [5].

Site selection for tidal energy converter (TEC) arrays consists of various practical and economical constraints, such as the magnitude of the resource, water depths appropriate for the chosen technology, navigational constraints, proximity to a suitable port for installation and maintenance, and grid connections [6,7]. However, one factor which is not routinely considered in site selection is the importance of tidal asymmetry [8]. From a resource and device perspective, it is clearly beneficial to select sites where

the tidal currents have an equal magnitude between the flood and ebb phases of the tide (tidal symmetry), and less desirable to exploit sites which have either strong flood- or ebb-dominance (tidal asymmetry). Tidal asymmetry not only affects the primary variables of the flow field such as velocity and water elevation — it is also expected to cause asymmetry in turbulence properties such as Reynolds stresses and turbulent kinetic energy, important variables in site selection [9]. For instance, there is strong turbulence asymmetry in the eastern English Channel due to the presence of quarter diurnal tidal harmonics [10]. It has also been demonstrated that exploitation of asymmetrical sites could have a greater environmental impact on morphodynamics than symmetrical sites, because of the way in which tidal energy extraction alters residual sediment transport pathways [11].

Tidal waves are progressively distorted and dampened as they propagate in shallow-water coastal regions [12]. Although tidal waves in such regions still satisfy the criteria of long waves (i.e. wavelength is much greater than water depth), in shallow water the amplitudes of the waves become a significant fraction of the total water depth [13]. As a result of these non-linear shallow-water processes, tidal waves in such regions are often more complex than their linear wave counterparts, with the occurrence of double high or low water, and asymmetries observed in velocity time series due

---

* Corresponding author.
  E-mail address: s.p.neill@bangor.ac.uk (S.P. Neill).

to the presence of overtides.[1] Tidal asymmetry can also be generated by other mechanisms such as topographic features (e.g. in the wake of an island) [14], or by meteorological effects. In the latter case, persistent seasonal baroclinic flows of up to 0.2 m s^{-1} in stratified shelf sea regions can play an important role in generating asymmetry [15], and hence affect the net tidal energy resource, and affect mechanisms such as the dispersal of pollutants and marine organisms [16].

In this paper, we discuss the origin of tidal asymmetry and its theoretical impact on net power output (Section 2). Next, we describe our Orkney case study (Section 3), to which we apply the 3D ROMS ocean model (Section 4). In Section 5, we present model results along a 30 km length of an energetic tidal channel in Orkney, demonstrating how the model simulations agree with theoretical estimates of tidal asymmetry. Finally, we discuss the implications of the simulated tidal asymmetry on the tidal energy resource, including a consideration of vertical variability and the potential for tidal phasing over small spatial scales (Section 6).

2. Tidal asymmetry

Since astronomical tides are generated by the combined gravitational forces of the Sun and the Moon, the frequencies of tidal constituents in the deep oceans directly relate to lunar or solar days, and can be expressed in terms of diurnal and semi-diurnal components. The propagation of (barotropic) tides in the deep ocean is primarily governed by linear processes, where their interactions generate sub-harmonic tides [12]. For instance, the combination of the principal semi-diurnal lunar (M_2) and solar (S_2) tidal constituents describes the spring neap cycle, with a frequency of,

$$\omega_{S_2} - \omega_{M_2} = \frac{1}{12\ \text{h}} - \frac{1}{12.4206\ \text{h}} = \frac{1}{14.765\ \text{days}} \tag{1}$$

where ω is the angular frequency.

Over continental shelves and in shallow coastal waters, other non-linear forces and processes such as friction, advection (due to advective inertia forces) and diffusion (due to turbulence) become increasingly responsible for the dynamics of the tides. As a result, the tidal signal is more complex in such regions, and can no longer be represented by simple linear superposition of semi-diurnal and diurnal components. Using the concept of Fourier series, by combining higher frequency tidal components or super-harmonic tides, any non-linear tidal signal can be reconstructed. Unlike astronomical tides, super-harmonic tidal components are generated by localised shallow water forces. Accordingly, the non-linear interaction of an astronomical tidal component with itself and other tidal components generates overtides and compound tides, respectively, with higher frequencies, e.g.

$$M_4\left(2\omega_{M_2}\right), M_6\left(3\omega_{M_2}\right), S_6\left(3\omega_{S_2}\right), MS_4\left(\omega_{M_2} + \omega_{S_2}\right), \\ MN_4\left(\omega_{M_2} + \omega_{N_2}\right), \cdots \tag{2}$$

Overtides and compound tides are the main causes of tidal asymmetry, and their role in understanding and accurately simulating tides is very important in some regions [17]. Using simple mathematics, it can be easily shown that the nature of tidal asymmetry is related to the phase difference between semi-diurnal and quarter-diurnal tidal constituents. Further, Speer et al. [18] showed that,
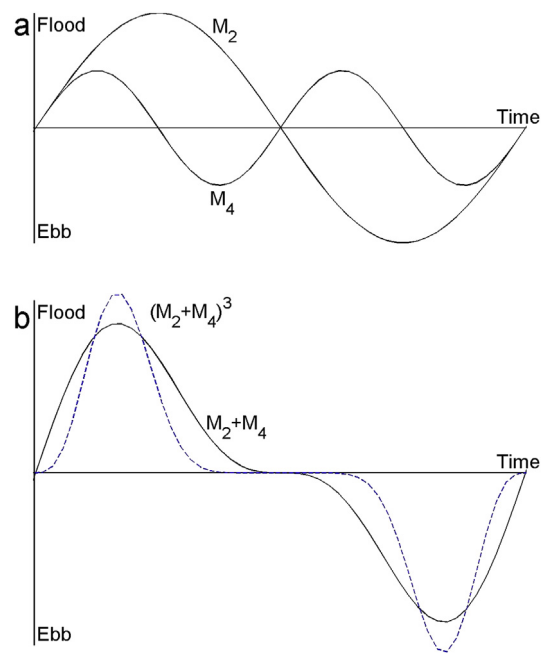
---

[1] A harmonic tidal constituent with a speed that is an exact multiple of one of the fundamental constituents.

Fig. 1. Combination of M_2 and M_4 tidal currents resulting in tidal symmetry. (a) Tidal currents for individual constituents, and (b) tidal currents (solid line) and power (blue dashed line) resulting from superposition of M_2 and M_4 constituents. Based on [19]. (For interpretation of the references to colour in this figure legend, the reader is referred to the web version of this article.)
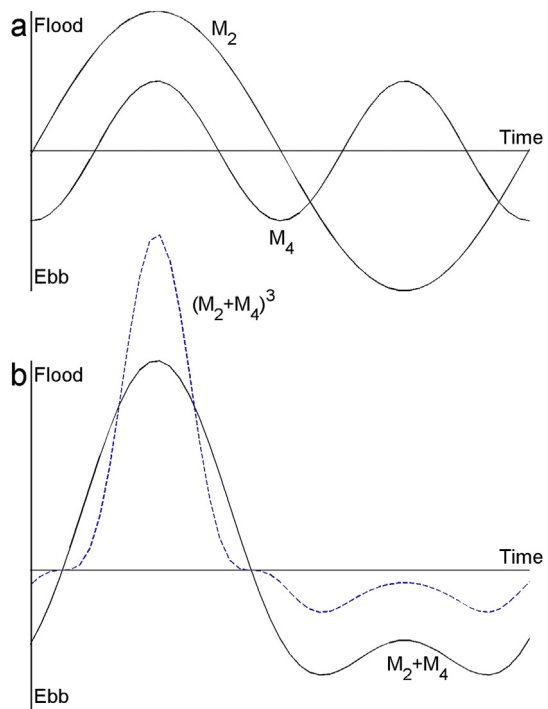

Fig. 2. Combination of M_2 and M_4 tidal currents resulting in tidal asymmetry. (a) Tidal currents for individual constituents, and (b) tidal currents (solid line) and power (blue dashed line) resulting from superposition of M_2 and M_4 constituents. Based on [19]. (For interpretation of the references to colour in this figure legend, the reader is referred to the web version of this article.)

$$2\phi_{M_2} - \phi_{M_4} \approx \phi_{M_2} + \phi_{S_2} - \phi_{MS_4} \approx \phi_{M_2} + \phi_{N_2} - \phi_{MN_4} \qquad (3)$$

It is generally the phase relationship between the principal semi-diurnal tidal current (M_2) and its first harmonic (M_4) that dominates tidal asymmetry [19,20]. Although the combination of M_2 and M_4 tidal currents in Fig. 1a results in a distorted tide (Fig. 1b), the flood and ebb tides are equal in magnitude, as is the net power (a function of velocity cubed) generated during the flood and ebb phases of the tidal cycle. By combining M_2 and M_4 tidal currents as in Fig. 2a, however, the flood tide is stronger than the ebb (Fig. 2b). Although there is no net residual flow, the integrated cube of the velocity (U^3) is greater during the flood phase of the tide. Hence, there will be a strong bias of power production in favour of the flood phase of the tidal cycle. In the case where the flood and ebb currents are equal

$$2\phi_{M_2} = \phi_{M_4} + 90° \qquad (4)$$

and where there is a maximum asymmetry

$$2\phi_{M_2} = \phi_{M_4} \qquad (5)$$

where ϕ_{M_2} and ϕ_{M_4} are the phases (in degrees) of the M_2 and M_4 tidal currents, respectively. Hence, the function

$$2\phi_{M_2} - \phi_{M_4} \qquad (6)$$

quantifies tidal asymmetry.

To examine the impact which tidal asymmetry has on net power output, we develop a modelling case study of Orkney, described in the following sections.
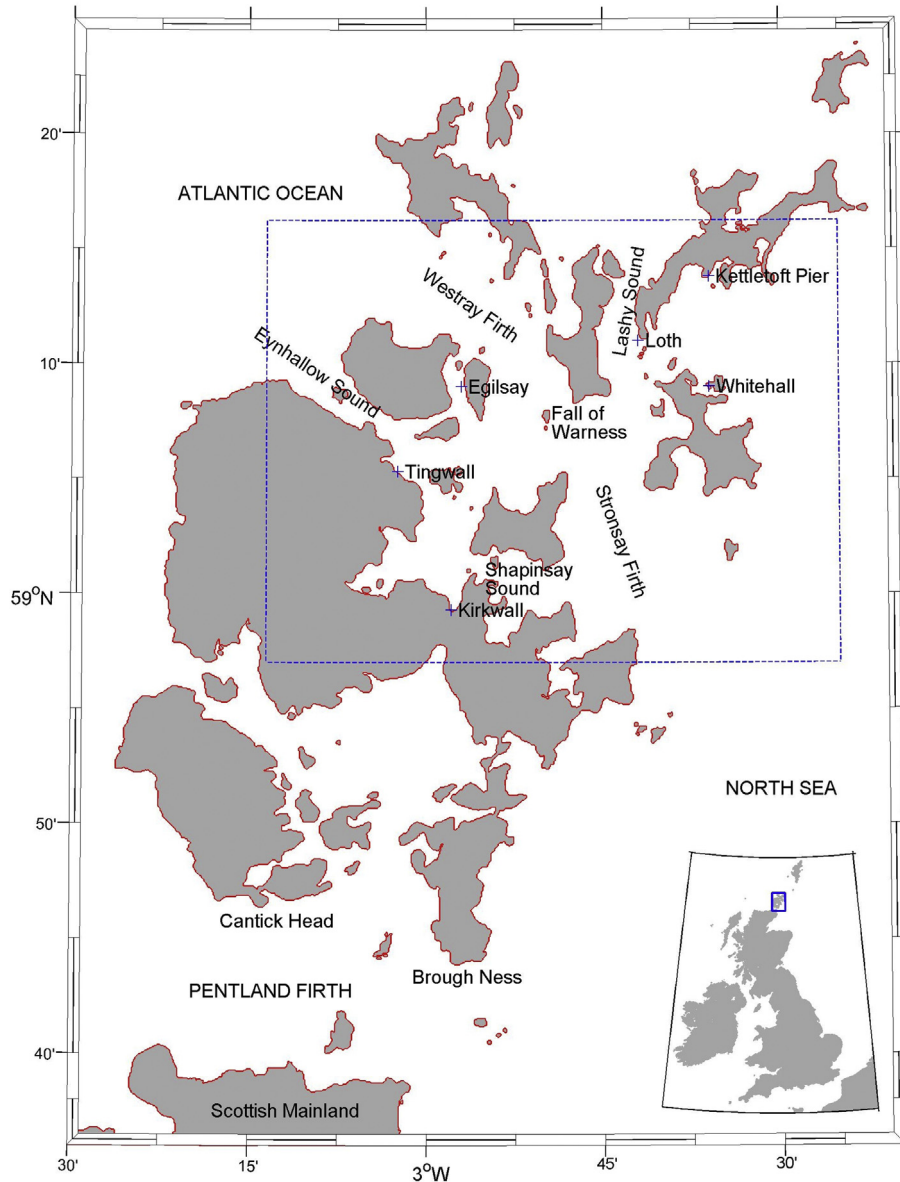

Fig. 3. Principal locations in Orkney and surrounding waters. The dashed box shows the boundaries of the high resolution nested model, and tide gauge stations used for model validation (labelled) are shown as blue crosses. Inset shows the location of Orkney in relation to the British Isles. (For interpretation of the references to colour in this figure legend, the reader is referred to the web version of this article.)

3. Case study – Orkney

Orkney is an archipelago in the north of Scotland, separated from the Scottish mainland by the 12 km width of the Pentland Firth, itself an area with a prominent tidal energy resource [21]. Orkney is comprised of around 70 islands, separated by a series of bays and energetic tidal channels (Fig. 3). Orkney is mesotidal; however, tidal waves in the region, dominated by the principal semidiurnal lunar (M_2) and solar (S_2) constituents, take around two and a half hours to propagate around Orkney from the western to the eastern approaches to the Pentland Firth (Fig. 4), leading to a considerable phase lag across Orkney. This phase lag results in a strong pressure gradient across Orkney, driving very strong tidal flows through the Pentland Firth and along the Firths of Orkney. For example, the M_2 phase lag between the Atlantic approach of Westray Firth and the North Sea approach of the connecting Stronsay Firth (Fig. 3) is around $65°$, i.e. 2.25 h, and the resulting flow is channelled through constrictions which narrow to around 5 km, with water depths in the range 25–50 m.

The tidal currents flowing through the inter-island channels of Orkney exceed 3 m s^{-1} in many regions [1], in conjunction with water depths in the range 25–50 m, suitable for the deployment of the majority of first generation TEC devices. The marine renewable energy potential of Orkney has been recognized by the formation in 2003 of the European Marine Energy Centre (EMEC), which provides a wave test site to the west of Orkney, and a tidal test site in the Fall of Warness, situated where Westray Firth joins Stronsay Firth (Fig. 3). There are currently 6 strategic sites in Orkney under active development (Table 1), and many devices currently being tested at EMEC (Table 2).

4. Numerical modelling

4.1. ROMS

ROMS (Regional Ocean Modeling System) is an advanced open-source three-dimensional (3D) model under active development by a large and diverse research community, led by Rutgers University and the University of California, Los Angeles (www.myroms.org). ROMS is a free-surface hydrostatic ocean circulation model based on finite-difference approximations of the

Table 1
Active tidal energy projects in Orkney (data from The Crown Estate).

Site name	Owner(s) of tenant	Capacity (MW)
Westray South	SSE Renewables Developments (UK) Ltd.	200
Cantick Head	SSE Renewables Holdings (UK) Ltd. & OpenHydro Site Development Ltd.	200
Brough Ness	Marine Current Turbines Ltd.	100
Lashy Sound	Scotrenewables Tidal Energy	30
Fall of Warness	EMEC	n/a
Shapinsay Sound	EMEC	n/a

Reynolds-averaged Navier–Stokes equations. It uses stretched, terrain-following (sigma) coordinates in the vertical, and orthogonal curvilinear coordinates in the horizontal. A wide variety of turbulence submodels, advection schemes, and boundary conditions are available. ROMS can also be readily coupled to atmospheric and wave models, and includes sediment dynamics and morphodynamics [22]. ROMS has been used to examine a range of oceanographic processes at a wide range of scales from ocean basin [23] to archipelagos [24].

Flow conditions at potential tidal energy sites are usually modelled by two-dimensional (2D) depth-averaged models, which are based on the shallow water equations (e.g. Ref. [25]). While these models provide reliable information about current strengths and the feasibility of the site for tidal energy development, they lack the capability to simulate 3D characteristics of the tidal flow, including turbulence. Consequently, observational techniques such as acoustic Doppler current profilers (ADCPs) have been employed to assess the turbulence properties at tidal energy sites [9]. However, deployment and retrieval of ADCP moorings is difficult in regions of strong tidal flow, and ADCP turbulence estimates are made at particular locations within a site, and so are difficult to justify at early stages of site selection due to cost and time constraints. One advantage of implementing 3D models like ROMS is their ability to estimate turbulence characteristics of the flow, and their spatial and temporal variability. Despite significant uncertainties in turbulence modelling, and sub-grid scales of turbulence, recent research has demonstrated the success of ROMS in understanding and quantifying
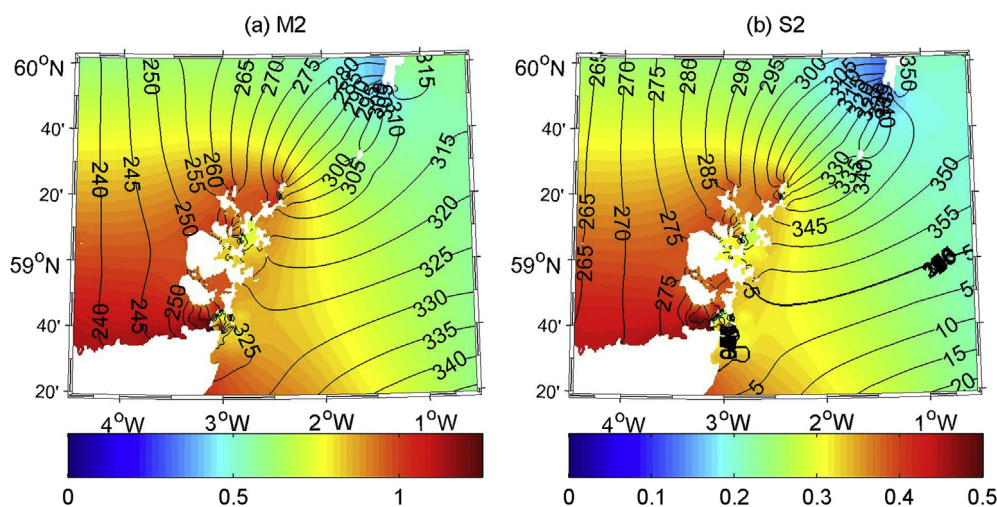

Fig. 4. M_2 and S_2 co-tidal charts calculated from the north of Scotland regional ROMS model (Section 4). Colour scale is amplitude (m), and contours are phase (degrees relative to Greenwich).

Table 2
Tidal devices currently being tested at EMEC (data from EMEC).

Device	Country	Capacity (MW)
Andritz Hydro Hammerfest	Norway	1
Atlantis Resources Corporation	England	1
Bluewater Energy Services	Netherlands	1
Kawasaki Heavy Industries	Japan	1
OpenHydro	Ireland	0.25
Scotrenewables Tidal Power Ltd.	Scotland	2
Tidal Generation Ltd.	England	1
Voith Hydro	Germany	1

Table 3
ROMS modelled amplitude H (m) and phase g (degrees relative to Greenwich) compared with values at tidal stations around Orkney for M_2 and S_2 constituents. Locations of tidal stations are shown in Fig. 3. Observations were obtained from Admiralty Tide Tables.

Station	M_2				S_2			
	Observed		Modelled		Observed		Modelled	
	H	g	H	g	H	g	H	g
Kirkwall	0.84	301	0.87	297	0.29	339	0.31	327
Egilsay	0.88	282	0.86	287	0.32	316	0.31	316
Whitehall	0.88	310	0.92	313	0.31	345	0.34	344
Loth	0.74	300	0.78	302	0.26	336	0.28	333
Kettletoft Pier	0.92	312	0.92	313	0.33	347	0.34	344
Tingwall	0.86	276	0.85	286	0.31	310	0.31	315

turbulence properties such as turbulent dissipation rate and turbulent kinetic energy, and its suitability for turbulence studies at tidal energy sites [26].

ROMS applies the Generic Length Scale (GLS) model for turbulence closure. Depending on the selection of GLS parameters, existing two equation models such as $k-\varepsilon$ and $k-\omega$, or more recent closure models, can be implemented. Previous research has demonstrated that implementation of these schemes lead to similar results across a number of case studies [27]. In particular, the $k-\varepsilon$ model has shown reasonable performance for ROMS model studies with similar horizontal grid resolution (65 m) to that applied here (Section 4.2).

4.2. Model implementation

To provide boundary conditions for our high resolution Orkney model, it was necessary to first run a north of Scotland regional model at coarser resolution. The regional model extended from 4°30′W to 0°30′W, and from 58°18′N to 60°03′N, encompassing the Pentland Firth, Orkney, and part of Shetland (Fig. 4). The regional model had a horizontal grid spacing of 1/120 × 1/228° (approximately 500 m × 500 m), and was forced at the boundaries by FES2012 currents and elevations for the M_2 and S_2 constituents. FES2012 [28] is available at 1/16° and is a considerably enhanced and accurate global tidal model solution, even when compared with previous sophisticated solutions such as FES2004 [29]. Bathymetry for the regional model was interpolated from 1/120° GEBCO data. The regional model was run with 10 equally distributed vertical (sigma) levels for a period of 15 days, and tidal analysis of the elevations and depth-averaged velocities used to generate boundary forcing for the inner nested high resolution Orkney model.

The high resolution Orkney model extended from 3°13.5′W to 2°25′W and from 58°57′N to 59°16′N at a grid resolution of 1/750 × 1/1451° (approximately 75 m × 75 m) (Fig. 5). Bathymetry was interpolated from relatively high resolution (approximately
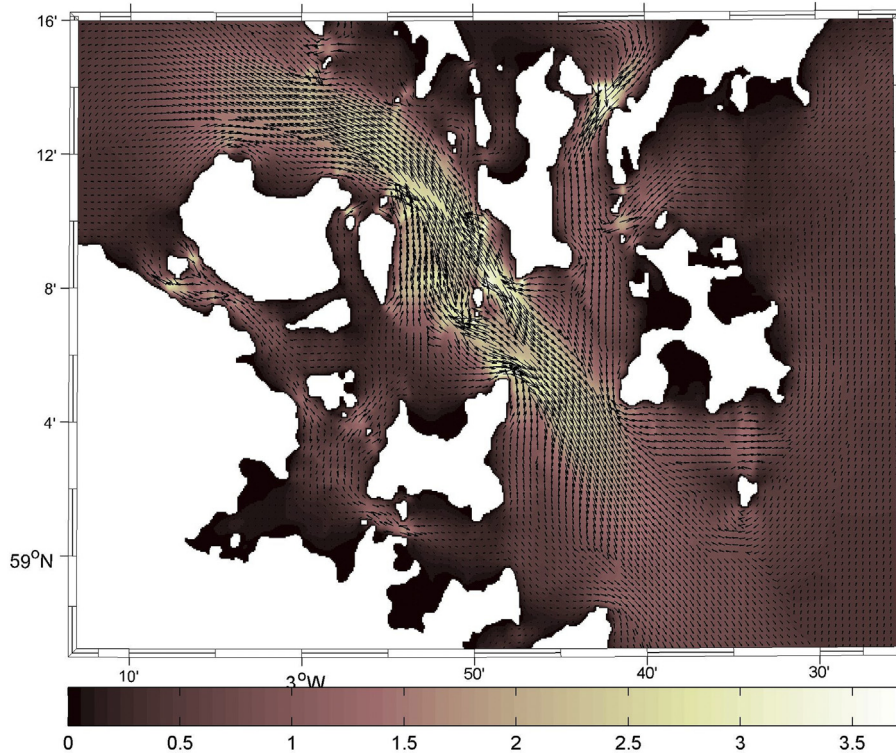

Fig. 5. Peak current speed (colour scale) and the associated peak spring velocity vectors. For clarity, only every 5th vector in the zonal and meridional directions have been plotted.

200 m) gridded multibeam data provided by St. Andrew's University. The model domain encompasses the principal high tidal flow regions of Orkney, including Westray Firth and Stronsay Firth, and the EMEC tidal test site at the Fall of Warness. The model configuration used the GLS turbulence model, tuned to represent the $k-\varepsilon$ model, and included horizontal harmonic mixing to provide subgrid scale dissipation of momentum [30], and quadratic bottom friction with a drag coefficient $C_D = 0.003$. This value for the drag coefficient is consistent with previous ROMS studies which simulate the flow through energetic tidal channels, and these studies have demonstrated that the ROMS model is not particularly sensitive to the value of C_D [26,31]. The model was again run with 10 vertical levels for a period of 15 days.

4.3. Model validation

To validate the vertical tide, we made use of the harmonic constants published in Admiralty Tide Tables, which are based on harmonic analysis of observations which have a minimum record length of one month [32]. The regional model was validated at 14 tide gauge stations throughout the region, with a root-mean-square-error (RMSE) in amplitude of 8.3 cm for M_2, and 3.7 cm for S_2, based on harmonic analysis of the 15 days of model simulation - a sufficient record length to separate the M_2 and S_2 constituents [13]. The corresponding RMSE in phase was 6.8° and 7.5° for the M_2 and S_2 tidal constituents, respectively. We present the validation of the high resolution Orkney model in more detail (Table 3). For the high resolution model, the RMSE in amplitude for the 6 available tide gauge stations was 2.7 cm for M_2, and 1.7 cm for S_2, again based on harmonic analysis of the 15 day model simulation. The RMSE in phase was 5.0° and 5.5° for the M_2 and S_2 tidal constituents, respectively.

Table 4
Tidal analysis of elevation time series at the 21 selected locations. H is the amplitude (in metres), and g is the phase (in degrees relative to Greenwich). The final column shows the percentage ratio of the M_4 to M_2 amplitude.

Location	M_2		S_2		M_4		MS_4		H_{M_4}/H_{M_2}
	H	g	H	g	H	g	H	g	
1	0.90	211	0.37	289	0.04	209	0.02	283	4.0
2	0.88	212	0.36	290	0.03	210	0.02	282	3.4
3	0.89	213	0.36	291	0.03	211	0.02	283	3.8
4	0.89	214	0.36	292	0.05	208	0.03	282	5.6
5	0.89	216	0.36	294	0.05	206	0.03	279	5.7
6	0.89	217	0.36	296	0.06	205	0.04	277	6.4
7	0.88	219	0.35	298	0.06	203	0.04	275	6.7
8	0.87	222	0.35	300	0.06	202	0.04	274	6.7
9	0.85	224	0.34	303	0.07	201	0.05	274	8.0
10	0.83	227	0.33	306	0.07	202	0.05	275	8.3
11	0.82	230	0.32	310	0.07	203	0.05	276	8.0
12	0.81	234	0.32	313	0.06	204	0.04	276	7.1
13	0.80	237	0.32	317	0.06	207	0.04	279	7.0
14	0.78	242	0.31	323	0.07	203	0.05	276	9.4
15	0.75	249	0.29	331	0.06	200	0.04	271	7.4
16	0.75	252	0.29	335	0.04	202	0.02	269	4.8
17	0.76	254	0.30	337	0.03	209	0.02	272	3.7
18	0.78	256	0.30	339	0.04	214	0.02	281	4.7
19	0.79	258	0.31	342	0.03	214	0.02	281	4.3
20	0.79	261	0.31	345	0.03	218	0.02	286	4.1
21	0.80	263	0.31	347	0.03	222	0.02	290	3.2

Detailed analysed tidal current constituent data is difficult to obtain for the study region, particularly since a large part of the site is commercial. However, limited results were obtained from analysis of a 32 day ADCP mooring at the Fall of Warness EMEC tidal test
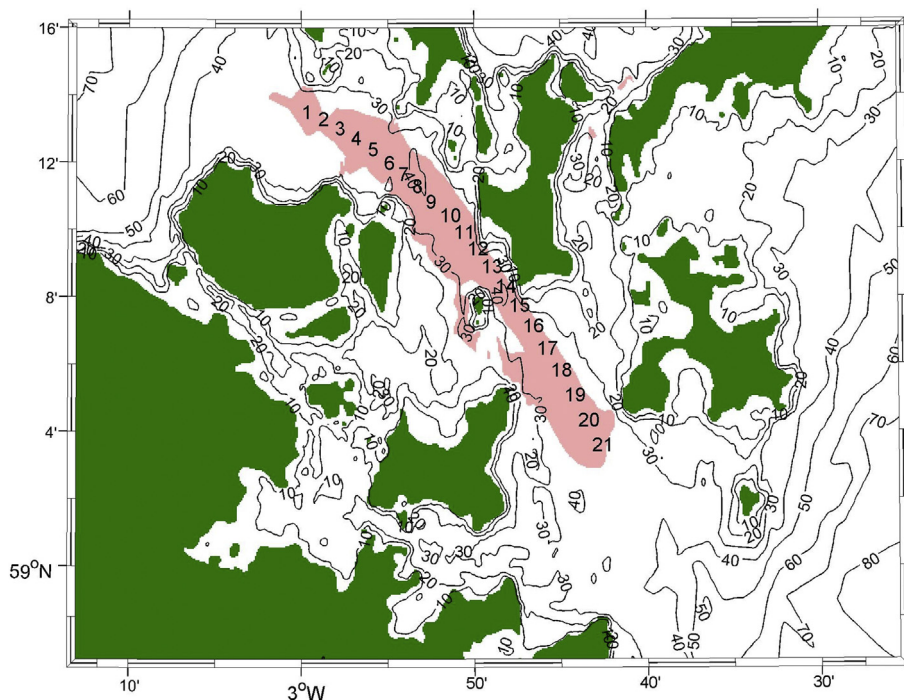

Fig. 6. Masked region showing the 21 locations selected for detailed analysis. Green = land; light red = region where water depth is between 25 and 50 m, and where the peak spring current exceeds 2 m s^{-1}. The EMEC tidal test site (Fall of Warness) spans locations 12–14. Contours are water depths in metres relative to mean sea level. (For interpretation of the references to colour in this figure legend, the reader is referred to the web version of this article.)
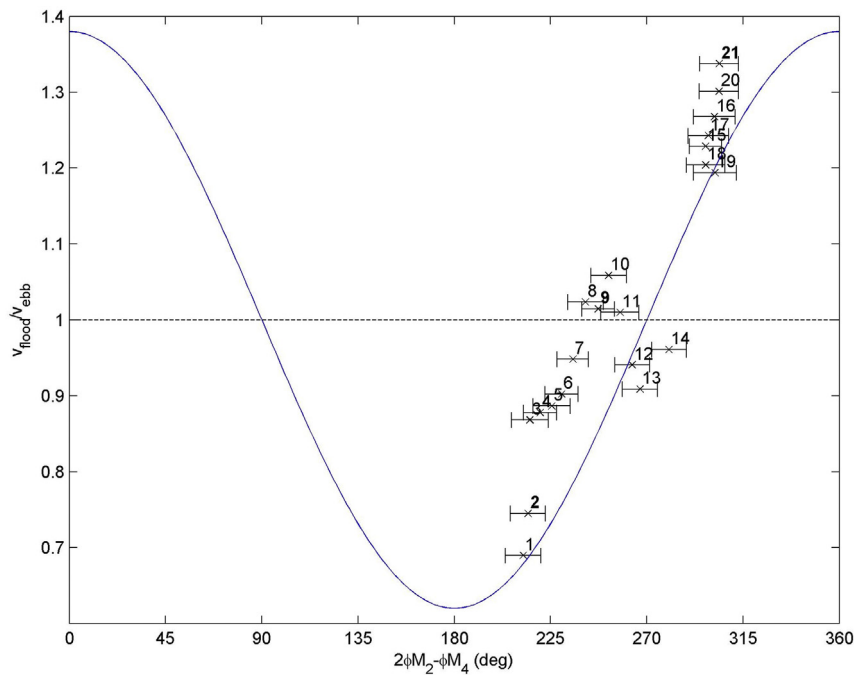
Fig. 7. Modelled tidal asymmetry and theoretical asymmetry, based on Eq. (6) and numerical calculations of idealized tidal residuals presented in Neill et al. [11]. Error bars are associated with the 95% confidence intervals estimated by the tidal analysis [42]. Numbers refer to sites 1–21 (Fig. 6), and time series of the sites in bold (2,9,21) are presented in more detail in Figs. 8–11.

site [33]. The validation data at this location (2°48.38′W, 59°08.15′N) are only available for amplitude, but our modelled M_2 amplitude of 2.42 m s^{-1} (compared to an observed value of 2.49 m s^{-1}), and a modelled S_2 amplitude of 0.95 m s^{-1} (compared to an observed value of 1.14 m s^{-1}) gives us confidence in our results. This is not intended as a detailed resource study, but rather a study which examines the role of tidal asymmetry on the resource. Further, since our phase validation for the vertical tide which (a) drives the pressure gradient, and (b) controls tidal asymmetry, is excellent (Table 3), we consider our model suitable for this purpose.

5. Results

5.1. Tidal currents

The peak depth-averaged tidal currents and the corresponding peak velocity vectors are shown in Fig. 5. Clearly, tidal flow is strongest at the constrictions of narrow channels (e.g. Lashy Sound, Eynhallow Sound and, in particular, the Fall of Warness). The peak current speed reaches 3.7 m s^{-1} in Lashy Sound and the Fall of Warness, and since the model was forced with the two principal semi-diurnal tidal constituents, M_2 and S_2, these represent peak spring tidal currents. The peak velocity vectors provide a qualitative overview of the tidal asymmetry [19], and the tidal flow appears to be largely ebb-dominant in Westray Firth, and flood-dominant in Stronsay Firth.[2] Where these two Firths join, i.e. in the vicinity of the Fall of Warness, the circulation is further complicated by the presence of strong residual

eddies with length scales of around 4–5 km [34]. However, the tidal currents in this region appear to be more symmetrical, and divergence of the peak velocity vectors indicates that this is a bed-load parting zone [19]. The bathymetric/topographic restriction of the Fall of Warness impedes the flow along the channel, which is driven by the tidal pressure gradient. This impedance results in an acceleration of the flow downstream of the restriction. This leads to a divergence of the residual flow centred on the Fall of Warness, which is further complicated by variability in bathymetry and geometry along and across the channel (Fig. 5).

If we restrict our analysis only to sites where water depth is in the range 25–50 m, and where the peak spring currents exceed 2 m s^{-1}, we can concentrate on locations which are suitable for the majority of first generation TEC devices (Fig. 6). These sites are primarily located in Westray Firth and Stronsay Firth, with a small additional region to the northeast in Lashy Sound. The total area where these depth and velocity criteria are satisfied within the model domain is around 70 km^2 – a substantial region for tidal energy arrays. We selected 21 sites evenly distributed along a 30 km longitudinal transect through Westray Firth and Stronsay Firth, representing a large variability in tidal asymmetry with which to examine its influence on the tidal energy resource.

If we perform tidal analysis on the elevation time series at each of the 21 selected locations (Table 4), we can calculate the phase relationship between the M_2 and M_4 constituents, and so calculate the theoretical asymmetry based on Eq. (6). If we calculate the mean depth-averaged flood velocity over a spring-neap cycle at each location (v_{flood}) and divide by the mean depth-averaged ebb velocity (v_{ebb}), we have a metric for tidal asymmetry (v_{flood}/v_{ebb}) [8]. We plot this value in relation to Eq. (6) and numerical calculations of idealized tidal residuals presented in Neill et al. [11], demonstrating a good fit to the theory

---

[2] Since the tidal wave propagates eastwards across the north of Scotland (Fig. 4), the tidal currents are directed approximately southeastward along these Firths during the flood phase of the tide.

(Fig. 7), with a value of $r^2 = 0.81$. Errors associated with the agreement between our model results of tidal asymmetry and the theoretical asymmetry are due to a combination of the irregular nature of the site (i.e. complex longitudinal and lateral variations in bathymetry/topography), a weak M_4/M_2 amplitude signal, or the importance of other tidal constituents (Table 4). However, provided we can quantify the phase relationship between the M_2 tidal constituent and its first overtide, M_4, for any proposed site, it is possible to provide a good estimate of the degree of tidal asymmetry.

To examine the vertical velocity structure in relation to tidal asymmetry, we also present detailed time series at three contrasting locations: site 2 (ebb-dominant), site 9 (symmetrical), and site 21 (flood-dominant) (Fig. 8). Above the boundary layer, the asymmetry is evident at all depths in the water column, and is more pronounced during spring tides.

5.2. Power

Based on the published power curve for the 1.2 MW Strangford Narrows SeaGen S deployment [35], we calculated the power output for a single SeaGen device hypothetically installed at three contrasting sites (Fig. 9). The top and bottom panels of this figure (the highly asymmetrical locations) highlight two points. Firstly, and of lesser importance, it is possible at highly asymmetrical sites such as these, that the cut-in speed for a tidal energy device is sometimes exceeded on one half of the tidal cycle, but not the reverse. This occurs at sites 2 and 21 for days 12–17, since the cut-in speed for the SeaGen device is around 1 m s^{-1}. However, of more importance, is the extreme asymmetry which occurs in the power time series, in relation to a strong asymmetry in the velocity time series. Since power output is related to velocity cubed, there are some instances during spring tides (e.g. days 6–9 for location 21)
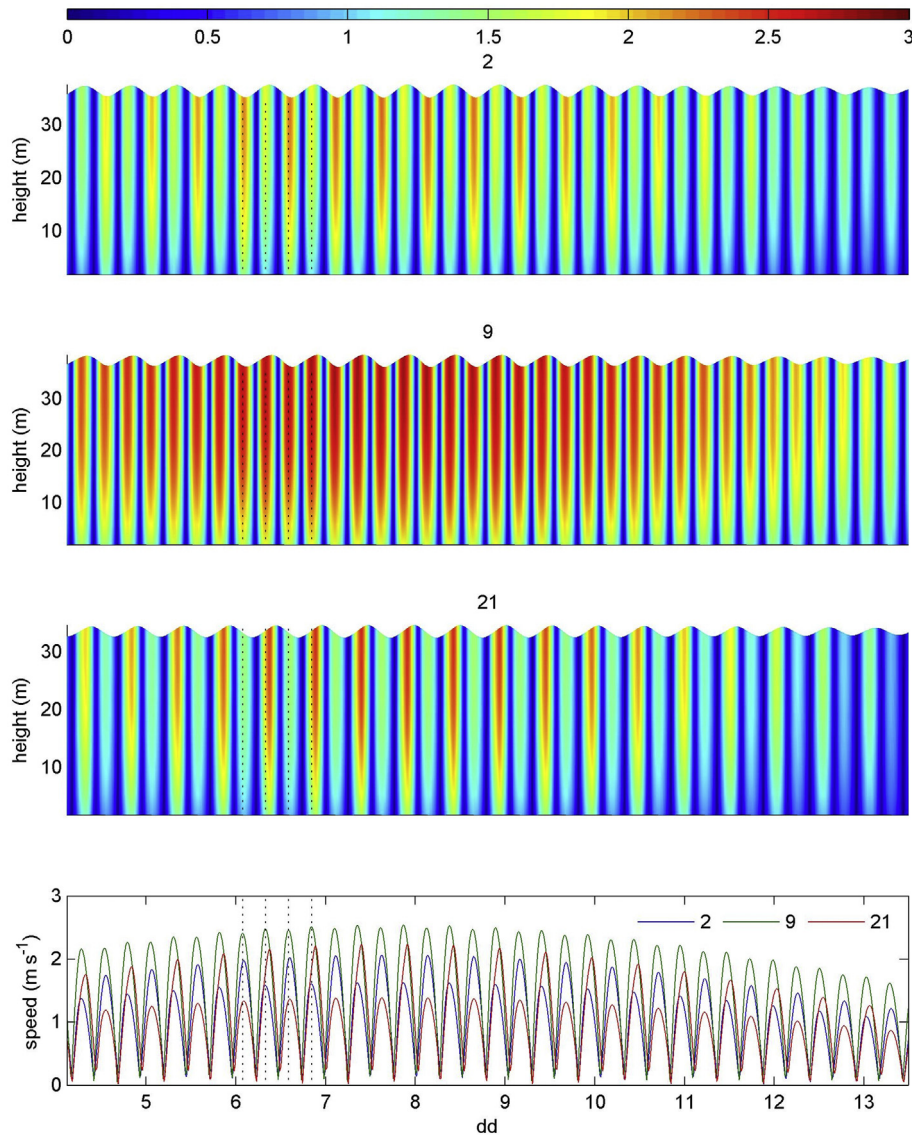

Fig. 8. Time series of simulated current speed in January 2000 at three contrasting sites: site 2 (ebb-dominant), site 9 (almost symmetrical), and site 21 (flood-dominant). The lower panel shows a time series of depth-averaged current speed. For reference, vertical dashed lines are located at peak flood and ebb conditions for site 9.

when the peak power generated on the flood phase of the tide exceeds the peak power generated on the ebb phase of the tide by a factor of four.

5.3. Turbulence

We also present detailed time series of the simulated turbulent kinetic energy (k) per unit mass

$$k = \frac{1}{2}\left(u'^2 + v'^2 + w'^2\right) \tag{7}$$

at three contrasting locations: site 2 (ebb-dominant), site 9 (symmetrical), and site 21 (flood-dominant) (Fig. 10). The corresponding plot for the rate of dissipation (ε) of k is shown in Fig. 11, defined as

$$\frac{\mathrm{d}k}{\mathrm{d}t} \cong P - \varepsilon \tag{8}$$

where P is the rate of production. By comparing these turbulence metrics with the velocity time series (Fig. 8), it is clear that even a relatively modest asymmetry in velocity can translate into a large asymmetry in the turbulence properties. Although sites 2 and 21 have the strongest asymmetry, this point is made clearer by considering the velocity time series at site 9 (Fig. 8) (an almost symmetrical site, with $v_{flood}/v_{ebb} = 1.01$, Fig. 7). This almost indiscernible asymmetry in the velocity time series manifests itself as a strong asymmetry in TKE (Fig. 10). The production of turbulent kinetic energy is generally proportional to the magnitude of the velocity gradient ($P \propto [(\partial U/\partial z)^2 + (\partial V/\partial z)]^2$). Therefore, for a specific

velocity distribution (e.g. a logarithmic distribution), this gradient will be proportional to the current strength. Therefore, we expect magnified turbulence asymmetry due to asymmetry in the current strength.

6. Discussion

We have developed a high resolution 3D model of Orkney, and examined the role of tidal asymmetry along a 30 km channel which passes through the EMEC tidal test site at the Fall of Warness. Our analysis over a range of sites along this channel, with various degrees of asymmetry from flood-dominant to ebb-dominant, has demonstrated that even modest asymmetry in the velocity field can translate into a significant asymmetry in the power generated on each half of the tidal cycle. Further, simulated turbulence properties of the flow are particularly sensitive to asymmetries in velocity. Analogous to wind power generation, turbulent fluctuations in the velocity field may lead to reduced turbine performance. It can also cause excessive cyclic loading on the device which may eventually lead to material fatigue and decreased lifespan of a turbine. Therefore, assessment of the turbulence quantities of the flow before and after installation of tidal stream devices is crucial for site development [9,36]. It should be noted that our analysis is based on undisturbed flow fields, i.e. we did not account for energy losses due to artificial energy extraction since we only considered single devices. However, large arrays of devices would significantly modify the flow field, and it has been demonstrated that such extraction from tidal channels would lead to a reduction in asymmetry [37], with implications for environmental impacts [11].
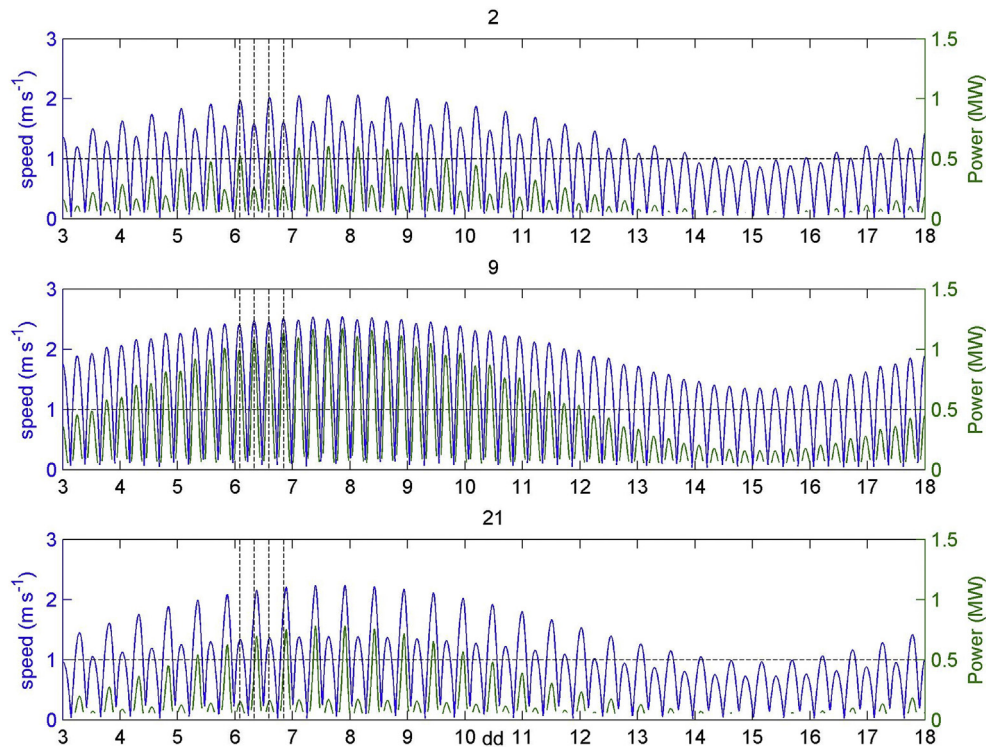

Fig. 9. Time series of depth-averaged current speed and the power which would be generated by a SeaGen device at three contrasting sites, January 2000. Horizontal dashed line is the cut-in speed (1 m s^{-1}) for the SeaGen device.

6.1. Power/hub heights

In accordance with other studies [38,39], we demonstrated in Section 5.2 that a small velocity asymmetry translates into a large power asymmetry, since the latter is a function of velocity cubed. However, this analysis was based on the simulated depth-averaged currents, but developers will also be interested in how this relates to different levels within the water column, i.e. representing a range of TEC device hub heights. To achieve this, we considered a vertical range of sensitivity over which it is appropriate to examine asymmetry in power density. If we assume a turbine diameter of 20 m (i.e. SeaGen S Mk2), and allow 5 m bed and navigation clearance, then it is appropriate to examine hub heights of 15 m, 20 m, and 25 m above the bed, provided water depth is a minimum of hub height plus 15 m (i.e.

we cannot apply the full sensitivity analysis to all of our study sites which range in depth from 32 to 40 m). Further, we need to use an alternative metric than the ratio $P_{\text{flood}}/P_{\text{ebb}}$, since such a ratio does not give practical information on how power would be affected, for example a percentage. Therefore, we use the metrics $(V_{\text{flood}} - V_{\text{ebb}})/\overline{V}$ and $(P_{\text{flood}} - P_{\text{ebb}})/\overline{P}$ (where $\overline{V}$ and $\overline{P}$ are the mean values of velocity and power, respectively, over a spring-neap cycle at each water depth) to describe vertical variations in flood/ebb velocity and power asymmetry, respectively. The result of this sensitivity analysis is presented in Fig. 12. Since the metrics used to quantify velocity and power asymmetry are percentages, this figure makes it clear that approximately 30% velocity asymmetry translates into 100% power asymmetry. Further, at almost all sites there is stronger asymmetry higher in the water column. Typically, at the more asymmetrical sites, an
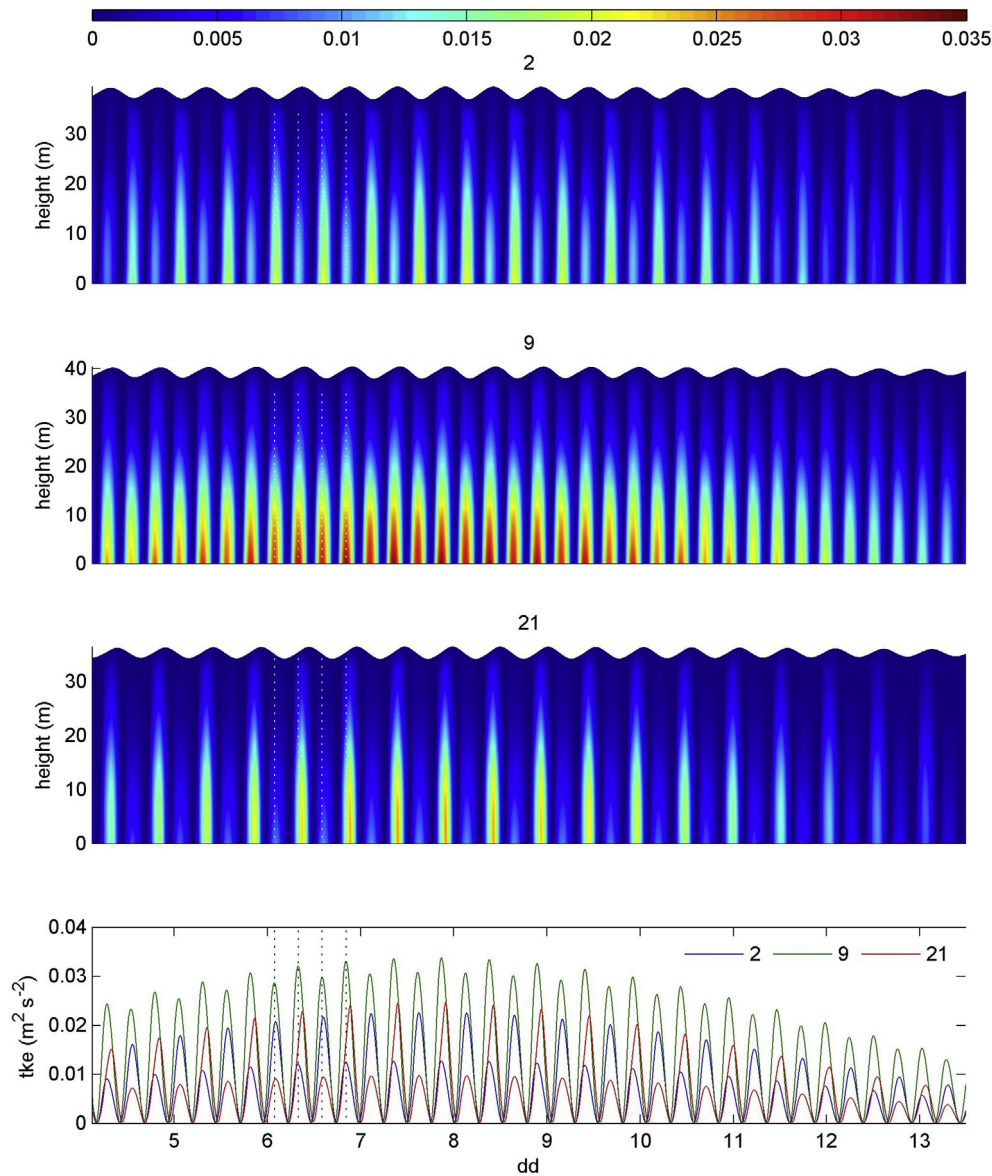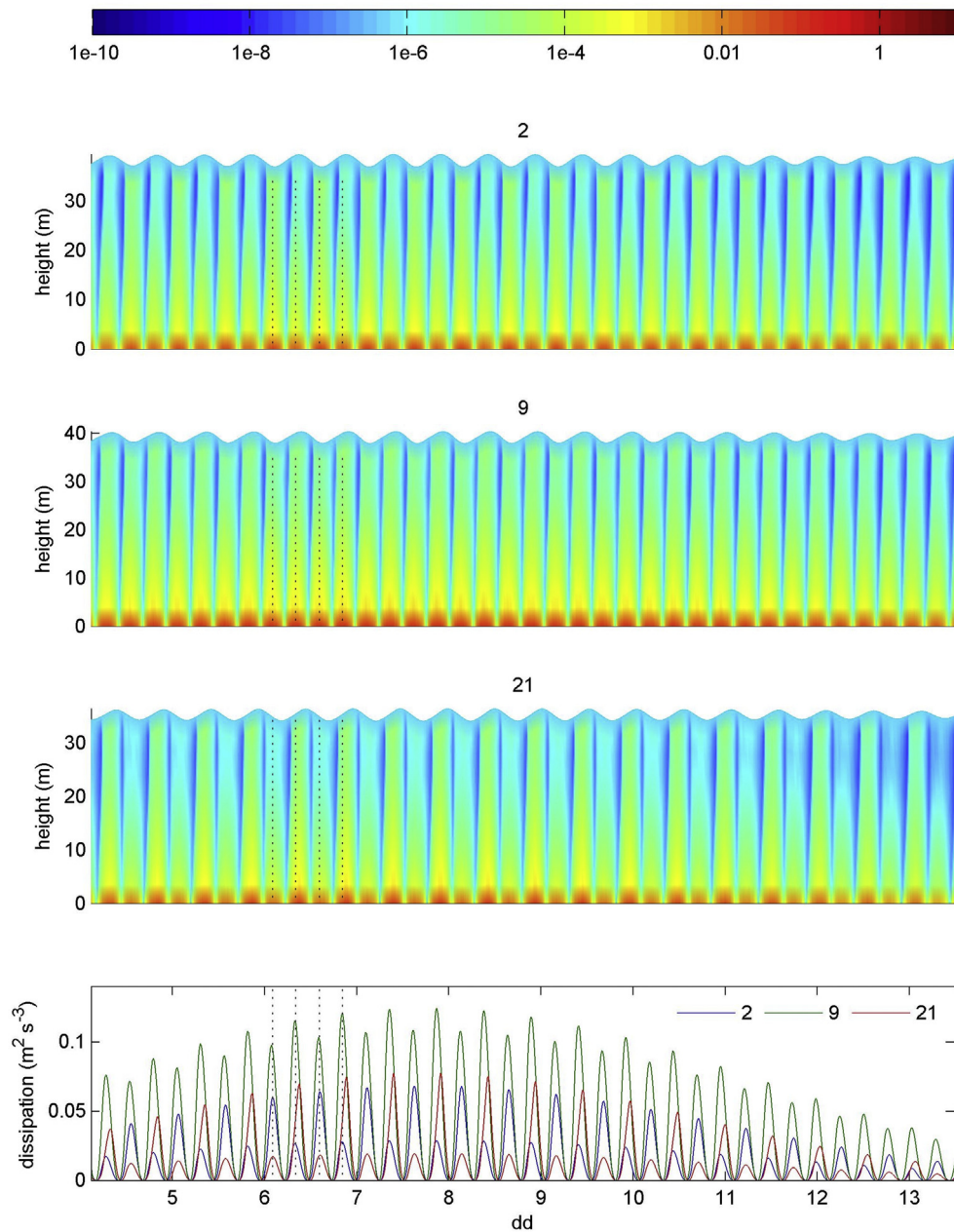

Fig. 10. Time series of simulated turbulent kinetic energy in January 2000 at three contrasting sites: site 2 (ebb-dominant), site 9 (almost symmetrical), and site 21 (flood-dominant). The lower panel shows a time series of TKE at the model cell closest to the bed. For reference, vertical dashed lines are located at peak flood and ebb conditions for site 9.

increase in hub height from 15 m to 20 m above the bed is associated with a 1% increase in velocity asymmetry, and a 3% corresponding increase in power asymmetry. Therefore, selection of hub height (and, implicitly, the technology selected for a particular site) could be a critical factor for an asymmetrical site, since it will affect net power output.

6.2. Non-tidal effects

Meteorological processes, such as wind stress induced velocity profiles [13], can also lead to velocity (and hence power) asymmetry. Our test channel is aligned approximately northwest/southeast, and so is exposed to winds (and associated wind-driven currents) from the Atlantic and North Sea, respectively, from these directions. Indeed, Admiralty Chart 2250 (Orkney Islands eastern sheet) explicitly states "Race during S.E. gale" at the Fall of Warness. We therefore decided to consider the influence on power asymmetry of strong wind events aligned with our test channel. From analysis of 10 years (2002–2011) of hourly wind data from Kirkwall airport, gales, i.e. wind speeds ≥ 17 m s^{-1}, occurred 0.51% of the time. The proportion of these gales emanating from the southeast quadrant, i.e. in alignment with the SE approach to

Fig. 11. Time series of simulated turbulent dissipation in January 2000 at three contrasting sites: site 2 (ebb-dominant), site 9 (almost symmetrical), and site 21 (flood-dominant). The lower panel shows a time series of turbulent dissipation at the model cell closest to the bed. For reference, vertical dashed lines are located at peak flood and ebb conditions for site 9.
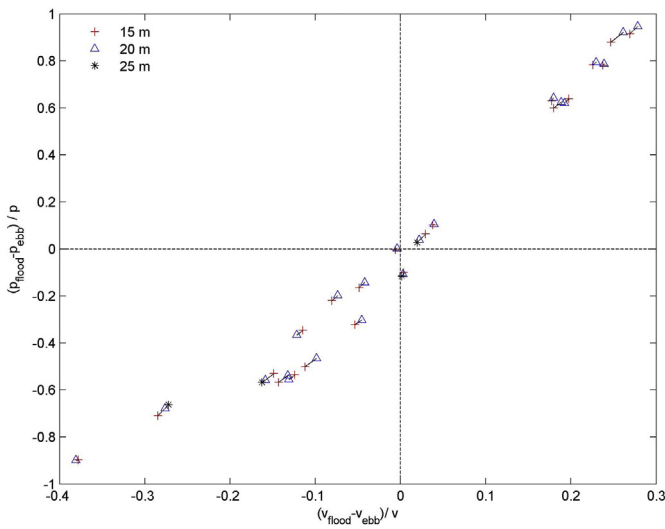
Fig. 12. Flood-ebb asymmetry in velocity and power at three different hub heights. Lines of connectivity indicate how the velocity and power ratios vary with hub height at each location. Note that the 25 m hub height is only shown for stations where $h \geq 40$ m.

Stronsay Firth, is 10.1% (of the gale record), with a mean wind speed of 18.5 m s^{-1}, a mean wind direction of 158° (SSE), with a range of 130−180° (SE to S). In addition to astronomical tides, we forced the model with this steady mean gale wind speed and direction, and examined the output at the study sites during spring and neap tidal cycles (Fig. 13). During periods of spring tides, a strong gale aligned with the channel has minimal relative impact on tidal power asymmetry, other than at the water surface where wind-driven currents are strongest (Fig. 13a). However, during periods of neap tides, the relative impact on asymmetry is much greater, with a consistent impact at all of the considered hub heights (15−25 m), and particularly at the water surface (Fig. 13b). The impact on tidal power asymmetry at the 25 m hub height during neap tides is around 4%, and the impact at the water surface is around 14%. Since power output is an order of magnitude lower during neap tides (e.g. Fig. 9), wind-driven currents are not expected to have a significant contribution on altering net tidal power asymmetry, especially considering the low frequency of strong wind conditions. Although the entire meteorological associated velocity field has not been included in our model simulation (for example, storm surge pressure gradient driven flows), we suggest that astronomical processes, such as consideration of additional tidal constituents, will have a more important role than non-tidal processes.

6.3. Potential for tidal phasing

It has been suggested that the aggregate outputs from a number of dispersed tidal energy sites have the potential to provide base load [40]. However, recent research has demonstrated that there is insufficient diversity between UK sites identified for first generation tidal current arrays to be considered as a firm power source [41]. Here, we wish to investigate if there is scope for tidal phasing at more localised scales, particularly with respect to tidal asymmetry. The results of the harmonic analysis of the vertical tide in Table 4 give a misleading view on the potential for tidal phasing across our study site. For example, there is a maximum M_2 phase difference of 52° at
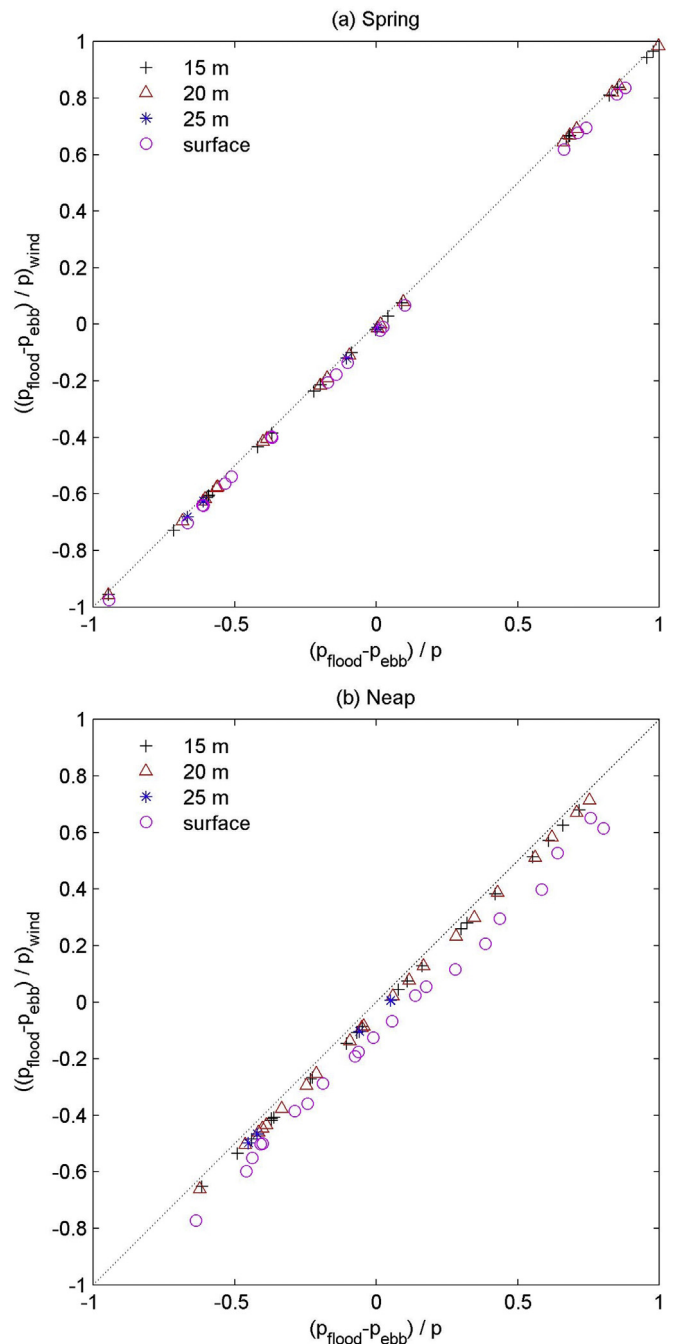

Fig. 13. Change in power asymmetry at different hub heights in the water column due to the addition of a SSE gale during (a) spring, and (b) neap, tidal cycles. Dashed line is the line of equality.

either end of the 30 km site, representing a time lag of 1.8 h (the corresponding S_2 values for phase and time lag are 58° and 1.9 h, respectively). However, such elevation phase lags result in a pressure gradient across the study site, and it is this pressure gradient which is translated into the horizontal tide, i.e. the tidal currents. Performing harmonic analysis of the tidal currents across our 21 locations (Table 5), we find that there is minimal potential for direct tidal phasing along the study site, e.g. there is a lag of 12° (i.e. 25 min) in the M_2 tidal currents between the peripheral stations 1 and 21. However, although there is no direct

Table 5
Harmonic analysis of the tidal currents for stations 1–21. H is the tidal current amplitude (m s^{-1}), and g is the phase in degrees relative to Greenwich.

Location	M$_2$		S$_2$		M$_4$		MS$_4$		H_{M_4}/H_{M_2}
	H	g	H	g	H	g	H	g	
1	1.41	17	0.56	93	0.07	95	0.05	177	4.64
2	1.34	18	0.53	93	0.05	277	0.04	178	3.97
3	1.41	19	0.56	93	0.04	254	0.03	332	3.10
4	1.63	17	0.65	92	0.05	44	0.03	294	3.30
5	1.65	15	0.65	90	0.06	36	0.04	103	3.68
6	1.73	14	0.68	88	0.07	33	0.04	103	3.79
7	1.77	13	0.69	87	0.06	39	0.03	115	3.18
8	1.78	13	0.69	87	0.04	51	0.02	126	2.07
9	1.92	14	0.74	88	0.02	223	0.02	287	1.15
10	1.98	15	0.77	90	0.02	197	0.02	282	0.84
11	2.00	16	0.79	91	0.02	214	0.02	283	1.18
12	1.98	16	0.79	92	0.04	52	0.03	311	2.24
13	2.02	17	0.81	93	0.04	58	0.02	167	1.93
14	2.24	16	0.88	91	0.05	35	0.04	100	2.32
15	2.03	15	0.80	91	0.13	206	0.10	279	6.43
16	1.66	18	0.67	93	0.16	218	0.13	291	9.61
17	1.47	22	0.60	97	0.11	224	0.10	300	7.60
18	1.53	24	0.62	98	0.08	229	0.08	306	5.46
19	1.48	25	0.59	99	0.07	255	0.07	325	4.57
20	1.44	27	0.58	101	0.09	284	0.08	349	6.05
21	1.28	29	0.52	104	0.10	285	0.08	355	7.69

scope for tidal phasing along Westray Firth and Stronsay Firth, there is scope for capitalizing on the strong tidal asymmetry across the site to provide a balanced power generation. If we consider together the ebb-dominant station 2 ($v_{flood}/v_{ebb} = 0.69$)

and the flood-dominant station 21 ($v_{flood}/v_{ebb} = 1.34$), it is possible to offset the flood/ebb asymmetry in power output (Fig. 14b) to provide a more balanced source of power. If we consider all of the 21 study sites together (Fig. 14c), although tidal phasing at this small spatial scale does not allow us to generate electricity over all phases of the tidal cycle, it does provide the potential to produce a very smooth and balanced power output between the flood and ebb phases of the tidal cycle.

7. Conclusions

Our 3D tidal model of an energetic tidal channel in Orkney has demonstrated that the phase relationship between the principal semi-diurnal lunar constituent, M$_2$, and its first harmonic, M$_4$, can be used to predict the degree of asymmetry in velocity, and hence power, at potential tidal energy sites. In accordance with previous modelling studies, we have demonstrated that relatively modest asymmetries in velocity can result in large asymmetries in power density, since the latter is a function of velocity cubed. Our model simulations indicate that a 30% asymmetry in velocity translates into a 100% asymmetry in power density. We have also shown that the degree of asymmetry in power density will not vary significantly with different hub heights in the water column, and demonstrate that consideration of opposing (i.e. flood-dominant versus ebb-dominant) asymmetrical sites over small spatial scales can maximise net power generation over the full tidal cycle.
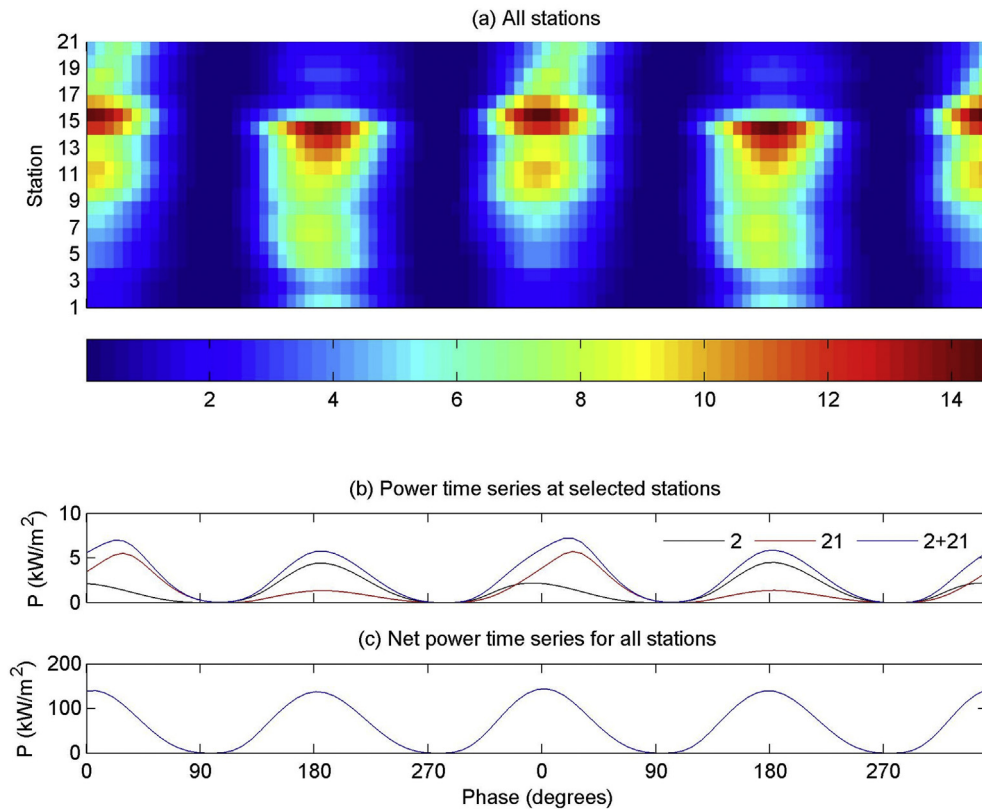

Fig. 14. Power density (in kW m^{-2}) over two spring tidal cycles.

Acknowledgements

References

[1] Bryden IG, Couch SJ. ME1 marine energy extraction: tidal resource analysis. Renew Energy 2006;31:133–9.

[2] Sánchez M, Iglesias G, Carballo R, Fraguela JA. Power peaks against installed capacity in tidal stream energy. IET Renew Power Gener 2013;7:246–53.

[3] Shields MA, Woolf DK, Grist EP, Kerr SA, Jackson A, Harris RE, et al. Marine renewable energy: the ecological implications of altering the hydrodynamics of the marine environment. Ocean Coast Manag 2011;54:2–9.

[4] Ramos V, Carballo R, Álvarez M, Sánchez M, Iglesias G. Assessment of the impacts of tidal stream energy through high-resolution numerical modeling. Energy 2013;61:541–54.

[5] Neill SP, Jordan JR, Couch SJ. Impact of tidal energy converter (TEC) arrays on the dynamics of headland sand banks. Renew Energy 2012;37:387–97.

[6] Couch SJ, Bryden IG. Tidal current energy extraction: hydrodynamic resource characteristics. Proc Inst Mech Eng Part J Eng Marit Environ 2006;220:185–94.

[7] Iglesias G, Sánchez M, Carballo R, Fernández H. The TSE index – a new tool for selecting tidal stream sites in depth-limited regions. Renew Energy 2012;48:350–7.

[8] Gooch S, Thomson J, Polagye B, Meggitt D. Site characterization for tidal power. In: OCEANS 2009, MTS/IEEE Biloxi-Marine Technology for our future: global and local challenges; 2009. pp. 1–10.

[9] Thomson J, Polagye B, Durgesh V, Richmond MC. Measurements of turbulence at two tidal energy sites in Puget Sound, WA. IEEE J Ocean Eng 2012;37:363–74.

[10] Korotenko K, Sentchev A, Schmitt FG, Jouanneau N. Variability of turbulent quantities in the tidal bottom boundary layer: case study in the eastern English Channel. Cont Shelf Res 2013;58:21–31.

[11] Neill SP, Litt EJ, Couch SJ, Davies AG. The impact of tidal stream turbines on large-scale sediment dynamics. Renew Energy 2009;34:2803–12.

[12] Provost CL. Nonlinear tidal interactions in shallow water; chapIn Generation of overtides and compound tides (review); 1991. pp. 269–95.

[13] Pugh DT. Tides, surges and mean sea-level. Wiley; 1987.

[14] Neill SP, Elliott AJ. Observations and simulations of an unsteady island wake in the Firth of Forth, Scotland. Ocean Dyn 2004;54:324–32.

[15] Lee PLM, Dawson MN, Neill SP, Robins PE, Houghton JDR, Doyle TK, et al. Identification of genetically and oceanographically distinct blooms of jellyfish. J R Soc Interface 2013;10:20120920.

[16] Robins PE, Neill SP, Giménez L, Jenkins SR, Malham SK. Physical and biological controls on larval dispersal and connectivity in a highly energetic shelf sea. Limnol Oceanogr 2013;58:505–24.

[17] Gallo MN, Vinzon SB. Generation of overtides and compound tides in Amazon estuary. Ocean Dyn 2005;55:441–8.

[18] Speer PE, Aubrey DG, Friedrichs CT. Nonlinear hydrodynamics of shallow tidal inlet/bay systems. Tidal Hydrodyn; 1991:321–39.

[19] Pingree RD, Griffiths DK. Sand transport paths around the British Isles resulting from the M_2 and M_4 tidal interactions. J Mar Biol Assoc UK 1979;59:497–513.

[20] Friedrichs CT, Aubrey DG. Non-linear tidal distortion in shallow well-mixed estuaries: a synthesis. Estuar Coast Shelf S 1988;27:521–45.

[21] Adcock TAA, Draper S, Houlsby GT, Borthwick AGL, Serhadlıoğlu S. The available power from tidal stream turbines in the Pentland Firth. Proc R Soc A Math Phys Eng Sci 2013;469:2157.

[22] Warner JC, Sherwood CR, Signell RP, Harris CK, Arango HG. Development of a three-dimensional, regional, coupled wave, current, and sediment-transport model. Comput Geosci 2008;34:1284–306.

[23] Chassignet EP, Arango HG, Dietrich D, Ezer T, Ghil M, Haidvogel DB, et al. DAMEE-NAB: the base experiments. Dyn Atmos Oceans 2000;32:155–83.

[24] Han W, Moore AM, Levin J, Zhang B, Arango HG, Curchitser E, et al. Seasonal surface ocean circulation and dynamics in the Philippine Archipelago region during 200–42008. Dyn Atmos Oceans 2009;47:114–37.

[25] Blunden LS, Bahaj AS. Initial evaluation of tidal stream energy resources at Portland Bill, UK. Renew Energy 2006;31:121–32.

[26] Thyng KM, Riley JJ, Thomson J. Inference of turbulence parameters from a ROMS simulation using the k-ε closure scheme. Ocean Model 2013;72:104–18.

[27] Warner JC, Sherwood CR, Arango HG, Signell RP. Performance of four turbulence closure models implemented using a generic length scale method. Ocean Model 2005;8:81–113.

[28] Carrère L, Lyard F, Cancet M, Guillot A, Roblou L. FES2012: a new global tidal model taking taking advantage of nearly 20 years of altimetry. In: Proceedings of meeting "20 Years of Altimetry", Venice 2012; 2012.

[29] Lyard F, Lefèvre F, Letellier T, Francis O. Modelling the global ocean tides: a modern insight from FES2004. Ocean Dyn 2006;56:394–415.

[30] Wajsowicz RC. A consistent formulation of the anisotropic stress tensor for use in models of the large-scale ocean circulation. J Comput Phys 1993;105:333–8.

[31] Sutherland DA, MacCready P, Banas NS, Smedstad LF. A model study of the Salish Sea estuarine circulation. J Phys Oceanogr 2011;41:1125–43.

[32] UK Hydrographic Office. Admiralty tide tables, vol. 1. United Kingdom and Ireland: UKHO; 2013.

[33] Stiven T, Couch SJ, Iyer AS. Assessing the impact of ADCP resolution and sampling rate on tidal current energy project economics. In: Oceans 2011 IEEE, Santander, Spain, 6–9 September 2011; 2011.

[34] Lawrence J, Kofoed-Hansen H, Chevalier C. High-resolution metocean modelling at EMEC's (UK) marine energy test sites. In: Proceedings of the 8th European Wave and Tidal Energy Conference, Uppsala, Sweden; 2009.

[35] Macenri J, Thiringer T, Reed M. Power quality and flicker performance of the tidal energy converter, SeaGen. In: 44th International Conference on Large High Voltage Electric Systems 2012, Paris, 26–31 August 2012; 2012.

[36] Blunden L, Bahaj A. Tidal energy resource assessment for tidal stream generators. Proc Inst Mech Eng Part A J Power Energy 2007;221:137–46.

[37] Adcock TAA, Draper S. Power extraction from tidal channels – multiple tidal constituents, compound tides and overtides. Renew Energy 2014;63:797–806.

[38] Carballo R, Iglesias G, Castro A. Numerical model evaluation of tidal stream energy resources in the Ría de Muros (NW Spain). Renew Energy 2009;34:1517–24.

[39] Sánchez M, Carballo R, Ramos V, Iglesias G. Tidal stream energy impact on the transient and residual flow in an estuary: a 3D analysis. Appl Energy 2014;116:167–77.

[40] Clarke JA, Connor G, Grant AD, Johnstone CM. Regulating the output characteristics of tidal current power stations to facilitate better base load matching over the lunar cycle. Renew Energy 2006;31:173–80.

[41] Iyer AS, Couch SJ, Harrison GP, Wallace AR. Variability and phasing of tidal current energy around the United Kingdom. Renew Energy 2013;51:343–57.

[42] Pawlowicz R, Beardsley B, Lentz S. Classical tidal harmonic analysis including error estimates in MATLAB using T_TIDE. Comput Geosci 2002;28:929–37.

.4   Published work P-III-A
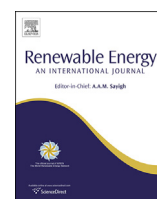
Effect of waves on the tidal energy resource at a planned tidal stream array

CrossMark

M. Reza Hashemi[*], Simon P. Neill, Peter E. Robins, Alan G. Davies, Matt J. Lewis

School of Ocean Sciences, Bangor University, Menai Bridge, UK

ARTICLE INFO

ABSTRACT

Wave–current interaction (WCI) processes can potentially alter tidal currents, and consequently affect the tidal stream resource at wave exposed sites. In this research, a high resolution coupled wave-tide model of a proposed tidal stream array has been developed. We investigated the effect of WCI processes on the tidal resource of the site for typical dominant wave scenarios of the region. We have implemented a simplified method to include the effect of waves on bottom friction. The results show that as a consequence of the combined effects of the wave radiation stresses and enhanced bottom friction, the tidal energy resource can be reduced by up to 20% and 15%, for extreme and mean winter wave scenarios, respectively. Whilst this study assessed the impact for a site relatively exposed to waves, the magnitude of this effect is variable depending on the wave climate of a region, and is expected to be different, particularly, in sites which are more exposed to waves. Such effects can be investigated in detail in future studies using a similar procedure to that presented here. It was also shown that the wind generated currents due to wind shear stress can alter the distribution of this effect.

© 2014 The Authors. Published by Elsevier Ltd. This is an open access article under the CC BY license (http://creativecommons.org/licenses/by/3.0/).

1. Introduction

The NW European shelf seas are amongst several regions in the world where relatively strong waves are present at many locations that are potentially suitable for the development of tidal stream arrays [1]. Waves can have a critical effect on planning, operation, maintenance, and generally, assessment of the interactions of a tidal energy converter (TEC) device with the marine environment. For instance, wave-induced loads have an important role in the TEC design process [2]. Additionally, wave–current interaction processes affect the turbulence, and the dynamics of sediment transport [3]; therefore, they should be considered when the impact of a TEC device, or an array of such devices, on the environment is studied.

Wave effects can be investigated on various forms of ocean currents – which are driven by forces generated by wind, air pressure, heating and cooling, Coriolis, and astronomical tidal currents; however, tidal-stream sites are usually located in shallow regions of shelf seas which are vertically well mixed and dominated by tidal forcing [4]. Further, the development of tidal-stream sites is primarily based on tidally generated currents. Therefore, the interaction of astronomical tidal currents and waves is of primary importance at tidal-stream sites, in this respect.

Ocean models are widely used to characterise the tidal energy resources of potential tidal-stream sites (e.g. Refs. [5–7]), in conjunction with direct measurement of currents. While these models can simulate tidal currents using relatively established procedures, simulating the effect of waves on tidal currents usually requires additional modelling steps, including the development of a wave model, and a coupling procedure. Apart from a few studies [1,6,8,9], the interaction of waves and tidal currents has not generally been considered in the assessment of marine renewable energy resources (e.g. Refs. [10–12,7]). In particular, much more effort has been invested in characterising the effect of tides on the wave energy resource [1,6,8], in comparison with quantifying the effect of waves on the tidal energy resource. Nevertheless, previous research has shown that wave–current interaction processes can change the hydrodynamics of tidal currents via several mechanisms such as wave induced forces and enhanced bottom friction (e.g. Refs. [13–15]), which could considerably alter the tidal energy resource of a site. These effects can be significant for water depths less than 50 m [16], where the majority of first generation tidal devices are likely to operate [17].

The theory of wave effects on currents has been extensively developed in previous research, and can be implemented using a range of coupled Ocean-Wave-Sediment Transport models [18,19].

---

* Corresponding author.
E-mail address: r.hashemi@bangor.ac.uk (M.R. Hashemi).

However, few studies have attempted to simulate the interaction of tides and waves over the northwest European shelf seas [20,21]. For instance, Bolanos-Sanchez et al. [22] and Bolanos et al. [23] coupled the POLCOMS (Proudman Oceanographic Laboratory Coastal Ocean Modelling System) ocean model and the WAM (WAve Model), and implemented several wave–current interaction processes, including wave refraction by currents, bottom friction, enhanced wind drag due to waves, Stokes drift, wave radiation stresses, and Doppler velocity. The POLCOMS-WAM coupled modelling system has been applied in a number of research studies, such as surge prediction in the Irish Sea [24].

Among coupled modelling systems which can simulate the interaction of tidal currents and waves, TELEMAC is an open access code which is used frequently for tidal energy resource assessment, both for academic research and commercial projects [25,11,26,27]. The TELEMAC numerical discretisation is based on the unstructured finite element/volume method, and allows the user to refine the mesh in regions of interest, without encountering complications which arise from the nesting procedure. In addition to

hydrodynamic modules, TELEMAC has a spectral wave module, TOMAWAC (TELEMAC-based Operational Model Addressing Wave Action Computation), which can simulate the evolution of waves on a mesh which is common to all modules, and export the wave parameters to the current model for the inclusion of wave–current interaction processes [28]. TELEMAC has been previously used to model complex coastal regions where wave-tide interaction plays a key role in sediment transport [29].

In this research, the effect of waves on the tidal energy resource at a proposed tidal stream array has been investigated. The site is within the coastal waters of Anglesey, North Wales, which is one of the hot spots for tidal stream development, and is likely to be the site of one of the first commercial tidal arrays in UK waters.

Section 2 introduces the study region, sources of data, and numerical models used in this study. In particular, the details of the methodology which have been implemented to study the effect of waves on the tidal energy resource is discussed in Section 2.5. All symbols used to describe model formulations or wave current interaction formulae are listed in Table 1. The results are presented in Section 3, which demonstrate the effect of waves on the tidal energy resource in various forms: wave forces, enhanced bottom friction, and combined effects. Section 4 provides additional discussion on the effect of wind generated currents, and highlights topics for further research (e.g. 3-D effects). Finally, our conclusions are summarised in Section 5.

2. Methods

2.1. Study region

The Irish Sea is a highly energetic shelf sea region, with high tidal velocities generated where flow is constricted around headlands [30]. One such example is the northwestern headland of Anglesey (Fig. 1a), a large island located off the NW coast of Wales, where tidal flow is constricted by a bathymetric feature called the Skerries and hence further accelerated.

Due to proximity of the Skerries site to a good grid connection and Holyhead port, suitable bathymetry and peak spring tidal currents in excess of 2.5 m/s [25], Marine Current Turbines (MCT)/Siemens has proposed to install a tidal stream array off the NW coast of Anglesey. The array site is a sound between the Isle of Anglesey and a small group of islands known as the Skerries, less than 1 km from the coast. The proposed tidal stream array consists of five SeaGen S 2 MW tidal stream turbines, with a total array capacity of around 10 MW (www.marineturbines.com). More information on the device can be found at the MCT and SeaGen websites (www.seageneration.co.uk). Apart from this site, a Crown Estate tidal energy demonstration zone has been planned to the west of Holy Island which is close to this site. Other tidal energy companies are also looking for suitable sites in this region for tidal energy development.

2.2. Description of models

Although a number of models have been developed for this region (e.g. Refs. [31,12]), these studies have focused mainly on tides or sediment transport [25]. Wave characteristics at potential tidal stream sites should be considered in several respects, such as wave induced hydrodynamic loading, operation and maintenance, wave-tide interactions, and sediment transport. Accordingly, a coupled tide-wave model of the region, which includes the effect of waves on currents and vice versa, was developed using the TELEMAC modelling system [32].
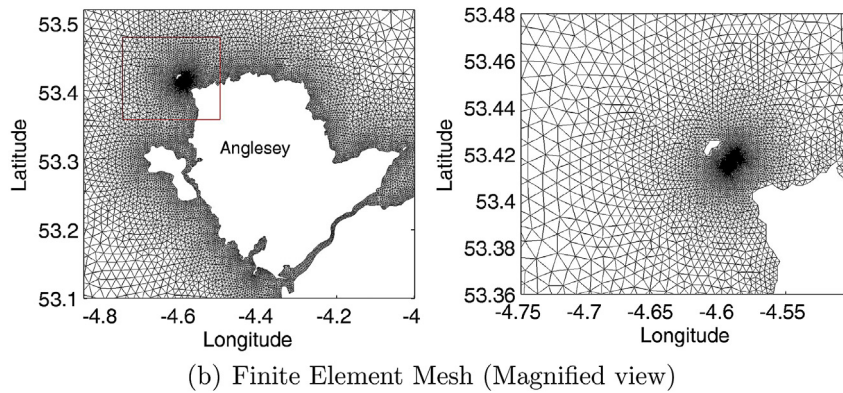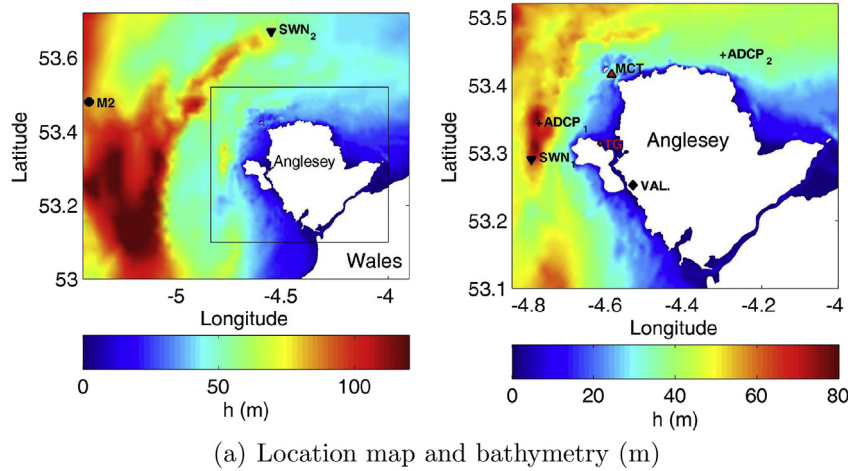
Table 1
List of symbols.

Symbol	Description
A	Semi orbital wave excursion, $A = U_w T_w/2\pi$.
C	Chezy coefficient, $C = \sqrt{(g/C_d)}$.
C^*	Enhanced Chezy coefficient due to WCI near the bed.
C_D	Drag coefficient.
C_D^*	Enhanced drag coefficient due to WCI near the bed.
C_g	Wave group velocity, $\frac{1}{2}(1 + 2kh/\sinh 2kh)$.
d	Grain diameter ($d = d_{50}$, median grain size).
E	Spectral energy density function $E = E(\sigma, \theta)$.
f_w	Wave friction factor, $f_w = 0.237(A/k_s)^{-0.52}$ [3].
F_x, F_y	Wave induced forces; $F = \sqrt{F_x^2 + F_y^2}$.
h	Water depth.
H_s	Significant wave height.
I	Percentage effect of WCI on current power over a tidal period.
k	Wave number.
k_s	Nikuradse bed roughness.
k_a	Apparent (enhanced) bed roughness due to WCI.
M	Number of data points for computing the mean absolute error.
n	Ratio of the wave group velocity to the wave celerity, C_g/C.
N	Wave action density function.
p	Water pressure.
$\bar{P}$	Average tidal power.
$\mathbf{Q}$	Various source and sink terms in the wave conservation energy.
S_h	Source or sink of mass in continuity equation.
S_i	Source or sink of momentum in i direction (x or y).
S_{xx}	Component of the radiation stress tensor, evaluated by: $\int \int \frac{E}{2} \left[2n(\cos\theta)^2 + (2n-1) \right] d\sigma d\theta$.
S_{yy}	Component of the radiation stress tensor, evaluated by: $\int \int \frac{E}{2} [2n(\sin\theta)^2 + (2n-1)] d\sigma d\theta$.
S_{xy}	Component of the radiation stress tensor, evaluated by: $S_{xy} = S_{yx} = \int \int En \sin\theta \cos\theta d\sigma d\theta$.
T_w	Wave period.
T_{sn}	Spring neap cycle period, about 14.765 days.
u_c	Depth-averaged current velocity.; $u_c = |\mathbf{u}|$.
u_c^*	Depth-averaged current velocity affected by wave–current interaction.
U_w	Near bed wave induced orbital velocity.
z_s	Free surface elevation.
$\mathbf{u}$	Depth averaged current velocity vector.
γ	A coefficient used to compute apparent bed roughness; $\gamma = 0.80 + \varphi - 0.3\varphi^2$.
θ	Angle of propagation for waves.
λ	Ratio of the pure wave to pure current bed shear stresses.
ξ	Ratio of the enhanced drag coefficient to drag coefficient.
σ	Wave angular frequency, $\sigma = 2\pi/T_w$.
τ_c	Current induced bed shear stress.
τ_w	Wave induced bed shear stress.
τ_m	Mean combined wave–current induced bed shear stress.
φ	Angle between wave direction and current direction.

(a) Location map and bathymetry (m)

(b) Finite Element Mesh (Magnified view)

Fig. 1. Study area, bathymetry, and a view of the unstructured mesh (part of the computational domain) used to discretise the domain. (a) also shows the locations of several points of interest as follows, MCT: Planned tidal stream array at the Skerries, Anglesey; TG: Holyhead tidal gauge station; ACDP: ADCP deployment; VAL.: Valley Met Office Station; M2: M2 Wave buoy; SWN₁, SWN₂: SWAN model output points.

2.2.1. TELEMAC modelling system

TELEMAC is a finite element or finite volume modelling system which was originally developed to simulate free surface flow. The theoretical/numerical formulation of TELEMAC is described in Hervouet [33], and its source codes and manuals are available online: www.telemacsystem.com. TELEMAC comprises a suite of modules for the simulation of hydrodynamic and morphodynamic processes in oceanic/coastal environments including shallow water (horizontal) flows (TELEMAC-2D), 3-D flows (TELEMAC-3D), sediment transport and bed evolution (SISYPHE), and waves (TOMA-WAC). Villaret et al. [28] recently presented several validation test cases of TELEMAC which involved various modules. In the latest version of TELEMAC (i.e. v6.3), the hydrodynamic (TELEMAC-2D), wave, and sediment transport modules are coupled: the modules exchange data at a user defined time step. More details about wave–current interaction simulation using TELEMAC is provided in Section 2.5. TELEMAC-2D, which has been used in this study, is based on the depth-averaged Navier Stokes Equations:

$$\frac{\partial h}{\partial t} + \mathbf{u} \cdot \nabla(h) + h \nabla \cdot \mathbf{u} = S_h \tag{1}$$

$$\frac{\partial u_i}{\partial t} + \mathbf{u} \cdot \nabla(u_i) = -g \frac{\partial z_s}{\partial x_i} + S_{u_i} + \frac{1}{h} \nabla \cdot (h \nu_t \nabla u_i), i = x, y \tag{2}$$

where h is the water depth, S_h represent sources/sinks of mass in the continuity equation, $\mathbf{u}$ is the depth averaged velocity, ν_t is the momentum diffusion coefficient (turbulence and dispersion), z_s is

the water elevation, S_{ui} represent other forces (friction, wave forces, wind stress, etc.), and i represents either x or y directions. TELEMAC benefits from an unstructured mesh, which allows the use of very high resolution mesh at locations of interest without resort to nesting. The model was used to characterise the tide and wave conditions in and around the Skerries.

TOMAWAC, the wave module of TELEMAC, is a third generation wave model which solves the evolution of the directional spectrum of the wave action. In realistic sea states, the wave energy is distributed over a range of frequencies and directions. The spectral energy density function is the intensity of the wave energy per unit frequency, per unit direction ($E = E(\sigma, \theta)$; see Table 1 for definition of symbols), and can represent the wave sea state at a particular time and location. In spectral models like TOMAWAC or SWAN, 'wave action density', rather than wave spectral density, is used as the state variable, since it is conserved in presence of ambient currents [34,35]. The wave action is defined as: $N(\overrightarrow{x}, \overrightarrow{k}, t) = E/(\rho g \sigma)$, and is conserved as follows.

$$\frac{\partial N}{\partial t} + (\mathbf{c_g} + \mathbf{u}) \cdot \nabla_{\overrightarrow{x}, \overrightarrow{k}}(N) = \mathbf{Q} \tag{3}$$

where $\mathbf{c_g} = (c_g k_x/k, c_g k_y/k)$, and $\mathbf{Q}$ represents various source and sink terms. TOMAWAC includes deep and shallow water physics such as refraction, white-capping, bottom friction and depth-induced wave breaking, as well as non-linear wave–wave quadruplet and triad interactions. TOMAWAC can be applied to a range of scales from continental shelf seas to coastal zones [34].
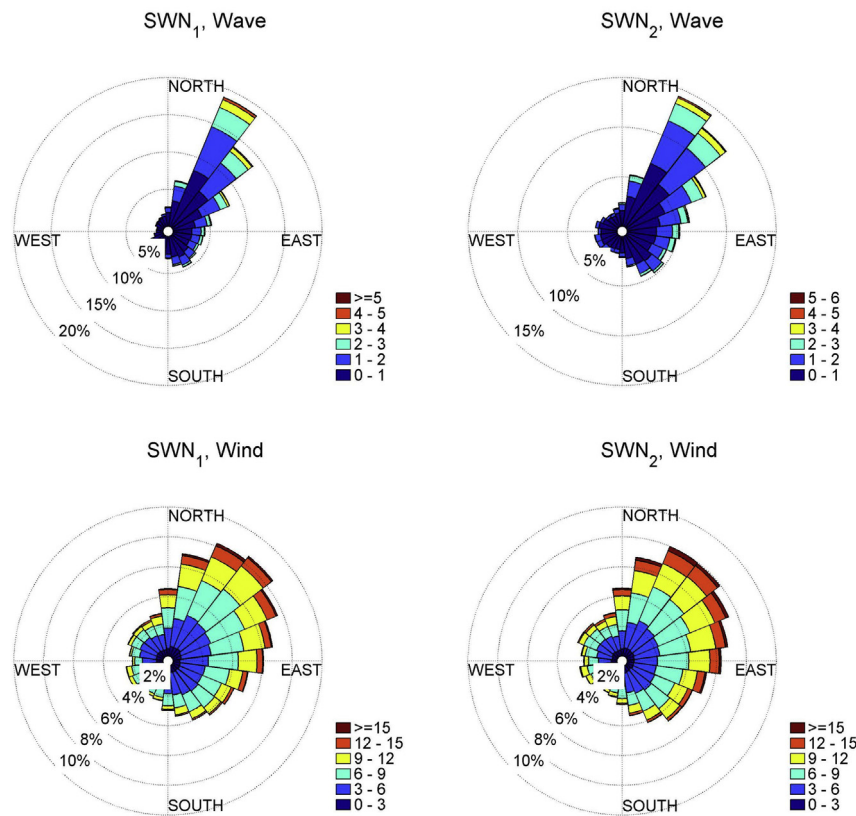
Fig. 2. Wave and wind roses for two locations (SWN$_1$ & SWN$_2$) near the tidal stream site (See Fig. 1a). The results are based on 10 years (2003–2012) of SWAN simulation for the NW European shelf seas. The colour scales for the waves and wind roses are significant wave height (m) and wind speed (m/s), respectively. (For interpretation of the references to colour in this figure legend, the reader is referred to the web version of this article.)

2.2.2. TELEMAC settings

An unstructured mesh of the region was created with variable resolution, being relatively fine (15–250 m) around the site and Anglesey, and coarser (500–2000 m) elsewhere in the Irish Sea (Fig. 1b). The model domain covers the whole Irish Sea, extending from 8° W to 2.5° W, and from 50° N to 56° N, which is necessary for wave modelling in order to generate sufficient fetch. Gridded Admiralty bathymetry data available at 200 m resolution (dig-imap.edina.ac.uk) was mapped on to the mesh. TELEMAC2D, the 2-D hydrodynamic module of TELEMAC, solves the 2-D shallow water equations using finite element method to simulate tidal currents, which is a good approximation for the fully mixed barotropic flows in this area. Tidal currents in the NW European shelf seas are dominated by M_2 and S_2: principal lunar and solar semidiurnal components, respectively [36]. The next three tidal constituents, which are relatively significant in some areas of the NW European shelf seas, are K_1 and O_1 lunar diurnal components, and the lunar elliptic semidiurnal constituent, N_2 [37]. Therefore, the open boundaries of the tidal model were forced by 5 tidal constituents (M_2, S_2, N_2, K_1, O_1) interpolated from FES2004 tidal data [37]. For friction, a constant Chezy's coefficient of 70 (approximately equivalent to $C_D = 0.0025$) was used, which led to convincing validation for water level and current speed for the astronomical tides at observation locations. The friction coefficient was then enhanced based on the wave parameters for WCI effects (Section 2.5.2).

TOMAWAC was applied to the same mesh and bathymetry as the TELEMAC2D model. Hourly wind forcing data was provided by the UK Met Office Integrated Data Archive System (MIDAS; for Valley station see Fig. 1). TOMAWAC was run in third-generation mode,

including Janssen's wind generation (WAM cycle 4), whitecapping, and quadruplet wave–wave interactions. The bottom friction and depth induced wave breaking were also included in the numerical simulations.

2.2.3. SWAN wave model

Since the high resolution coupled TELEMAC model was expensive to run for long periods of time, a SWAN (Simulating WAves Nearshore) model of the NW European Shelf seas was used to characterise the temporal variability of the wave climate over a decade of simulation. The SWAN model was developed and validated extensively in a previous research study [38].

SWAN is another open source third-generation numerical wave model which simulates random waves from deep waters to the surf zone and coastal regions in the spectral domain. SWAN has been described in Booij et al. [35] and is based on the Eulerian formulation of the discrete spectral balance of action density. It has been widely used for simulating waves at various scales (e.g. Refs. [38,39]). It accounts for refractive propagation over arbitrary bathymetry and ambient current fields. The physics and formulation of SWAN are similar to those of TOMAWAC described in Section 2.2.1; however, in SWAN, the wave action is formulated as a function of wave frequency and direction rather than wave number (used in TOMAWAC). Several processes including wind generation, whitecapping, quadruplet wave–wave interactions, and bottom dissipation are represented explicitly in SWAN.

2.2.4. SWAN settings

The SWAN wave model setting and its validation, which was applied for a decade (2003–2012) of simulation, are described in

detail in Neill and Hashemi [38]. It consisted of a parent model which included the entire North Atlantic at a grid resolution of 1/6° × 1/6°, extending from 60° W to 15° E, and from 40° N to 70° N. 2-D wave spectra were output hourly from the parent model and interpolated to the boundary of an inner nested model of the NW European shelf seas. The inner nested model had a grid resolution of 1/24°×1/24°, extending from 14° W to 11° E, and from 42° N to 62° N. Wind forcing was provided by European Centre for Medium-Range Weather Forecasts (ECMWF; www.ecmwf.int). ERA (European Research Area) Interim reanalysis full resolution data, which are available 3-hourly at a spatial resolution of 3/4°×3/4° were used. SWAN was run in third-generation mode, with Komen linear wave growth, white-capping, and quadruplet wave–wave interactions.

2.3. Wave climate of the region

In contrast to the astronomical tides, the wave climate of a region is highly variable. It has been previously shown that the wave climate of the NW European shelf seas is strongly related to the North Atlantic Oscillation, which has high inter-annual variability [38]. Fig. 2 shows the wave and wind roses at two points (Fig. 1a) off the NW of Anglesey based on the 10 year SWAN simulation. As this figure shows, the strongest and most frequent winds and waves are southwesterly. It is also clear that the probability of waves with significant wave height (H_s) greater than 5 m, or wind speeds in excess of 15 m/s, is quite low. Fig. 3b shows the variability of extreme significant wave heights during winter months to the west of Anglesey over the decade of simulation (Point SWN_1, Fig. 1). According to this figure, the probability of waves with H_s exceeding 5.5 m is very low. Further, January 2005 and December 2007 are the most extreme months in our record, with maximum significant wave heights of 6.7 m and 6.8 m, respectively. The expected (i.e. average) value of an extreme significant wave height during the winter period is 3.9 m. In terms of mean wave conditions (Fig. 3a), January is the most energetic month in this region, with expected significant wave heights of approximately 1.6 m (on average). Based on these wave statistics, the TOMAWAC model was forced with different southwesterly wind scenarios; wind speeds of 10 m/s and 15 m/s seemed appropriate to capture mean and extreme wave scenarios, with significant wave heights of 4.0 m and 1.8 m, respectively at SWN_1 (Fig. 1). In the next sections, TELEMAC2D and TOMAWAC are first validated, and then used to study the effect of waves on tidal energy resources of the site for these scenarios.

2.4. Model validation

The tidal model was validated at several tidal gauge stations within the Irish Sea. The validation results relatively near to the site is presented here. ADCP (acoustic Doppler current profiler) data collected during August 2013, at Holyhead Deep ($ADCP_1$, Fig. 1a), and February 2014, off the northern coast of Anglesey ($ADCP_2$, Fig. 1a), were used for current validation. Fig. 4a shows the comparison of model outputs and observed data at Holyhead tidal gauge. Table 2 also shows the performance of the model for water elevation and current velocity. The mean absolute error, which is reported in Table 2, is defined as.

$$\text{MAE} = \frac{1}{M} \sum_{i=1}^{M} \left| u_c^o(i) - u_c^m(i) \right| \tag{4}$$

where M is the number of data points, u_c^o and u_c^m are observed and predicted values of depth averaged velocities, respectively. The

current ellipses for M_2 and S_2 based on the model results and observations have also been compared in Fig. 4b. The model error for M_2 and S_2 amplitudes were 5 cm and 8 cm, and for phases were 2° and 1°, respectively. For $ADCP_1$, the errors of the current ellipse axes directions were 7° and 8° for M_2 and S_2 while less than 2% for magnitudes of the ellipses major axis. The small error in tidal ellipse directions may be associated with the 3-D nature of the flow [40] at this location, which is deeper than the surrounding areas. Similar discrepancies for current velocities have been reported in a previous study of the region which used ADCIRC depth averaged model [12]. Similar results can be seen for $ADCP_2$. The mean absolute error of current velocity for two measurement locations is less than 0.20 m/s. Overall, given the magnitudes of the errors, model performance for both tidal elevations and currents is convincing.

The theoretical average tidal stream energy per unit area (i.e., $\bar{P} = 1/2 T_{sn} \int \rho |u_c|^3 dt$) over a spring-neap cycle has been plotted in Fig. 5. As this figure shows, the Skerries and west coast of Holyhead are hot spots for tidal energy in northwest Wales. The peak tidal
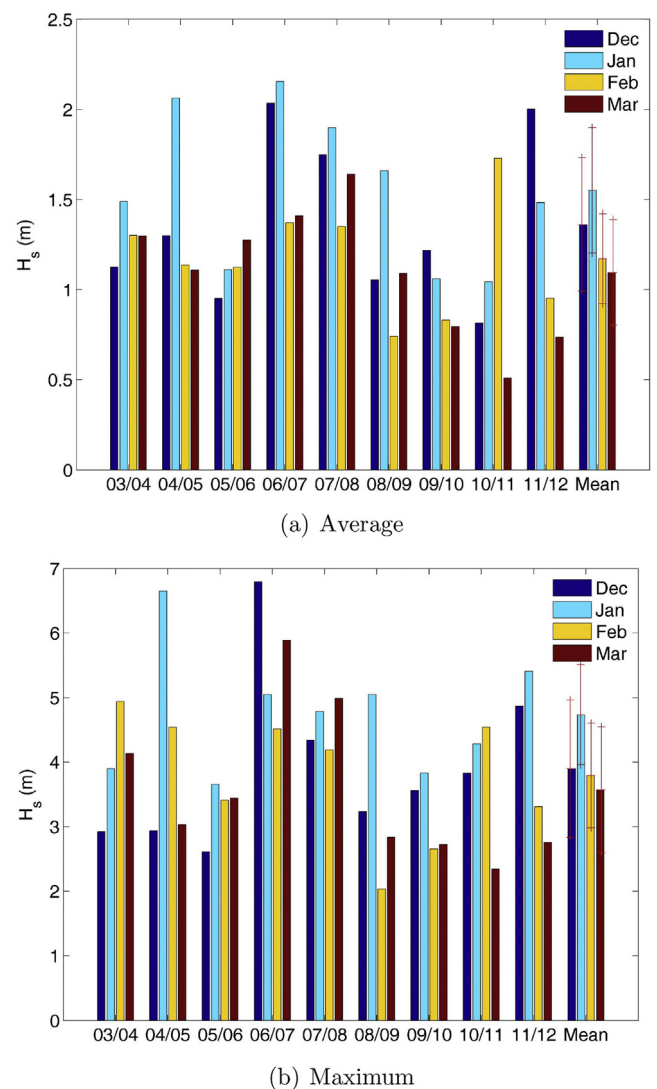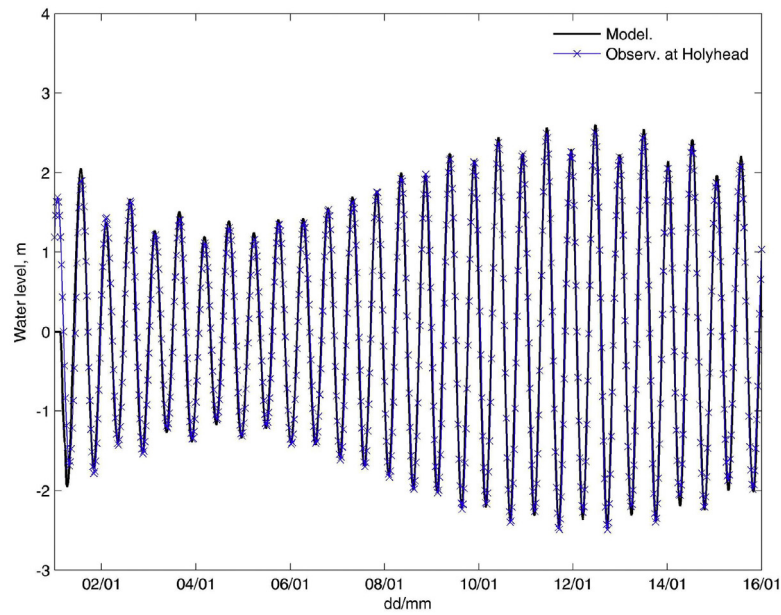

(a) Average

(b) Maximum

Fig. 3. Distribution of the average and maximum significant wave height at point SWN_1 (See Fig. 1a) over a decade (2003–2012) of simulation. January 2005, and December 2007 are the most extreme months with 6.7 m and 6.8 m significant wave heights, respectively. According to error-bars, which are based on 95% CI, the probability of these events is less than 5%.

(a) Astronomical tide at Holyhead during 1-16 January 2005.
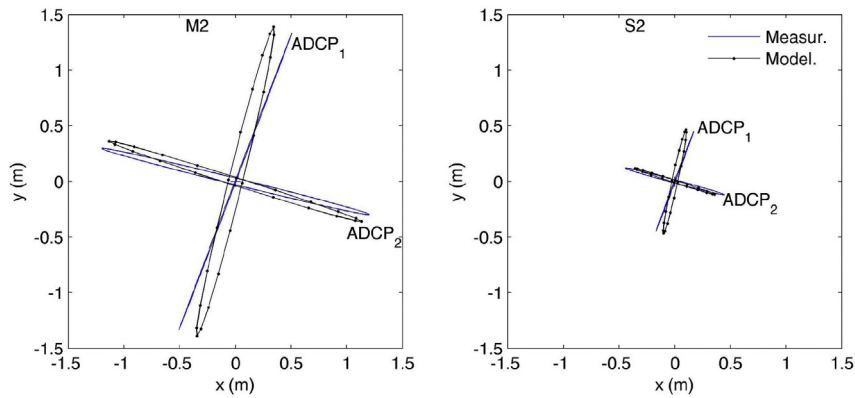
(b) Current ellipses (left M_2 and right S_2) at ADCP points (Fig. 1a)

Fig. 4. Sample validation of the tidal model for elevation and current velocity. See Table 2 for error magnitudes.

current velocity exceeds 3 m/s in parts of this region, and there is a relatively large area where peak tidal velocities exceed 2 m/s.

The TOMAWAC model of the region was validated for January 2005, which represents one of the most extreme months during our analysed period (Fig. 3). Within this month, periods of high, low and average wave condition existed, which provides a highly variable basis for testing the model. Fig. 6 shows the validation of significant wave height and wave period at the M2 wave buoy (Fig. 1), which is the closest available wave buoy to the site. The mean absolute errors for wave height and period are 0.38 m and 0.65 s, respectively, which is within an acceptable range of accuracy, compared with other models of this region (e.g. Ref. [38]). In particular, the model was able to capture the peak wave height on the eighth of January, which is important in the extreme wave scenario.

2.5. Formulation of wave effects on currents

Two important wave effects on currents are: wave induced momentum (or wave radiation stresses), and the enhancement of

Table 2
Performance of the tidal model (in terms of absolute error) for tidal elevation and velocity at a tidal gauge and 2 ADCP measurement points (see Fig. 1 for locations). The mean absolute error is presented for u_c. The variables in this table are defined as follows: a_h and a_h, tidal elevation amplitude and phase, respectively; C_{max} and C_{α}, current ellipse major axes magnitude and direction, respectively; u_c is the depth averaged velocity.

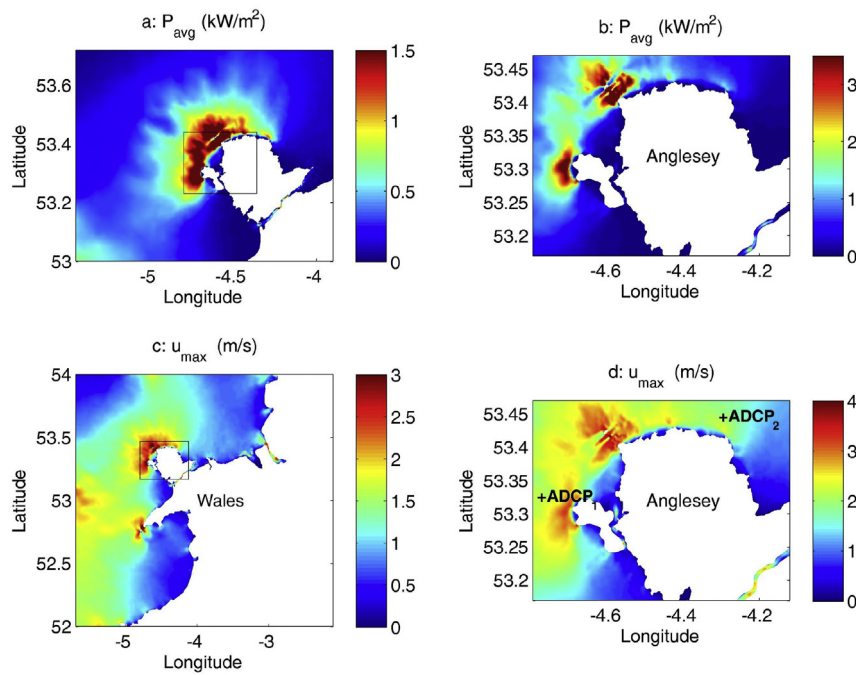| Variable		Error		
		TG		
M_2	a_h	5 cm		
	ϕ_h	2°	ACDP$_1$	ADCP$_2$
	C_{max}		0.02 m/s	0.04 m/s
	C_{α}		7°	4°
S_2	a_h	8 cm		
	ϕ_h	1°	ACDP$_1$	ADCP$_2$
	C_{max}		0.02 m/s	0.09 m/s
	C_{α}		8°	3°
u_c			0.20 m/s	0.14 m/s

Fig. 5. Simulated mean theoretical tidal stream power (P_{avg}) and peak tidal current velocity (u_{max}) over a spring-neap cycle. The ACDP deployment points are also shown for comparison.

the bottom friction felt by currents due to the interaction with the wave boundary layer. Both effects can be included in coupled wave-tide models by exporting the appropriate wave parameters to the tidal model, and modifying the corresponding parameters in the momentum equation. The effect of these processes on tidal energy is evaluated here by running the tidal model with and without WCI, and then computing the average tidal power. The relative difference, or the effect of a process, was computed using.

$$I = 100 \times \frac{\int \rho \left| u_c^* \right|^3 \mathrm{d}t - \int \rho \left| u_c \right|^3 \mathrm{d}t}{\int \rho \left| u_c^* \right|^3 \mathrm{d}t} \qquad (5)$$

where u_c^* is the tidal current affected by a wave–current interaction process, I is the percentage effect, and ρ is the water density. In a coupled TELEMAC2D-TOMAWAC model, the wave radiation forces
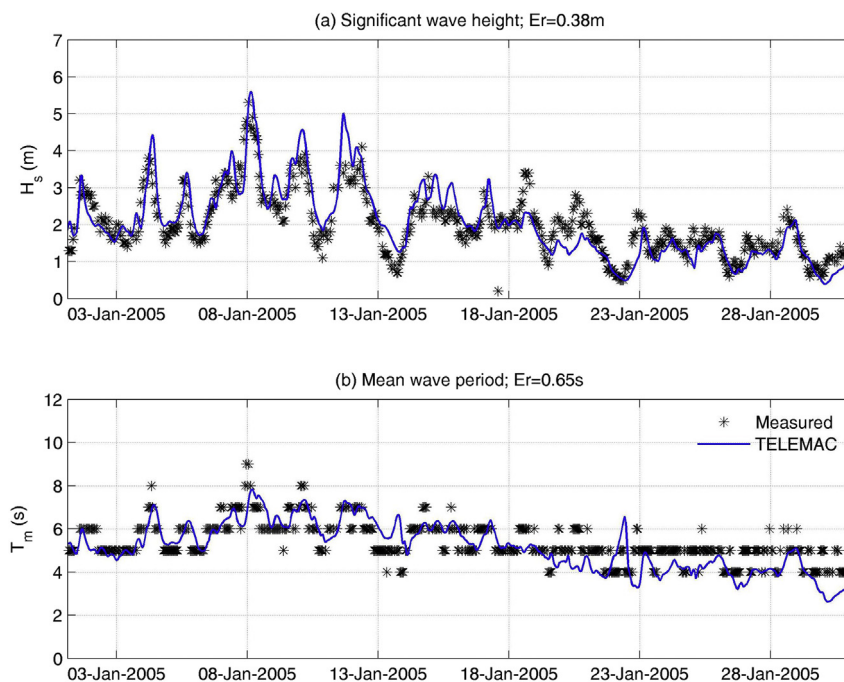
Fig. 6. Comparison of high resolution TOMAWAC results with observed data at M2 wave buoy (See Fig. 1a) during January 2005. The observed mean wave periods have a resolution of 1 s, while model results show more temporal fluctuations.
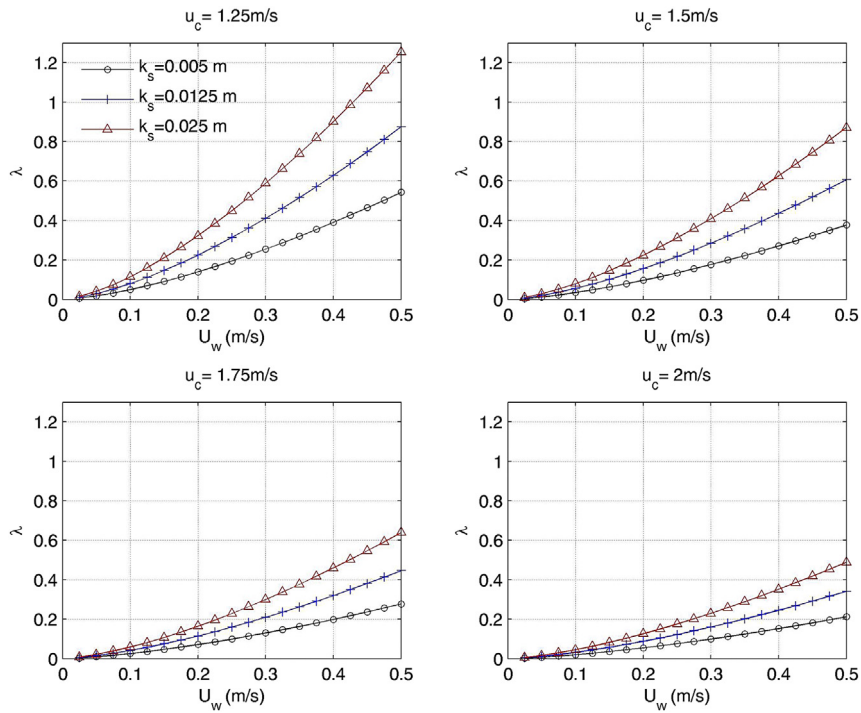
Fig. 7. Ratio of the pure wave to the pure current stresses (λ) for different wave and current conditions.

are automatically computed and fed back to the hydrodynamic model [41]. Further, although the effect of wave induced bed shear stresses are incorporated in the sediment transport module [42], the enhanced bottom friction due to WCI is not included in the hydrodynamic model (i.e. TELEMAC2D) formulations [41]. However, it is possible in the TELEMAC modelling system to modify the subroutines associated with bottom friction and include this process according to the wave parameters (Section 2.5.2).

2.5.1. Wave radiation stresses

Wave radiation stresses are the excess flow of momentum due to the presence of waves [43]. The wave induced forces are computed based on the gradient of the wave radiation stresses as follows [44],

$$F_x = -\left(\frac{\partial S_{xx}}{\partial x} + \frac{\partial S_{xy}}{\partial y}\right); \quad F_y = -\left(\frac{\partial S_{yy}}{\partial y} + \frac{\partial S_{yx}}{\partial x}\right) \tag{6}$$
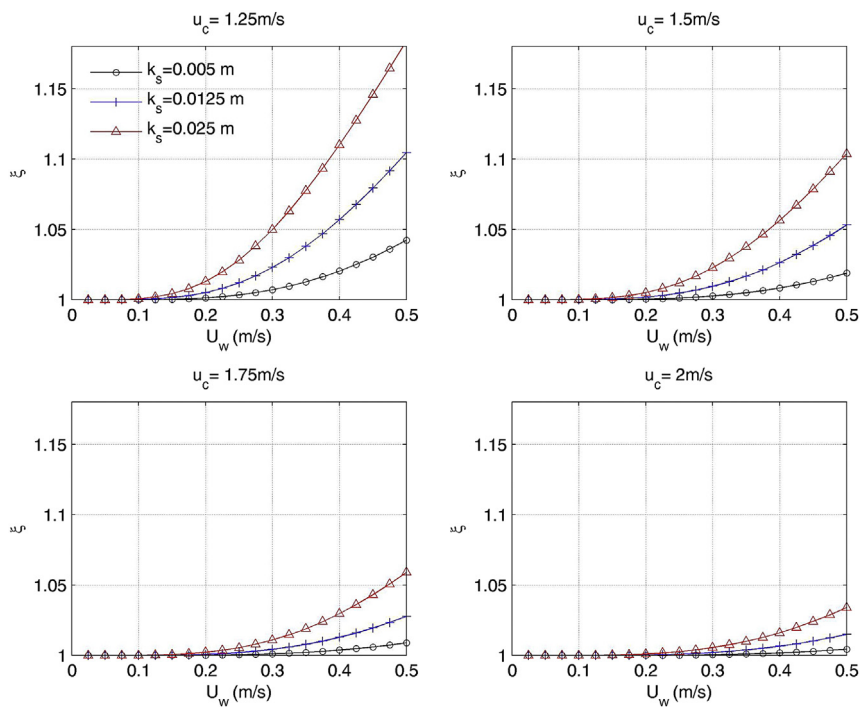
Fig. 8. Enhancement of the bottom drag coefficient due to WCI for a range of tidal currents. ξ is the ratio of the enhanced drag coefficient to the 'pure current' drag coefficient.

where F represents the wave force per unit surface area, and the wave radiation stresses (i.e., S_{ij}) have been defined in Table 1. By analogy, pressure forces are another form of body force, which are stresses generated by the gradient of the water pressure (i.e., $\partial p / \partial x = \rho g \partial h / \partial x$). In general, wave forces are dominant in the near-shore zone, where the gradients of the radiation stresses are high, and can explain wave set-up and longshore currents. In addition, they can potentially change the current velocity in a tidal stream site, especially if there is a dominant wave climate, and this can consequently affect the tidal energy resource.

2.5.2. Enhanced bottom friction

The interaction of waves with the current boundary layer leads to near-bed turbulence, and consequently the bed shear stress. This effect can reduce tidal currents, and since tidal power is proportional to velocity cubed, it can potentially decrease the tidal energy resource at a site. For instance, Wolf and Prandle [13], observed that the amplitudes of tidal currents reduce due to WCI. The WCI effect on the bottom boundary layer has been extensively studied in previous research (e.g. see Refs. [15,14,45,46]). Here, we investigate the sensitivity of bottom friction to this effect, and its implications in tidal energy resource assessment.

In general, ocean hydrodynamic models, like TELEMAC, have several options available to quantify bottom friction [32,47]. Therefore, to empirically account for enhanced friction due to WCI, the bed roughness length corresponding to the Nikuradse law of friction, the bottom drag coefficient corresponding to quadratic friction law, or Chezy coefficient corresponding to the Chezy law, can be modified. For instance, Van Rijn [45] introduced the following relation to enhance the bed roughness in the presence of waves.

$$k_a = k_s \exp\left(\gamma \frac{U_w}{u_c}\right) < 10, \quad \gamma = 0.80 + \varphi - 0.3\varphi^2 \tag{7}$$

where k_a and k_s represent the apparent and physical roughness, respectively; φ is the angle between wave direction and current direction in radians. In practice, the apparent bed roughness due to WCI can be an order of magnitude greater than the physical bed roughness. Alternatively, we applied the concept of mean (over the wave period) drag coefficient due to combined waves and current to increase bottom friction in the present research. The mean bed shear stress due to the combined action of waves and currents is given by Refs. [46,3],

$$\tau_m = \tau_c \left[1 + 1.2 \left(\frac{\tau_w}{\tau_c + \tau_w}\right)^{3.2}\right] \tag{8}$$

where τ_c and τ_w are bed shear stresses due to current alone or wave alone, respectively. The bed shear stresses are related to depth averaged current velocity through the drag coefficient,

$$\tau_c = \rho C_D u_c^2, \quad \tau_m = \rho C_D^* u_c^2 \tag{9}$$

where C_D and C_D^* are the drag coefficients in the absence and presence of waves, respectively; therefore, Eq. (8) can be written as,

$$\xi = \frac{C_D^*}{C_D} = \left[1 + 1.2 \left(\frac{\lambda}{1 + \lambda}\right)^{3.2}\right] < 2.2, \quad \lambda = \frac{\tau_w}{\tau_c} \tag{10}$$

Eq. (10) gives the ratio of the combined wave−current drag coefficient to the pure current drag coefficient (i.e. ξ) as a function of the ratio of the wave induced shear stress to the current induced bed shear stress (i.e. λ). The wave induced bed shear stress is a function of the bottom wave orbital velocities (U_w), and can be

computed using the wave parameters output from a wave model as follows [3],

$$\tau_w = \frac{1}{2} f_w U_w^2, \quad f_w = 0.237 \left(\frac{A}{k_s}\right)^{-0.52} \tag{11}$$

where f_w is the wave friction factor, k_s is Nikuradse bed roughness, and A is the semi orbital wave excursion (see Table 1). Given the dominant wave climate of a region, Eq. (10) (or alternatively Eq. (7)) can be implemented as a simple procedure to assess the effect of waves on the tidal energy resource in terms of enhanced bottom friction. Although more complex and computationally expensive methods are available in 3-D coupled wave-tide models like COAWST (Coupled Ocean Atmosphere Wave Sediment Transport [9,48]), we used this method which is more convenient and significantly less expensive. It is worth mentioning that other friction factors like the Chezy coefficient can be modified using ξ. Since $C = g/C_D^2$, the modified Chezy coefficient will be: $C^* = C/\sqrt{\xi}$.

Figs. 7 and 8 show the enhancement of the bottom drag coefficient due to WCI as a function of the wave induced orbital velocity for several wave and current scenarios. The sensitivity analysis has been carried out for the usual operational condition of a tidal stream site with currents of greater than 1.0 m/s (lower cut-in speed of TECs). In terms of the bed friction, k_s values of 0.005, 0.0125, and 0.025 correspond to seabed sediment grain sizes of 2 mm, 5 mm, and 10 mm, respectively (assuming $k_s = 2.5 d_{50}$), values that are typically observed at high energy sites [25].
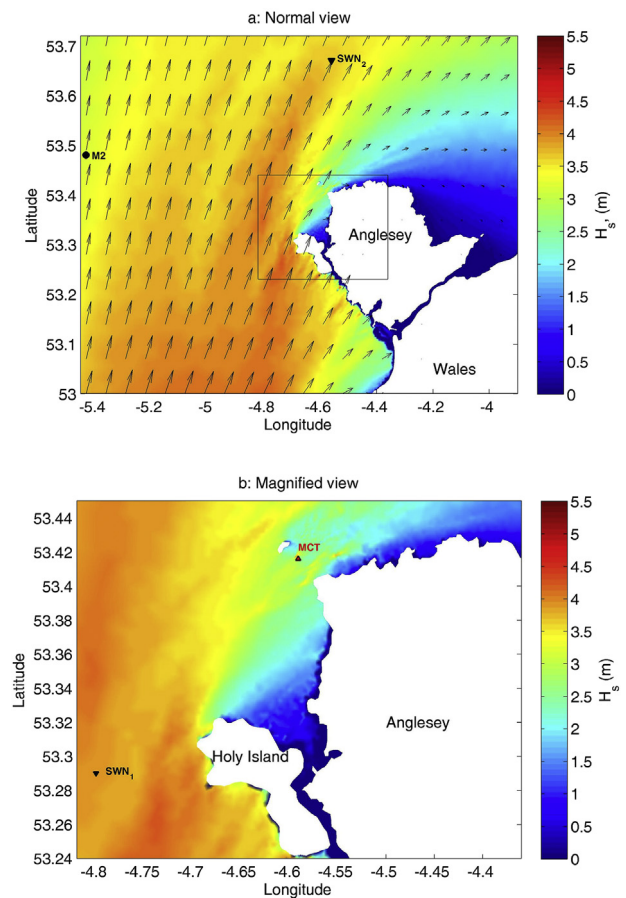

Fig. 9. Spatial distribution of the significant wave height (H_s) for a hypothetical scenario of a southwesterly 15 m/s wind. The colour scales are H_s in m. (For interpretation of the references to colour in this figure legend, the reader is referred to the web version of this article.)

The wave orbital velocity, estimated near the bed, which is the basis for the above computations can be directly output from a wave model like TOMAWAC. Alternatively, it can be parameterised using the surface wave parameters [49,50] or approximated by linear wave theory.

$$U_w = \frac{\pi H_s}{T_w \sinh(kh)} \quad (12)$$

where the wave number, k is computed using the linear dispersion equation ($\sigma^2 = gk\tanh kh$). In the absence of coupled wave-tide models, the above equation (or similar procedures) along with Fig. 8 give a quick estimate of the enhanced bottom friction, which then can be used to approximately compute the effect of WCI on the tidal energy.

3. Results

Based on the wave statistics of the site (Section 2.3), the TOM-AWAC model was forced with different southwesterly wind scenarios in stationary mode; wind speeds of 10 m/s and 15 m/s were selected to capture mean and extreme wave scenarios, respectively. To simulate the effect of waves on tidal currents, TELEMAC was run in fully coupled mode, where two-way feedbacks between the wave and the tide models were implemented.

3.1. Effect of wave forces on tidal energy

The spatial distribution of significant wave height for the extreme wave scenario is plotted in Fig. 9, which indicates a wave height of about 4 m at SWN$_1$. Further, Holy Island has a significant effect on the wave distribution over the NW part of Anglesey, including the Skerries site, for this scenario. The validated TOMAWAC wave model was then used to study the effect of WCI as an element of the coupled wave-tide model of the region. Fig. 10 shows the computed wave radiation stresses, and the corresponding wave forces for two typical wave scenarios. As this figure shows, apart from nearshore zones, the wave forces are also significant in the Skerries tidal stream site, particularly for the extreme wave scenario. Referring to Eq. (6), the gradient of the wave radiation stresses in this area generates the wave forces. Since wave radiation stresses are proportional to wave energy (see Table 1), the spatial change (i.e. gradient) in the wave height distribution leads to the generation of wave induced forces. Referring to Figs. 9 and 10, as a complex result of changes in the bathymetry and coastline, and Holy Island acting as an obstacle in the wave field, the wave height distribution, and consequently wave radiation stresses have a significant gradient around the Skerries. Fig. 11 shows the mean effect of these forces on tidal energy (in percent) over a tidal cycle. Considering the percentages of the impacts, the wave forces have slightly
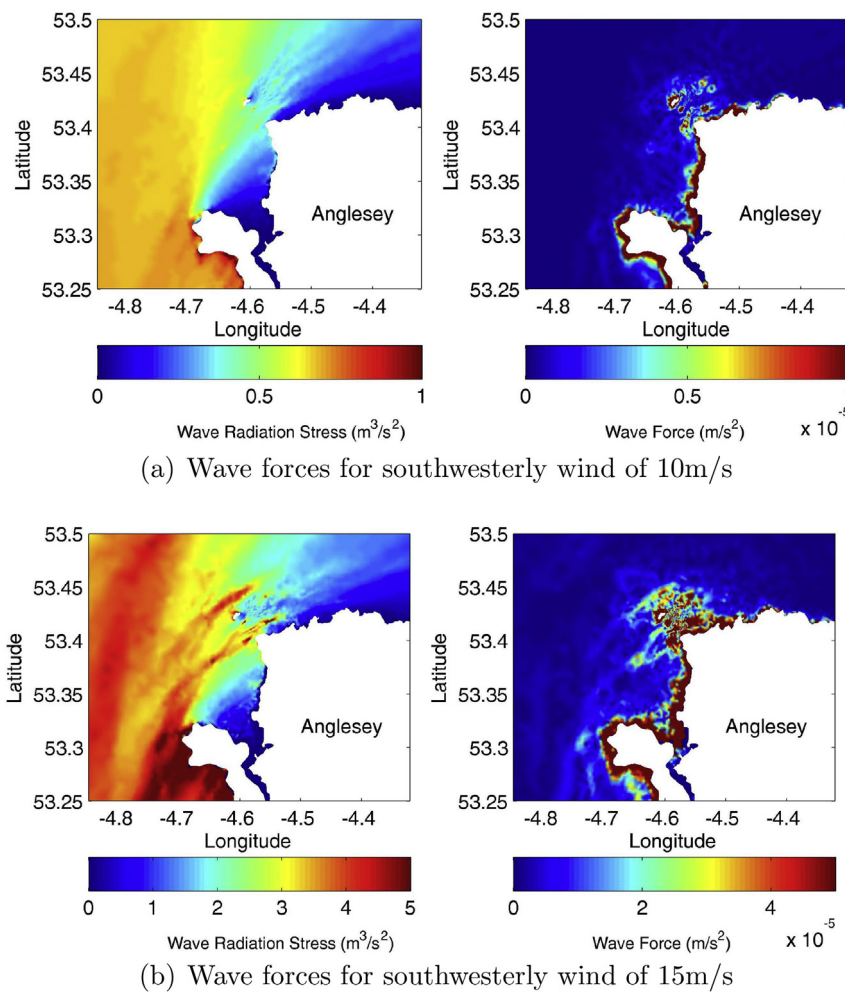

(a) Wave forces for southwesterly wind of 10m/s

(b) Wave forces for southwesterly wind of 15m/s

Fig. 10. Wave radiation stresses and wave forces (i.e. $F = \sqrt{F_x^2 + F_y^2}$) for two wind scenarios around the Skerries tidal stream site. Wave forces, which are usually expressed in N/m^2, have been normalised by water density and water depth. The wave radiation stresses have been normalised by water density (consistent with the TOMAWAC model outputs).

modified the tidal energy for the average wave scenario (3%), while they have more significant impact for the extreme scenario (7%). Since it is the difference of coupled wave-tide model and decoupled tide model that has been plotted, the effect is an overall reduction of the tidal energy, on average. It is worth mentioning that for the above scenarios, the direction of the wave forces do not change during a tidal cycle, as opposed to tidal currents. Therefore, wave forces, on average, had more effects on opposing currents in contrast to following currents. Nevertheless, the presence of wave forces leads to a new hydrodynamic current field which, in general, is spatially and temporally different from that produced in the absence of waves. Considering the tidal asymmetry of the site [12], further research is needed to study the implication of this asymmetry for tidal energy and sediment transport [51].

3.2. Effect of enhanced bottom friction on tidal energy

To implement the method described in Section 2.5.2, the orbital velocities, and other wave parameters, were computed for the two wave scenarios using TOMAWAC, and used to modify the bottom friction coefficient. The modified bottom friction coefficients were then fed back into the tidal model. This step can either be implemented with a separate code as in this research, or included in the subroutines of TELEMAC. Fig. 12 shows the near-bed wave orbital

velocities for the two wave scenarios. As this figure shows, the wave orbital velocities are about 0.30 m/s and 0.08 m/s for the two scenarios, which is equivalent to about a 5% and 1% increase in the bed friction enhancement factor (ξ), respectively (Fig. 8), or lower depending on the current speed and bed roughness. After computing the tidal power based on the modified friction, the effect as a percentage has been plotted in Fig. 13 which is, like the effect of wave forces, significant (6%) for the extreme wave case and very small (2%) for the average wave scenario. Since the effect is always negative (reduction in power), the absolute value has been plotted in this figure.

3.3. Combined effects

In the case of a fully coupled simulation, where wave radiation stresses and enhanced bottom friction are both incorporated in the tidal modelling, the impact of WCI is magnified due to the nonlinear nature of these processes. In other words, due to nonlinearity in the friction and wave induced force terms in the momentum equations, these effects are not simply superimposed. Fig. 14 shows the average effect of both processes on tidal power. As a consequence of WCI, tidal power can decrease by up to 20% and 15%, respectively, for the extreme and average scenarios, which represents a significant effect on the tidal stream resource.
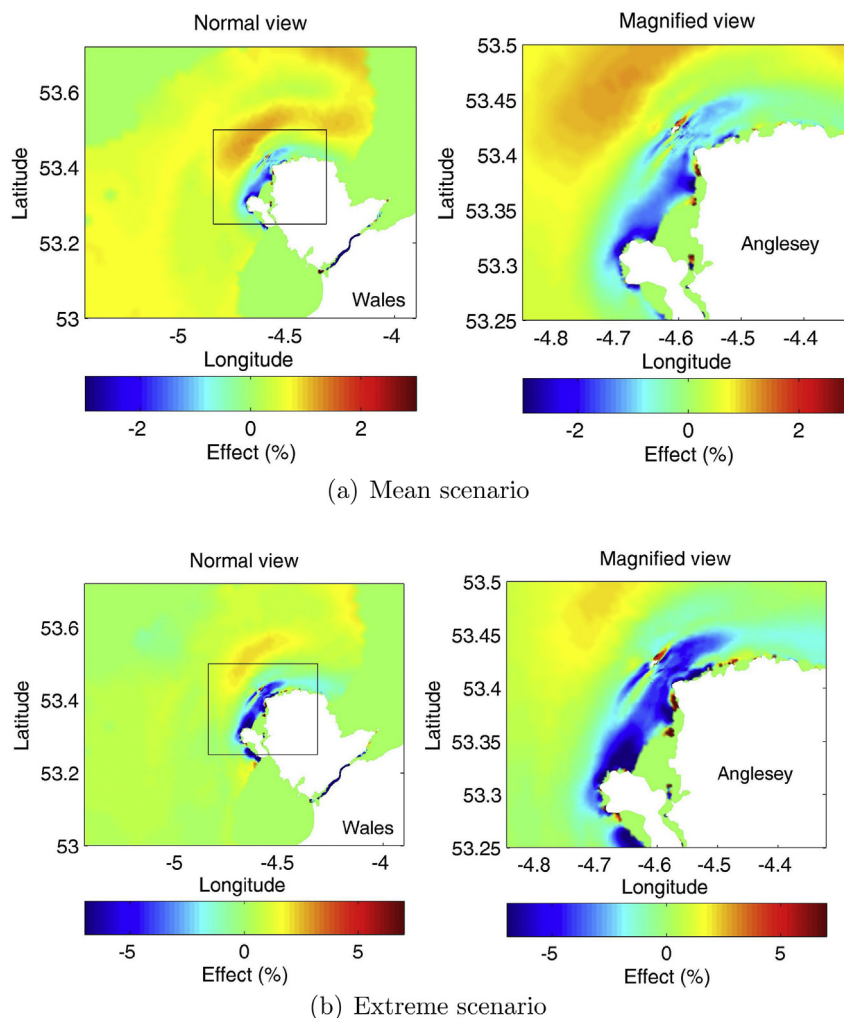

(a) Mean scenario

(b) Extreme scenario

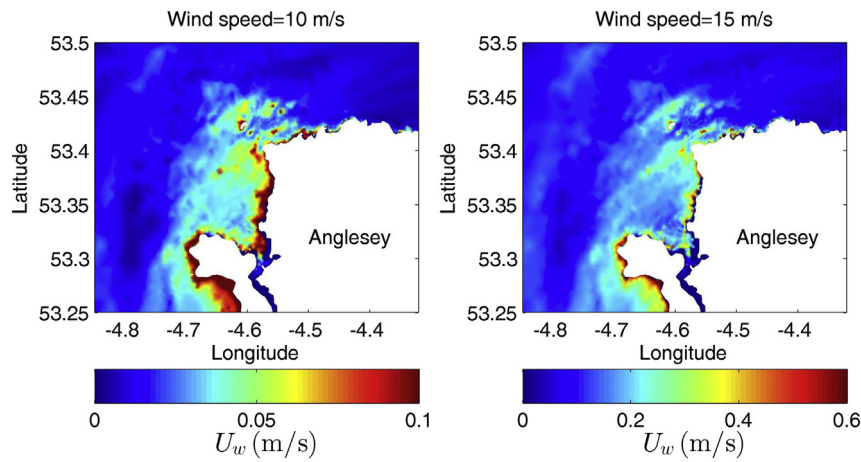**Fig. 11.** Effect of wave forces on the tidal stream power for two scenarios.

Fig. 12. Wave orbital velocities, U_w (m/s), around the Skerries tidal stream site, assuming two different wave scenarios.

4. Discussion

Another process of interest is wind-driven currents. The effect of wind generated currents can be added to wave effects by including wind shear stresses in the hydrodynamic model (TELEMAC-2D). Fig. 15 shows the results of superimposing the effect of wind generated currents on wave effects for the extreme scenario. As this figure shows, overall, the magnitude of the impact on the tidal energy resource does not change considerably — compared with Fig. 14 — while the distribution changes (reduction) in the vicinity of the tidal-stream site. The depth of penetration of wind generated currents in relation to hub heights of tidal energy devices is another topic of interest, which can be studied using 3-D models. This process can be examined in more detail in future studies. The results are generally in agreement with previous 3-D model studies at tidal energy sites 5.

The Skerries project is likely to be one of the first tidal stream arrays installed in UK waters. The wave climate of this region is moderate, so not as extreme as at other potential tidal stream sites such as NW Scotland, or the west coast of Ireland [38], both coastlines that are directly exposed to North Atlantic waves. Due to the highly non-linear nature of WCI effects, separate studies should be undertaken for other sites, but this research has attempted to provide a simple methodology for a popular hydrodynamic model (TELEMAC) which is used in research, and by developers, for tidal energy studies. It is expected that the effect of WCI processes will be much larger at more exposed tidal stream sites of the NW European shelf seas, but site specific modelling and analysis are required to confirm this and quantify these effects.

Moreover, to protect turbines from extreme wave loads, tidal-stream devices do not operate in extreme wave conditions. Therefore, the effect of waves on the practical tidal energy resource of a region may be unimportant for the extreme scenarios; nevertheless, the effect is still considerable for the average wave scenario, when tidal energy devices still operate. Due to various limitations such as the interactions of tidal devices at array scale, the available extractable tidal energy at a site is usually less than the theoretical tidal energy considered here [52]. The impact of wave-tide interaction on the practical extractable energy resource depends on specific devices and array configurations, and can be investigated as another step. Further, the sensitivity of the tidal resources of a region to bottom friction decreases as a result of substantial drag from a large tidal array [7]. This may reduce the effect of enhanced bottom friction due to waves. The interaction of waves and tidal currents has implications in design, efficiency, and loading of tidal energy devices which is the subject of other research (e.g. Refs. [53–55]).

The analysis which was accomplished in this research was based on depth-averaged quantities. The effect of various WCI processes
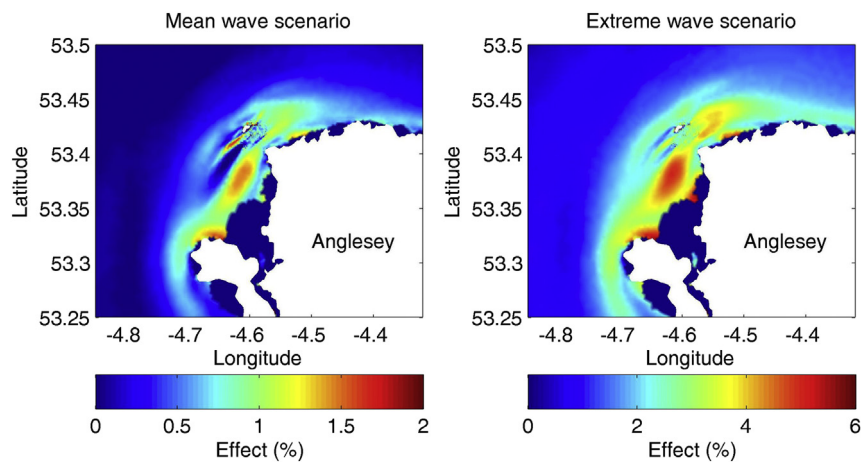

Fig. 13. Effect of enhanced bottom friction due to WCI on tidal stream energy around the Anglesey Skerries site, for two different wave scenarios.
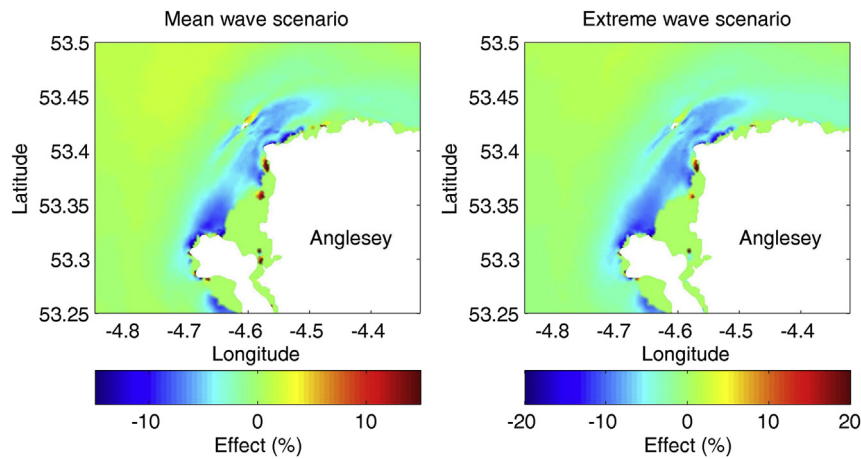
Fig. 14. Combined effect of the enhanced bottom friction (due to WCI) and wave radiation stresses on the tidal stream energy around the Anglesey Skerries site, for two different wave scenarios (15 m/s as the extreme and 10 m/s as the mean scenario).

varies throughout the water column, and given the hub-height of a particular TEC device, it will be useful to assess the vertical variability of these effects using 3-D models [9]. For instance, there is a debate over using depth-averaged radiation-stress gradient as a depth-uniform body force in ocean models [56]. The depth-dependent form of horizontal radiation stress gradient terms has also been proposed [57] and applied in 3-D models [48]. Other aspects such as tidal asymmetry and turbulence can be also addressed in future research [5].

Finally, although Eqs (7) and (8) are based on extensive observations made in previous studies, and it is current practice in ocean models to use similar relations to include wave–current interaction processes, the simultaneous measurement of tidal currents and waves at proposed tidal stream arrays can provide more insight into WCI related issues. Traditionally, deployment of wave buoys in regions of strong tidal currents is more challenging, and so wave data tends to be sparse in such regions. Referring to

Eq. (5), it is easy to show that $\delta P/P \propto 3 \times \delta u_c/u_c$, where δ is the variation.[1] Therefore, to observe a 6% change in power, one should be able to detect 2% change in the current measurement, which is likely to be about the order of magnitude of the measurement errors.

5. Conclusions

The effect of WCI processes on the tidal energy resource at the proposed Skerries tidal stream array has been investigated for mean and extreme wave scenarios. In terms of wave radiation stresses, it was shown that both wave forces, and their effect on the tidal energy resource, are significant for the extreme wave scenario, and can reach 7%. A simplified method developed here, which was presented to include the effect of WCI on bottom friction, can be used to assess the sensitivity of the tidal currents and tidal power to these processes, based on the wave climate of a region.

As a result of the combined effects of wave radiation stresses and enhanced bottom friction, the tidal energy resource can be reduced by up to 15% and 20% for mean and extreme winter wave scenarios, respectively, at the Skerries tidal stream site. The impact of these two processes is magnified when they are considered together, rather than separately, due to the nonlinear nature of the forces. For more exposed sites, e.g. NW of Scotland, the impact is expected to be greater. Also, wind generated currents change the distribution of this effect in the vicinity of the tidal-stream site.

The effect of WCI processes on tidal energy increases as the ratio of wave stress to current stress increases. Therefore, this effect is more significant for lower tidal energy sites which are exposed to strong waves, rather than higher tidal energy sites which are exposed to moderate waves.

Simultaneous measurement of waves and tidal currents at potential tidal stream sites is necessary to further investigate the impact of waves on various aspects of tidal energy development. However, it should be stressed that very high accuracy measurements would be required due to relatively small values of WCI processes compared with main parameters of the flow. Nevertheless, the effect of these processes can become significant with respect to other parameters like tidal energy or sediment transport.
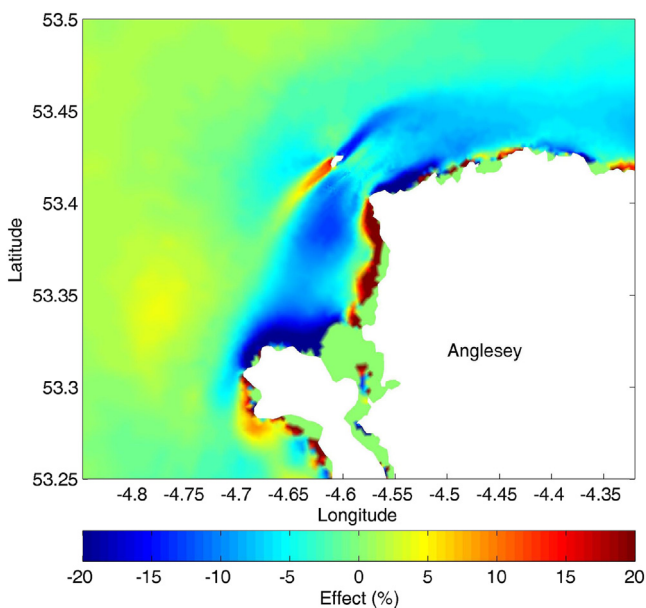

Fig. 15. Combined effect of the enhanced bottom friction (due to WCI), wave radiation stresses, and wind-generated currents on tidal stream power assuming a southwesterly wind of 15 m/s.

---

[1] $P \propto |u_c|^3$, therefore $\delta P \propto 3|u_c|^2 \delta u_c = 3|u_c|^3 \delta u_c/|u_c|$, which leads to $\delta P \propto 3P\delta u_c/|u_c|$.

Acknowledgements

References

[1] Hashemi MR, Neill SP. The role of tides in shelf-scale simulations of the wave energy resource. Renew Energy 2014;69:300–10.

[2] Galloway PW, Myers LE, Bahaj AS. Quantifying wave and yaw effects on a scale tidal stream turbine. Renew Energy 2014;63:297–307.

[3] Soulsby R. Dynamics of marine sands: a manual for practical applications. Thomas Telford; 1997.

[4] Simpson JH, Sharples J. Introduction to the physical and biological oceanography of shelf seas. Cambridge University Press; 2012.

[5] Neill SP, Hashemi MR, Lewis MJ. The role of tidal asymmetry in characterizing the tidal energy resource of Orkney. Renew Energy 2014;68:337–50.

[6] Saruwatari A, Ingram DM, Cradden L. Wave–current interaction effects on marine energy converters. Ocean Eng 2013;73:106–18.

[7] Adcock TAA, Draper S, Houlsby GT, Borthwick AGL, Serhadlıoğlu S. The available power from tidal stream turbines in the pentland firth. Proc R Soc A: Math Phys Eng Sci 2013;469(2157):20130072.

[8] Barbariol F, Benetazzo A, Carniel S, Sclavo M. Improving the assessment of wave energy resources by means of coupled wave-ocean numerical modeling. Renew Energy 2013;60:462–71.

[9] Lewis M, Neill SP, Hashemi MR. Realistic wave conditions and their influence on quantifying the tidal stream energy resource. Appl Energy 2014;136: 495–508.

[10] ABPmer. Atlas of UK marine renewable energy resources. Tech. Rep. Department for Business Enterprise & Regulatory Reform; 2008

[11] Blunden LS, Bahaj AS. Initial evaluation of tidal stream energy resources at Portland Bill, UK. Renew Energy 2006;31(2):121–32.

[12] Serhadlıoğlu S, Adcock TAA, Houlsby GT, Draper S, Borthwick AGL. Tidal stream energy resource assessment of the Anglesey Skerries. Int J Mar Energy 2013;3:e98–111.

[13] Wolf J, Prandle D. Some observations of wave–current interaction. Coast Eng 1999;37(3):471–85.

[14] Soulsby RL, Hamm L, Klopman G, Myrhaug D, Simons RR, Thomas GP. Wave-current interaction within and outside the bottom boundary layer. Coast Eng 1993;21(1):41–69.

[15] Davies AG, Soulsby RL, King HL. A numerical model of the combined wave and current bottom boundary layer. J Geophys Res Oceans (1978–2012) 1988;93(C1):491–508.

[16] Prandle D. The influence of bed friction and vertical eddy viscosity on tidal propagation. Cont Shelf Res 1997;17(11):1367–74.

[17] Couch SJ, Bryden I. Tidal current energy extraction: hydrodynamic resource characteristics. Proc Inst Mech Eng Part M: J Eng Marit Environ 2006;220: 185–94.

[18] Newberger P, Allen JS. Forcing a three-dimensional, hydrostatic, primitive-equation model for application in the surf zone: 1. formulation. J Geophys Res Oceans 2007;112(C8).

[19] Warner JC, Armstrong B, He R, Zambon JB. Development of a coupled ocean–atmosphere–wave–sediment transport (COAWST) modeling system. Ocean Model 2010;35(3):230–44.

[20] Wolf J. Coastal flooding: impacts of coupled wave–surge–tide models. Nat Hazards 2009;49(2):241–60.

[21] Hashemi MR, Neill SP, Davies AG. A coupled wave-tide model for NW European shelf seas. Geophys Astrophys fluid Dyn 2014. http://dx.doi.org/10.1080/03091929.2014.944909. In press.

[22] Bolanos-Sanchez R, Wolf J, Brown J, Osuna P, Monbaliu J, Sanchez-Arcilla A. Comparison of wave-current interaction formulation using polcoms-wam wave-current model. 2009.

[23] Bolanos R, Osuna P, Wolf J, Monbaliu J, Sanchez-Arcilla A. Development of the POLCOMS–WAM current–wave model. Ocean Model 2011;36(1):102–15.

[24] Brown JM, Souza AJ, Wolf J. An 11-year validation of wave-surge modelling in the Irish Sea, using a nested POLCOMS–WAM modelling system. Ocean Model 2010;33(1):118–28.

[25] Robins PE, Lewis MJ, Neill SP. Impact of tidal-stream arrays in relation to the natural variability of sedimentary processes. Renew Energy 2014;72:311–21.

[26] Burrows R, Walkington I, Yates N, Hedges T, Wolf J, Holt J. The tidal range energy potential of the west coast of the United Kingdom. Appl Ocean Res 2009;31(4):229–38.

[27] Hashemi M, Neill S, Davies A. A numerical study of wave and current fields around Ramsey island tidal energy resource assessment. In: XIXth TELEMAC-MASCARET User Conference. Oxford, United Kingdom; 2012.

[28] Villaret C, Hervouet JM, Kopmann R, Merkel U, Davies AG. Morphodynamic modeling using the Telemac finite-element system. Comput Geosci 2013;53: 105–13.

[29] Brown JM, Davies AG. Methods for medium-term prediction of the net sediment transport by waves and currents in complex coastal regions. Cont Shelf Res 2009;29(11):1502–14.

[30] Davies AM, Gerritsen H. An intercomparison of three-dimensional tidal hydrodynamic models of the Irish Sea. Tellus 1994;46(2):200–21.

[31] Walkington I, Burrows R. Modelling tidal stream power potential. Appl Ocean Res 2009;31(4):239–45.

[32] Hervouet JM. TELEMAC modelling system: an overview. Hydrol Process 2000;14(13):2209–10.

[33] Hervouet JM. Hydrodynamics of free surface flows: modelling with the finite element method. John Wiley & Sons; 2007.

[34] Benoit M, Marcos F, Becq F. Development of a third generation shallow-water wave model with unstructured spatial meshing. Coast Eng Proc 1996;25.

[35] Booij N, Ris R, Holthuijsen LH. A third-generation wave model for coastal regions: 1. Model description and validation. J Geophys Res Oceans 1999;104(C4):7649–66.

[36] Uehara K, Scourse JD, Horsburgh KJ, Lambeck K, Purcell AP. Tidal evolution of the northwest European shelf seas from the last glacial maximum to the present. J Geophys Res Oceans 2006;111(C9).

[37] Lyard F, Lefevre F, Letellier T, Francis O. Modelling the global ocean tides: modern insights from FES2004. Ocean Dyn 2006;56(5–6):394–415.

[38] Neill SP, Hashemi MR. Wave power variability over the northwest European shelf seas. Appl Energy 2013;106:31–46.

[39] Rusu E, Gonçalves M, Guedes Soares C. Evaluation of the wave transformation in an open bay with two spectral models. Ocean Eng 2011;38(16):1763–81.

[40] Stansby PK. Limitations of depth-averaged modeling for shallow wakes. J Hydraulic Eng 2006;132(7):737–40.

[41] Lang P. Telemac-2d user's manual. Tech. Rep. EDF R & D; 2013

[42] Tassi P, Villaret C. Sisyphe v6.3 user's manual. Tech. Rep. EDF R & D; 2014

[43] Longuet-Higgins MS, Stewart R. Radiation stresses in water waves; a physical discussion, with applications. Deep Sea Res Oceanogr Abstr 1964;11:529–62.

[44] Mei CC. The applied dynamics of ocean surface waves. World Sci 1989;1.

[45] Van Rijn LC. Unified view of sediment transport by currents and waves. I: initiation of motion, bed roughness, and bed-load transport. J Hydraulic Eng 2007;133(6):649–67.

[46] Soulsby R, Clarke S. Bed shear-stresses under combined waves and currents on smooth and rough beds. HR Wallingford; 2005. Report TR137.

[47] Shchepetkin AF, McWilliams JC. The regional oceanic modeling system (roms): a split-explicit, free-surface, topography-following-coordinate oceanic model. Ocean Model 2005;9(4):347–404.

[48] Warner JC, Sherwood CR, Signell RP, Harris CK, Arango HG. Development of a three-dimensional, regional, coupled wave, current, and sediment-transport model. Comput Geosci 2008;34(10):1284–306.

[49] Wiberg PL, Sherwood CR. Calculating wave-generated bottom orbital velocities from surface-wave parameters. Comput Geosci 2008;34(10):1243–62.

[50] Soulsby R. Calculating bottom orbital velocity beneath waves. Coast Eng 1987;11(4):371–80.

[51] Neill SP, Jordan JR, Couch SJ. Impact of tidal energy converter (TEC) arrays on the dynamics of headland sand banks. Renew Energy 2012;37(1):387–97.

[52] Garrett C, Cummins P. The power potential of tidal currents in channels. Proc R Soc A: Math Phys Eng Sci 2005;461(2060):2563–72.

[53] Gaurier B, Davies P, Deuff A, Germain G. Flume tank characterization of marine current turbine blade behaviour under current and wave loading. Renew Energy 2013;59:1–12.

[54] Bahaj AS, Batten W, McCann G. Experimental verifications of numerical predictions for the hydrodynamic performance of horizontal axis marine current turbines. Renew Energy 2007;32(15):2479–90.

[55] Clarke JA, Connor G, Grant AD, Johnstone CM. Design and testing of a contra-rotating tidal current turbine. Proc Inst Mech Eng Part A: J Power Energy 2007;221(2):171–9.

[56] Uchiyama Y, McWilliams JC, Shchepetkin AF. Wave–current interaction in an oceanic circulation model with a vortex-force formalism: application to the surf zone. Ocean Model 2010;34(1):16–35.

[57] Xia H, Xia Z, Zhu L. Vertical variation in radiation stress and wave-induced current. Coast Eng 2004;51(4):309–21.

.5 Published work P-IV

ELSEVIER

An enhanced depth-averaged tidal model for morphological studies in the presence of rotary currents

Simon P. Neill[a],[*], Mohammad R. Hashemi[b], Alan J. Elliott[a]

[a]*Centre for Applied Marine Sciences, University of Wales (Bangor), Marine Science Laboratories, Menai Bridge, LL59 5AB, UK*
[b]*Department of Water Engineering, Shiraz University, Shiraz, Iran*

Abstract

A simple and efficient method to improve morphological predictions using depth-averaged tidal models is presented. The method includes the contribution of secondary flows in sediment transport using the computed flow field from a depth-averaged model. The method has been validated for a case study using the 3D POLCOMS model and ADCP data. The enhanced depth-averaged tidal model along with the SWAN wave model are applied to morphological prediction around the Lleyn Peninsula and Bardsey Island as a case study in the Irish Sea. Due to the presence of a headland in this area two asymmetrical tidal eddies are developed in which the cyclonic eddy is stronger as a result of Coriolis effects. The results show that the enhanced model can effectively predict formation of sand banks at the centre of cyclonic eddies, while the depth-averaged model, due to its inability to accommodate secondary flow, is inadequate in this respect.
© 2006 Elsevier Ltd. All rights reserved.

Keywords: Coastal morphology; Sand banks; Coriolis force; Rotary currents; Secondary flow; Irish Sea

1. Introduction

Tidal stirring of the seas in the region of headlands may concentrate sediments and result in the formation of tidal banks (Pingree, 1978). Headlands produce characteristic eddy patterns which are a result of vorticity transfer from the tide to the residual flow. This vorticity generation is a result of two separate mechanisms (Robinson, 1981): increased flow near the headland tip creates a proportionally larger frictional force inshore, while a shallower depth inshore results in greater depth-averaged friction. Both mechanisms create a similar sense of vorticity, hence leading to eddy formation. As a result of these eddies, bed material is either lifted into suspension or transported as bed load around the eddy during periods of high tidal stress (Pingree, 1978). This may take place gradually within each tidal cycle or suddenly under storm conditions. The eddies are expected to generate secondary flows, with convergence towards the centre of the eddies at the bed and divergence at the surface. For curved shallow water flow, the circular motion of the eddy is maintained by an inward pressure gradient matching the centripetal force, and this pressure gradient forces a flow towards the centre of the eddy near the bed, where friction reduces the strength of the centripetal force

*Corresponding author. Tel.: +44 1248 713808;
fax: +44 1248 716729.
E-mail address: s.p.neill@bangor.ac.uk (S.P. Neill).

(Dyer and Huntley, 1999). For smaller flow speeds or curvature, the Coriolis force becomes more important. The original location for sand bank formation is controlled hydrodynamically (Pattiaratchi and Collins, 1987), but as the sand bank grows in dimensions, interaction between the tidal currents and the sand bank enhances the eddy, hence encouraging further bank growth until a state of equilibrium is reached.

Morphological models can be divided into three main categories depending on the timescale of simulation (de Vriend et al., 1993). Initial sedimentation/erosion (ISE) models go through the sequence of constituent models (e.g. tidal, wave, sediment transport and morphological) only once, hence the assumption is made that the bed topography is invariant for all models other than the final morphological model (i.e. no feedback mechanism exists between the evolving bedform and the hydrodynamics). The other two classes of model, where modelled bed evolution affects the hydrodynamics are medium-term morphodynamic models and long-term morphodynamic models, suitable for weekly and yearly time scales, respectively. In this paper, an ISE model is developed since the time scales studied are of order 1–2 days (i.e. a single storm event), therefore the expected change in bed level due to sediment transport during a storm will have a negligible effect on the hydrodynamics. It is calculated (in this paper) that the maximum change in bed level during a 48 h period (including a storm) is of order 0.1 m in water of depth 30 m. Assuming that depth changes of 10% have a significant effect on the hydrodynamics (Soulsby, 1997), a conservative estimate of timescales when an ISE model is no longer applicable in the chosen study area is of order 60 days. ISE models are generally considered to be diagnostic tools for morphological process analysis and not quantitative predictors of morphological evolution. In the current work, the aim is not to make accurate quantitative predictions of changing bedforms, but to examine the suitability of a method which includes secondary flow characteristics in 2D models, hence an ISE model is sufficient for the study.

With an increasing trend in computational power, there is a general shift occurring in morphological prediction from the use of 2D to 3D hydrodynamic simulations. However, it is not always necessary to make use of the vertical resolution in morphological models. In one example of the sedimentation of a breakwater, Lesser et al. (2004) obtained approximately the same results using a 3D morphological model as did Nicholson et al. (1997) using a simpler 2D model. Additionally, 3D models include complex 3D effects automatically, i.e. they do not necessarily increase understanding of a morphological situation. The additional computing power available may be of more use in many situations in improving the horizontal rather than the vertical resolution.

One of the advantages of 3D morphological models over 2D morphological models is that they include complex effects "by default". This can be a major issue in 2D sediment transport models of river meanders. In the real case, a helical secondary flow is induced by the flow curvature which leads to a bed load transport of material towards the inner bank of the meander. Erosion occurs on the outer banks and deposition occurs on the inner bank (Kikkawa et al., 1976). 3D models account for this effect by solving the vertical profile of secondary velocity in the river cross-section. 2D models, however, must be modified to account for this secondary effect (e.g. Struiksma et al., 1985). Assuming that bed load transport (compared to suspended load transport) has a major contribution to bed level change, a simplified method to be applied to 2D sediment transport models need only solve the near-bed contribution of secondary flow. The transport direction can then be calculated as the resultant of the main flow direction and this secondary flow direction. Such a method has been developed by several authors to study river meanders based on flow curvature and water depth (Kikkawa et al., 1976; Engelund, 1976). Attempts have been made to quantify the secondary flow velocity in tidal flows around headlands (Geyer, 1993; Alaee et al., 2004) using theoretical curves for secondary flow based on Kalkwijk and Booij (1986). Some authors have attempted to apply this simplified method to calculate the consequences for sand transport (and morphological change) due to secondary flow (e.g. Wang et al., 1995). However, as far as the authors of the present paper are aware, no-one has attempted to apply these methods to the evolution of sand banks which are generated by rotary currents (e.g. headland eddies). This paper attempts to address the latter issue.

A morphological model is described in Section 2, consisting of a tidal model, wave model, sediment transport model and bed level change model. In Section 3, the method for determining the secondary

flow based on flow curvature and other 2D flow field variables is discussed. The method is also verified using a three-dimensional model and ADCP data. In Section 4, the method is applied to a 2D modelling case study of a headland/island system in the Irish Sea. Finally, a discussion on the validity of the results and further justification of the method are given in Section 5.

2. Development of morphological model

The morphological model consists of an interaction between several different models: a tidal model for prediction of tidal currents, wind-generated currents and wind surge, a wave model for prediction of wave orbital velocity, a model to predict total sediment transport under the action of currents and waves, and finally a bed level change model to predict the morphological change. In this paper, 2D depth-averaged tidal modelling is considered for morphological studies although a 3D tidal model of the study area is developed for verification of the proposed method.

2.1. Hydrodynamic models

POLCOMS is the Proudman Oceanographic Laboratory Coastal Ocean Modelling System (Holt and James, 2001). POLCOMS is three-dimensional (using σ coordinates in the vertical) and is formulated in spherical coordinates. For turbulence closure, the Mellor–Yamada–Galperin level 2.5 scheme is used (Mellor and Yamada, 1974; Galperin et al., 1988). The model can also be run in depth-averaged mode, hence it is possible to examine both 2D and 3D current fields. Boundary conditions required for POLCOMS are elevation and the normal component of velocity. These are obtained by running an outer coarse grid and extracting time series of the boundary points for the inner nested region. A harmonic analysis is calculated for each time series using T_TIDE (Pawlowicz et al., 2002) to create an independent high-resolution model with no feedback to the outer nest. To include storm surges and wind-generated currents in the model, all of the model grids were run with a normal stress (atmospheric pressure) and shear stress (wind speed and direction) using 3-hourly spatially varying data obtained from Met Éireann. These additional surge components were extracted as a time series for the boundary points of the inner nested region and added to the tidal component. This procedure was

repeated for all levels of nesting from the outer grid, through intermediate grids and finally to the inner nested region.

SWAN (Simulating WAves Nearshore) is an Eulerian formulation of the discrete wave action balance equation (Booij et al., 1999). The model is discrete spectral in frequencies and directions and the kinematic behaviour of waves (including the effect of currents) is described with the linear theory of gravity waves. The deep water physics of SWAN are taken from the WAM model (Komen et al., 1994). SWAN is run by applying data of wind speed and direction firstly on a coarse outer grid. Tidal currents and water level are included in the SWAN simulation, using output from the POLCOMS model. A series of inner nested grids is then used, with boundary conditions of spectral density transferred from the outer to inner grids. Significant wave height H_s and peak wave period T_p are output for each grid point of the inner-most model, and used to calculate the bottom orbital velocity using the method described by Soulsby (1987).

2.2. Total sediment transport under action of waves and currents

Numerous non-cohesive sediment transport models exist in the literature and these are often compared against each another (e.g. Davies and Villaret, 2002). In this study, sediment transport is calculated as a total load transport by waves plus currents using the Soulsby–Van Rijn formula. It is based on the model of Van Rijn (1989) with curve fitting over a range of wave and current conditions by Soulsby (1997). This formulation contains a large enhancement of transport rate due to wave action. The wave action has an important contribution to the suspended load when considering total transport. The formula is valid for non-cohesive sediments in the range 0.1–2.0 mm. Bed roughness is parameterised using sediment size. Total sediment transport rate is

$$q_t = A_s \overline{U} \left[\left(\overline{U}^2 + \frac{0.018}{C_D} U_{rms}^2 \right)^{1/2} - \overline{U}_{cr} \right]^{2.4}$$
$$\times (1 - 1.6 \tan \beta_b), \tag{1}$$

where $A_s = A_{sb} + A_{ss}$ and

$$A_{sb} = \frac{0.005h(d_{50}/h)^{1.2}}{[(s-1)gd_{50}]^{1.2}}, \tag{2}$$

$$A_{ss} = \frac{0.012 d_{50} D_*^{-0.6}}{[(s-1)g d_{50}]^{1.2}} \tag{3}$$

and

$$\overline{U}_{cr} = 0.19 (d_{50})^{0.1} \log \frac{4h}{d_{90}} \quad \text{for } 100 \leqslant d_{50} \leqslant 500 \, \mu\text{m}, \tag{4}$$

or

$$\overline{U}_{cr} = 8.50 (d_{50})^{0.6} \log \frac{4h}{d_{90}} \quad \text{for } 500 \leqslant d_{50} \leqslant 2000 \, \mu\text{m}, \tag{5}$$

where $\overline{U}$ is the depth-averaged current velocity, U_{rms} is the root-mean-square wave orbital velocity, C_D is the drag coefficient due to current alone, $\overline{U}_{cr}$ is the threshold current velocity, β_b is the bed slope, h is the water depth, s is the relative density of sediment and D_* is the dimensionless grain size. The Soulsby–Van Rijn formula produces a scalar quantity for sediment transport. It is assumed that the direction of sediment transport is determined by the tidal flow and not the wave direction. Although longshore transport can easily be included as a source term in the sediment transport model, it was neglected in this study to allow a focus on the effects of rotary currents in the region of sand banks.

The method of calculating the total sediment transport was implemented using the 2D tidal model and the wave model (Section 2.1). This provides a source term for the morphological model (Section 2.3), hence bed evolution due to tidal and wave effects can be studied.

2.3. Bed level change model

When considering long-term morphodynamics, it is important to include the interaction between the hydrodynamic and the morphodynamic components of the scheme (Nicholson et al., 1997). In this paper, the timescale is of order 48 h, hence this feedback has not been included. Generally, the results of two-dimensional morphological models are sufficient for practical applications, but three-dimensional models have the advantage that complex three-dimensional flow effects (despite a possible lack of understanding) can be automatically included in a simulation (Lesser et al., 2004). However, for this study the use of a 3D morphological model is not helpful since a method is sought to reduce the complexity (and similarly reduce computational time) of a three-dimensional problem to two dimensions.

Assuming that the sediment content of the water column does not change significantly over time, morphological development can be modelled in two-dimensions using (e.g. Van der Molen et al., 2004)

$$\frac{\partial z}{\partial t} = -\frac{1}{1-p} \left\{ \frac{\partial q_x}{\partial x} + \frac{\partial q_y}{\partial y} \right\}, \tag{6}$$

where z is the bed level, p is the bed porosity and q_i is the transport of sediment in the i direction. This equation, known as the Exner equation, was solved using the Lax–Friedrichs finite differencing scheme which has first order accuracy (Chung, 2003).

3. Secondary flow and enhanced 2D tidal model

3.1. Effect of rotary currents on morphodynamics

Secondary flow leads to an accumulation of tea leaves at the centre of a tea cup after stirring with a spoon. This tea cup phenomenon is described in several papers (e.g. Pingree, 1978) but is usually taken as an analogy for sediment dynamics in practical situations. Taking into consideration the curvature of a river meander rather than the curvature of a tea cup, this phenomenon has been applied to the movement of river sediments (Kikkawa et al., 1976). A more detailed theory of the secondary circulation due to flow curvature is explained in Section 3.2. However, for the purposes of this section it is sufficient to say that there is a surface divergence of suspended material and a convergence of bed material at the centre of an eddy. In the case of a river meander, this will lead to scour at the outer banks and deposition along the inner banks since the movement of bed load material is towards the centre of curvature. The same phenomenon exists in tidal flows, particularly in the case of eddies due to headlands and islands (an island can be considered as a headland with a line of symmetry). A headland eddy will cause material to gather at the centre of the eddy, the process being approximately symmetrical between flood and ebb, resulting in the formation of two sand banks. However, for increasing latitude headlands, the system becomes progressively less symmetrical until one of the residual eddies is considerably stronger than the other, hence material tends to be gathered preferentially in the region of one residual eddy and a single sand bank is

generated (Pingree, 1978). This is a result of the increasing importance of Coriolis force with latitude and its importance is indicated by the Rossby number. In Section 4, a case study is examined in which there is a single sand bank due to tidal asymmetry of a headland. Similar convergence of bed material due to secondary flow will exist in eddies created by tidal flow around groynes and harbours as another engineering application.

3.2. Earlier theories of secondary flow based on river hydraulics

The concept of secondary flow which causes a helical or spiral motion of water particles in curved current fields was first investigated for curved open channel flow (e.g. Van Bendegom, 1947) and is discussed in this section. As Fig. 1 shows, the secondary flow component occurs in a plane perpendicular to the main flow direction. Although the magnitude of secondary flow (as with main flow) is zero at the bed (no-slip), the maximum occurs slightly above the bed and so is important for bed load transport. After Falcón (1984), consider the Navier–Stokes equation in the radial direction for a curved steady flow field in a very simplified case

$$\frac{U_m^2}{gr} = \frac{\partial h}{\partial r} - \frac{1}{\rho g}\frac{\partial \tau_{zr}}{\partial z}, \tag{7}$$

where U_m is main current velocity, τ_{zr} is radial shear stress, ρ is the density of water and r is the radial coordinate. This equation has three basic terms: pressure gradient term, centripetal force term and the radial shear stress term. Assuming a hydrostatic pressure distribution, the radial pressure gradient is
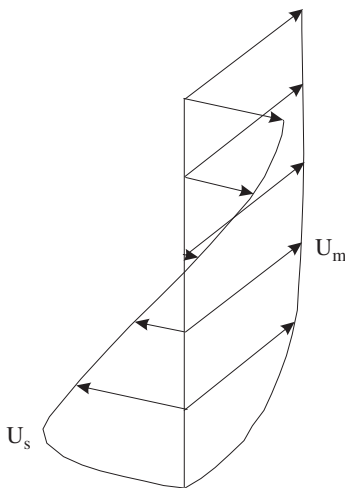

Fig. 1. Secondary flow generated due to flow curvature.

equal to the radial water surface slope. Hence, there is no significant variation of this term in the vertical direction. Due to bed resistance, however, a boundary layer develops near the bed which causes a vertical variation in the streamwise velocity (U_m) and hence a vertical variation in centripetal force. The difference between centripetal and pressure gradient is balanced by the radial shear stress gradient. The radial shear stress is related to the secondary component of velocity through the Boussinesq equation (Boussinesq, 1872)

$$\tau_{zr} = \rho\varepsilon\frac{\partial U_s}{\partial z}, \tag{8}$$

where U_s is secondary flow velocity and ε is eddy viscosity. Substituting τ_{zr} into Eq. (7), the simplified relation between main and secondary flow velocity may be written as

$$\frac{U_m^2}{gr} = \frac{\partial h}{\partial r} - \frac{\varepsilon}{g}\frac{\partial^2 U_s}{\partial z^2}. \tag{9}$$

By implementing the above discussion, some researchers (mainly for estimation of secondary flow in rivers) have attempted to quantify the secondary flow based on the main flow characteristics (e.g. Engelund, 1974; Kikkawa et al., 1976). Generally, the magnitude of the secondary flow is shown to be proportional to the main flow velocity, curvature of the main flow field and water depth which can be written as

$$\chi = \frac{U_s}{\overline{U}_m} = KhF(\zeta, Cz^*), \tag{10}$$

where χ is the strength of secondary flow, ζ is relative depth and $\overline{U}_m$ is the depth-averaged main velocity, Cz^* is the dimensionless Chezy coefficient (i.e., $Cz^* = Cz/\sqrt{g}$ where Cz is the Chezy coefficient), K is curvature (i.e., $1/R$, where R is radius of curvature) and $F(\zeta, Cz^*)$ is a coefficient which represents the effect of bed resistance on the vertical distribution of main flow and varies with depth. For example, Engelund (1974, 1976) derived the function

$$F(\zeta, Cz^*) = 13Cz^*[\tfrac{1}{2}(\alpha - 1)\zeta^2 + \tfrac{1}{6}\beta\zeta^4 - \tfrac{1}{30}\beta^2\zeta^6 + K_0(\alpha, \beta)], \tag{11}$$

where α, β and K_0 are also functions of Cz^* and are constants.

Although the above concept is valid in certain circumstances for oceanographic flows, there are some other factors which should be considered in

these environments. These factors are discussed in the next section.

3.3. Secondary flow in the oceanic environment

Due to the importance of Coriolis effects and an increase in water depth compared with river flow, the theory of secondary flow is more complicated in the marine environment. Kalkwijk and Booij (1986) presented a more complete method to evaluate secondary flow. The secondary flow can be computed based on the main flow field as

$$\frac{\partial U_s}{\partial t} + U_m \frac{\partial U_s}{\partial l} - \overline{U_m \frac{\partial U_s}{\partial l}} - \frac{\partial}{\partial z}\left(\varepsilon \frac{\partial U_s}{\partial z}\right) - \frac{\tau_0}{\rho h}$$
$$= -\frac{\overline{U_m^2} - U_m^2}{R} - f(U_m - \overline{U_m}), \qquad (12)$$

where the overbar denotes a depth mean quantity, l is the streamwise direction, τ_0 is bottom friction in the direction normal to the streamline and f is the Coriolis parameter. It should be noted, that $(\overline{U_m^2} - U_m^2)/R$ and $f(U_m - \overline{U_m})$ are forcing functions which produce secondary currents produced by curvature and Coriolis, respectively. Interestingly, the contribution of Coriolis does not depend on the magnitude of main flow, but changes sign according to the orientation of the eddy (assuming that ε is proportional to $\overline{U_m}$ as in fully developed uniform flow). Due to the linearity of Eq. (12) the effects of curvature and Coriolis can be computed and added separately.

Using Eq. (12) and a numerical study of an idealised domain, Alaee et al. (2004) suggested four regimes which quantify the relative importance of Coriolis/centripetal acceleration and advection/friction in the generation of maximum secondary flow (Table 1). The maximum secondary flow occurs at the surface and near the bed (see Fig. 1). When Coriolis is dominant the strength of the secondary flow is proportional to the Coriolis coefficient rather than flow curvature. Similarly, for relatively deep water (when the water depth ≫ Ekman layer) secondary flow strength is not affected by bed resistance and hence is not proportional to water depth. The equivalent Reynolds number (Re_f) in Table 1, which indicates the ratio of depth to a typical horizontal length scale, and Rossby number (Ro_m), which is a ratio of curvature to Coriolis force, are used to find the flow regime. The river flow case, which was discussed in the previous section, is equivalent to regime C where curvature and bed resistance dominate.

According to the above discussion, in cases where Coriolis effects have a significant contribution, the secondary flow is magnified in a cyclonic eddy and reduced in an anticyclonic eddy. These effects can be approximately quantified using the main flow field (Alaee et al., 2004; Kalkwijk and Booij, 1986).

The magnitude of the secondary flow near the bottom affects bed load transport direction and magnitude. Hence, in terms of morphological studies, this value should be considered in more detail rather than the vertical profile of the secondary velocity. Fig. 2 shows the strength of the near-bed secondary flow for different methods for a case in which curvature and bed friction dominate. Secondary flows are around 0–20% of the main flow for a given range of curvature and water depths in Engelund's method while this range may be increased to 0–30% using Kalkwijk and Booij (1986).

3.4. Problems associated with 2D tidal modelling of rotary current fields

Due to a large saving of computational effort compared with three-dimensional models, depth-averaged

Table 1
Simplified equations for predicting the secondary flow near the bed, based on the relative importance of governing factors

Regime	Equation	$R_{om} = 2U_m/fR$	$R_{ef} = H/LC_D$	Dominant factors
A	$U_s = K_A fh/C_D$	<1	<1	Coriolis-friction
B	$U_s = K_B fL$	<1	>1	Coriolis-advection
C	$U_s = K_C h\overline{U}_m/C_D R$	>1	<1	Curvature-friction
D	$U_s = K_D L\overline{U}_m/R$	>1	>1	Curvature-advection

K_i is a calibration coefficient where i is the flow regime. Regime C corresponds to river flow case. Referring to Eq. (10), $U_s = F(1, C_z^*)h\overline{U}_m/R$ which is the same equation in this table with different calibrating coefficient.
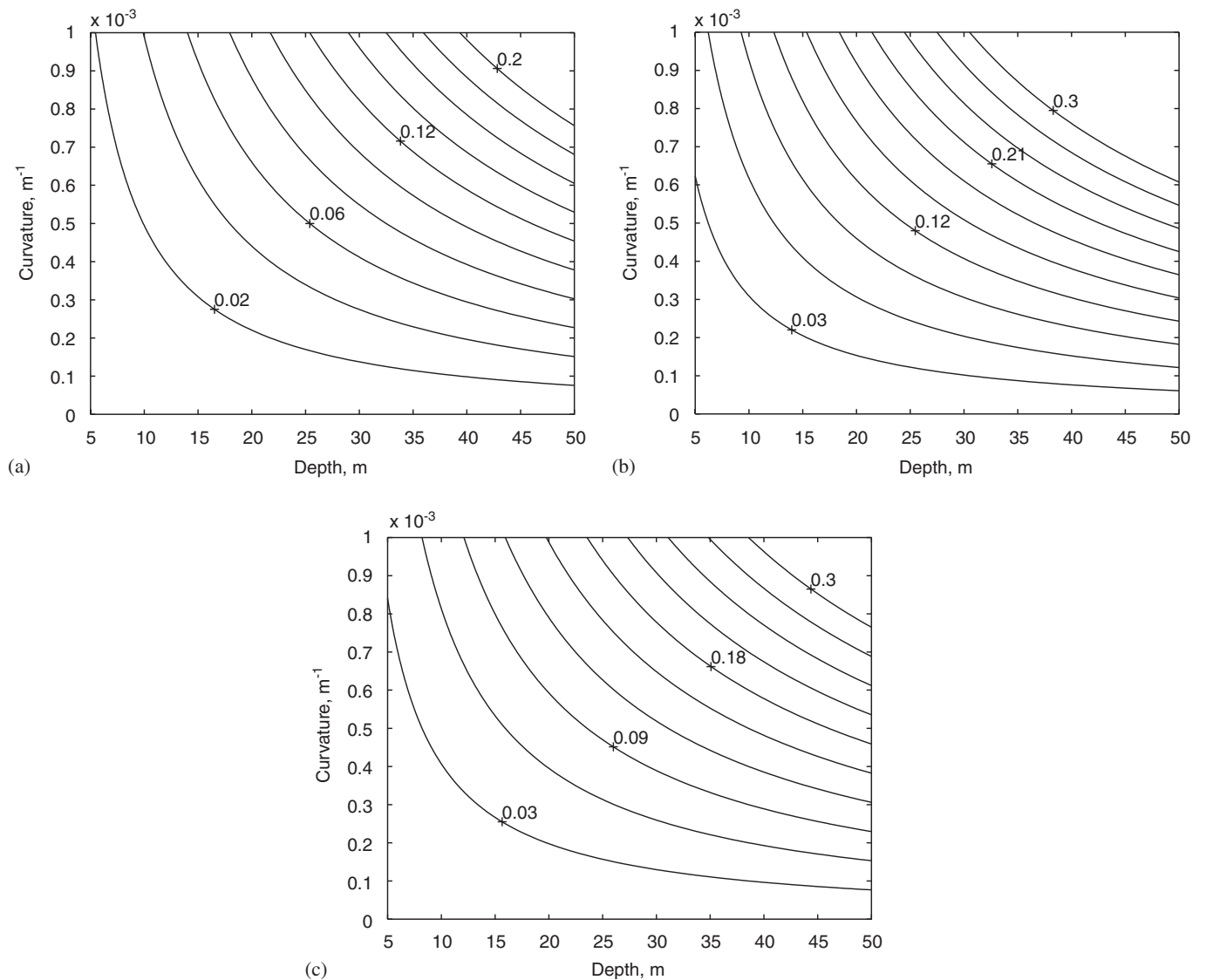
Fig. 2. Secondary flow ($\chi = U_s/U_m$) close to the bed, predicted by different formulations of secondary flow profile: (a) Engelund (1974), (b) Kikkawa et al. (1976), (c) Kalkwijk and Booij (1986).

models are still commonly used for coastal modelling. The vertical variation in velocity distribution is neglected in depth-averaged models, hence they cannot directly calculate secondary flow. Consider an idealised two-dimensional free vortex field. It is expected that this pattern of flow accumulates sediment toward the centre of the vortex. However, it can be easily shown that assuming only the main component of the flow field, no sediment movement will occur toward the centre.

Since the direction of total load transport is assumed to be in the same direction as the flow, there is no component for sediment transport in the radial direction. Referring to the Exner equation

(Eq. (6)), the bed level change for a free vortex is

$$\frac{\partial z}{\partial t} = -\nabla \cdot \boldsymbol{q} = -\frac{1}{r}\frac{\partial(rq_r)}{\partial r} - \frac{1}{r}\frac{\partial q_\theta}{\partial \theta} = -\frac{1}{r}\frac{\partial(0)}{\partial r}$$
$$-\frac{1}{r}\frac{\partial q_\theta(r)}{\partial \theta} = 0, \tag{13}$$

where q_r and q_θ are the radial and angular components of total load transport. For this case, the sediment always moves around a closed path and there is no mechanism which causes sediment movement towards the centre of the eddy. In a similar manner, depth-averaged models which consider only the main component of velocity are not able to detect this type of morphological change for circulatory flow fields.

By including the secondary flow (using Eq. (10)), morphodynamic predictions in the presence of rotary currents are likely to improve. Considering again the idealised vortex problem and including secondary flow transport, if it is assumed that the directions of sediment transport and current are the same, then

$$\chi = \frac{u_r}{u_\theta} = \frac{q_r}{q_\theta} \Longrightarrow q_r = \chi q_\theta. \qquad (14)$$

Consequently

$$\frac{\partial z}{\partial t} = -\nabla.\boldsymbol{q} = -\frac{1}{r}\frac{\partial(r(\chi q_\theta))}{\partial r} + 0 \neq 0 \qquad (15)$$

which causes a movement of sediment towards the centre.

3.5. Treatment of 2D tidal model for secondary currents based on curvature of flow field

From the previous discussion, secondary flows can be approximately predicted by the depth-averaged flow field. Subsequently, the direction and magnitude of sediment transport should be modified in accordance to the strength of secondary flow as

$$\theta_\chi = \tan^{-1}(\chi), \quad q_{t\chi} = \chi q_t, \qquad (16)$$

where θ_χ represents the correction angle and $q_{t\chi}$ represents the correction magnitude. It should be noted that the direction of secondary flow is always perpendicular to the main flow and is towards the eddy centre. In a complex time-varying flow field containing many eddies with different circulations, this direction can be recognised by the sign of the curvature function.

As an initial step in quantifying the strength and direction of secondary flow, the curvature of the flow field should be computed at each grid point for every time step of the morphological model. The curvature of a streamline is (e.g. Theisel, 1995)

$$K = \frac{\det\left(\dfrac{\mathrm{d}L\,\mathrm{d}^2L}{\mathrm{d}t\;\mathrm{d}t}\right)'}{\left|\dfrac{\mathrm{d}L}{\mathrm{d}t}\right|^3}$$

$$= \frac{u^2\dfrac{\partial v}{\partial x} - v^2\dfrac{\partial u}{\partial y} + uv\left(\dfrac{\partial v}{\partial y} - \dfrac{\partial u}{\partial x}\right)}{(u^2 + v^2)^{3/2}}, \qquad (17)$$

where $L(t) = (x(t), y(t))$ is the classic definition of a streamline in fluid dynamics. Therefore, the curva-ture field is a scalar field which takes negative or positive values depending on the direction of the eddies (i.e. cyclonic or anticyclonic). Since the streamlines do not depend on the magnitude of the flow field, the curvature field similarly does not depend on the magnitude of the velocity field.

After computing the curvature of the instantaneous velocity field, the next steps involve prediction of the strength of near-bed secondary flow by using Eq. (10) or Table 1 (depending on the flow regime), and then modification of the direction and magnitude of sediment transport using Eq. (16) and finally implementation of Eq. (6). This method can be applied for all four flow regimes (Table 1) in a similar manner. In regimes A and B the situation is simplified since the calculation of secondary flow is independent of mainstream velocity. The secondary flow in regimes C and D is based on flow curvature, mainstream velocity and either water depth and bed friction (regime C) or horizontal length scale (regime D).

In order to evaluate the proposed scheme, a case study is discussed in the next section.

4. Implementation of an enhanced 2D tidal model to the Lleyn Peninsula and Bardsey Island

At the north of Cardigan Bay in the Irish Sea lies the Lleyn Peninsula. The peninsula is orientated northeast/southwest and extends approximately 40 km, ending in a headland adjacent to deep ($\sim$30 m) water. At the tip of the headland, there is a narrow ($\sim$3 km) strait known as Bardsey Sound separating Bardsey Island (dimensions approximately 3 km $\times$ 1 km) from the peninsula (Fig. 3). Strong tidal eddies exist in the region of Bardsey Island, with currents of order 3 m s^{-1} (Elliott et al., 1995). Despite the complication of being a headland system with an island further offshore, the Bardsey Island system generally behaves as other headland systems with a residual flow away from the tip of the headland (Bardsey Island in this case) and residual eddies on either side of the headland/island (Pingree, 1978). Asymmetry of the residual eddy system is evidenced by the existence of a large (5 km $\times$ 1.5 km) sand bank to the southeast of Bardsey Island (Bastram Shoal), with no corresponding sand bank to the northwest (Fig. 3). A further large sand bank is situated to the east of Bardsey Sound (Devil's Ridge). The maintenance of these two sand banks will be examined in this section.
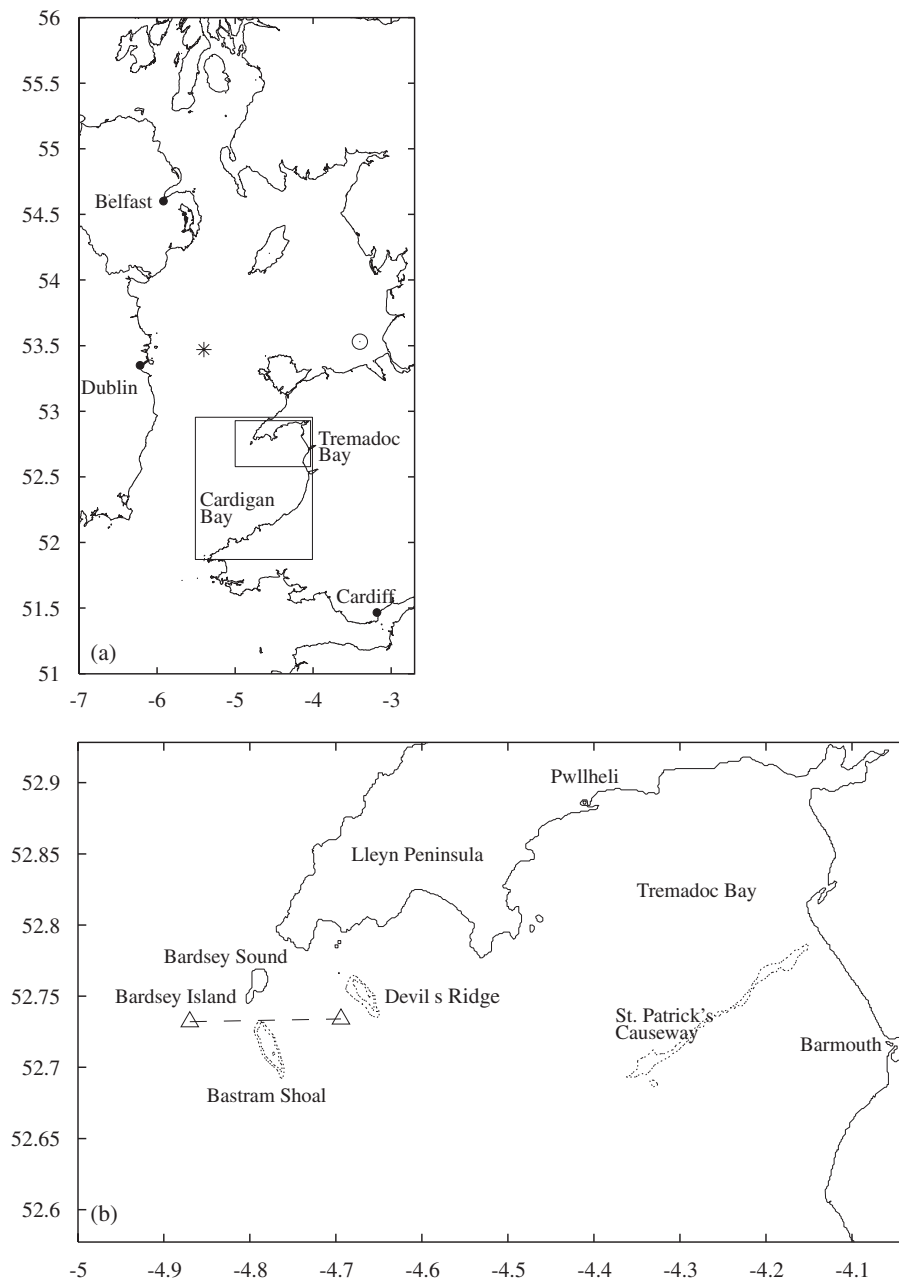
Fig. 3. SWAN model limits: outer Irish Sea grid, intermediate Cardigan Bay grid and inner Tremadoc Bay grid. ∗ is the position of the M2 wave buoy and ○ is the position of the Liverpool Bay wave buoy. The Irish Sea and Tremadoc Bay grids were also used by the POLCOMS tidal model. Sand banks close to Bardsey Island (dotted lines) are plotted as 15 and 20 m depth contours relative to MSL and St. Patrick's Causeway is plotted as 5 m depth contour. The triangles show the east/west limits of the ADCP transect which is plotted as a dashed line: (a) Irish sea, (b) Tremadoc Bay.

POLCOMS (Section 2.1) has been applied to Tremadoc Bay at a resolution of 300 m in the horizontal including the astronomical tide, surge and wind-generated currents. Although POLCOMS is three dimensional, it was applied in this format only to verify the method of calculating secondary flow (Section 3). In this paper, POLCOMS is mainly applied in depth-averaged form to calculate the depth-averaged velocity and hence quantify the

sediment transport due to currents. Details of the eddy systems that form behind Bardsey Island are given in Fig. 4a (flood) and Fig. 4b (ebb). The position and strength of eddies are in qualitative agreement with a numerical model by Elliott et al. (1995) and ADCP data. Clearly, the system of eddies is more pronounced on the ebb in comparison to the flood. Also calculated from the model of Tremadoc Bay were the tidal residual
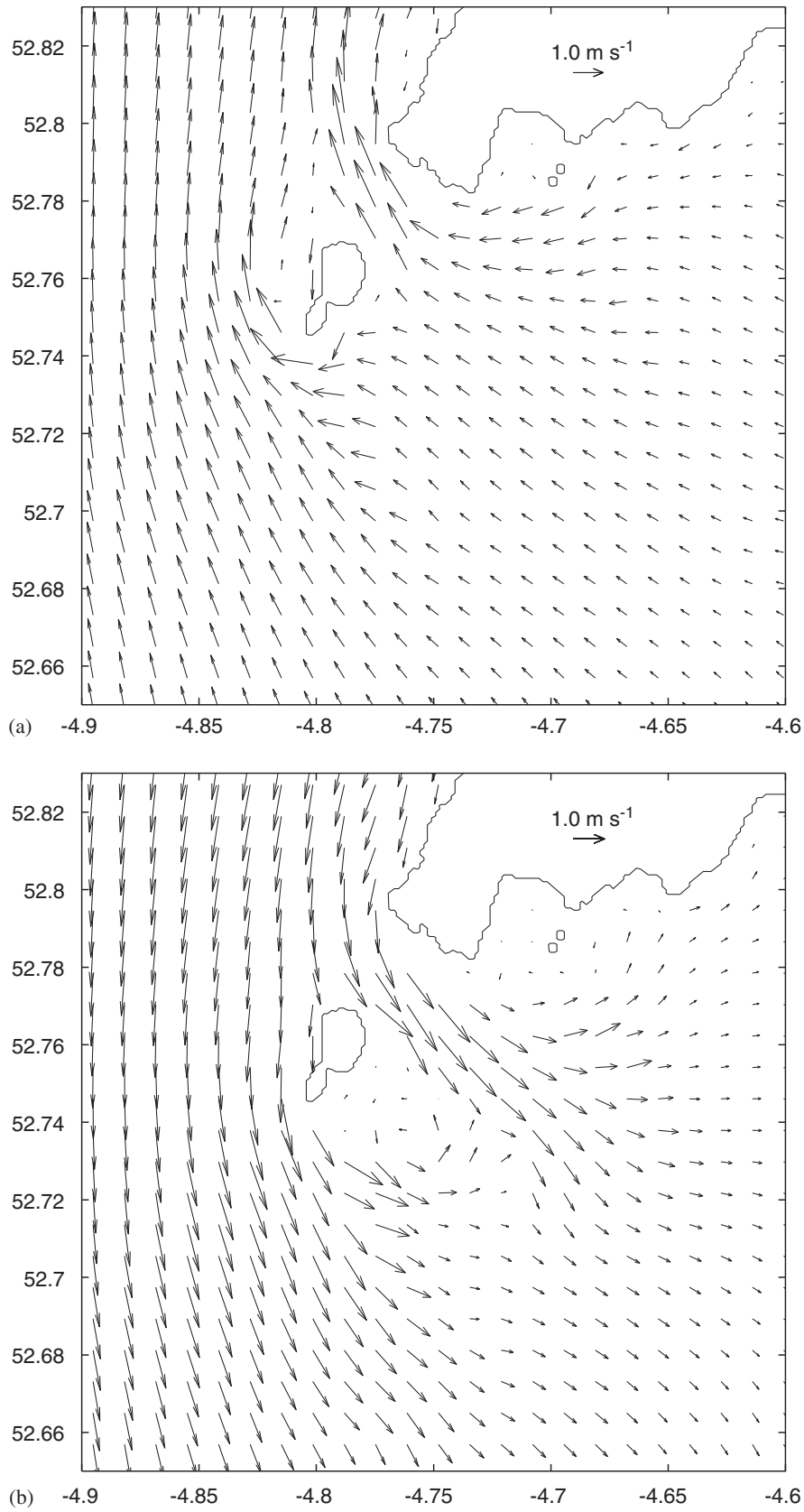
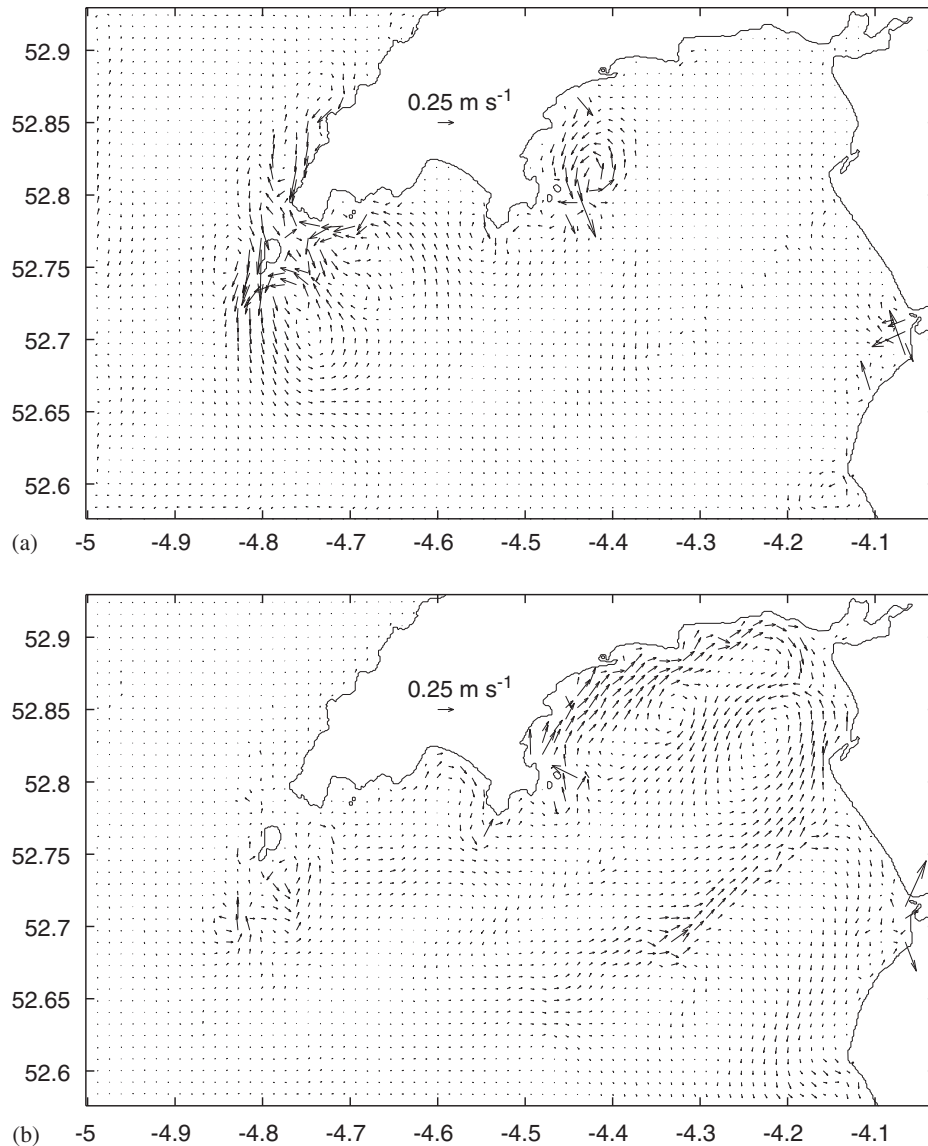Fig. 4. Details of simulated tidal eddies that form behind Bardsey Island: (a) flood, (b) ebb.

Fig. 5. Tidal and wind residual of depth-averaged modelled currents in Tremadoc Bay: (a) tidal residual currents, (b) wind-generated currents at storm peak.

currents (Fig. 5a) and the wind residual currents (Fig. 5b). The latter was calculated for the peak wind speed of the storm event. The ebbing system of eddies visible in Fig. 4b can be seen clearly in the tidal residual. The maximum velocity of the tidal residual in the region of Bardsey Island is approximately $0.25 \, \text{m s}^{-1}$. This is of the same order as the wind residual around Bardsey Island, but the wind component is only of importance in regions of shallow water, hence regions of significant wind residual close to Bardsey Island are isolated. The wind residual dominates over the tidal residual along St. Patrick's Causeway and the shallow water region in the northeast part of Tremadoc Bay. Therefore, the tidal residual dom-

inates around Bardsey Island but the wind residual dominates in the northeast part of Tremadoc Bay.

SWAN (Section 2.1) was implemented in this study by first considering an outer grid of the Irish Sea (Fig. 3). Wind data were applied to the sea surface at a time interval of 3 h and spatial resolution of $0.25° \times 0.25°$. The SWAN model of the Irish Sea has been validated for a storm event in January 2005. During this storm, the three-hourly average of wind speed exceeded $22 \, \text{m s}^{-1}$ in the centre of the Irish Sea and the wave direction was generally from the southwest. SWAN output of H_s was compared with wave buoy data in Liverpool Bay (Fig. 6a) and the M2 buoy in the
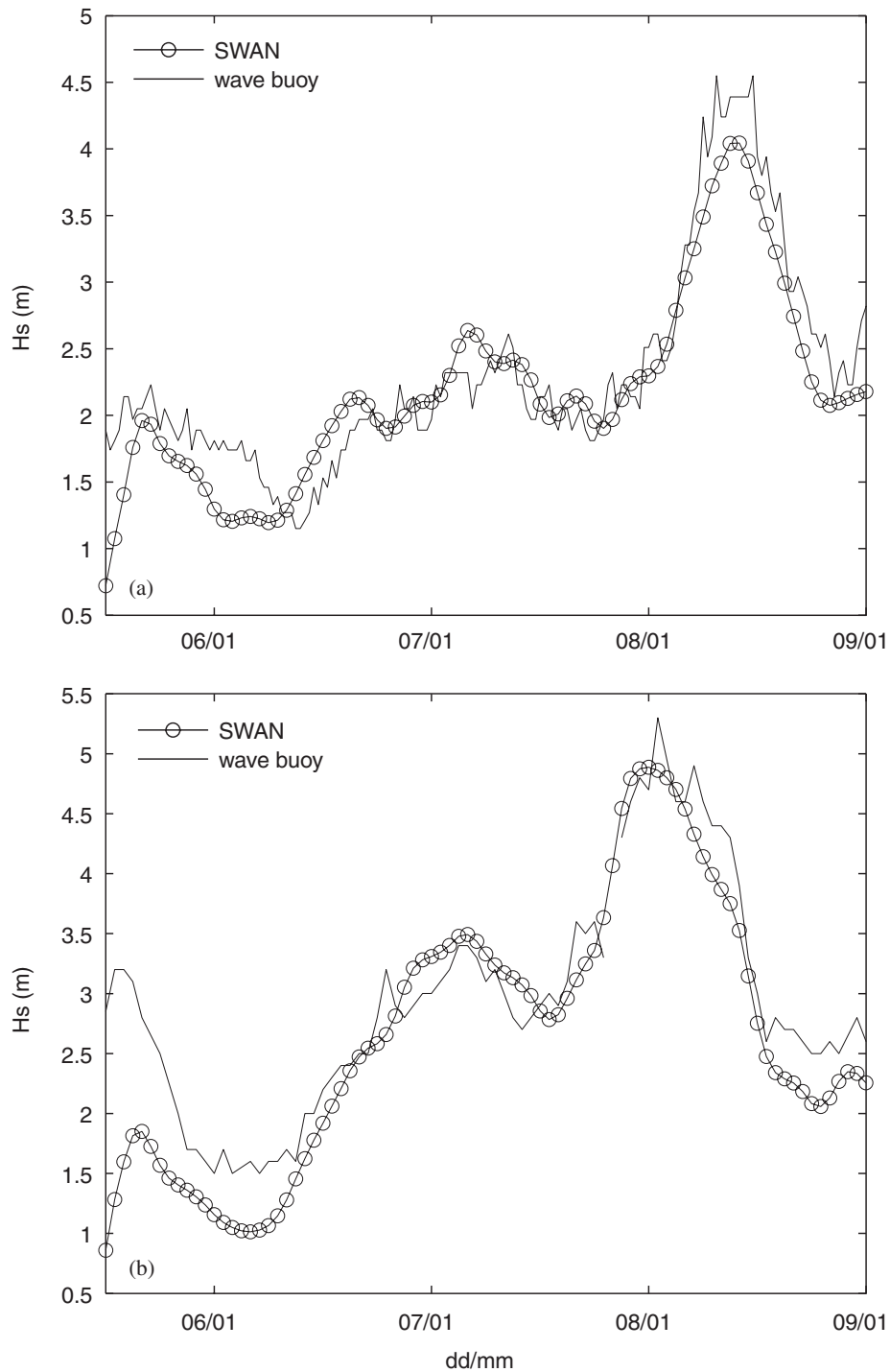
Fig. 6. Validation of SWAN with wave buoy data for storm event in Irish Sea, January 2005: (a) Liverpool Bay, (b) M2 buoy.

centre of the Irish Sea (Fig. 6b). Note in these figures that H_s in the SWAN model spins up from zero (initial condition). Validation was excellent at both locations for amplitude and phase of significant wave height, with this storm producing $H_s \sim 5.5\,\mathrm{m}$ in the centre of the Irish Sea. Boundary conditions of spectral density were extracted from

the Irish Sea model to run firstly a nested Cardigan Bay wave model and subsequently a nested Tremadoc Bay wave model. The January 2005 storm was used for the calculation of sediment transport. It is important to state that whereas the wave action enhances the movement of sediment (especially during such a storm) it does not affect the

direction of transport which is determined solely by the tidal current direction in the Soulsby–van Rijn formula.

4.1. Verification of predicted secondary flow in an eddy with in situ data and a 3D model

According to Section 3.3, the main factors which dominate the secondary flow can be identified from Table 1. Due to large variations in the range of the parameters, there are no strict values for the Rossby or equivalent Reynolds number. However, it seems that due to high flow curvature near the headland and relatively shallow water, regime C (river flow regime) is a good approximation. For example, using $C_D = 0.003$, $U_m = 1\,\text{m s}^{-1}$, $L = 10\,\text{km}$, $h = 25\,\text{m}$ and $R = 3000\,\text{m}$, the Rossby and Reynolds numbers are 5.77 and 0.83, respectively, which implies regime C. This selection of regime can be confirmed by comparing in situ measurements of secondary flow with values predicted by Engelund's method (a method which is based on the river flow regime).

In the first instance, POLCOMS was used with 20 σ layers to validate the method of Engelund when applied to the coastal zone. This was further validated with ADCP data collected in a cruise in the region of Bardsey Island in 1992 (Elliott et al., 1995). A 300 kHz ADCP was used to collect data along an east/west transect to the south of Bardsey Island over a period of 14 h from 18/5/1992–19/5/1992 (the transect position is shown in Fig. 3b). The bin depth was 2 m and the averaging interval was 10 min. At various locations and times throughout the transect, the ADCP recorded velocities in the eddy zone during the ebbing tide. The POLCOMS model was run for the time period of the ADCP survey and profiles of u and v were extracted at the positions of the ADCP profiles. The modelled and ADCP velocity profiles were transferred into primary and secondary velocity components based on the depth-averaged velocity, hence the secondary velocity could be compared to Engelund's method. The comparison between the three dimensional model and the ADCP data is good for the six profiles selected (Fig. 7), especially considering the uncertainties in taking a profile through an unsteady eddy system. Engelund's method gave a good approximation of the secondary velocity, hence its application to an eddy modelled in two dimensions can be justified. With reference to Fig. 2, other methods which have been developed to calculate

secondary flow near the bed will give values in the same range.

4.2. Morphological model with and without secondary flow correction

Before examining the results of the morphological model, the residual flow and its curvature field are presented (Fig. 8). The curvature is calculated locally from Eq. (17). Hence, it is not a simple function which follows, for example, the streamlines of the flow. Generally, the curvature is high at the core of eddies and where strong tidal streams occur, e.g. Bardsey Sound. Curvature takes no account of the magnitude of the flow field, it is only the direction of flow which is used in its calculation. Positive curvature indicates a cyclonic eddy and negative curvature indicates an anti-cyclonic eddy. It is in the regions of high curvature that Eq. (10) has a significant effect on the secondary flow, hence this occurs close to the eddy centres (Fig. 8a). It can be seen in Fig. 8b that the centres of residual eddies close to Bardsey Island approximately correspond to the locations of sand banks. Therefore, the magnitude of the secondary flow is calculated to be higher close to the banks where flow curvature is greatest. The magnitude is limited, however, by shallower water over the crests of the banks, hence Eq. (10) is likely to be maximised close to, but not directly over, the banks. The residual flow in the region of Bardsey Island consists of two dominating eddies, one on either side of the island (northwest and southeast eddies). The eddy to the southeast of the island is stronger due to the contribution of Coriolis force (Pingree, 1978) and is approximately positioned over a sand bank. In the region of the sand bank to the east of Bardsey Island, there is a complex residual flow. This system is more complex than the headland system studied by Pingree (1978) due to presence of Bardsey Sound. The result of this complication, however, is enhanced flow curvature (and hence higher secondary flow) in the region of the banks.

The morphological model was firstly run without the secondary flow correction for a 48 h period, covering the storm event of 8–9 January 2005. Values of sediment size were parameterised from shoreline data collected regularly during 1997–2003 in Tremadoc Bay (Gwynedd Council, 2004). Mean values at mean sea level (MSL) were $d_{50} = 0.5\,\text{mm}$ and $d_{90} = 1.0\,\text{mm}$. The morphological model was then run with the correction for secondary flow to
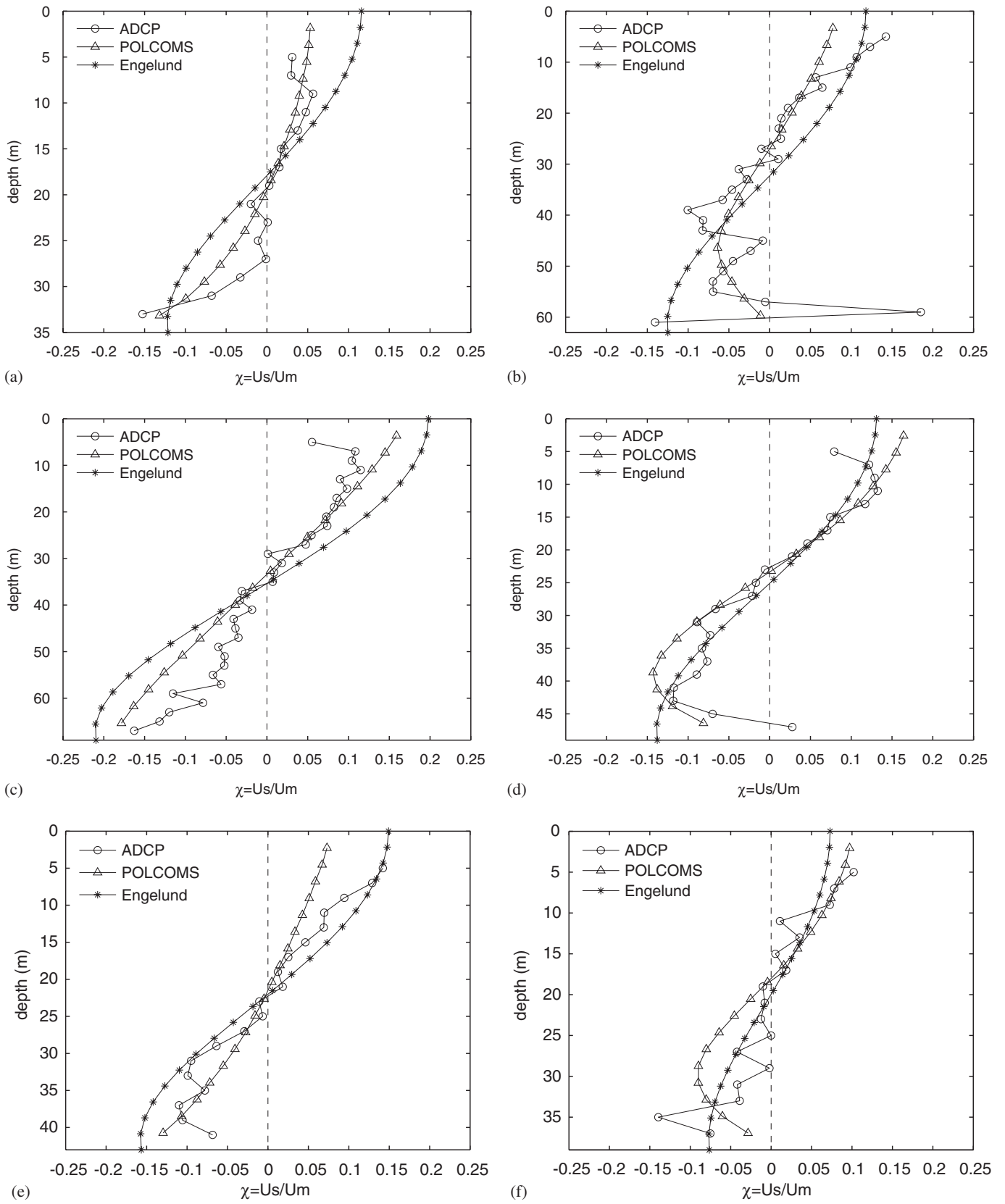
Fig. 7. Comparison between ADCP, POLCOMS and Engelund's theoretical secondary velocity profiles (Eqs. (10) and (11)) in the ebb eddy at different times on 19th May 1992 (springs). Time is also given relative to low water (LW) noting that the tide in this region approximates to a progressive wave: (a) $04\!:\!06(LW+0\!:\!11)$, (b) $04\!:\!24(LW+0\!:\!29)$, (c) $04\!:\!36(LW+0\!:\!41)$, (d) $06\!:\!06(LW+2\!:\!11)$, (e) $06\!:\!24(LW+2\!:\!29)$, (f) $06\!:\!30(LW+2\!:\!35)$.
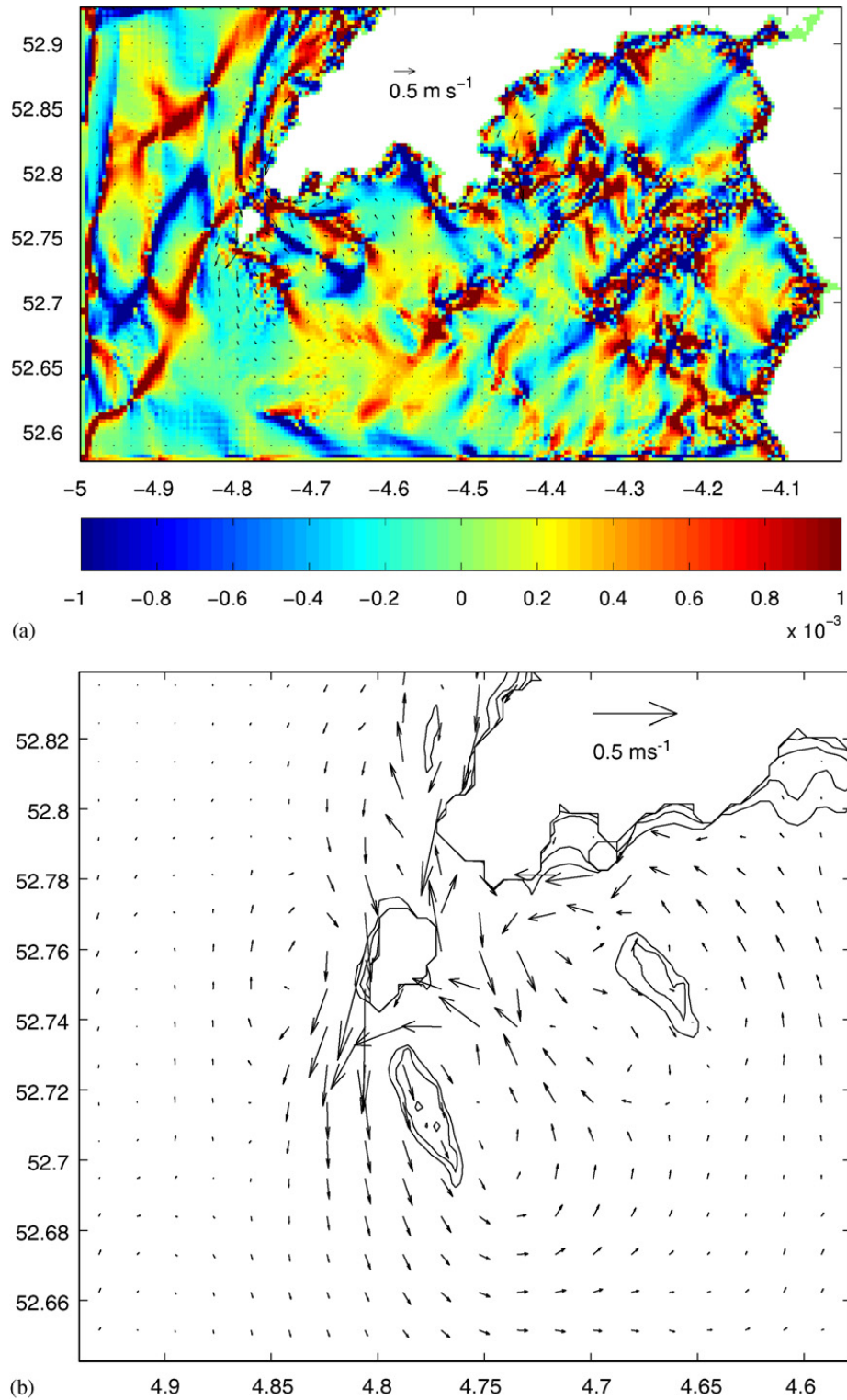
Fig. 8. Curvature and residual currents in Tremadoc Bay calculated using model output depth-averaged tidal currents. Colour scale is curvature and vectors are residual currents. Contours are bottom depth in intervals of 5 m, showing two sand banks: one to the south and one to the east of Bardsey Island. Note that the curvature of the residual currents is calculated for illustration only. In the morphological method, curvature was calculated for the instantaneous velocity: (a) curvature field (m^{-1}) of tidal residual currents, (b) residual tidal current in the region of Bardsey Island.

give the output shown in Fig. 9a. Strong sources and sinks occur due to localised shear in the velocity, e.g. at the tips of headlands and islands.

Of more interest to this study, however, is the convergence of sediment in the region of sand banks which are plotted as contour lines of sea bed
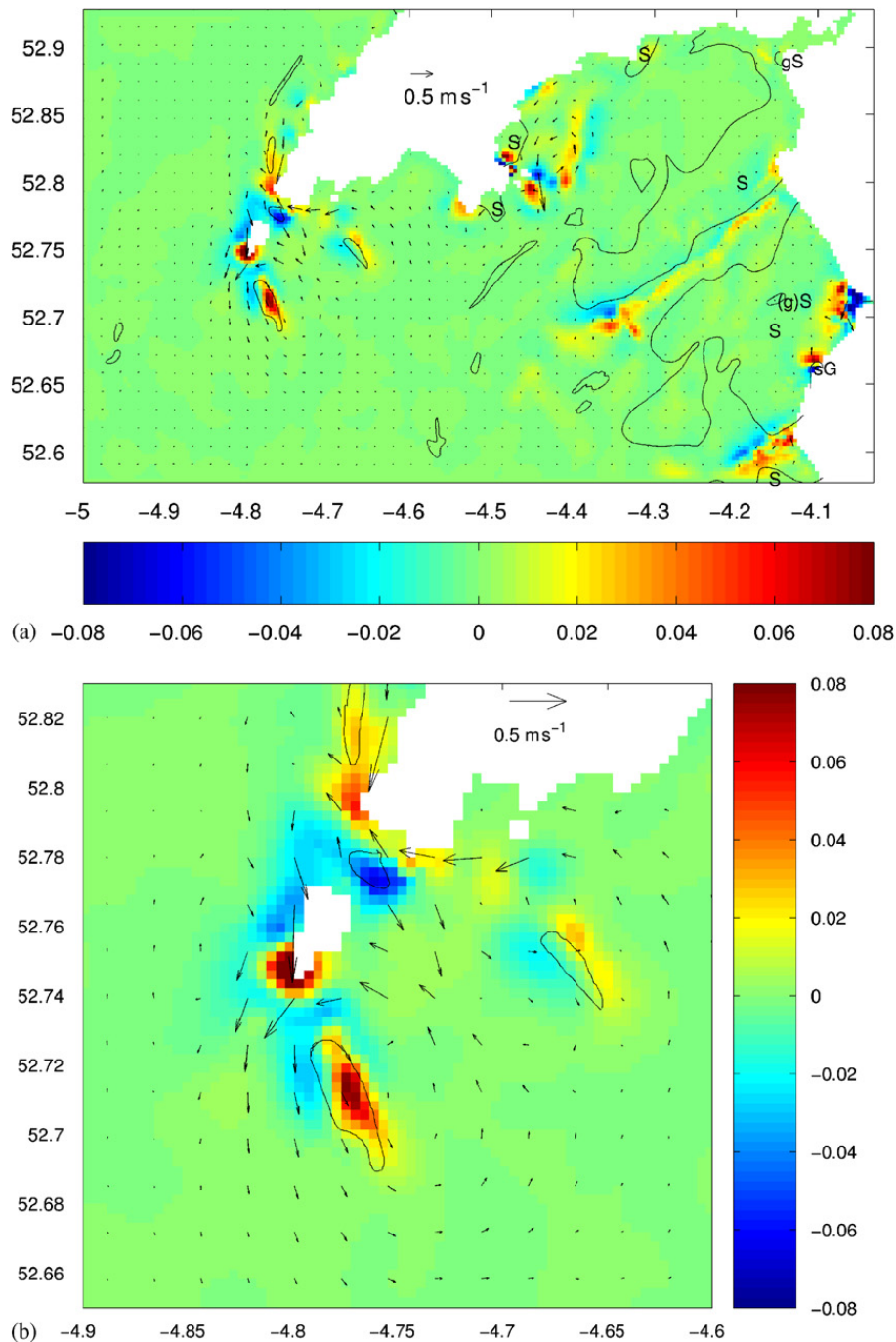
Fig. 9. Change in bed level during storm event for case with secondary flow correction. Contours in (a) are areas of sea bed sand digitised from British Geological Survey (1988). Enclosed contours offshore are areas of sea bed sand unless labelled otherwise. Contours which meet the coastline are all labelled individually. Key is S: sand, gS: gravelly sand, (g)S: slightly gravelly sand. Colour scale is bed change in metres: (a) change in bed level (m) in Tremadoc Bay, (b) change in bed level (m) around Bardsey Island.

sediment type. There is an accumulation of material over the bank to the southeast of Bardsey Island (Bastram Shoal). There is also a corresponding region of erosion around the northwest end of Bastram Shoal. The other major sand bank is Devil's Ridge to the east of Bardsey Island. There is some minor deposition over this bank which can be

seen more clearly in the detail plot of the region around Bardsey Island (Fig. 9b).

Fig. 10 shows the difference between the two model runs where the case without secondary flow was subtracted from the case with secondary flow. In both major sand banks close to Bardsey Island, there was a significant increase in deposition. The
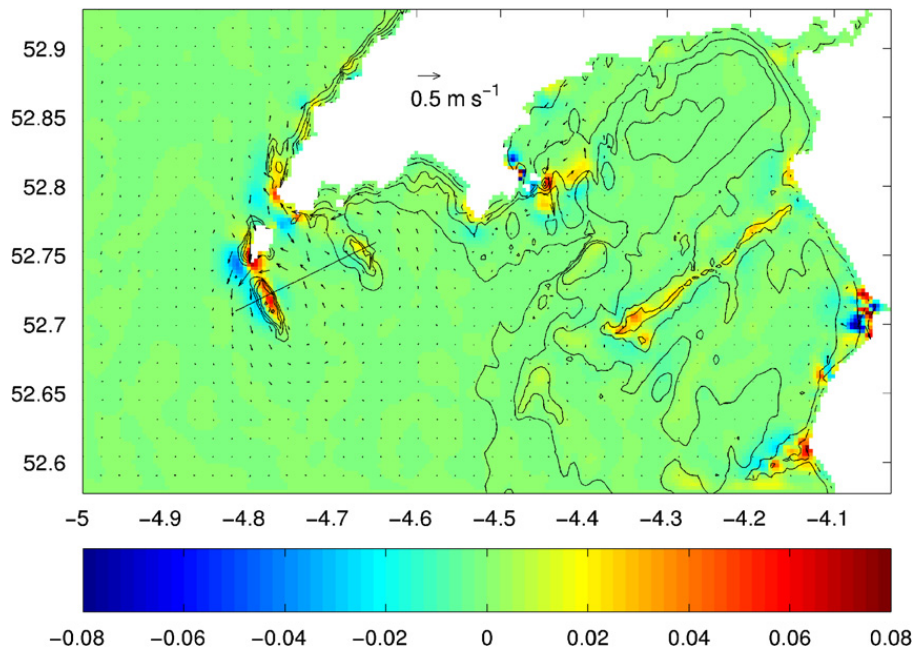
Fig. 10. Enhancement of bed level predicted by morphological model before and after correction for secondary flow for storm event. Colour scale is in metres, vectors are residual tidal currents and contours are bathymetry in the range 0–25 m relative to MSL in 5 m intervals. The cross section shown as a straight solid black line is plotted in Fig. 11.

increase in bed height over Bastram Shoal was in the region of 0.05 m, whereas the increase in bed height over Devil's Ridge was in the region of 0.02 m. Cross sections of the bed levels and change in bed levels between the two simulations are plotted in Fig. 11. For a single storm event, the change in bed level before considering the effect of secondary flow and after considering the effect of secondary flow is significant, especially as there was a predicted change of sign in the cross section plotted through Bastram Shoal (although this partially reflects the change in the horizontal distribution of the sediment between the two model runs). It is also clear from Fig. 10 that the change in bed level due to the addition of the secondary flow is close to, but not at, the centre of the residual eddies. Note also the enhancement of modelled bed level change along St. Patrick's causeway, a 20 km linear sand ridge running northeast/southwest.

5. Discussion

St. Patrick's Causeway has experienced an enhancement of bed level accumulation with addition of the secondary flow correction. On initial inspection, this is unusual since the residual currents are low in that region. However, examination of the curvature function (Fig. 8a) reveals that the curvature is high along St. Patrick's Causeway.

It is the wave action which is primarily responsible for sediment suspension along the length of the causeway and this is enhanced by the secondary flow which is a function of flow curvature. However, this predicted change in bed level along St. Patrick's Causeway flags another issue. The morphological model (Eq. (6)) assumes that there is an active erodible layer throughout the domain. This is clearly not the case in gravelly regions such as St. Patrick's Causeway. Hence, it is the potential bed level change which is modelled and is only of relevance in sandy regions of the same selected characteristic grain size. Fig. 9a is a plot of the enhanced change in bed level due to the secondary flow correction with the addition of contours of sand regions taken from British Geological Survey (1988). This is an over-simplification since the regions not plotted (i.e. bed materials other than sand) are wide-ranging, covering a distribution of bed sediment from mud and silt through to gravel and rock. Fig. 9a shows, however, the potential source of sand available for bed level change. The validity of the prediction of sources can be assessed by checking whether they correspond with regions of sea bed sands. In some instances this does tend to be the case (e.g. Bardsey Sound) but in others it is not the case (e.g. the southwest tip of St. Patrick's Causeway). However, the source at the tip of the causeway corresponds with a region of gravelly
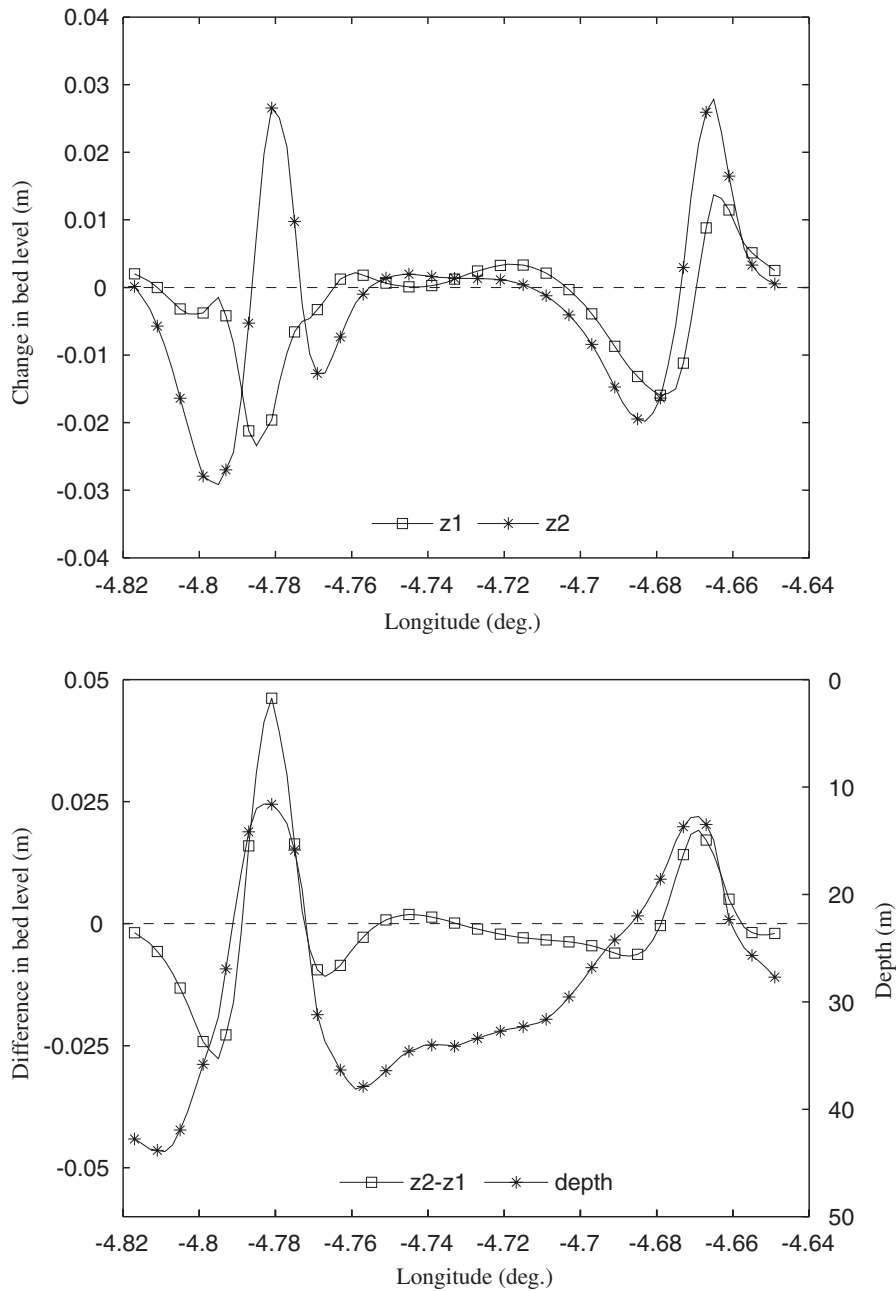
Fig. 11. Cross sections of bed level predicted by morphological model after 48 h and bathymetry. $z1$ is the case without secondary flow correction and $z2$ is the case with secondary flow correction: (a) bed change for each case, (b) difference between the two cases and bathymetry.

muddy sand. This includes a number of factions and is not simply rock or gravel which would preclude the region as a source. It may be possible to correct the morphological model by considering an initial condition of sediment distribution using the contours shown in Fig. 9a. With an assumed thickness of bed sediment (i.e. an active layer) for this initial condition (unless more accurate information is available), this source of sediment could be used in the morphological model to restrict sediment erosion to areas where there is (theoretically) a source rather than a potential source. To implement this method to anything other than first order accuracy, some knowledge of the particle size distribution of sand in these contoured regions would be required.

Using characteristic dimensions for the Bardsey Island case study of $h = 25\,\mathrm{m}$, $d_{50} = 0.5\,\mathrm{mm}$, $\overline{U} = 1\,\mathrm{m\,s^{-1}}$ and $U_{rms} = 0.5\,\mathrm{m\,s^{-1}}$ (from the numerical models), a theoretical suspended sediment concentration profile can be calculated for the combined

case of waves plus currents using a Rouse profile (Soulsby, 1997). With this grain size, the calculation suggests that 90% of the suspended sediment transport occurs in the bottom 20% of the water column. Hence, the method of applying the directional correction based on flow curvature to both the bed and the suspended loads is justified (any significant component of suspended sediment above mid-depth would actually be transported away from the centre of curvature using Engelund's analytical method). However, the direction of sediment transport is recognised to be more complicated than stated here. Davies and Villaret (2002) calculate that whereas the suspended load approximately follows the current direction, the bed load is influenced by the wave direction. The direction of total transport (bed load and suspended load) is somewhere between these two, hence the waves are likely to have a greater effect on the direction of sediment movement than is assumed here. However, the direction has been simplified to equal the current direction in this paper to remove part of the uncertainty in wave direction during a storm event. If the assumption is made that the direction of sediment transport is generally due to the tidal current, this case applies to any storm event rather than storm waves travelling in a particular direction (ignoring a systematic bias in a site such as Tremadoc Bay where waves generally travel from the southwest). Hence, more general statements can be made about the longer term prospect of sediment movements and morphological change. In the sediment transport model, the waves provide a stirring mechanism to place sediment into suspension, but the direction of movement is decided by the tidal current. This direction is modified by the secondary flow based on local curvature of the depth-averaged velocity, but is not modified by the wave direction. Also, over a tidal cycle the tidal current direction at each location will have varied by a maximum of $\sim180°$, hence the mean direction of sediment transport is dominated by the tidal current direction rather than the wave direction. Therefore, the tidal residual may be a good approximation to the direction of sediment movement over timescales greater than the semi-diurnal period.

In order to investigate the importance of bathymetry in generating the eddies, the tidal model was also run for a case where the bathymetry was set to a constant value (50 m) throughout the domain (flat bed case). The general pattern in the residual

tidal current was found to be similar to the real bathymetry case, i.e. dominant eddies to the southeast and northeast of Bardsey Island. However, the diameter of the southeast eddy (in particular) was much larger since the effect of bottom friction was reduced. This simple change in bathymetry indicates that it is the coastline which is responsible for generating the eddies around Bardsey Island. The bathymetry, particularly the existing sand banks, distort the eddy. Hence, beginning with a flat bed and running the sediment transport model and subsequently the morphological model, it is possible to generate the sand banks. To implement this fully, a feedback mechanism is required between the morphological and hydrodynamic models to accommodate a significantly altered bathymetry. Other geological factors which may have an effect on the evolving bathymetry should also be taken into account.

The region of the Irish Sea around Bardsey Island is unstratified throughout the year (Elliott et al., 1991). Therefore, extreme values of secondary circulations attributed to a density interface will not occur near Bardsey Island. The case of stratification was discussed at length by Geyer (1993) for Gay Head. He observed significant stratification in the region of Gay Head which led to large observed shears in the streamwise velocity profiles. This resulted in large shears in the secondary velocity profiles. His results were used to dispute the secondary flow theory (based on flow curvature) of Kalkwijk and Booij (1986) as being applicable to oceanic flows.

6. Conclusions

An analytical formula for predicting secondary flow based on the main flow field was applied to tidal flow past a headland. The theoretical depth profile of secondary flow has been compared to a 3D tidal model and ADCP data taken through eddies generated by a headland, with good agreement. In the case study, analogous to river flow, curvature and friction were the dominant factors for the generation of secondary flow. Using the near-bed secondary velocity induced by flow curvature, the method was applied to a total sediment transport and morphological model which produced enhanced accumulation of sediment in the region of existing sand banks.

It has been demonstrated that this procedure for secondary flow correction can enhance the

formation of a sand bank at the centre of a cyclonic headland-generated eddy compared to simple depth-averaged models. Various analytical methods exist in the literature which give similar results to estimate secondary flow. For any study where the inclusion of secondary flows in depth-averaged models may be appropriate, it is recommended that the major factors which dominate the generation of secondary flow are estimated. Then, an appropriate method to calculate secondary flow can be selected and calibrated using in situ flow data or a 3D numerical model.

Notation

C_D	drag coefficient
Cz	Chezy coefficient
Cz^*	dimensionless Chezy coefficient
d_{50}	median grain diameter
d_{90}	grain diamater for which 90% of grains by mass is finer
D_*	dimensionless grain size
f	Coriolis parameter
g	acceleration due to gravity
h	total water depth
H_s	significant wave height
K	curvature
K_A, K_B, K_C, K_D	calibration coefficients
l	length in the streamwise direction
L	horizontal length scale
p	bed porosity
q_r, q_θ	transport of sediment in the r, θ direction
q_x, q_y	transport of sediment in the x, y direction
q_t	total sediment transport
$q_{t\chi}$	sediment transport magnitude correction
r	radial coordinate
R	radius of curvature
Re_f	equivalent Reynolds number
Ro_m	Rossby number
s	relative density of sediment
t	time
T_p	peak wave direction
$\overline{U}$	depth-averaged current velocity
$\overline{U}_{cr}$	threshold current velocity
U_m	main current velocity
U_r	radial velocity
U_{rms}	root-mean-square wave orbital velocity
U_s	secondary flow velocity
U_θ	angular velocity
z	bed level
α, β, K_0	constants in Engelund formula
β_b	bed slope
χ	strength of secondary flow
ε	eddy viscosity
ϕ	wave direction
ρ	density of sea water
τ_0	bottom friction
τ_{zr}	radial shear stress
θ	angular polar coordinate
θ_χ	sediment transport direction correction
ζ	proportion of depth
Γ	vortex strength
Φ	potential field

Acknowledgements

References

Alaee, M., Ivey, G., Pattiaratchi, C., 2004. Secondary circulation induced by flow curvature and Coriolis effects around headlands and islands. Ocean Dynamics 54, 27–38.

Booij, N., Ris, R.C., Holthuijsen, L.H., 1999. A third-generation wave model for coastal regions—1. Model description and validation. Journal of Geophysical Research 104 (C4), 7649–7666.

Boussinesq, J., 1872. Théorie des ondes et des remous qui se propagent le long d'un canal rectangulaire horizontal, en communiquant au liquide contenu dans ce canal des vitesses sensiblement pareilles de la surface au fond. Journal de Mathematiques Pures et Appliquees 2, 55–108.

British Geological Survey, 1988. Cardigan bay sea bed sediments: sheet 52N 06W, scale 1:250000. Ordnance Survey, Southampton.

Chung, T., 2003. Computational Fluid Dynamics. Cambridge University Press, Cambridge.

Davies, A.G., Villaret, C., 2002. Prediction of sand transport rates by waves and currents in the coastal zone. Continental Shelf Research 22, 2725–2737.

de Vriend, H.J., Zyserman, J., Nicholson, J., Roelvink, J.A., Pechon, P., Southgate, H.N., 1993. Medium-term 2DH coastal area modelling. Coastal Engineering 21, 193–224.

Dyer, K.R., Huntley, D.A., 1999. The origin, classification and modelling of sand banks and ridges. Continental Shelf Research 19, 1285–1330.

Elliott, A., Clarke, T., Li, Z., 1991. Monthly distributions of surface and bottom temperatures in the north-west European shelf seas. Continental Shelf Research 11, 453–466.

Elliott, A., Bowers, D., Jones, B., 1995. Tidal currents near Bardsey Sound. Hydrographic Journal 78, 13–18.

Engelund, F., 1974. Flow and bed topography in channel bends. Journal of Hydraulic Division-ASCE 100, 1631–1648.

Engelund, F., 1976. Flow and bed topography in channel bends. Journal of Hydraulic Division-ASCE 102, 416–418.

Falcón, M., 1984. Secondary flow in curved open channels. Annual Review of Fluid Mechanics 16, 179–193.

Galperin, B., Kantha, L., Hassid, S., Rossati, A., 1988. A quasi-equilibrium turbulent energy model for geophysical flows. Journal of the Atmospheric Sciences 45, 55–62.

Geyer, W., 1993. Three-dimensional tidal flow around headlands. Journal of Geophysical Research 98, 955–966.

Gwynedd Council, 2004. Marian y De and Traeth Crugan sediment sampling results. Technical Report, Coast Protection Unit, Dolgellau.

Holt, J.T., James, I.D., 2001. An s coordinate density evolving model of the northwest European continental shelf: 1. Model description and density structure. Journal of Geophysical Research 106, 14015–14034.

Kalkwijk, J., Booij, R., 1986. Adaptation of secondary flow in nearly-horizontal flow. Journal of Hydraulic Research 24, 19–37.

Kikkawa, H., Ikeda, S., Kitagawa, A., 1976. Flow and bed topography in curved open channels. Journal of Hydraulic Division-ASCE 102, 1627–1642.

Komen, G., Cavaleri, L., Donelan, M., Hasselmann, K., Hasselmann, S., Janssen, P., 1994. Dynamics and Modelling of Ocean Waves. Cambridge University Press, Cambridge.

Lesser, G., Roelvink, J., Van Kester, J., Stelling, G., 2004. Development and validation of a three-dimensional morphological model. Coastal Engineering 51, 883–915.

Mellor, G., Yamada, T., 1974. A heirarchy of turbulence closure models for planetary boundary layers. Journal of the Atmosheric Sciences 31, 1791–1806.

Nicholson, J., Broker, I., Roelvink, J., Price, D., Tanguy, J., Moreno, L., 1997. Intercomparison of coastal area morpho-dynamic models. Coastal Engineering 31, 97–123.

Pattiaratchi, C., Collins, M., 1987. Mechanisms for linear sandbank formation and maintenance in relation to dynamical oceanographic observations. Progress in Oceanography 19, 117–176.

Pawlowicz, R., Beardsley, B., Lentz, S., 2002. Classical tidal harmonic analysis including error estimates in MATLAB using T_TIDE. Computers and Geosciences 28, 929–937.

Pingree, R.D., 1978. The formation of the Shambles and other banks by tidal stirring of the seas. Journal of Marine Biological Association UK 58, 211–226.

Robinson, I., 1981. Tidal vorticity and residual circulation. Deep-Sea Research 28, 195–212.

Soulsby, R., 1987. Calculating bottom orbital velocity beneath waves. Coastal Engineering 11, 371–380.

Soulsby, R., 1997. Dynamics of marine sands. Technical Report SR 466, HR Wallingford.

Struiksma, N., Olesen, K.W., Flokstra, C., De Vriend, H.J., 1985. Bed deformation in curved alluvial channels. Journal of Hydraulic Research 23, 57–79.

Theisel, H., 1995. Vector field curvature and applications. Ph.D. Thesis, Rostock University, Germany.

Van Bendegom, L., 1947. Some consideration on river morphology and river training. De Ingenieur 59, B1–B12.

Van der Molen, J., Gerrits, J., de Swart, H., 2004. Modelling the morphodynamics of a tidal shelf sea. Continental Shelf Research 24, 483–507.

Van Rijn, L., 1989. Sediment transport by currents and waves. Technical Report H461, Delft Hydraulics.

Wang, Z., Louters, T., de Vriend, H., 1995. Morphodynamic modelling for a tidal inlet in the Wadden Sea. Marine Geology 126, 289–300.

.6 Published work P-V

A model of inter-annual variability in beach levels

Simon P. Neill [a,*], Alan J. Elliott [a], Mohammad R. Hashemi [b]

[a] *School of Ocean Sciences, Marine Science Laboratories, Bangor University, Menai Bridge LL59 5AB, UK*
[b] *Department of Water Engineering, Shiraz University, Shiraz, Iran*

ABSTRACT

Beach profile data, collected twice per year at 19 stations over a 25 km length of coastline in Tremadoc Bay, have been analysed to quantify the inter-annual variability in beach levels over a 7 year period and the results compared against the output of a numerical model. Using hourly wind data as forcing, the morphological development of northern Tremadoc Bay was simulated by wave, tidal, longshore transport, total transport and bed level change models. The modelling methodology was efficient and innovative, allowing realistic simulations of long duration with a time step of 1 h, hence capturing the high frequency nature of wind events. The model was run for each of the 7 autumn/winter periods (generally November–April) and the modelled net change in beach levels compared with the data from all 19 stations. The model results had reasonable agreement with the beach profile surveys. However, the observed magnitude of bed level change in the bay lagged the model output by 1 year, indicating that sediment processes acting over a larger area are important in a relatively localised study of inter-annual variability.

© 2008 Elsevier Ltd. All rights reserved.

1. Introduction

Tremadoc Bay is located at the northern end of Cardigan Bay in the eastern Irish Sea (Fig. 1). During the past 20 years, several sections of the coastline in the region have been reinforced with rock armour to protect dune systems from erosion caused by winter storms. The coastal dunes act to protect the low lying adjacent land from coastal flooding. During the first few years of the 21st century, the dunes suffered damage during severe winter storms and the local authorities were required to make urgent reinforcements to the rock armour. With increased storm frequency (rather than intensity) predicted over the northeast Atlantic due to climate change (Houghton et al., 2001; Schmidt et al., 1998; WASA, 1998), the problem of coastal flooding is likely to be exacerbated in the future. The goal of the present study was therefore to provide insight to the local authorities of the processes involved in the erosion of the dunes by tidal currents and storm generated waves. This study involved an analysis of in situ (beach profile) data and the development of a morphological model.

As part of the monitoring programme of the local authority, beaches are surveyed at specified locations in northern Tremadoc Bay twice per year (once in the spring and once in the autumn). There are 19 stations distributed along the coastline from 5 km

west of the Dwyryd Estuary to Abersoch (Fig. 1), a distance of approximately 25 km. The monitoring has been continuous from 1997 to 2005.

The focus of this study is Traeth Crugan, a beach to the west of Pwllheli (Fig. 1). The backshore is characterised by a single, narrow sand dune ridge. The height of the dune is generally 3–5 m and the crest width is approximately 3–4 m. Much of the dune system is poorly vegetated, hence the system is vulnerable to erosion and coastal flooding. This has been an engineering problem since 1967 when erosion was first noted, and timber groynes were placed along the beach in 1974. Since 1976, rock armour has been placed on the beach and frequently extended/strengthened. During February 2002, a large tide and prolonged southerly wind caused significant damage to the dune system to the east of the rock armour. As well as considerably extending the rock armour after this storm, the beach was nourished with $34 \times 10^3 \, \mathrm{m}^3$ of sand and gravel dredged from the harbour entrance at Pwllheli. The problem at Traeth Crugan continues, especially as climate change research generally predicts more short term storms (Alexandersson et al., 2000; WASA, 1998; Beniston et al., 2007). Since the foreshore of Traeth Crugan is designated a site of special scientific interest (SSSI), the problem, and the impact of possible engineering solutions, is sensitive to the natural environment.

Morphological changes in the nearshore zone occur (and have been studied) over a range of scales. Generally, studies of this nature focus on the detail at a single site, e.g. the detailed topographic surveys of Teignmouth over a time period of 2 months (Van Lancker et al., 2004), or cover a range of independent

* Corresponding author. Tel.: +44 1248 713808; fax: +44 1248 716729.
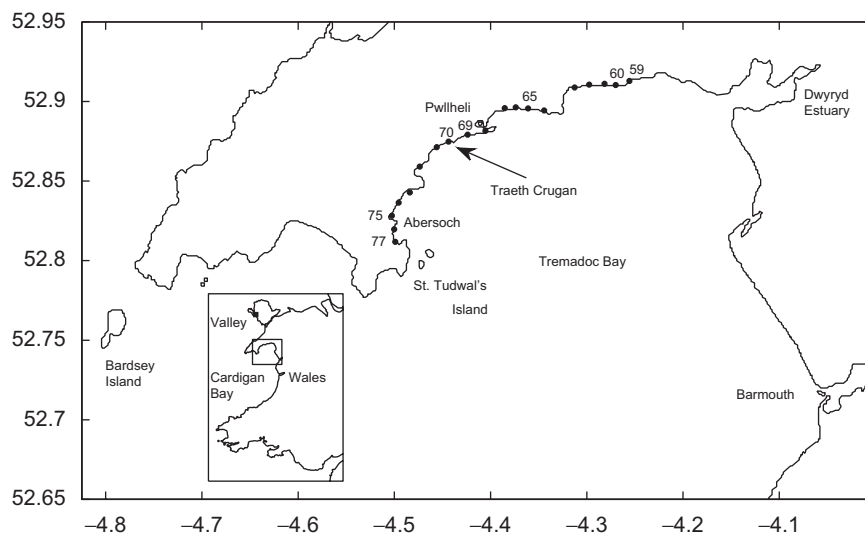*E-mail address:* s.p.neill@bangor.ac.uk (S.P. Neill).

Fig. 1. Location of Tremadoc Bay and Traeth Crugan. The 19 beach profile locations are plotted as filled circles, with reference numbers shown for selected stations. Beach profile data was obtained for all stations twice per year from 1997 to 2004.

coastal locations, e.g. a range of sites along the coastline of western Ireland to study historical shoreline change over a time scale of 200 years (Cooper et al., 2004). However, studies of large scale rhythmic changes (i.e. alternate cells of erosion and deposition along a coastline) are more useful to this current work in Tremadoc Bay, e.g. the longshore transport study of Cape Lookout, North Carolina, where coastal cells of order 1 km were studied (Park and Wells, 2005).

The time scale and repeat interval of each survey is crucial to the sediment transport processes (and subsequent morphological change) being studied. Historical shoreline changes spanning centuries (e.g. Cooper et al., 2004) are pertinent to assessing change of land use or perhaps climate change, but the available data are usually not of good quality or have insufficient temporal resolution to study seasonal or yearly evolution. At the other end of the scale are detailed surveys over very short time periods (e.g. Hill et al., 2004) which suffer from uncertainty in the observed temporal trend in beach profiles (i.e. it is not known whether a short term observation of a seasonal trend is a long term trend or an anomaly). Assuming that storms are the dominant mechanism leading to morphological change along a coastline, one sampling strategy would be a survey immediately before and a survey immediately after a storm event. The data set available to this project is biannual, collected in the spring and autumn. Hence, constraints can be placed on the data by comparing beach profiles immediately before and after the dominant autumn/winter storm season.

There are two main approaches to predicting coastal morphology: data based and process based (Reeve et al., 2004). By correlating past measurements of beach profiles with environmental forcings, it is possible to use statistical methods to predict beach response to future climate forcings. Such methods can be applied through techniques such as empirical orthogonal function (EOF) analysis (Hashimoto and Uda, 1980). Deterministic process-based models can be either relatively simple (e.g. observed offshore wave climate transformed to shallow water and applied to empirical sediment transport and continuity formulae) or can incorporate numerical models to calculate the hydrodynamics and morphological response over relatively large areas. In the latter, a series of two-dimensional (2D) numerical tidal and wave models are applied over a domain. These hydrodynamic forcings are applied (at the appropriate morphological time scale) to sediment transport formulae and sediment continuity to predict bed level

change over the desired time scale. This is the modelling approach developed in this paper.

Many studies exist in the literature on the use of wave models to describe the evolution of beaches. Studies at the qualitative end of the spectrum use wave models to infer the paths of sediment transport and subsequent morphological change (e.g. Cooper et al., 2004). These simple wave models are either wave refraction models (Carter et al., 1982) or model monochromatic waves (e.g. Park and Wells, 2005). Of more use to the present study in Tremadoc Bay are spectral wave models such as SWAN (Booij et al., 1999) which include the natural statistical distribution of wave height, period and direction (SWAN is described further in Section 3.1). To make a quantitative morphological study, a model for sediment transport and bed level changes is required. In a few studies (e.g. Ranasinghe et al., 2004), total load sediment transport formulae are used such as Bailard (1981). However, it is more common for a longshore transport formulation to be used to predict sediment transport in the nearshore zone (e.g. Kamphuis, 1991). To capture high frequency events, a relatively short time step (e.g. 1 h) should be used for all stages of modelling, rather than data reduction (e.g. Latteux, 1995; Jones et al., 2007).

In this study, a morphological model is developed, consisting of wave, tidal, longshore transport, total transport and bed level change modules. Efficient methods are applied to the tidal and wave models to allow multiple morphological simulations of time scales ~6 months at high temporal (hourly) and spatial (100 m) resolution over a relatively large geographic area (~220 km^2) without significant data reduction. The aim of the study is to determine whether such a model can successfully reproduce bulk features observed in beach profile data. In addition, we will be determining whether such a model can be used as a tool to study inter-annual variability of beach levels due to inter-annual variability of wind forcing. This has important implications with climate change since storm frequency is likely to increase in the northeast Atlantic (WASA, 1998).

The data sources are described in Section 2, consisting of the hydrography of the study area, wind and beach profile data. A morphological model is developed in Section 3 consisting of wave, tidal, sediment transport (longshore and total transport) and bed level change models. The model is applied and compared with 7 years of beach profile data in Section 4, and sources of model error are discussed in Section 5.
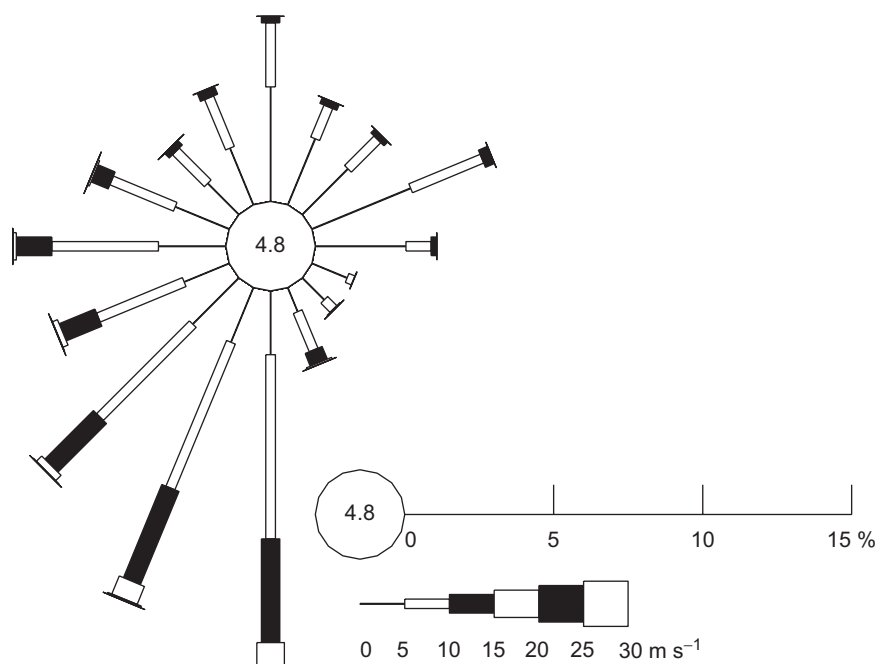
Fig. 2. Wind rose for Valley meteorological station, 1992–2004.

2. Data

2.1. Hydrography of the study area

Tremadoc Bay is a shallow water bay (mean depth of order 10–20 m) with semi-diurnal tides of range 4.5 m (spring) and 1.5 m (neap). Tidal currents in the bay are variable with speeds of order $1-2\,\mathrm{m\,s^{-1}}$ in the region around St. Tudwal's Island and of order $0.1\,\mathrm{m\,s^{-1}}$ in the northeast of the bay (Neill et al., 2007). This latter region stratifies during the summer. Numerous sandy beaches are distributed along Tremadoc Bay, interspersed by rocky promontories. Many of the beaches are popular for tourism and leisure activities, particularly those close to Pwllheli. The town of Pwllheli has a marina, and the entrance to the harbour has to be dredged annually due to sediment accumulation. This dredged material is stockpiled and used for beach nourishment as required. The wave climate in Tremadoc Bay is generally from the southwest, relating to the dominant wind direction which is also southwest (Section 2.2).

2.2. Wind data

Wind data at Valley (Fig. 1) is representative of conditions in Tremadoc Bay as confirmed by correlations at several (coarse temporal resolution) meteorological stations in the bay. Valley was used as the data source for model forcing (Section 3) since a long term data set at high resolution (hourly) was available at this, the closest synoptic meteorological station to Tremadoc Bay. Valley is approximately 40 km north of Tremadoc Bay, but is central to the Irish Sea, making it a reasonable location to represent wind conditions over a wider region. Since the wave modelling methodology assumes a spatially uniform wind field (Section 3.1), such a central location is desired. Jones (1999) demonstrated that such an assumption is valid for a region such as the central Irish Sea which has a length scale of around 300 km. Fig. 2 shows the wind rose for Valley from 1992 to 2004, a time period covering the beach profile data set. The most frequent wind direction is SSW (210°, $6.3\,\mathrm{m\,s^{-1}}$), but the highest magnitude wind events tend to be southwesterly. Since the meteorological

Table 1
Details of beach profile surveys from autumn in one year to spring in the following year

Autumn survey date	Spring survey date	Length (days)
12/11/1997	08/04/1998	148
01/12/1998	27/05/1999	182
08/10/1999	04/05/2000	211
12/10/2000	05/06/2001	236
16/11/2001	25/04/2002	162
18/11/2002	29/04/2003	162
04/11/2003	04/05/2004	182

station at Valley is exposed to the Irish Sea to the southwest, it is an ideal location in which to measure these major southwesterly wind events with minimal topographic effects.

2.3. Beach profile data

Beach profile data for years 1997–2004 for 19 stations in Tremadoc Bay have been provided by Gwynedd Council (Fig. 1, Table 1). Each profile was surveyed twice per year. With such a large quantity of raw data, presentation had to be considerably condensed. Hence, two adjacent profiles have been selected for detailed plotting[1]: a profile with a dune system (station 69) and a profile with rock armour (station 70). At each profile location, a fixed land reference point was used as a starting point, and horizontal and vertical measurements were taken along the beach profile to a horizontal distance which extended to mean sea level (MSL). Bearings were strictly defined so that each beach profile was normal to the coastline. The positions of the stations and bearings were accurately duplicated at each repeat interval of the surveys (~6 months). Beach surveys taken during the spring were plotted since this period indicates the annual trend as well as showing a snapshot of the beach profiles immediately after the autumn/winter storm period. Autumn surveys are less useful in

---

[1] Although all data were used for bulk comparison, see later.
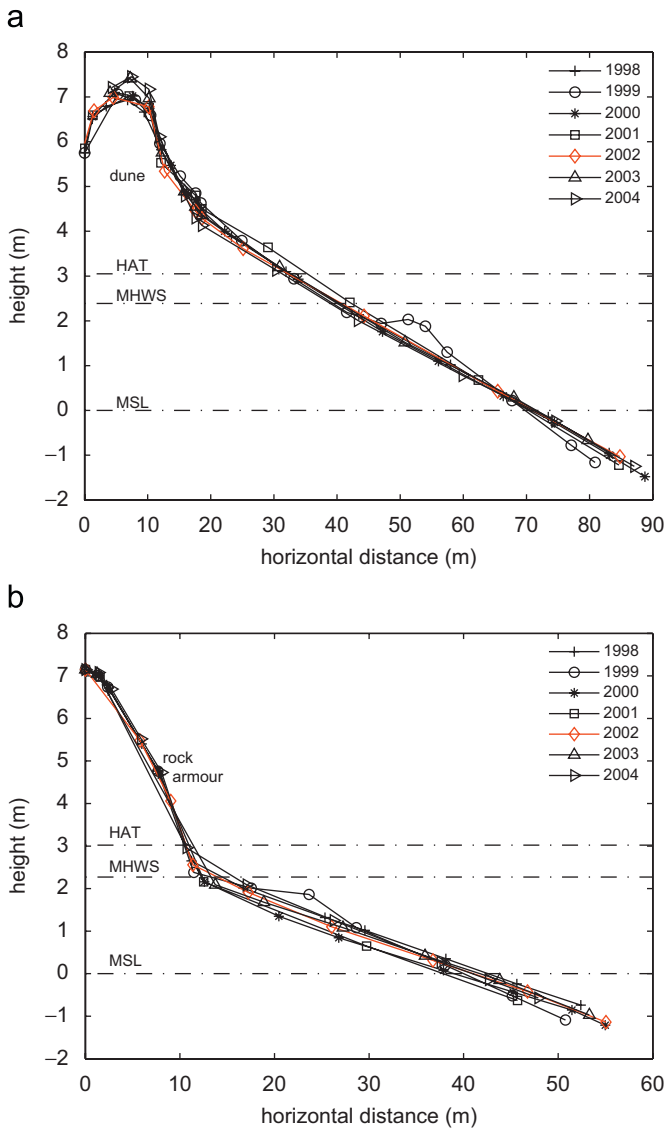
a

b

Fig. 3. Annual (spring) beach profile surveys for years 1998–2004. The levels of mean sea level (MSL), mean high water springs (MHWS) and highest astronomical tide (HAT) are plotted as dot-dashed lines: (a) station 69 (dune system) and (b) station 70 (rock armour).

Fig. 4. Difference between autumn and spring beach levels calculated between mean sea level and highest astronomical tide for all beach profile data.

assessing the impact of storms since they include the summer beach recharge due to swell waves over a period when storms are rare. Since the morphological model does not include swell waves (Section 3), inter-annual variability of beach levels is here taken to be the change in bed level occurring over the autumn/winter storm period.

Profiles from 1998 to 2004 of a dune beach (station 69) are plotted in Fig. 3a and profiles of a rock armour beach (station 70) are plotted in Fig. 3b. In the case of the dune beach, the crest of the dune grew in 2003 and continued to grow until 2004. In 2002 the dune was undercut on its beach face. This reflects the storm damage which is known to have occurred in February 2002 (Section 1). Winds were either from the SSW (65%) or south (35%) during this storm with a peak wind speed of $24.2\,\mathrm{m\,s^{-1}}$ (meteorological data at Valley). In the period following this storm, the beach was nourished with $34 \times 10^3\,\mathrm{m^3}$ of dredged material from Pwllheli marina. Note that in the case of both locations (station 69 and station 70), a beach berm has been captured between MSL and mean high water spring (MHWS) due to the timing of the spring 1999 survey in relation to the preceding wave
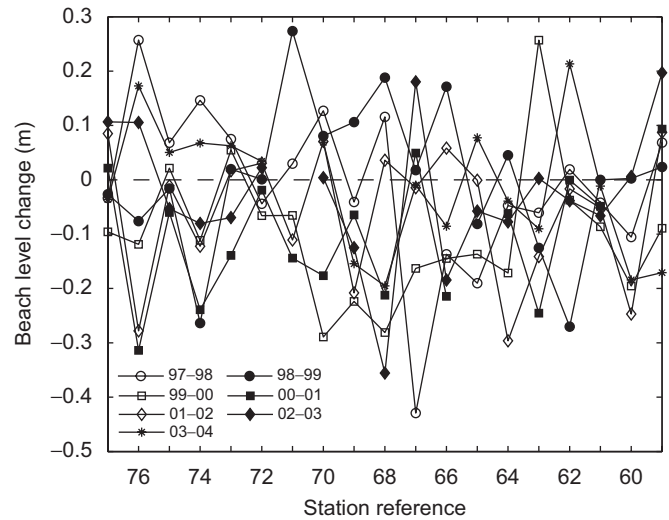
activity. Such features generally form due to swell waves and are destroyed by storm waves. This indicates, therefore, that there was either minimal storm activity or considerable swell activity in the early part of 1999.

For all stations, the mean beach level between MSL and highest astronomical tide (HAT) was calculated for each beach profile survey (autumn and spring). Since the horizontal resolution of raw beach profile data varied between each station and for each survey date, it was necessary to interpolate this raw data to a common sampling interval. A 1 m linear interpolation was found to be a suitable method to capture details over the range of profiles, and to accurately define the intercept of each profile with both MSL and HAT. For each location and survey date, the 1 m re-sampled data was averaged for all data points bounded by these two datums. This produced a single value of beach level for each profile at the time of each survey. By subtracting the autumn beach level in year n from the spring beach level in year $n + 1$, this gives an objective measure of the change in beach level due to the autumn/winter storm season at each of the 19 locations. This calculation was made for all 7 seasons, enabling an inter-annual comparison to be made (Fig. 4). Alternative methods such as the momentary coastline (MCL) (Van Koningsveld and Mulder, 2004) could have been used to calculate the inter-annual variability, but the change in beach level provides a measurement which can be compared directly with the model output (Section 3).

3. Morphological model

The morphological model consists of wave, tidal, sediment transport (longshore transport and total transport) and bed level change modules.

3.1. Wave model (SWAN)

A wave model was used to determine the effect of wind speed and direction on wave characteristics, primarily significant wave height, wave period and wave direction. SWAN (Simulating Waves Nearshore) is an Eulerian formulation of the discrete wave action balance equation (Booij et al., 1999). The model is spectral discrete in frequencies and directions and the kinematic behaviour of the waves is described with the linear theory of gravity waves. The

deep water physics of SWAN are taken from the WAM model (Komen et al., 1994). SWAN has two modes: stationary and non-stationary. Non-stationary mode is time dependent, hence the evolution of the wave field for a storm can be modelled realistically, using boundary conditions of time-varying wind speed and direction. This is, however, computationally expensive since a time step $\ll$ wind forcing time step is required for stability depending on the spatial cell size (Elliott and Neill, 2007). Since a long time series (>1 year) simulation was required for this study, a more economical method was used. This involved running SWAN in stationary mode.

In stationary mode, the evolution of the action density N is governed by the time-independent wave action balance equation (Booij et al., 1999)

$$\frac{\partial}{\partial x}c_x N + \frac{\partial}{\partial y}c_y N + \frac{\partial}{\partial \sigma}c_\sigma N + \frac{\partial}{\partial \theta}c_\theta N = \frac{S}{\sigma} \tag{1}$$

where c_x and c_y are the propagation velocities in the x and y directions, σ is frequency, θ is wave direction and S represents the source terms, i.e. generation, dissipation and non-linear wave–wave interactions.
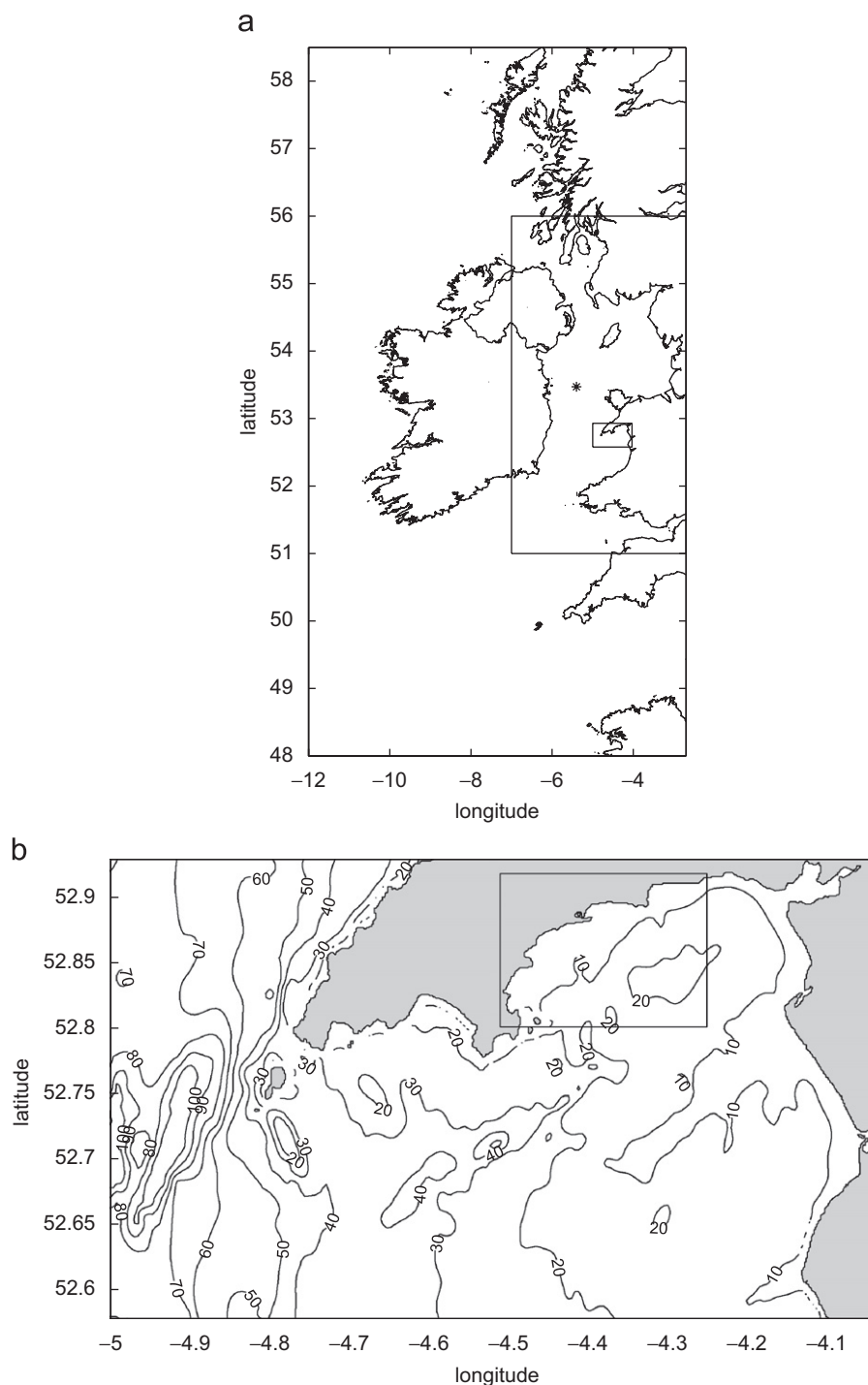

Fig. 5. Wave model nests. The asterisk shows the position of the M2 wave buoy (used for validation of the wave model): (a) Shelf Sea, Irish Sea and Tremadoc Bay nests. (b) Tremadoc Bay and Traeth Crugan nests. Contours are of bathymetry (in metres) relative to mean sea level.
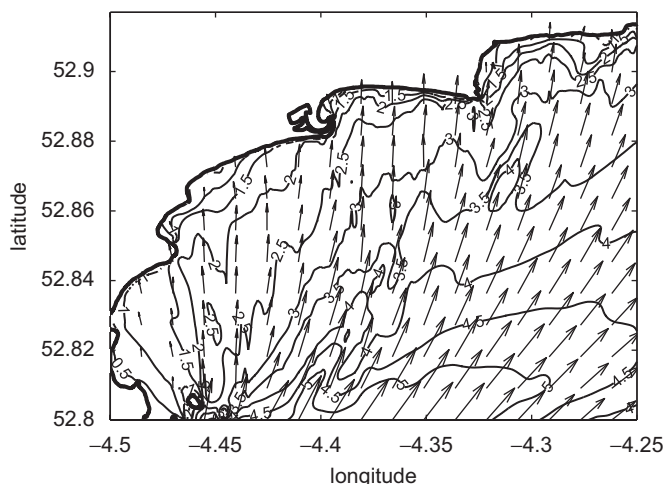
Fig. 6. SWAN output from Traeth Crugan model of H_s contours (m) and vectors of direction θ_p with magnitude H_s for SW wind with speed 24 m s^{-1} (∼47 kn). Every tenth modelled vector is shown for clarity.

From the 12 year analysis of wind data at Valley on Anglesey (Fig. 2), a suitable range of discrete wind direction and speed bins was selected using $\theta = 0, 15, \ldots, 345°$ and $W_r = 2, 4, \ldots, 30$ m s^{-1}, respectively (i.e. $24 \times 15 = 360$ simulations). SWAN was run in stationary mode by applying each of these wind vectors as a constant over the entire model domain. An outer shelf model was run initially at a resolution of 12 km (Fig. 5a) with a high resolution (1.85 km) nested model of the Irish Sea run with boundary conditions of the action density spectrum extracted from the outer grid. Bathymetry data for the shelf model was provided by the Proudman Oceanographic Laboratory (Liverpool), and data for the Irish Sea from Brown et al. (1999). Within this Irish Sea grid was nested a 300 m resolution model of Tremadoc Bay, and nested within this was a 100 m resolution model of Traeth Crugan (Fig. 5b). Bathymetry for the Tremadoc Bay and Traeth Crugan models was digitised from Admiralty Charts 1971 and 1512, based on survey data collected between 1961 and 1983, hence a potential source of error. A typical output of H_s and θ_p is shown in Fig. 6 for a SW wind of speed 24 m s^{-1} (∼47 kn). For each cell of the Traeth Crugan grid, a matrix of H_s, T_p, θ_p and U_{rms} (output directly from the spectral model rather than calculated using linear theory) was produced for the range of wind speeds and directions. For validation, matrices of H_s and T_p at the position of the M2 buoy (Fig. 5a) are shown in Fig. 7. From this matrix, the dominant wind direction for producing high significant wave heights at the M2 buoy is southerly (180°), relating to the longest fetch. The method has been validated with hourly data of H_s and T_p over a period of 3 months in 2005 (Fig. 8) using hourly wind data at Valley meteorological station applied to the lookup tables. The agreement is excellent for such a simple statistical method, but it should be remembered that a third generation wave model was used at high resolution, hence considerable computational effort was required to compute the lookup tables.

3.2. Tidal model (POLCOMS)

POLCOMS is the Proudman Oceanographic Laboratory Coastal Ocean Modelling System (Holt and James, 2001). POLCOMS is three dimensional (using σ coordinates in the vertical) and is formulated in spherical coordinates. For turbulence closure, the Mellor–Yamada–Galperin level 2.5 scheme is used (Mellor and Yamada, 1974; Galperin et al., 1988). Boundary conditions required for POLCOMS are elevation and the normal component of velocity. POLCOMS was applied in this study by first running a 12 km outer
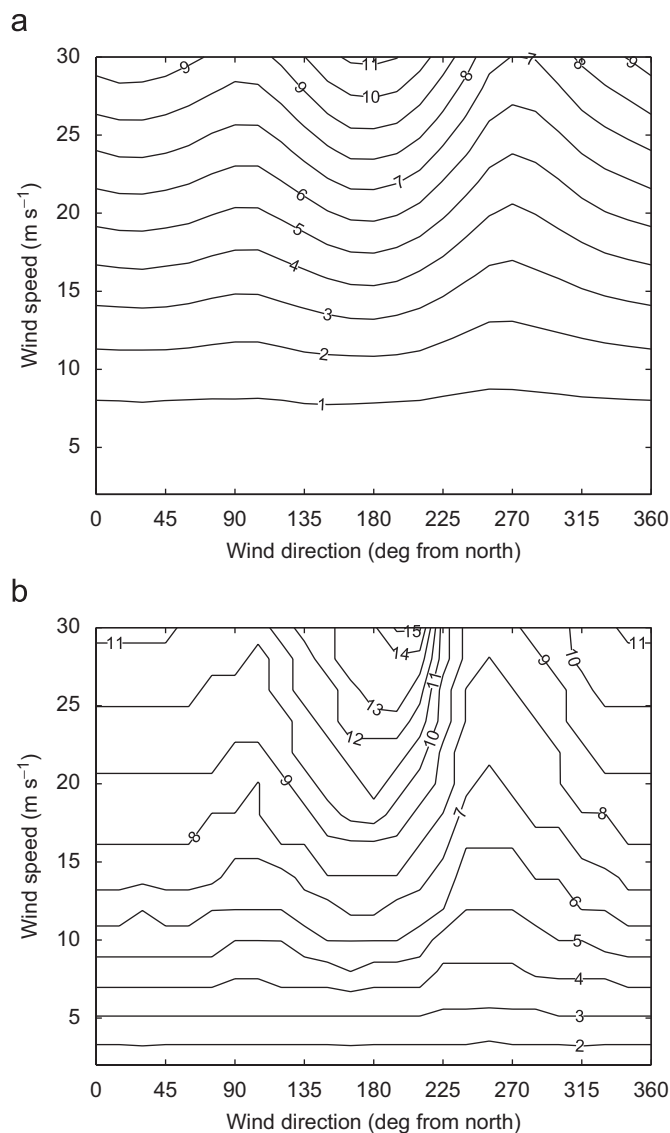

Fig. 7. Graphical representation of significant wave height and peak wave period matrices at M2 buoy (for location, see Fig. 5a) based on SWAN stationary wave model of a range of wind speeds and directions. (a) H_s (m) and (b) T_p (s).

grid of the northwest European continental shelf (12°W−12°E and 48°N−62°N) with astronomical boundary conditions and bathymetry provided by the Proudman Oceanographic Laboratory. An hourly time series of elevation and velocity was stored at the boundary locations of the first inner nested region: the Irish Sea (Fig. 5a) (grid details as in Section 3.1). Harmonic analysis was performed on each time series to create an independent high-resolution Irish Sea model with no feedback to the outer nest. This process was repeated on a second nested region of Tremadoc Bay (Fig. 5b) and finally on an inner nested region of Traeth Crugan (Fig. 5b), both grids as described in Section 3.1. For this morphological study, the two dominant constituents at Pwllheli were used to force the model: M_2 and S_2. The modelled astronomical tide was validated with data from the UK Tide Gauge Network (Table 2). M_2 current ellipses for Traeth Crugan are plotted in Fig. 9. Currents in the region of Traeth Crugan are generally low (of order 0.2 m s^{-1}). To the south of Traeth Crugan, the currents are rectilinear, with the semimajor axis aligned approximately north/south. Closer to the coastline, the character of the tidal currents is more rotary, particularly to the southeast of Pwllheli harbour. The amplitudes and phases of the astronomical
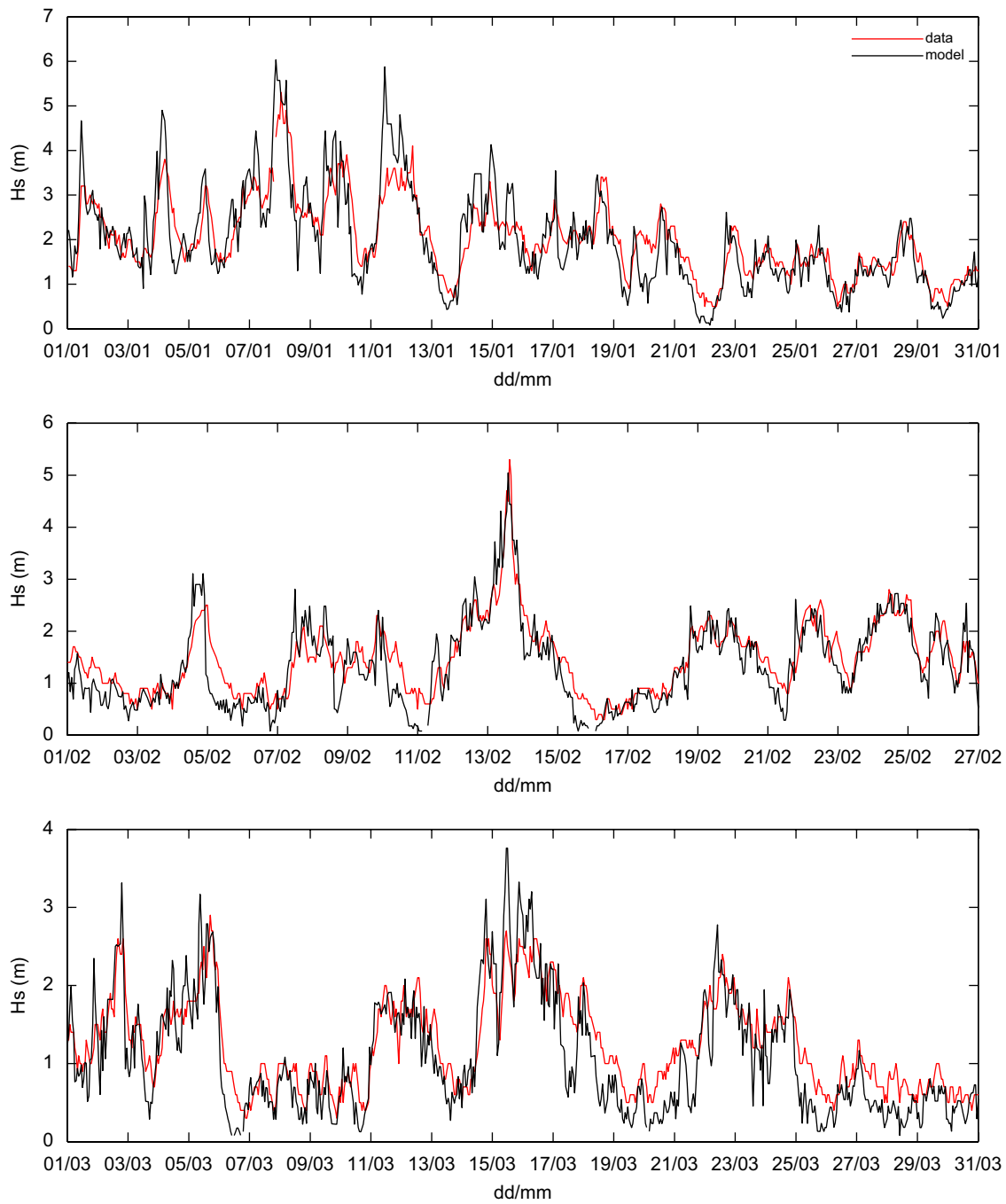
Fig. 8. Agreement between H_s measured at M2 wave buoy and H_s modelled by SWAN, January–March 2005.

Table 2
POLCOMS modelled amplitude ζ (m) and phase g (deg) compared with values at tidal stations around Tremadoc Bay for M_2 and S_2 constituents

Station	M_2				S_2			
	Data		Model		Data		Model	
	ζ	g	ζ	g	ζ	g	ζ	g
Barmouth	1.47	244	1.52	243	0.53	283	0.59	287
Pwllheli	1.47	241	1.49	247	0.58	279	0.57	291

constituents at each cell of the Traeth Crugan grid were used with tidal prediction (of velocity components) to provide an economical method (since it is not restricted by the length of timestep) for tidal input to the total transport model (Section 3.4).

Wind-driven flow was neglected by the model, justified as follows. The mean wind speed over a typical simulated autumn/ winter period (2001–2002) was $7.2 \, \mathrm{m \, s^{-1}}$. Assuming that the surface current (U_s) has a speed of approximately 3% of the wind speed (Bowden, 1983), $U_s = 0.2 \, \mathrm{m \, s^{-1}}$. A roughness length z_0 can be taken as a function of wind speed, and the depth at which wind-driven flow is assumed to be zero (z_c) can be scaled on
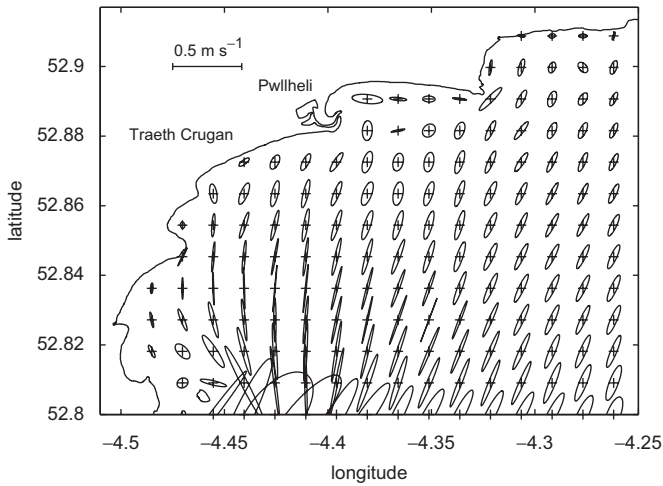
Fig. 9. POLCOMS modelled M_2 current ellipses for Traeth Crugan. Every tenth modelled ellipse is plotted for clarity.

wavelength. Therefore, the vertical profile of wind-driven currents can be calculated using

$$u(z) = U_s \left(1 - \frac{\log(z/z_0)}{\log(z_c/z_0)} \right) \tag{2}$$

The mean water depth in the model domain is 12.8 m. The mean wavelength over the domain during the modelled period was 17 m, hence the wind-driven vertical profile can be calculated and reveals that u reduces to of order 0.01 m s^{-1} in the bottom 1 m of the water column. The mean tidal velocity and root-mean-squared wave orbital velocity over the same modelled period were 0.09 and 0.05 m s^{-1}, respectively, averaged over the entire domain. Hence, the wind-induced currents at the bed are an order of magnitude less than either the mean tidal currents or the mean wave orbital velocity. Since bed shear stress is a function of velocity squared, bed stress due to wind-driven currents is correspondingly two orders of magnitude less than either tide- or wave-induced bed stress.

3.3. Longshore transport model

The CERC formula (USACE, 2001) is commonly used for the estimation of longshore transport in practical or engineering applications (e.g. Miller, 1999). However, several more complicated longshore transport formulae which include additional parameters have been developed and compared to each other via experimental or field data (Van Wellen et al., 2000; Bayram et al., 2001; Soulsby and Damgaard, 2005). Kamphuis (1991) developed a longshore transport equation based on physical model experiments and dimensional analysis. He found that using controlled model test results in the laboratory may yield more accurate results compared with field studies because of uncertainties associated with field measurements and subjectivity of interpreting field measurement results (USACE, 2004). In the present study, therefore, the method of Kamphuis (1991) was used to estimate the longshore transport. The longshore transport rate can be estimated as

$$Q_{lst} = 2.27 H_{sb}^2 T_p^{1.5} m_b^{0.75} d_{50}^{-0.25} \sin^{0.6}(2\theta_b) \tag{3}$$

where Q_{lst} is the longshore transport rate (in kg s^{-1} m^{-1}), H_{sb} is the significant wave height at breaking, T_p is the peak wave period, m_b is the beach slope from the breaker line to the shoreline, d_{50} is the median grain size and θ_b is the wave angle at breaking (the angle which the wave crest forms with the

coastline). The application of Eq. (3) is not ideal for our model resolution of 100 m, since we have not fully resolved wave characteristics at breaking. However, it provides a reasonable compromise between the relatively high resolution output (spatial and temporal) from the wave model and the desired accuracy of sediment transport in the surf zone. It is anticipated that future developments of the modelling methodology will incorporate higher resolution of processes in the inner nearshore zone.

Eq. (3) was implemented by applying a time series of hourly wind speed and direction values to the lookup tables described in Section 3.1. Each coastal grid cell at the resolution of the wave model (100 m) was flagged and properties of H_s, T_p and θ_p extracted. Rather than using the discrete cells to derive the angle of the coastline relative to the incoming wave, a high resolution vector (rather than raster) coastline was used to calculate the angle of the coastline (by using the position in the coastline vector nearest to the centre of each discrete coastline cell). This is important in longshore transport modelling since Eq. (3) produces a scalar quantity, and the direction of transport along the coast is sensitive to the orientation of the coastline. Values of sediment size were parameterised from a particle size analysis of shoreline data collected in 1997 and 2003 in Tremadoc Bay (Gwynedd Council, 2004). From this data, the mean value at MSL was $d_{50} = 0.4$ mm.

Using typical measured and modelled values, the width of the surf zone was calculated using the following empirical formulae for breaking waves in shoaling water (USACE, 2001)

$$\frac{H_b}{H_0'} = \frac{0.563}{(H_0'/L_0)^{0.2}}, \quad \frac{d_b}{H_b} = 1.28 \tag{4}$$

where H_b is the breaker height, d_b is the breaking depth, H_0' is the unrefracted deepwater wave height and L_0 is the deepwater wave length. For example, with a beach slope of 0.08 (Fig. 3) and typical storm values of $H_s = 3$ m and $T_p = 7$ s, the width of the surf zone is $\sim$50 m. Since the model is fixed grid (resolution 100 m) at MSL this equates to the centre of the coastal grid cells. Hence, application of Eq. (3) at grid cells adjacent to the coastline is justified.

3.4. Total transport model

Numerous non-cohesive sediment transport models exist in the literature and these are often compared against each other (e.g. Davies and Villaret, 2002). In this study, sediment transport is calculated as a total load transport by waves plus currents using the Soulsby-Van Rijn formula (1997). It is based on the model of Van Rijn (1989) with curve fitting over a range of wave and current conditions by Soulsby (1997). This formulation contains a large enhancement of transport rate due to wave action. The wave action has an important contribution to the suspended load when considering total transport in shallow waters. The formula is valid for non-cohesive sediments in the range of 0.1–2.0 mm. Total sediment transport rate (in kg s^{-1} m^{-1}) is

$$Q_t = \rho_s A_s \bar{U} \left[\left(\bar{U}^2 + \frac{0.018}{C_D} U_{rms}^2 \right)^{1/2} \right.$$
$$\left. - \bar{U}_{cr} \right]^{2.4} (1 - 1.6 \tan \beta_b) \tag{5}$$

where $A_s = A_{sb} + A_{ss}$ and

$$A_{sb} = \frac{0.005h(d_{50}/h)^{1.2}}{[(s-1)gd_{50}]^{1.2}} \tag{6}$$

$$A_{ss} = \frac{0.012 d_{50} D_*^{-0.6}}{[(s-1)gd_{50}]^{1.2}} \qquad (7)$$

and

$$\overline{U}_{cr} = 0.19(d_{50})^{0.1} \log \frac{4h}{d_{90}} \quad \text{for}$$
$$100 \leqslant d_{50} \leqslant 500 \, \mu\text{m} \qquad (8)$$

or

$$\overline{U}_{cr} = 8.50(d_{50})^{0.6} \log \frac{4h}{d_{90}} \quad \text{for}$$
$$500 \leqslant d_{50} \leqslant 2000 \, \mu\text{m} \qquad (9)$$

where $\overline{U}$ is the depth-averaged current velocity, U_{rms} is the root-mean-square wave orbital velocity, C_D is the drag coefficient due to current alone, $\overline{U}_{cr}$ is the threshold current velocity, ρ_s is the density of sediment, β_b is the bed slope, h is the water depth, s is the relative density of sediment and D_* is the dimensionless grain size. For the typical water depths in Tremadoc Bay (12.8 m), the threshold current velocity was calculated as $\sim 0.4 \, \text{m s}^{-1}$ using $d_{50} = 0.4 \, \text{mm}$. Importantly, the direction of total sediment transport is determined by the tidal flow and not the wave direction. The relatively simple and easy to apply Soulsby-Van Rijn formula enables reasonable predictions to be made of sediment transport in combined wave–current conditions during storm and mean events as demonstrated by in situ studies (e.g. Williams and Rose, 2001). Eq. (5) was implemented in this study by using a lookup table for U_{rms} (Section 3.1) and tidal current prediction (Section 3.2) at each grid cell in the model except for the grid cells adjacent to the coastline where the sediment flux was assumed to be dominated by longshore transport (Section 3.3). This assumption is justified since tidal currents in the cells adjacent the coastline were small (Fig. 9). In addition, the modelled magnitude of longshore transport was found to be ⩾ the magnitude of total transport close to the coastline (Section 4).

3.5. Bed level change model

Nicholson et al. (1997) have stated that, when considering long-term morphodynamics, it is important to include the interaction between the hydrodynamic and the morphodynamic components of the scheme. In the present paper, the time scale is of order 6 months, but the expected ratio of bed change to mean water depth was found to be small (of order 0.01), hence bathymetry changes will be negligible and this feedback has not been included.

Assuming that the sediment content of the water column does not change significantly over time, morphological development can be modelled in two dimensions using (e.g. Van der Molen et al., 2004)

$$\frac{\partial z}{\partial t} = -\frac{1}{1-p} \left\{ \frac{\partial q_x}{\partial x} + \frac{\partial q_y}{\partial y} \right\} \qquad (10)$$

where z is the bed level, p is the bed porosity and q_i is transport of sediment in the i direction (from Eqs. (3) and (5)). This equation, known as the Exner equation, was solved using the Lax-Friedrichs finite differencing scheme which has first order accuracy (Chung, 2003).

4. Model results

Hourly wind data at Valley was used in conjunction with the lookup tables generated by the wave model (Section 3.1) to provide hourly hindcasts of wave conditions for each cell of the Traeth Crugan (100 m) grid. Each of the grid cells adjacent to the
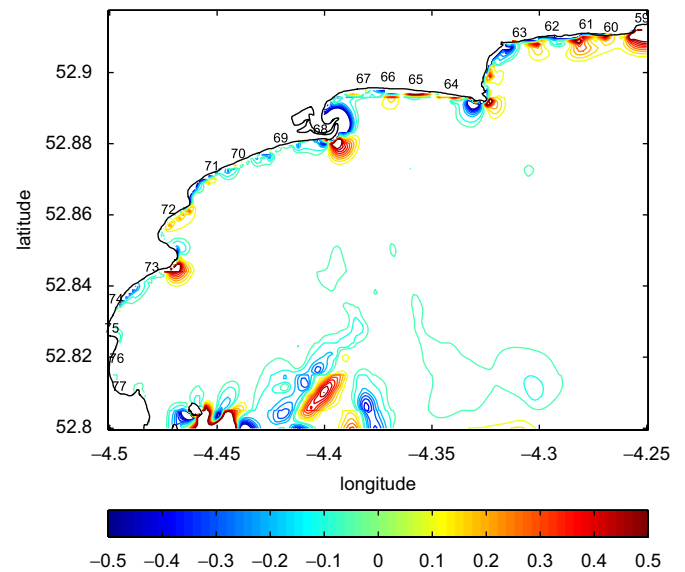

Fig. 10. Contour plot of modelled bed level change from 16/11/01 to 25/04/02. Colour scale is bed level change in metres. Numbers along coastline indicate beach profile station reference.

coastline was flagged and the longshore transport model applied at these locations (Section 3.3). At all other grid cells, the total transport model was applied (Section 3.4) with hydrodynamic input from the wave and tidal models. Finally, the Exner equation was applied to calculate the change in bed level (Section 3.5). This modelling methodology was applied over each of the ($\sim$6 month) periods of beach profile surveys, i.e. from autumn in one year to spring in the following year (Table 1). A typical contour plot of the resulting change in bed level from 16/11/01 to 25/04/02 is given in Fig. 10 and typical time series of modelled sediment transport and bed level change at station 70 are given in Fig. 11.

Along most of the coastline, the simulations generally show an alternating series of sources and sinks, but with localised discrepancies (Fig. 10). The magnitude of bed level change along the coastline was greatest at headlands where polar systems of erosion and deposition developed. Note that the Lax-Friedrichs scheme has introduced a small amount of 2D diffusion into the bed level change model, hence the sources and sinks tend to diffuse away from the coastline.

Significant wave height is closely related to wind speed (Figs. 11a and b). Wind direction is not critical since winds (and hence waves) tend to emanate from the S to SW sector in the study region, and waves tend to be refracted approximately normal to the coastline in shallow water. Longshore transport, however, is critically dependent on wave direction in addition to a threshold wave energy (Fig. 11c). Total transport in the region of Traeth Crugan is ⩽ longshore transport (Fig. 11d) (however, total transport is important further offshore, e.g. the shallow regions centred around 4.4°W, 52.81°N). The resulting bed level change (Fig. 11e) tends to occur suddenly during a storm event (steep positive gradient) but then to diffuse relatively slowly after a sustained period of storm activity. Bed change can be positive or negative at a particular station during a simulation.

In Fig. 12, the modelled bed level change at the coastal cells closest to each of the beach profile locations is plotted at the end of each $\sim$6 month simulation, noting that the x-axis (station reference) is reversed to provide a similar orientation to Fig. 10. The modelled data is plotted along with the observed change in beach level at each station over the same time period. The observations were processed as described in Section 2.3 and
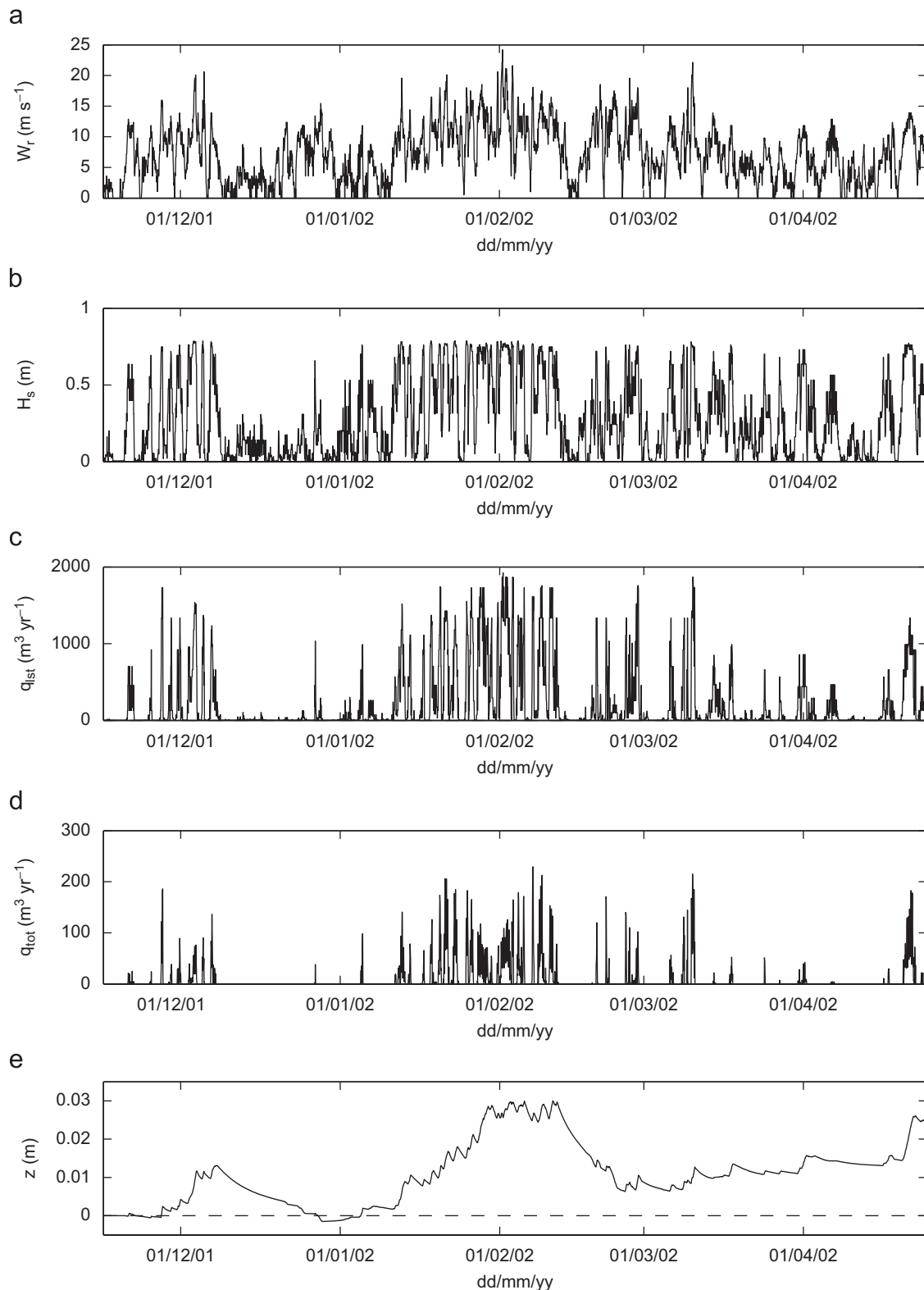
Fig. 11. Time series of wind speed (at Valley), significant wave height, longshore transport, total transport and bed level change at Traeth Crugan (station 70) from 16/11/01 to 25/04/02. Longshore transport, wave height and bed level change are output at model grid cell adjacent to the coastline. Total transport is output at the second model grid cell normal to the coastline: (a) wind speed, (b) significant wave height, (c) longshore transport, (d) total transport and (e) bed level change.

represent the change in beach levels between MSL and HAT. It is acknowledged that this method provides only a proxy for sediment movements due to longshore and total sediment transport, but the agreements in Fig. 12 are reasonable.

5. Discussion

The bed level change in the near coastal zone predicted by a morphological model of longshore and total sediment transport
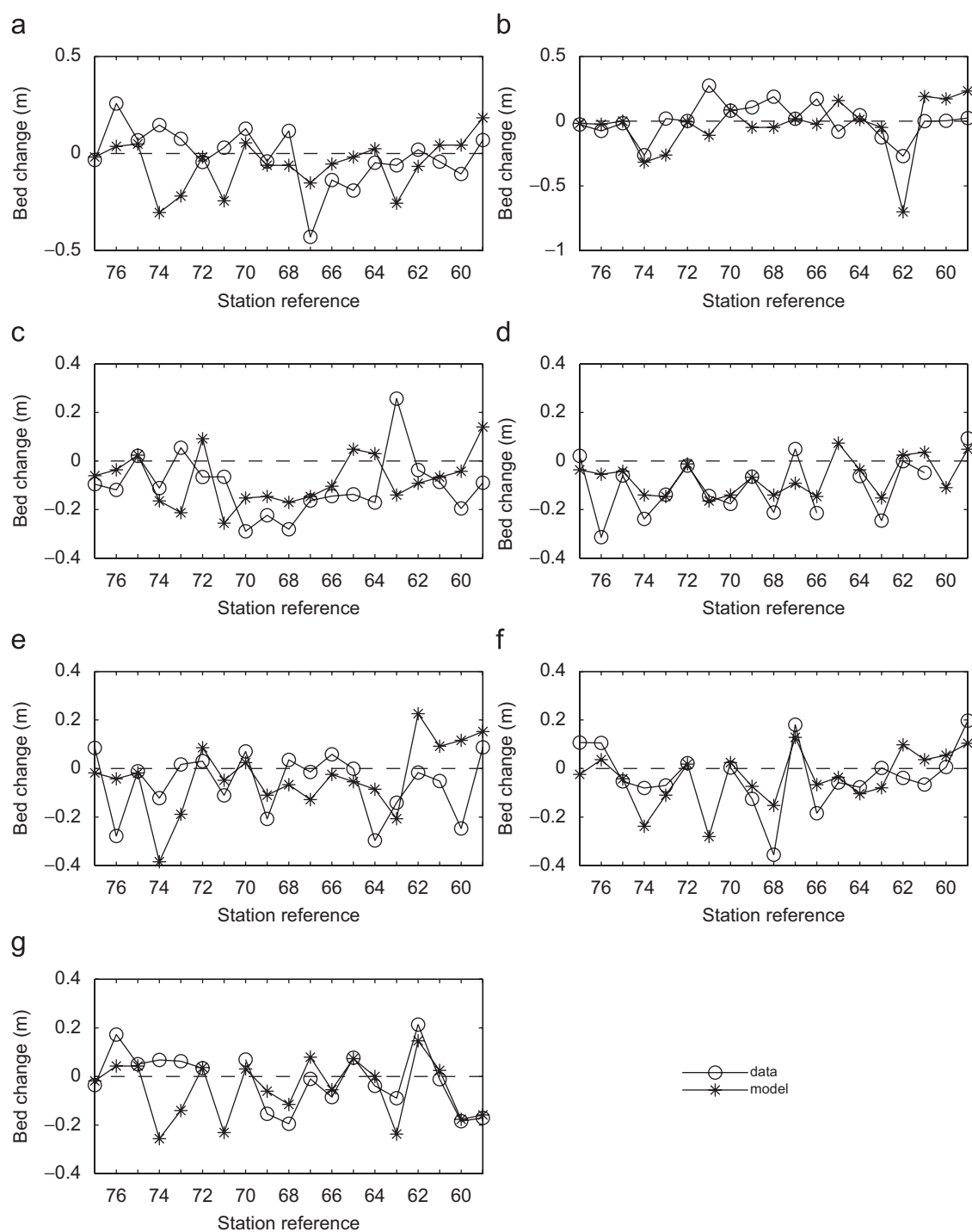
Fig. 12. Comparison between modelled and observed change in beach level for all years for all 19 stations: (a) 1997–1998, (b) 1998–1999, (c) 1999–2000, (d) 2000–2001, (e) 2001–2002, (f) 2002–2003 and (g) 2003–2004.

(with hydrodynamics provided by wave and tidal models) had reasonable agreement with observed beach level changes (Fig. 12). The model successfully captured much of the detail in the along shore erosion/deposition pattern. The overall mean error (for all 19 stations and for all 7 autumn/winter periods) between model and data was calculated to give an indication of the error in magnitude. This error was 0.11 m, which is of the same order as the observed magnitude changes. Hence, caution is required when interpreting this data. However, considering uncertainties in morphological modelling (e.g. empirical sediment transport formulae), this is not considered to be an unreasonable

error in magnitude. Sources of this error are discussed further below.

Magnitude errors between model and data are due to (a) processes absent from the modelling methodology and (b) inaccuracies in representing the processes present. In the latter case, the key sources of error are in the empirical sediment transport formulae, model resolution (particularly the lack of resolving waves at breaking) and the accuracy of the lookup table technique for wave prediction. By tuning the empirical formulae (particularly Eq. (3)), it may be possible to reduce the error in magnitude. However, in the absence of local in situ measurements

of longshore transport, it is difficult to justify such tuning. Since the wave model used a fixed grid (100 m resolution), it was not possible to accurately transform the offshore waves to the surf zone (a resolution of order 2–5 m would be required to resolve wave breaking). A suggested extension to the methodology is to nest a more detailed near-shore wave model within the (relatively) coarse 100 m grid. This further nested model would transform waves from a location approximately 100 m (i.e. one model grid cell) from the coastline to the location of wave breaking. A one-dimensional model applied at each coastal grid cell would suffice for this application, hence minimising the additional computational cost.

Clearly, the lookup table technique for wave prediction has reasonable accuracy over long time periods but has substantial local errors (Fig. 8). Wave energy for high magnitude wind events is often over-estimated since the technique is based on instantaneous wind speed and hence contains no 'memory' of wave energy. In addition, the assumption was made that wind was spatially uniform over a large geographical region. Finally, the source of wind data for the lookup tables was spatially remote from Tremadoc Bay, hence no account was taken of the influence of local topography on wind. However, the use of wind data from Valley meteorological station was justified in terms of the available temporal resolution (hourly) and its central location in relation to the Irish Sea (Section 2.2). Other sources of model error include the dated bathymetric surveys (Section 3.1) and the assumed sediment particle size distribution, taken as constant over the model domain.

The method presented in this paper for morphological modelling takes no account of swell waves which are suggested to recharge beaches after storm damage (USACE, 2001). There is no equivalent economical method to the wave modelling presented here (Section 3.1) which can include swell waves in (for example) the form of lookup tables since they are generated externally to the computational domain. For this reason, it is only realistic to apply the morphological model over relatively short time periods (e.g. 6 months). In addition, the assumption was made that an infinite supply of sediment was available for the model simulations, since all of the surveyed beaches were sandy beaches (i.e. sediment was redistributed throughout the model domain). This is a realistic assumption in the inner nearshore zone, but is less realistic further offshore. The total transport formula calculates potential and not actual transport since the seabed composition varies throughout Tremadoc Bay (BGS, 1988). Tremadoc Bay is composed of regions of sand, gravel, mud and combinations thereof. This problem could be partially resolved by imposing an initial condition of sediment distribution (i.e. sand), including a specified depth of sand deposits in the form of an erodible layer.

One of the objectives of developing this model was to assess its suitability for studying inter-annual variability of beach level changes over the autumn/winter storm period. This can be quantified for both beach profile data and model output in the following way. The mean absolute change in beach (or bed) level was calculated using

$$\frac{1}{m}\sum_{i=1}^{m}|\Delta Z_i| \qquad (11)$$

where $m\ (=19)$ is the number of beach profile locations and ΔZ is the change in bed level from the autumn survey to the spring survey (which also corresponds to the modelled period). This calculation was made for each of the seven ~6 month periods. Hence, the information contained in Fig. 12 was reduced to a single value (per year) for the in situ data and a single value for the model data. These values represent the magnitude of
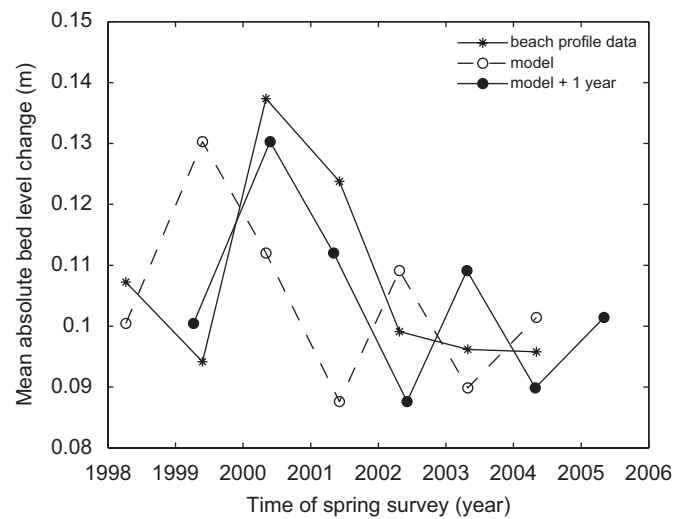

Fig. 13. Mean absolute bed level change for all 19 stations for all 7 years: in situ beach profile data and model data. The model data is also shown lagged by 1 year.

sediment movement over the relevant time scale, but give no indication as to the distribution of sediment. The values are plotted in Fig. 13 as a function of time (defined as the time of spring survey). It is clear that the model results lead the observations by approximately 1 year. Therefore, also plotted is the mean absolute bed level change for the model outputs lagged by 1 year.

Since the model results lead the beach profile observations by 1 year, this represents, apart from errors in the modelling methodology discussed above, sources of sediment external to the domain. It is suggested that storms from the previous autumn/winter season may have moved sediment from an adjacent coastal sediment sub-cell into the north of Tremadoc Bay. Two such sediment sub-cells exist in the region (Cooper and Pontee, 2006): one extending from Bardsey Island to the Dwyryd Estuary (Fig. 1) and the other extending from the Dwyryd Estuary to the south of Cardigan Bay. This quantity of sediment is placed into storage (e.g. in the extensive sand deposits at the mouth of the bar built Dwyryd Estuary) and then redistributed within Tremadoc Bay in the following year. Therefore, in terms of the magnitude of beach level changes, the observations would be expected to lag a model based on local sediment transport.

The model generally under-predicted the magnitude of beach level change over the model domain by O(0.01 m) (Fig. 13). However, there was one significant exception: the observations for the autumn/winter period 2002–2003 (from the above discussion, this magnitude is proportional to the model output and hence the sediment transport for the period 2001–2002, i.e. $n-1$). The model over-estimated the mean magnitude of beach level change by O(0.01 m) over this period. It was during February 2002 when significant dune damage was recorded and urgent rock armour repairs were made (Section 1), and the sudden change in bed level can be seen in Fig. 11e (the actual date of the storm was 1–2 February and the peak wind speed was 24.2 m s⁻¹). Since the lookup table technique for wave prediction often over-estimates the wave energy for high magnitude wind events (Fig. 8), it is likely that for a major storm such as occurred in February 2002, the model has over-estimated the magnitude of bed level change and the discrepancy is discernable at the end of the simulation period, i.e. 3 months later (Fig. 11e).

The time series of bed level change (Fig. 11e) shows how the timing of the beach profile surveys is critical to the understanding of modelled processes. The storm activity around the beginning of

February 2002 led to a localised increase in bed level of order 0.03 m. However, if the beach were to be surveyed at the beginning of March 2002, little net change would be discernable at this location (according to the model). It is only the modest storm activity towards the end of April 2002 which has contributed directly to the increase in bed level observed at the end of the simulation period.

6. Conclusions

An efficient morphological model was developed consisting of wave, tidal, longshore transport, total transport and bed level change modules. The model is suitable for application to relatively long duration high resolution (hourly) simulations, and hence includes the effect of high frequency wind events. The model had reasonable agreement with beach profile data over ∼6 month time periods. With further work, it may be possible to minimise many of the sources of error within the model without significantly compromising the computational efficiency, e.g. the nesting of a high-resolution one-dimensional wave model to predict accurately the wave characteristics at breaking, or extending the morphological computational domain to include sediment processes acting over a larger area. Other errors, such as the inclusion of swell waves, are not easily minimised without resorting to less efficient numerical techniques (i.e. explicit time-stepping models applied over large regions).

Acknowledgements

References

Alexandersson, H., Tuomenvirta, H., Schmith, T., Iden, K., 2000. Trends of storms in NW Europe derived from an updated pressure data set. Climate Research 14, 71–73.

Bailard, J.A., 1981. An energetics total load sediment transport model for a plane sloping beach. Journal of Geophysical Research 86, 10938–10954.

Bayram, A., Larson, M., Miller, H.C., Kraus, N.C., 2001. Cross-shore distribution of longshore sediment transport: comparison between predictive formulas and field measurements. Coastal Engineering 44, 79–99.

Beniston, M., Stephenson, D.B., Christensen, O.B., Ferro, C.A.T., Frei, C., Goyette, S., Halsnaes, K., Holt, T., Jylha, K., Koffi, B., Palutikof, J., Scholl, R., Semmler, T., Woth, K., 2007. Future extreme events in European climate: an exploration of regional climate model projections. Climatic Change 81 (Suppl. 1), 71–95.

BGS, 1988. Cardigan Bay: Sheet 52N 06W, Sea Bed Sediments. British Geological Survey.

Booij, N., Ris, R.C., Holthuijsen, L.H., 1999. A third-generation wave model for coastal regions—1. Model description and validation. Journal of Geophysical Research 104 (C4), 7649–7666.

Bowden, K.F., 1983. Physical Oceanography of Coastal Waters. Ellis Horwood, Chichester.

Brown, J., Joyce, A.E., Aldridge, J.N., Young, E.F., Fernand, L., Gurbutt, P.A., 1999. Further identification and acquisition of bathymetric data for Irish Sea modelling. DETR Research Contract CW0753.

Carter, R.W.G., Lowry, P., Stone, G.W., 1982. Sub-tidal ebb-shoal control of shoreline erosion via wave refraction, Magilligan Foreland, Northern Ireland. Marine Geology 48, M17–M25.

Chung, T.J., 2003. Computational Fluid Dynamics. Cambridge University Press, Cambridge.

Cooper, J.A.G., Jackson, D.W.T., Navas, F., McKenna, J., Malvarez, G., 2004. Identifying storm impacts on an embayed, high-energy coastline: examples from western Ireland. Marine Geology 210, 261–280.

Cooper, N.J., Pontee, N.I., 2006. Appraisal and evolution of the littoral 'sediment cell' concept in applied coastal management: experiences from England and Wales. Ocean & Coastal Management 49, 498–510.

Davies, A.G., Villaret, C., 2002. Prediction of sand transport rates by waves and currents in the coastal zone. Continental Shelf Research 22, 2725–2737.

Elliott, A.J., Neill, S.P., 2007. Simulating storm waves in the Irish Sea. Proceedings of the Institution of Civil Engineers—Maritime Engineering 160, 57–64.

Galperin, B., Kantha, L.H., Hassid, S., Rossati, A., 1988. A quasi-equilibrium turbulent energy model for geophysical flows. Journal of the Atmospheric Sciences 45, 55–62.

Gwynedd Council, 2004. Marian y De and Traeth Crugan sediment sampling results. Technical Report, Coast Protection Unit, Dolgellau.

Hashimoto, H., Uda, T., 1980. An application of an empirical prediction model of beach profile change to Ogawara Coast. Coastal Engineering Japan 23, 191–204.

Hill, H.W., Kelley, J.T., Belknap, D.F., Dickson, S.M., 2004. The effects of storms and storm-generated currents on sand beaches in Southern Maine, USA. Marine Geology 210, 149–168.

Holt, J.T., James, I.D., 2001. An s coordinate density evolving model of the northwest European continental shelf: 1 model description and density structure. Journal of Geophysical Research 106 (C7), 14015–14034.

Houghton, J.T., Ding, Y., Griggs, D.J., Noguer, M., Van der Linden, P.J., Dai, X., Maskell, K., Johnson, C.A. (Eds.), 2001. Climate Change 2001: The Scientific Basis. Cambridge University Press, Cambridge, IPCC, 2001.

Jones, B., 1999. The use of numerical weather prediction model output in spill modelling. Spill Science & Technology Bulletin 5, 153–159.

Jones, O.P., Petersen, O.S., Kofoed-Hansen, H., 2007. Modelling of complex coastal environments: some considerations for best practise. Coastal Engineering 54, 717–733.

Kamphuis, J.W., 1991. Alongshore sediment transport rate. Journal of Waterway Port Coastal and Ocean Engineering—ASCE 117, 624–640.

Komen, G.J., Cavaleri, L., Donelan, M., Hasselmann, K., Hasselmann, S., Janssen, P.A.E.M., 1994. Dynamics and Modelling of Ocean Waves. Cambridge University Press.

Latteux, B., 1995. Techniques for long-term morphological simulation under tidal action. Marine Geology 126, 129–141.

Mellor, G.L., Yamada, T., 1974. A heirarchy of turbulence closure models for planetary boundary layers. Journal of the Atmospheric Sciences 31, 1791–1806.

Miller, H.C., 1999. Field measurements of longshore sediment transport during storms. Coastal Engineering 36, 301–321.

Neill, S.P., Hashemi, M.R., Elliott, A.J., 2007. An enhanced depth-averaged tidal model for morphological studies in the presence of rotary currents. Continental Shelf Research 27, 82–102.

Nicholson, J., Broker, I., Roelvink, J.A., Price, D., Tanguy, J.M., Moreno, L., 1997. Intercomparison of coastal area morphodynamic models. Coastal Engineering 31, 97–123.

Park, J.-Y., Wells, J.T., 2005. Longshore transport at Cape Lookout, North Carolina: shoal evolution and the regional sediment budget. Journal of Coastal Research 21, 1–17.

Ranasinghe, R., Symonds, G., Black, K., Holman, R., 2004. Morphodynamics of intermediate beaches: a video imaging and numerical modelling study. Coastal Engineering 51, 629–655.

Reeve, D., Chadwick, A., Fleming, C., 2004. Coastal Engineering: Process, Theory and Design Practice. Spon Press, Oxon, 461pp.

Schmidt, T., Kaas, E., Li, T.S., 1998. Northeast Atlantic winter storminess 1875–1995 re-analysed. Climate Dynamics 14, 529–536.

Soulsby, R.L., 1997. Dynamics of marine sands. Technical Report SR 466, HR Wallingford.

Soulsby, R.L., Damgaard, J.S., 2005. Bedload sediment transport in coastal waters. Coastal Engineering 52, 673–689.

USACE, 2001. Shore Protection Manual. Books for Business, New York, 532pp.

USACE, 2004. Dependence of total longshore sediment transport rates on incident wave parameters. Technical Report ERDC/CHL CHETN-IV-62, US Army Corps of Engineers.

Van der Molen, J., Gerrits, J., de Swart, H.E., 2004. Modelling the morphodynamics of a tidal shelf sea. Continental Shelf Research 24, 483–507.

Van Koningsveld, M., Mulder, J.P.M., 2004. Sustainable coastal policy developments in The Netherlands: a systematic approach revealed. Journal of Coastal Research 20, 375–385.

Van Lancker, V., Lanckneus, J., Hearn, S., Hoekstra, P., Levoy, F., Miles, J., Moerkerke, G., Monfort, O., Whitehouse, R., 2004. Coastal and nearshore morphology, bedforms and sediment transport pathways at Teignmouth (UK). Continental Shelf Research 24, 1171–1202.

Van Rijn, L.C., 1989. Sediment transport by currents and waves. Technical Report H461, Delft Hydraulics.

Van Wellen, E.V., Chadwick, A.J., Mason, T., 2000. A review and assessment of longshore sediment transport equations for coarse-grained beaches. Coastal Engineering 40, 243–275.

WASA, 1998. Changing waves and storms in the northeast Atlantic. Bulletin of the American Meteorological Society 79, 741–760.

Williams, J.J., Rose, C.P., 2001. Measured and predicted rates of sediment transport in storm conditions. Marine Geology 179, 121–133.

.7 Published work P-VI

Using an artificial neural network to model seasonal changes in beach profiles

M.R. Hashemi [a,*], Z. Ghadampour [b], S.P. Neill [c]

[a] Department of Water Engineering, Shiraz University, Shiraz 71441-65186, Iran
[b] Department of Civil and Environmental Engineering, Shiraz University, Shiraz, Iran
[c] School of Ocean Sciences, Bangor University, Marine Science Laboratories, Menai Bridge LL59 5AB, UK

ARTICLE INFO

ABSTRACT

An artificial neural network (ANN) was applied to predict seasonal beach profile evolution at various locations along the Tremadoc Bay, eastern Irish Sea. The beach profile variations in 19 stations for a period of about 7 years were studied using ANN. The model results were compared with field data. The most critical part of constructing ANN was the selection of minimum effective input data and the choice of proper activation function. Accordingly, some numerical techniques such as principal component analysis and correlation analysis were employed to detect the proper dataset. The geometric properties of the beach, wind data, local wave climate, and the corresponding beach level changes were fed to a feedforward backpropagation ANN. The performance of less than 0.0007 (mean square error) was achieved. The trained ANN model results had very good agreement with the beach profile surveys for the test data. Results of this study show that ANN can predict seasonal beach profile changes effectively, and the ANN results are generally more accurate when compared with computationally expensive mathematical model of the same study region. The ANN model results can be improved by the addition of more data, but the applicability of this method is limited to the range of the training data.

© 2010 Elsevier Ltd. All rights reserved.

1. Introduction

The response of a beach to the natural environment is a challenging problem in the study of coastal morphology. The prediction of beach profile evolution under the action of waves and currents is one of the most important tasks in coastal engineering. Various factors such as wind and wave climates, the angle and the slope of the beach, tidal level, sediment grain size, storm frequency and the geology of the region can affect the formation and variation of beach profiles. The relationship between the beach profile changes and other forcing parameters can be linear or non-linear (Gunawardena et al., 2009), and generally depends on the temporal and spatial scale of the study area (Larson et al., 2000, 2003).

Different approaches are cited in the literature and by practicing engineers to predict variations in beach profiles caused by external driving forces (Gunawardena et al., 2009). Process-based mathematical and numerical models are one of the main approaches for the prediction of beach profile changes. Deterministic process-based models can either be relatively simple (e.g. observed offshore wave climate transformed to shallow water and

applied to empirical sediment transport and continuity formulae) or can incorporate sophisticated two- or three-dimensional hydrodynamic models to calculate the hydrodynamics and morphological response over relatively large areas (Neill et al., 2008). Using numerical modeling, several models can be developed and linked to study beach profile changes on a variety of timescales. A wave model, tidal current model, sediment transport model (alongshore and cross-shore transport) and finally a morphological model should be developed, validated using field data and linked to each other for a specific study site. By employing this technique, significant progress has been achieved in the prediction of beach level changes (Neill et al., 2008; Ranasinghe et al., 2004). However, such techniques require considerable computational effort. In addition, there are still compelling discrepancies between model results and measured data (Neill et al., 2008). Uncertainties in understanding nearshore processes such as wave breaking, wave reflection, refraction, diffraction and longshore transport may be regarded as the main sources of error. In particular, the sediment transport, erosion and accretion rates along the shore are mostly estimated based on empirical formula and the physical mechanisms are not yet fully understood (Jones et al., 2007). Accordingly, other methods such as probabilistic models (Dong and Chen, 1999), wavelet models (e.g. Reeve et al., 2007), inverse models (Karunarathna et al., 2009) and data-based models have been introduced in this area.

---

* Corresponding author. Tel./fax: +98 7112286130.
E-mail address: hashemi@shirazu.ac.ir (M.R. Hashemi).

In data-based methods, by correlating past measurements of beach profiles with environmental forcings, it is possible to use black box models to predict beach profile response to future climate forcing. The beach profile data are collected using traditional survey techniques, video imagery, remote sensing (Kroon et al., 2007) and Differential Global Position System (DGPS). Various techniques such as non-linear complex empirical orthogonal functions (EOF), principal oscillation patterns (POP), singular spectrum analysis (SSA), canonical correlation analysis (CCA) and multichannel singular spectrum analysis (MSSA) have been applied in this regard (Reeve et al., 2007; Różyński, 2003).

Another branch of data-based models is Artificial Intelligence (AI). AI techniques are less expensive compared with physical-based numerical models and avoid the uncertainties involved in physical modeling. AI, in common with other data-based approaches, makes use of only the measured data, and is a practical tool which can be used to predict changes to the coastline as a response to changes in the forcing mechanisms. This tool is particularly useful in coastal application because many coastal engineers are interested in prediction (rather than deep understanding) of changes in the coastal zone as a response to changes in wave and tidal climates.

AI techniques such as artificial neural networks (ANNs) have been previously successfully applied to coastal studies (Chau, 2006), wave prediction (Lee et al., 2009; Kalra et al., 2005), ripple and beach bar behavior and location (Pape et al., 2007; Yan et al., 2008), coastal water level prediction (Huang et al., 2003; Ghorbani et al., 2010; Makarynska and Makarynskyy, 2008; Lee et al., 2007), wind–wave analysis (Browne et al., 2007; Herman et al., 2009), head–bay geometry (Iglesias et al., 2009), tidal prediction (Liang et al., 2008), break water design (Panizzo and Briganti, 2007; Yagci et al., 2005) and estimation of suspended sediment concentrations (Cipollini et al., 2001; Teodoro et al., 2007). The application of AI techniques such as neural network, fuzzy logic and genetic algorithm in predicting beach level change is a promising new branch of research. Although it has its own

limitations (e.g. lack of physics and dependence on good quality training data), it can be examined in parallel with enhancing present physics-based numerical models. The performance of these two approaches against one another, in comparison with field data, can also be studied.

The purpose of this study is to investigate the potential of ANN to predict beach profile changes in a case study (Tremadoc Bay, eastern Irish Sea). The study region and in situ data are described in Section 2. An additional source of input data for the ANN, a wave model, is also explained in some detail in this section. The ANN model, including its input parameters and architecture, is introduced in Section 3. The model structure contains input vector, hidden layer, internal parameters, model training and evaluation, described in Section 4. Finally, the ANN results are presented and discussed in Section 5.

2. Study region and data sources

2.1. Study region

Tremadoc Bay is a shallow water bay (mean depth of order $10-20$ m) located in the eastern Irish Sea (Fig. 1). The bay has semi-diurnal tides of range 4.5 m (spring) and 1.5 m (neap). Tidal currents in the bay are variable, with speeds of order $1-2$ m s^{-1} in the region around St. Tudwal's Island and of order 0.1 m s^{-1} in the northeast of the bay (Neill et al., 2007). This latter region stratifies during the summer. Numerous sandy beaches are distributed along the Tremadoc Bay, interspersed by rocky promontories. Many of the beaches are popular for tourism and leisure activities, particularly those close to Pwllheli. The town of Pwllheli has a marina, and the entrance to the harbor has to be dredged annually due to sediment accumulation. This dredged material (of order 10×10^3 m^3 per year) is stockpiled and used for beach nourishment as required. The wave climate in Tremadoc Bay is generally from the southwest, relating to the dominant
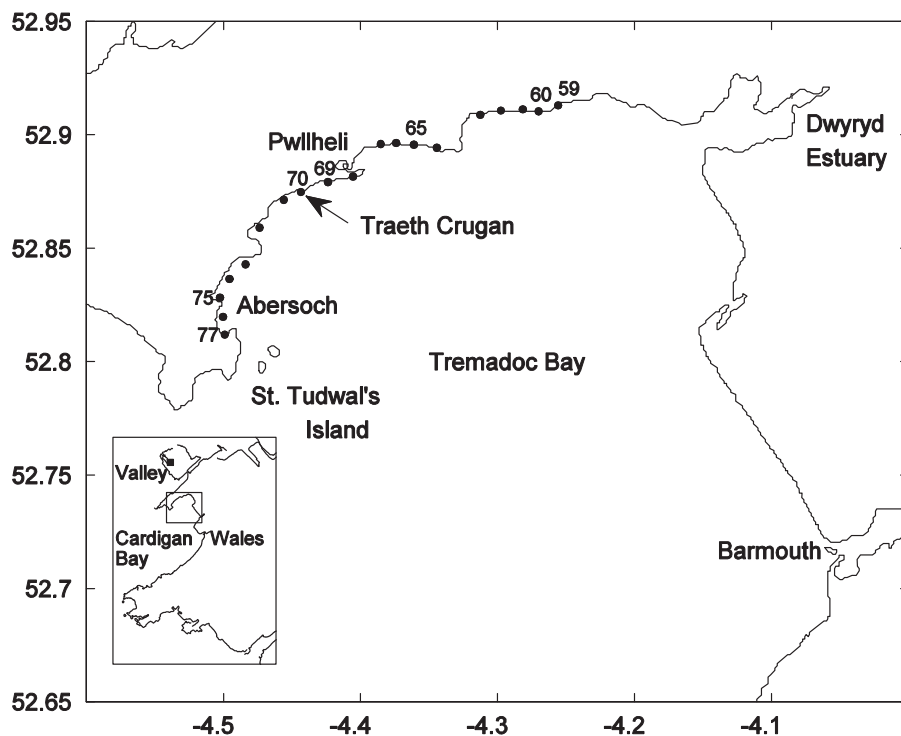

Fig. 1. Location of Tremadoc Bay and Traeth Crugan.

wind direction which is also southwesterly. Mathematical models have already been developed and used to predict sand bank formation (Neill et al., 2007) and beach profile changes in this region (Neill et al., 2008).

2.2. Beach profile data

Beach profile data for years 1997−2004 for 19 stations (59–77) in Tremadoc Bay were provided by the local authority, Gwynedd Council (Fig. 1, Table 1). The profiles were mostly surveyed with a Trimble RTK GPS system (currently the R8 GNS model) which is accurate to within 5–20 mm. A few of the profiles were surveyed using a Nikon total station (current model NPL-332) which is accurate to 5 mm (around the accuracy of GPS). Fig. 2 shows a typical beach profile data at station 68. Each profile was generally surveyed twice per year, but there are a few gaps in the datasets due to site access issues (e.g. the UK foot-and-mouth crisis in 2001). At each profile location, a fixed land reference point was used as a starting point, and horizontal and vertical measurements were taken along the beach profile to a horizontal distance which extended to mean sea level (MSL). Bearings were strictly defined so that each beach profile was normal to the coastline. The positions of the stations and bearings were accurately duplicated at each repeat interval of the surveys (≈ 6 months). Since the horizontal resolution of raw beach profile data varied between each station and for each survey date (the distance between profile points vary from 1 m up

to 40 m), it was necessary to interpolate the raw data to a common sampling interval. Although ANN can also be used for interpolation, a 1 m linear interpolation was found to be a suitable method to capture details over the range of profiles, and to accurately define the intercept of each profile with both MSL and highest astronomical tide (HAT). For each location and survey date, the 1 m re-sampled data was averaged for all data points bounded by these two datum.

2.3. Wind data

Wind data at Valley (Fig. 1) is representative of conditions in Tremadoc Bay, as confirmed by correlations at several (coarse temporal resolution) meteorological stations in the bay (Neill et al., 2007, 2008). Valley was used as the wind data source since a long term dataset at high temporal resolution (hourly) was available at this, the closest synoptic meteorological station to Tremadoc Bay. Fig. 3. shows the time series of the wind speed for this station. The most frequent wind direction is SSW (210°), but the highest magnitude (storm) events tend to be southwesterly. Since the meteorological station at Valley is exposed to the Irish Sea to the southwest, it is an ideal location in which to measure these major southwesterly wind events with minimal topographic effects.

2.4. Nearshore wave model (SWAN)

An important factor in assessing beach profile changes is wave height. Since wave buoy data were not available close to the study region, a wave model was used to determine the effect of wind speed and direction on wave characteristics; primarily significant wave height, wave period and wave direction. In practice, application of the ANN method would require data from at least one wave buoy close to the study region, hence we have used a modeled wave climate as a surrogate. Since a long time series (> 1 year) simulation was required for this study, the spectral wave model SWAN was applied in stationary mode (Booij et al., 1999). As mentioned, the ANN has been also used in prediction of the wave parameters in the previous researches (e.g. Makarynskyy

Table 1
Survey date at spring and autumn.

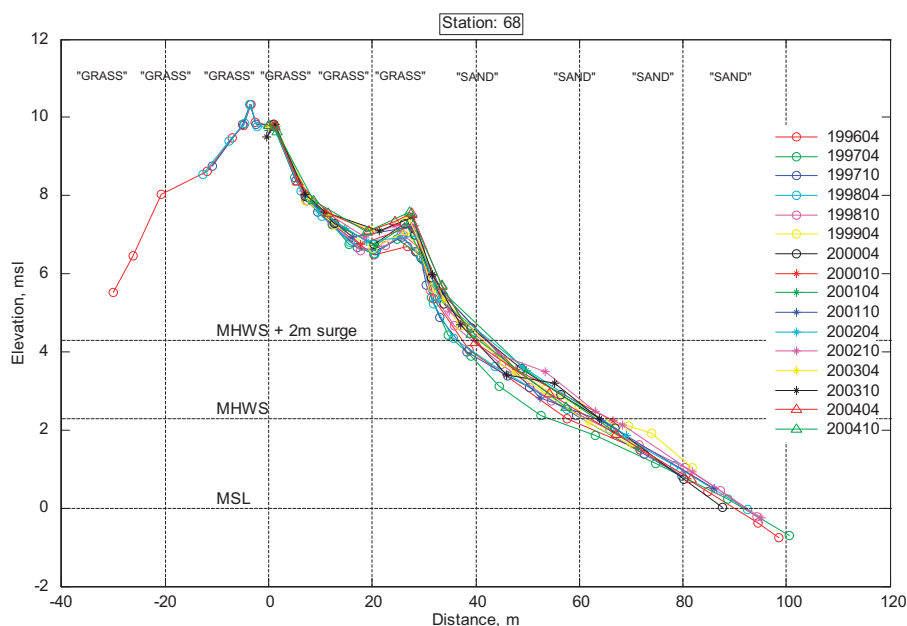| Autumn survey date	Spring survey date	Length(days)
12 November 1997	08 April 1998	148
01 December 1998	27 May 1999	182
08 October 1999	04 May 2000	211
12 October 2000	05 June 2001	236
16 November 2001	25 April 2002	162
18 November 2002	29 April 2003	162
04 November 2003	04 May 2004	182

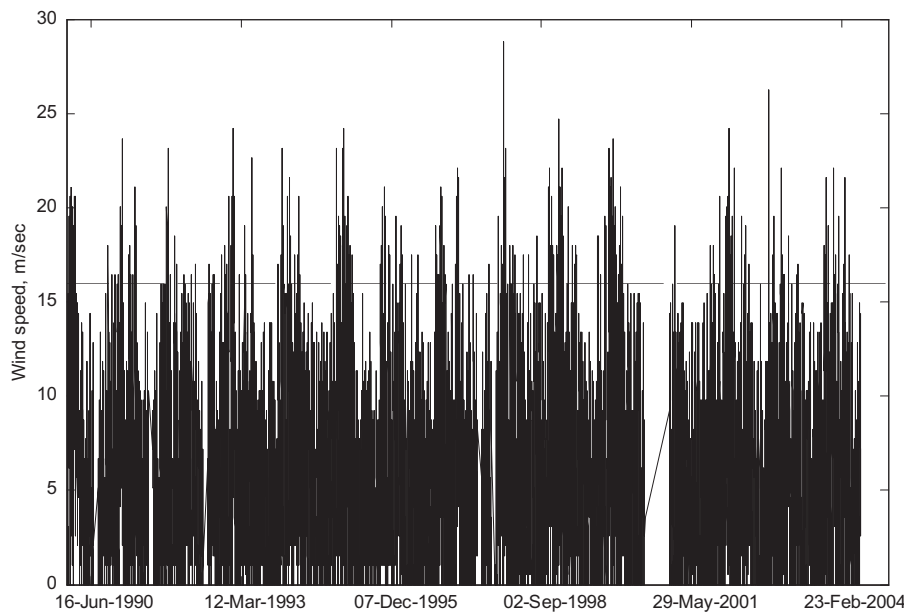**Fig. 2.** Beach profile surveys between 1996 and 2004 for a typical station in the study area, St. 68.

Fig. 3. Wind speed time series at Valley meteorological station, covering the time interval of beach profile surveys. The horizontal line 16 m/s represents a moderate gale.

and Makarynska, 2007) and particularly in Irish Sea (Makarynskyy, 2004). Nevertheless, SWAN model results were satisfactory for the study area (Neill et al., 2008) and was selected for this research. In stationary mode, the evolution of the action density N is governed by the time-independent wave action balance equation

$$\frac{\partial}{\partial x}c_x N + \frac{\partial}{\partial y}c_y N + \frac{\partial}{\partial \sigma}c_\sigma N + \frac{\partial}{\partial \theta}c_\theta N = \frac{S}{\sigma}$$

where c_x and c_y are the propagation velocities in the x and y directions, σ the frequency, θ the wave direction and S represents the source terms, i.e. generation, dissipation and non-linear wave–wave interactions. For each cell of the model grid, a matrix of significant wave height (H_s) and peak wave period (T_p) was produced as a lookup table using a discrete range of wind speeds and directions held constant over the entire model domain. From a consideration of the wind climate over the study region, a suitable range of discrete wind direction and speed bins was selected as $\theta=0,15,\ldots,345$ degrees and $W_r=2,4,\ldots,30$ m s^{-1}, respectively (i.e. $24\times15=360$ simulations) (Neill et al., 2008). The final products of the model (time series of H_s and T_p) were derived by applying actual wind data to the lookup tables. An outer shelf model was run initially at a resolution of $\sim$12 km (Neill et al., 2009) with a high resolution (1.85 km) nested model of the Irish Sea run with boundary conditions of the action density spectrum extracted from the outer grid (Neill et al., 2008). Within this Irish Sea grid was nested a 300 m resolution model of Tremadoc Bay and nested within this was a 100 m resolution innermost model of the region around Traeth Crugan (Fig. 4). Bathymetry for the Tremadoc Bay and Traeth Crugan models was digitized from Admiralty Charts 1971 and 1512, based on survey data collected between 1961 and 1983, hence a recognized source of error due to subsequent sediment erosion/deposition. However, this bathymetry data has been used successfully in previous studies (e.g. Neill et al., 2007, 2008). For each cell of the Traeth Crugan grid, a matrix of H_s, T_p and wave direction was produced for the range of wind speeds and directions. The method has been successfully validated with H_s and T_p in a wide range of water depths and for a wide range of wave exposures (Neill et al., 2008, 2009). Due to the good agreement between model and data, particularly over seasonal timescales, the use of a wave model as a

surrogate for in situ wave climate is not expected to introduce significant errors for this ANN study.

3. Artificial intelligence model structure

3.1. Introduction to artificial neural networks

Neural networks emerged as a field of study within AI in the late-1800s. It was invented by shared efforts of engineers, physicists, mathematicians, computer scientists, and neuroscientists (Bishop, 1995). Neural Networks were inspired by biological findings relating to the behavior of the brain as a network of units called neurons (Fig. 5). The human brain is estimated to have around 10 billion neurons, each connected on average to 10,000 other neurons. Each neuron receives signals through synapses that control the effects of the signal on the neuron. These synaptic connections are believed to play a key role in the behavior of the brain. By virtue of analogy of the human brain and ANN, the three basic components of the (artificial) neuron are:

1. The synapses or connecting links that provide weights (Fig. 5), w_j, to the input values, x_j for $j=1,\ldots,m$;
   The weights in neural nets are also often designed to minimize the error in a training dataset.
2. An adder that sums the weighted input values to compute the input to the activation function $v = w_0 + \sum_{j=1}^{m} x_j w_j$, where the bias, w_0, is a numerical value associated with the neuron.
3. An activation function g that maps v to $g(v)$, the output value of the neuron. This function is a monotone function (Fausett, 1994).

The main elements of an ANN are architecture, learning algorithm and activation function. The architecture of ANN is defined as the pattern of connections of neurons. The method of determining the weights is referred to as the learning or training method, and activation functions transform the input data to output in a neuron (Fausett, 1994).
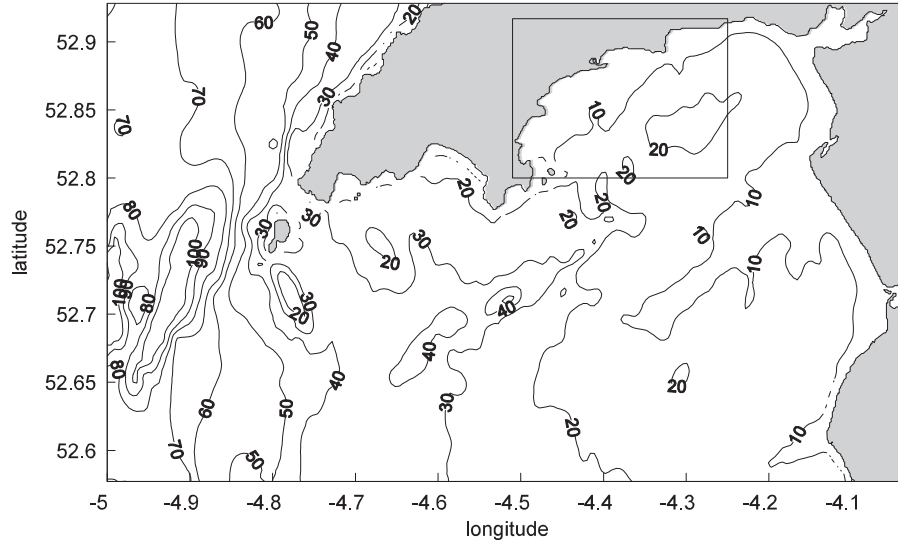
Fig. 4. Intermediate (Tremadoc Bay) and innermost (Traeth Crugan) wave model nests. Contours are of bathymetry (in meters) relative to mean sea level and shaded areas are land.
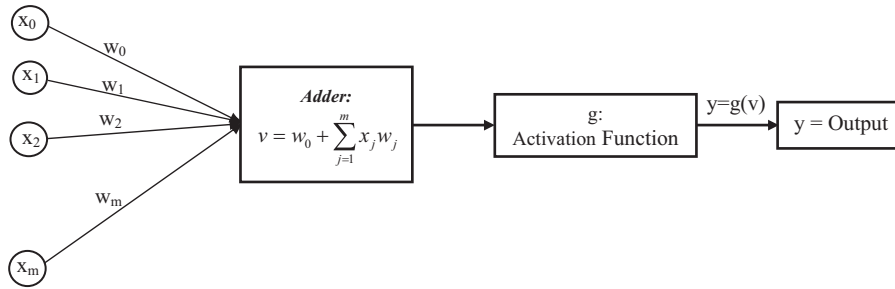

Fig. 5. Schematics of a mathematical model of a neuron.

Table 2
Selected storm characteristics. The storms between surveys are grouped by lines.

Storm	Date	Time	Duration, h	Mean wind speed, m/s	Max wind speed, m/s	Direction
1	22 January 1990	22:00:00	7	19.2	20.6	S
2	04 February 1990	01:00:00	16	18.7	20.1	S
3	05 February 1990	00:00:00	11	18.1	19.0	S
4	25 February 1990	23:00:00	9	19.3	20.6	SW
5	27 February 1990	09:00:00	6	18.7	19.5	W
6	05 January 1991	10:00:00	18	20.4	23.7	WSW
7	31 October 1991	02:00:00	7	19.1	20.1	S
8	15 January 1993	01:00:00	7	20.7	22.6	S
9	16 January 1993	10:00:00	7	18.1	18.5	S
10	16 January 1993	19:00:00	8	20.6	24.2	S
11	23 January 1993	17:00:00	10	19.1	20.6	SW
12	08 December 1993	17:00:00	10	20.7	23.2	W
13	17 December 1994	10:00:00	6	18.2	19.5	S
14	16 January 1995	05:00:00	8	18.4	19.5	S
15	17 January 1995	17:00:00	9	19.5	23.2	SSW
16	21 January 1995	11:00:00	8	19.8	24.2	SW
17	06 October 1995	03:00:00	6	18.7	20.1	S
18	25 October 1995	23:00:00	6	18.8	19.5	SSW
19	28 October 1996	08:00:00	8	19.3	21.1	SSW
20	17 February 1997	09:00:00	11	18.5	19.5	SSW
21	19 February 1997	07:00:00	9	20.8	22.1	SSW
22	01 March 1997	10:00:00	16	19.2	21.6	SSW
23	24 December 1997	14:00:00	9	23.7	28.8	SW
24	03 January 1998	13:00:00	9	18.7	20.1	W
25	20 October 1998	19:00:00	6	19.4	21.1	SSW
26	26 December 1998	11:00:00	15	21.0	24.7	SW
27	15 January 1999	05:00:00	12	19.7	22.1	SW
28	26 November 1999	01:00:00	11	20.1	23.2	SSW
29	28 November 1999	08:00:00	10	20.0	21.6	SSW
30	03 December 1999	01:00:00	8	19.9	21.1	WSW
31	08 December 1999	18:00:00	12	19.4	21.6	WSW

Table 2 (*continued*)

Storm	Date	Time	Duration, h	Mean wind speed, m/s	Max wind speed, m/s	Direction
32	23 December 1999	15:00:00	6	21.1	23.7	S
33	07 January 2000	08:00:00	10	18.1	20.1	SSW
34	09 February 2000	22:00:00	7	19.7	21.1	SSW
35	27 February 2000	05:00:00	6	18.6	19.5	SSW
36	03 October 2000	15:00:00	6	19.7	21.6	S
37	02 December 2000	01:00:00	6	18.2	19.5	SSW
38	31 December 2000	13:00:00	9	19.3	22.1	S
39	06 February 2001	13:00:00	6	18.2	19.0	SSW
40	03 December 2001	13:00:00	8	18.6	20.1	S
41	01 February 2002	04:00:00	9	20.7	24.2	S
42	02 February 2002	00:00:00	8	20.0	21.1	SSW
43	10 March 2002	04:00:00	8	19.4	22.1	SSW
44	24 May 2002	10:00:00	6	17.9	19.0	SSW
45	16 January 2003	23:00:00	7	19.4	22.1	S
46	14 November 2003	04:00:00	7	19.5	21.6	SSW
47	03 February 2004	05:00:00	7	18.3	19.5	SSW

Table 3
Correlation coefficient (r) of the input vector potential variables.

Input variable	Duration	Mean wind speed (m/s)	Max wind speed(m/s)	Wind direction	Number of successive wind	Number of wind	H_s (mean)	T_p (mean)	Direction of wave (mean)	Angle of beach	H_s (max)	T_p (max)	Direction of wave (max)
Duration	1.00	0.52	0.50	−0.45	0.38	0.26	−0.06	0.00	−0.18	0.00	−0.02	0.08	−0.12
Mean wind speed (m/s)	0.52	1.00	0.97	−0.57	0.10	0.11	−0.04	0.12	−0.25	0.00	0.08	0.25	−0.15
Max wind speed (m/s)	0.50	0.97	1.00	−0.57	−0.03	0.03	−0.04	0.12	−0.25	0.00	0.07	0.24	−0.15
Wind direction	−0.45	−0.57	−0.57	1.00	0.14	−0.04	0.11	−0.13	0.44	−0.01	−0.03	−0.30	0.32
Number of successive wind	0.38	0.10	−0.03	0.14	1.00	0.75	0.02	−0.05	0.04	0.01	0.01	0.00	0.06
Number of wind	0.26	0.11	0.03	−0.04	0.75	1.00	0.00	−0.04	−0.06	0.02	0.04	0.08	0.05
H_s (mean)	−0.06	−0.04	−0.04	0.11	0.02	0.00	1.00	0.65	−0.78	0.76	0.98	0.49	−0.86
T_p (mean)	0.00	0.12	0.12	−0.13	−0.05	−0.04	0.65	1.00	−0.56	0.42	0.67	0.89	−0.58
Direction of wave (mean)	−0.18	−0.25	−0.25	0.44	0.04	−0.06	−0.78	−0.56	1.00	−0.66	−0.81	−0.53	0.96
Angle of beach	0.00	0.00	0.00	−0.01	0.01	0.02	0.76	0.42	−0.66	1.00	0.76	0.27	−0.72
H_s (max)	−0.02	0.08	0.07	−0.03	0.01	0.04	0.98	0.67	−0.81	0.76	1.00	0.56	−0.86
T_p (max)	0.08	0.25	0.24	−0.30	0.00	0.08	0.49	0.89	−0.53	0.27	0.56	1.00	−0.47
Direction of wave (max)	−0.12	−0.15	−0.15	0.32	0.06	0.05	−0.86	−0.58	0.96	−0.72	−0.86	−0.47	1.00

3.2. Network architecture

While numerous ANN architectures have been researched, the most successful applications in data mining and simulations have been multilayer feedforward networks (Iglesias et al., 2009; Ni, 2008).

3.3. Feedforward backpropagation (FFBP) neural network

As mentioned, the network architecture and learning algorithm are the main characteristics of a neural network. The FFBP network architecture consists of the input layer, the hidden layer(s) and the output layer. The FFBP learning algorithm is divided into feedforward and backpropagation stages. For a given network architecture, in the feedforward stage, the effect of the input vector is propagated to the network, layer by layer, using connectivity between neurons. The weight of each connection is constant during the feedforward stage. Consequently, the response of the network to the input layer is represented as an output layer which is not necessarily equal to the real output. The network output is compared to the real output and the error is calculated. Errors produced during the feedforward stage must be minimized using the error backpropagation algorithm. During the backpropagation stage, the errors are passed through the network in the backward direction, and the weights are adjusted using the gradient decent method (Haykin, 1999).

Given a set of input and output data (usually 80% of the data are used for training and 20% for the test of ANN (Bing et al., 2008),

FFBP algorithm can be summarized as follows:

1. Using the input data and starting with predefined weights, the computations proceed from the input layer towards the output layer.
2. By comparing desired and computed outputs, the mean square errors are computed and backpropagated in the reverse direction (i.e. output to input) using the gradient descent method. This procedure leads to the adjustment of the weights and bias.
3. Steps 1 and 2 are repeated until the stopping criteria are satisfied.

The optimum network is the network which can be trained and tested using a minimal number of weights, neurons and hidden layers. Moreover, the transfer function influences the accuracy of ANN in addition to the computational cost. Therefore, the network architecture should be designed to minimize the computational cost given the desired accuracy.

This study employs a standard backpropagation algorithm for training. The structure of ANN presented here is not complex, and the problem is not a very time consuming one. So, the trial and error procedure was used to optimize the number of hidden neurons (Rumelhart et al., 1986). However, more effective methods are available for complicated and time consuming networks (e.g. Miller et al., 1995).

The accuracy of ANN is evaluated by the mean square error

$$MSE = \frac{\sum_{i=1}^{N} (y_i - \hat{y}_i)^2}{N}$$

where y_i is the observed data, $\hat{y}_i$ the calculated data, and N the number of observations. The elevations of the beach at each profile were used as y_i which will be explained in more detail later.

4. Model structure

The correct selection of input and output vectors, along with network parameters, is a key step towards designing a powerful ANN. Learning too many input–output samples may lead to over-fitting or over-training the problem. In this situation, more hidden neurons and computational effort are required, but the ability of the network to generalize between similar input and output is lost. To prevent over-training, or to make valid generalizations, the network architecture must be designed in a manner which is consistent with the physics of the problem. The transfer functions must also be selected to be as simple as possible in the absence of any prior knowledge (Haykin, 1999).

Since the training and test datasets are limited, it is desirable to reduce the number of unknown weighting coefficients as much
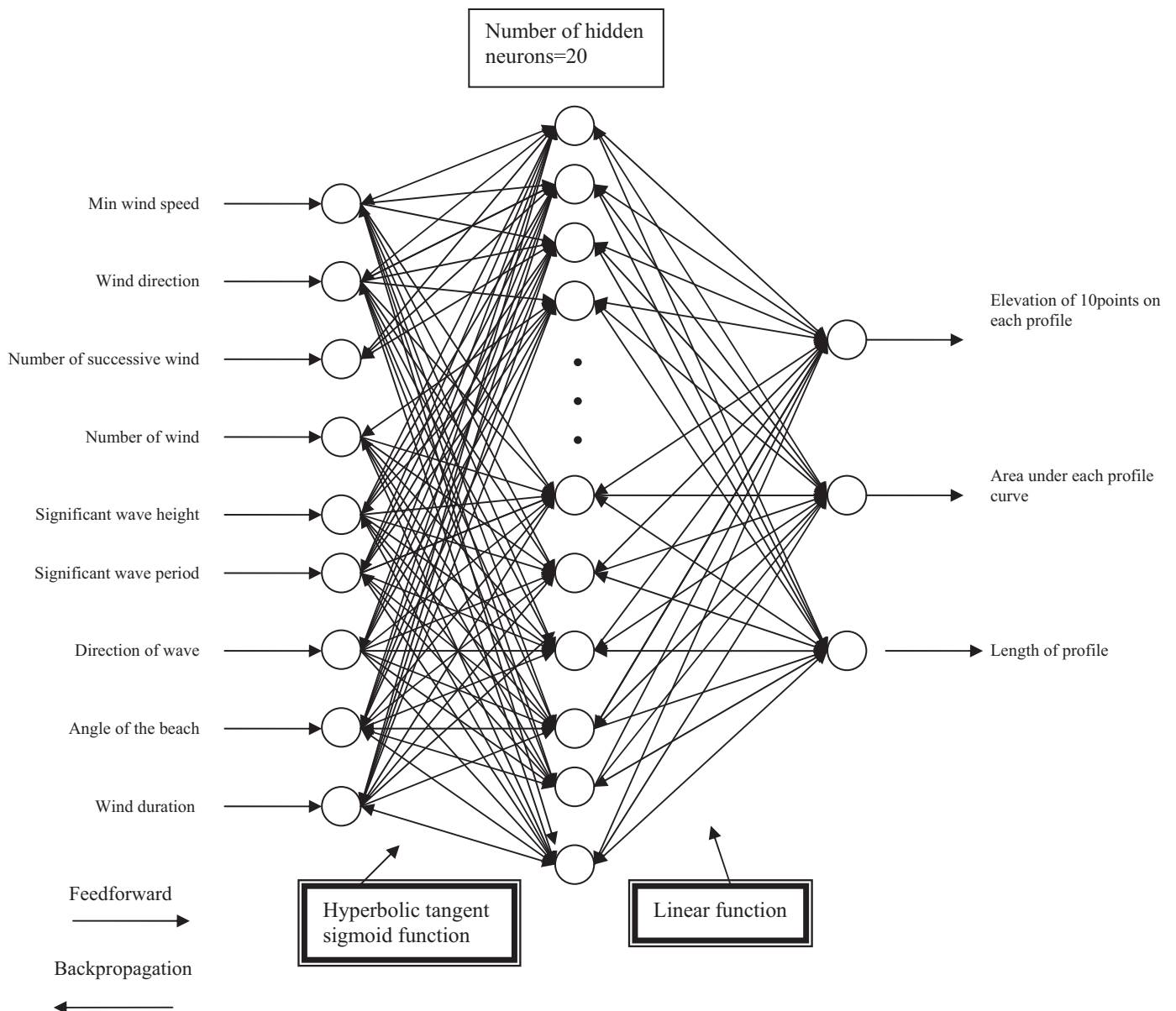
Fig. 6. The structure of ANN used for beach profile prediction.

as possible. The numbers of unknown weighting coefficients are directly proportional to the size of input and output vectors, the number of hidden neurons in each hidden layer, and the number of hidden layers. Numerical experiments on the data used for the

present research demonstrates that unwise selection of these elements leads to poor ANN results.

4.1. Selection of input vector

As a first step in the design of the network architecture, the input parameters which affect the outputs should be determined. The spatial and temporal beach profiles are the final output of ANN. Accordingly, all of the physical factors which affect the beach profile changes such as wind speed, wave characteristics, beach angle, beach material properties and tidal data are potential candidates for input vectors. To account for the effect of the wind, the time series of the wind between two profile surveys was analyzed, and several statistical parameters derived, such as maximum wind speed, average of mean wind speed, storm durations and so on. By setting up a threshold value for wind speed (for instance $16 \, \mathrm{m \, s^{-1}}$—a moderate gale) on the time series, the number of 'storms' between two surveys can be evaluated. If storms occur successively, their effect on the beach may be intensified. Hence, the number of successive storms is also recorded as another input variable. For the time interval of each storm, the storm duration, average and maximum wind speed, average wind direction and other important factors were evaluated. Table 2 shows the results of the analysis of the wind data. These storm parameters were used as candidates for the wind part of the input vector.

To decrease the size of input vectors, highly correlated data should be excluded. In general, some phenomena are so complicated and have many affecting parameters where their relationships are not well understood. In such cases, analytical techniques such as cross-correlation and principal component analysis (PCA) may be employed for the selection of effective input data (Maier and Dandy, 1997; Johnson and Wichern, 2003). Cross-correlation can only detect linear dependency of variables. Hence, if the relation of variables is non-linear, this method will be approximate for input reduction. The selection of input vector parameters requires a combination of experience with data, and the use of analytical methods. As mentioned above, the size of the input vector should be minimized to construct an effective ANN.

Table 4
Eigenvalues of input data for PCA method.

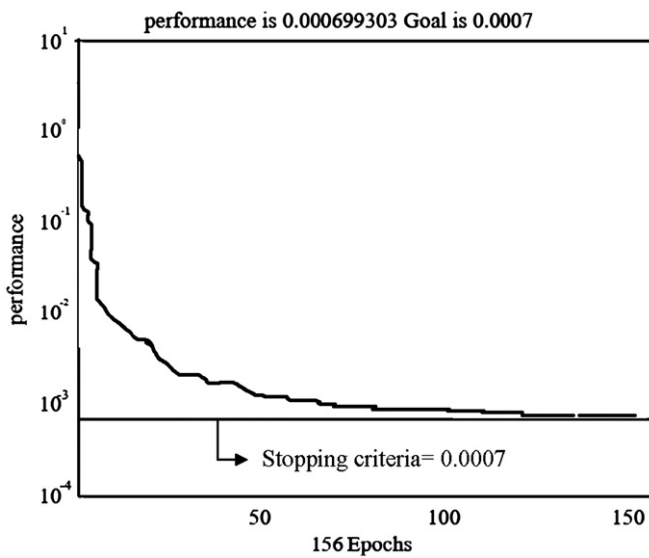| Eigenvalue #1 | 13,189.1471 |
Eigenvalue #2	371.9301
Eigenvalue #3	88.6518
Eigenvalue #4	5.5762
Eigenvalue #5	3.2186
Eigenvalue #6	1.4169
Eigenvalue #7	0.6458
Eigenvalue #8	0.0712
Eigenvalue #9	0.0171
Eigenvalue #10	0.0061

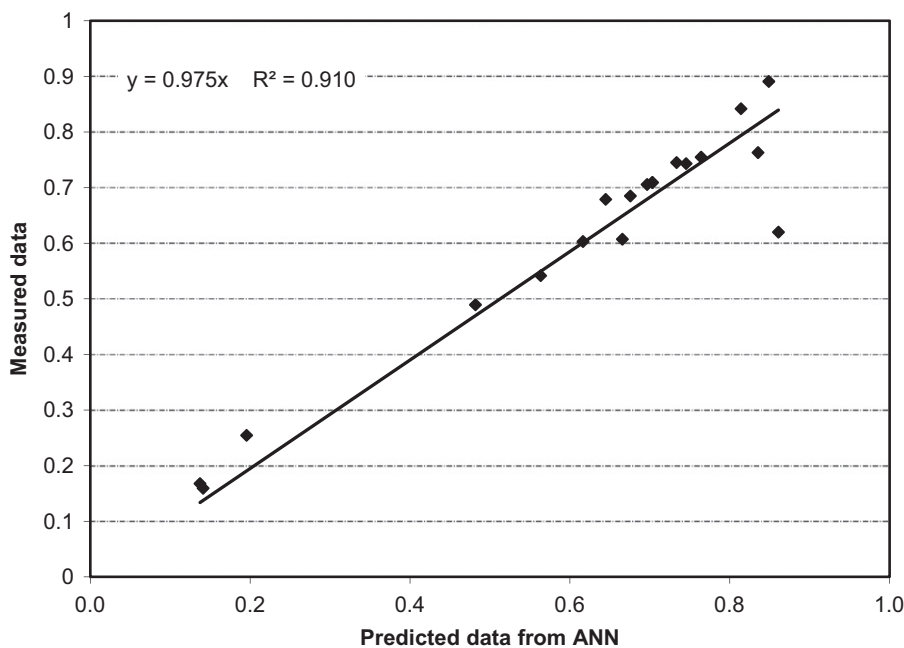

Fig. 7. Performance of ANN for 156 epochs.

Fig. 8. Comparison of predicted beach profile against measured beach profiles at different locations and times.

Therefore, minimal data which best represents the entire dataset should be chosen (Maier and Dandy, 1997).

Apart from experience with such data, two analytical methods were used to detect significant input data: cross-correlation matrices and PCA. The method having the better performance was used for this purpose.

In the cross-correlation method, the correlation between each pair of input data was determined (Table 3). In cases of high coefficient of determination ($R^2 > 0.8$), one of the input data can be omitted from input vector. For example, maximum wind speed has a high coefficient of determination with mean wind speed and can be omitted. Fig. 6 shows the screened selected input and output data, based on correlation analysis.

The idea of PCA is to transform the input data, including correlated components, into another smaller input vector having uncorrelated

components. The computation of the principal components consists of three steps. Firstly, each data value is subtracted from its mean value. Next, the correlation of data with each other are computed and stored in the covariance matrix. Finally, the eigenvalues and eigenvectors of this matrix are computed. The eigenvector corresponding to the first maximum eigenvalue is the first principal component axis. The eigenvector corresponding to the second eigenvalue is regarded as the second principal component and so on. After the computation of principal components, they can be used instead of actual data for ANN input. Although principal components, unlike actual input data, are physically meaningless, they can reduce the size of input data effectively, and hence improve ANN performance. Table 4 shows the results of PCA for the input data considered in this study. Based on this table, three components, namely eigenvalues one to three, are sufficient to represent the input data.
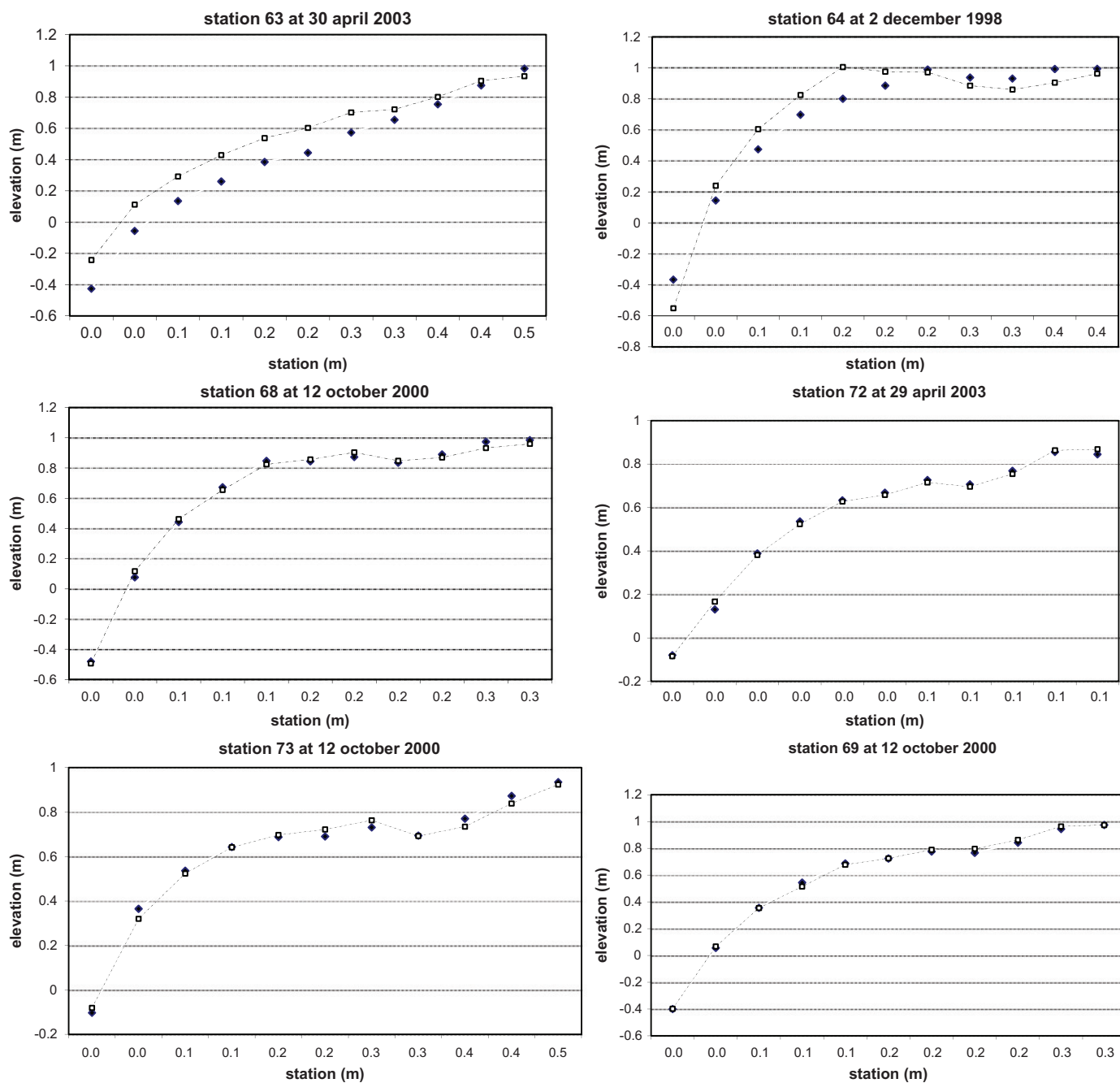
Fig. 9. Comparing predicted (dash lines) against measured beach profiles (points) at different locations and times (test data). Comparing predicted (dash lines) against measured beach profiles (points) at different locations and times (test data).
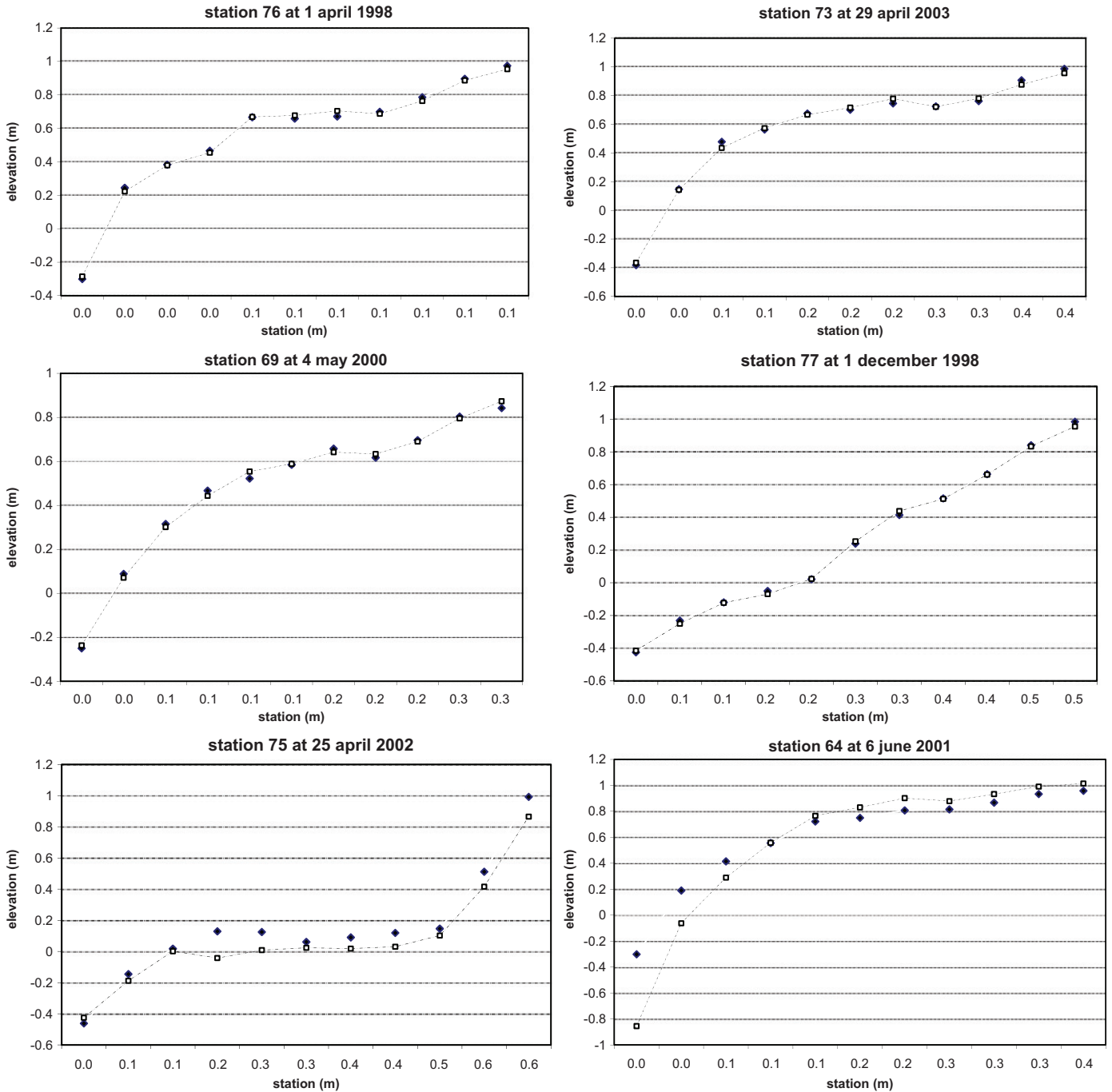
Fig. 9. (*Continued*)

After training ANN using the input data provided by the two methods described above, it was observed that the correlation matrix method leads to better performance compared with PCA (performance of ANN (evaluated by MSE) is 0.0054 for PCA and 0.0007 for correlation matrixes). Therefore, the correlation matrix method was adopted in this study.

4.2. Selection of hidden layers

A number of empirical relationships between the number of training samples and the number of connection weights have been suggested in the literature (Haykin, 1999). However, the network geometry is highly dependent on the problem and the properties of the available data. The optimum ANN architecture which can effectively capture the relationship between the input and output data is usually determined by trial and error. For the present application, an ANN having one hidden layer was used. This has also been suggested from the mathematical viewpoint by previous research (Hornik, 1993). The addition of more hidden layers did not improve the results. Twenty hidden neurons for the hidden layers were used by trial and error (Rumelhart et al., 1986).

4.3. Internal parameters of the model

Different types of activation function can be used in FFBP ANN, such as sigmoid, linear and tangent. A suitable activation function

for hidden and output layers is problem-dependent. In the present study, the hyperbolic tangent sigmoid (tansig) function for hidden layers and linear (purelin) in the output layers led to satisfactory results (Fausett, 1994).

Since the tansig activation function was used in the model, the input–output data were normalized in the range −1 to 1 to fall within the function limits. A standard backpropagation algorithm was employed to estimate the network parameters. The performance of the algorithm is sensitive to the correct setting of the learning rate. The learning rate is related to the complexity of the local error surface and cannot be determined before training. The performance of the steepest descent algorithm can be improved if the learning rate is allowed to evolve during the training process (Fausett, 1994).

4.4. Model training and evaluation

The designed structure of the ANN model for predicting beach profile evolution consists of 9 input neurons, 20 hidden neurons in one layer and 12 output neurons (Fig. 6). The available data were divided into training (80%) and test data (20%). Fig. 7 shows the performance of ANN model during the training process. The maximum number of epochs was set 200. As can be seen, the performance goal (0.0007 mean square error) was achieved after 156 epochs. In the next section, the results of the model in predicting seasonal beach level changes are presented and discussed in some detail.

5. Model results and discussion

The trained model was verified using the remaining 20% of data (i.e. test data). The main objective of the model is to predict spatial and temporal variations of beach profiles due to storm waves. The predicted beach profiles and the area under the beach profiles were compared against measured data for several stations, as shown in Figs. 8 and 9. It should be emphasized that since the test data were randomly selected from 20% of beach profile data, all of the profile data have not been presented in these figures. Furthermore, the agreement of ANN model results and measured data for the other 80% of data (training data) was satisfactorily controlled using performance criterion (MSE less than 0.0007). The horizontal and vertical axes in Fig. 9 represent the normalized horizontal distance and beach elevation, respectively. The RMSE and correlation coefficient between predicted and measured data are shown in Table 5. As these figures and table suggest, the predicted results are generally highly significant with the measured data. Therefore, it can be claimed that ANN can effectively capture the relationship

between input and output for beach profile changes in this case study. Nevertheless, some major and minor discrepancies are observed at certain times for certain stations (e.g. Station 64 on 6 June or St. 63 on 30 April). These discrepancies can be associated with several factors such as lack of sufficient training data, in addition to some effective factors which have not been included in the ANN model. For instance, the effect of tidal currents on beach profile changes was ignored, and the wave model does not account for swell waves. The spatial variations of beach material such as grain size distribution and cohesion were not considered. The measurement errors (input and/or output) can be regarded as another source of discrepancy.

Considering the results of highly sophisticated mathematical models for the same case study (Neill et al., 2008), the results of ANN are quite convincing. ANN is also inexpensive in terms of computational cost. It does not require the calibration and verification of empirical sediment transport equations (e.g. long-shore and cross-shore transport) or beach level change models. However, despite these advantages of the ANN model, there are various drawbacks and shortcomings of black box models. The most important shortcoming is the dependency of the model on good quality data for training, particularly output data. Consequently, ANN models, unlike mathematical models, cannot be used in extreme conditions which have not been trained for. For instance, ANN prediction may not be reliable for a severe storm event (e.g. a 1 in 100 year event) which has not been covered by the training dataset. Extreme value theory (EVT) may also be useful in regions where rare events naturally appear. If human activities lead to a change in beach levels, e.g. the impact of coastal defenses or port construction, ANN may be of minimal use. Overall, the ANN model is an efficient and flexible numerical tool which can be helpful in prediction of conditions occurring within the range of the historical data. Its use can be recommended in parallel with mathematical models. The performance of the model can be improved by increasing the quantity and quality of the training data and the input data.

6. Conclusion

The performance of the neural network technique was examined in predicting seasonal beach profile evolution in a small bay. Several ANN architectures were designed for this specific data and evaluated for modeling beach profile changes, and the mean square error was used for the evaluation criteria. The ANN model converged to the desired mean square error (MSE) (0.0007) for the training data, and the MSE was within the acceptable range for the test data. The performance of ANN can be significantly improved by omitting correlated data, and the correlation matrix method was used in this case to omit unnecessary data. The type of transfer function also has a key role in obtaining a converged ANN model. The *tansig* function gives satisfactory results for this type of data.

The results of this study show that ANN can be used as an effective tool in predicting beach profile evolution. The ANN results are more convincing than results obtained by mathematical models of the same region, due to complexity and uncertainties associated with physical understanding of morphodynamics in the coastal zone. In addition, considerably less computational effort is required to construct an ANN model. However, the application of ANN is limited to the historical training data and it cannot be applied in hypothetical situations such as future port construction or extreme events which have not been incorporated in the training data. The combined application of mathematical models and artificial intelligence is recommended to model these types of the processes. Although

Table 5
Comparison of RMSE and correlation coefficient between measured and predicted beach profiles.

Station	Date	RMSE	Correlation coefficient
77	1 December 1998	0.0151	0.9989
76	8 April 1998	0.0176	0.9975
63	30 April 2003	0.1319	0.7050
64	2 December 1998	0.1141	0.9389
64	6 June 2001	0.1948	0.9930
68	12 October 2000	0.0254	0.9968
69	4 May 2000	0.0187	0.9965
69	12 October 2000	0.0165	0.9986
72	29 April 2003	0.0157	0.9971
73	12 October 2000	0.0258	0.9912
73	29 April 2003	0.0228	0.9964
75	25 April 2002	0.0452	0.9903

good results were obtained for the Tremadoc Bay case study, as more data is appended to the data archive, it should lead to improved ANN results.

Acknowledgements

References

Bing, Y., Qing, H.Z., Onyx, W.H.W., 2008. Prediction of sand ripple geometry under waves using an artificial neural network. Computers and Geosciences 34, 1655–1664.

Bishop, C.M., 1995. Neural Networks for Pattern Recognition. Oxford University Press, New York.

Booij, N., Ris, R.C., Holthuijsen, L.H., 1999. A third-generation wave model for coastal regions—1. Model description and validation. Journal of Geophysical Research—Oceans 104, 7649–7666.

Browne, M., Castelle, B., Strauss, D., Tomlinson, R., Blumenstein, M., Lane, C., 2007. Near-shore swells estimation from a global wind–wave model: spectral process, linear, and artificial neural network models. Coastal Engineering 54, 445–460.

Chau, K., 2006. A review on the integration of artificial intelligence into coastal modeling. Journal of Environmental Management 80, 47–57.

Cipollini, P., Corsini, G., Diani, M., Grasso, R., 2001. Retrieval of sea water optically active parameters from hyperspectral data by means of generalized radial basis function neural networks. IEEE Transactions on Geoscience and Remote Sensing 39, 1508–1524.

Dong, P., Chen, H., 1999. A probability method for predicting time-dependent long-term shoreline erosion. Coastal Engineering 36, 243–261.

Fausett, L., 1994. Fundamentals of Neural Networks Architectures, Algorithms and Applications. Prentice-Hall International.

Ghorbani, M.A., Khatibi, R., Aytek, A., Makarynskyy, O., Shiri, J., 2010. Sea water level forecasting using genetic programming and comparing the performance with artificial neural networks. Computers and Geosciences 36 (5), 620–627.

Gunawardena, Y., Ilic, S., Pinkerton, H., Romanowicz, R., 2009. Nonlinear transfer function modelling of beach morphology at Duck, North Carolina. Coastal Engineering 56, 46–58.

Haykin, S., 1999. Neural Network—A Comprehensive Foundation. Prentice-Hall, New Jersey.

Herman, A., Kaiser, R., Niemeyer, H.D., 2009. Wind–wave variability in a shallow tidal sea—spectral modelling combined with neural network methods. Coastal Engineering 56, 759–772.

Hornik, K., 1993. Some new results on neural network approximation. Neural Networks 6 (8), 1069–1072.

Huang, W., Murray, C., Kraus, N., Rosati, J., 2003. Development of a regional neural network for coastal water level predictions. Ocean Engineering 30, 2275–2295.

Iglesias, G., López, I., Carballo, R., Castro, A., 2009. Headland-bay beach planform and tidal range: a neural network model. Geomorphology 112, 135–143.

Johnson, R.A., Wichern, D.W., 2003. Applied Multivariate Statistical Analysis. Prentice-Hall of India.

Jones, O.P., Petersen, O.S., Kofoed-Hansen, H., 2007. Modelling of complex coastal environments: some considerations for best practise. Coastal Engineering 54, 717–733.

Kalra, R., Deo, M.C., Kumar, R., Agarwal, V.K., 2005. Artificial neural network to translate offshore satellite wave data to coastal locations. Ocean Engineering 32, 1917–1932.

Karunarathna, H., Reeve, D., Spivack, M., 2009. Beach profile evolution as an inverse problem. Continental Shelf Research 29, 2234–2239.

Kroon, A., Davidson, M.A., Aarninkhof, S.G.J., Archetti, R., Armaroli, C., Gonzalez, M., Medri, S., Osorio, A., Aagaard, T., Holman, R.A., Spanhoff, R., 2007. Application of remote sensing video systems to coastline management problems. Coastal Engineering 54, 493–505.

Larson, M., Capobianco, M., Hanson, H., 2000. Relationship between beach profiles and waves at Duck, North Carolina, determined by canonical correlation analysis. Marine Geology 163, 275–288.

Larson, M., Capobianco, M., Jansen, H., Różyński, G., Southgate, H.N., Stive, M., Wijnberg, K.M., Hulscher, S., 2003. Analysis and modeling of field data on coastal morphological evolution over yearly and decadal time scales. Part 1: Background and linear techniques. Journal of Coastal Research 19, 760–775.

Lee, K.H., Mizutani, N., Kim, D.S., Fujii, T., 2009. Estimation of wave breaking in gravel beach using artificial neural network. In: Proceedings of the International Offshore and Polar Engineering Conference, pp. 951–957.

Lee, T.-L., Makarynskyy, O., Shao, C.-C., 2007. A combined harmonic analysis—artificial neural network methodology for tidal predictions. Journal of Coastal Research 23 (3), 764–770.

Liang, S.X., Li, M.C., Sun, Z.C., 2008. Prediction models for tidal level including strong meteorologic effects using a neural network. Ocean Engineering 35, 666–675.

Maier, H.R., Dandy, G.C., 1997. Determining inputs for neural network models of multivariate time series. Computer-Aided Civil and Infrastructure Engineering 12, 353–368.

Makarynska, D., Makarynskyy, O., 2008. Predicting sea level variations at the Cocos (Keeling) Islands with artificial neural networks. Computers and Geosciences 34 (12), 1910–1917.

Makarynskyy, O., 2004. Improving wave predictions with artificial neural networks. Ocean Engineering 31 (5–6), 709–724.

Makarynskyy, O., Makarynska, D., 2007. Wave prediction and data supplementation with artificial neural networks. Journal of Coastal Research 23 (4), 951–960.

Miller, D.M., Kaminsky, E.J., Rana, S., 1995. Neural network classification of remote-sensing data. Computers and Geosciences 21, 377–386.

Neill, S.P., Elliott, A.J., Hashemi, M.R., 2008. A model of inter-annual variability in beach levels. Continental Shelf Research 28, 1769–1781.

Neill, S.P., Hashemi, M.R., Elliott, A.J., 2007. An enhanced depth-averaged tidal model for morphological studies in the presence of rotary currents. Continental Shelf Research 27, 82–102.

Neill, S.P., Scourse, J.D., Biggs, G.R., Uehara, K., 2009. Changes in wave climate over the northwest European shelf seas during the last 12,000 years. Journal of Geophysical Research 114, C06015.

Ni, X., 2008. Research of data mining based on neural networks, world academy of science. Engineering and Technology 39, 381–384.

Panizzo, A., Briganti, R., 2007. Analysis of wave transmission behind low-crested breakwaters using neural networks. Coastal Engineering 54, 643–656.

Pape, L., Ruessink, B.G., Wiering, M.A., Turner, I.L., 2007. Recurrent neural network modeling of nearshore sandbar behavior. Neural Networks 20, 509–518.

Ranasinghe, R., Symonds, G., Black, K., Holman, R., 2004. Morphodynamics of intermediate beaches: a video imaging and numerical modelling study. Coastal Engineering 51, 629–655.

Reeve, D., Li, Y., Lark, M., Simmonds, D., 2007. An investigation of the multi-scale temporal variability of beach profiles at Duck using wavelet packet transforms. Coastal Engineering 54, 401–415.

Różyński, G., 2003. Coastal Nearshore Morphology in Terms of Large Data Sets. Institute of the Hydroengineering of the Polish Academy of Sciences (IBW PAN) (83-85708-51-0).

Rumelhart, D.E., Hinton, G.E., Williams, R.J., 1986. Learning representations by back-propagating errors. Nature 323, 533–536.

Teodoro, A.C., Veloso-Gomes, F., Gonçalves, H., 2007. Retrieving TSM concentration from multispectral satellite data by multiple regression and artificial neural networks. IEEE Transactions on Geoscience and Remote Sensing 45, 1342–1350.

Yagci, O., Mercan, D.E., Cigizoglu, H.K., Kabdasli, M.S., 2005. Artificial intelligence methods in breakwater damage ratio estimation. Ocean Engineering 32, 2088–2106.

Yan, B., Zhang, Q.H., Wai, O.W.H., 2008. Prediction of sand ripple geometry under waves using an artificial neural network. Computers and Geosciences 34, 1655–1664.
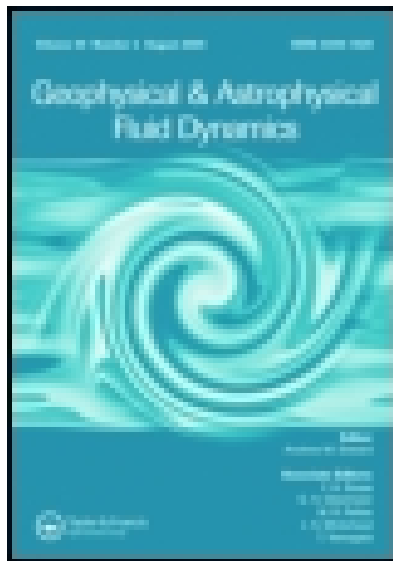
.8 Published work P-VII

Geophysical & Astrophysical Fluid Dynamics

A coupled tide-wave model for the NW European shelf seas

M. Reza Hashemi[a], Simon P. Neill[a] & Alan G. Davies[a]

[a] School of Ocean Sciences, Bangor University, Menai Bridge, UK.
Published online: 14 Aug 2014.

CrossMark

Click for updates

PLEASE SCROLL DOWN FOR ARTICLE

Taylor & Francis
Taylor & Francis Group

A coupled tide-wave model for the NW European shelf seas

M. REZA HASHEMI*, SIMON P. NEILL and ALAN G. DAVIES

School of Ocean Sciences, Bangor University, Menai Bridge, UK

Understanding the interaction of tides and waves is essential in many studies, including marine renewable energy, sediment transport, long-term seabed morphodynamics, storm surges and the impacts of climate change. In the present research, a COAWST model of the NW European shelf seas has been developed and applied to a number of physical processes. Although many aspects of wave–current interaction can be investigated by this model, our focus is on the interaction of barotropic tides and waves at shelf scale. While the COWAST model was about five times more computationally expensive than running decoupled ROMS (ocean model) and SWAN (wave model), it provided an integrated modelling system which could incorporate many wave–tide interaction processes, and produce the tide and wave parameters in a unified file system with a convenient post-processing capacity. Some applications of the model such as the effect of tides on quantifying the wave energy resource, which exceeded 10% in parts of the region, and the effect of waves on the calculation of the bottom stress, which was dominant in parts of the North Sea and Scotland, during an energetic wave period are presented, and some challenges are discussed. It was also shown that the model performance in the prediction of the wave parameters can improve by 25% in some places where the wave-tide interaction is significant.

Keywords: UK shelf seas; NW European shelf seas; SWAN; ROMS; COAWST; Wave-tide interactions

1. Introduction

The NW European shelf seas, and in particular the UK shelf seas, dissipate around 10% of global tidal energy (i.e. 0.25 TW; see Egbert and Ray 2003), and are also considered to be amongst the most energetic of wave climates, due to their exposure to the North Atlantic. Therefore, understanding the interaction of tides and waves is essential in many studies of this region, including studies of marine renewable energy (Hashemi and Neill 2014), sediment transport, long-term seabed morphodynamics, storm surges and the impacts of climate change.

A few studies have attempted to model the interaction of tides and waves over the north-west European shelf seas (Wolf 2009). For instance, Bolanos-Sanchez *et al.* (2009) coupled the POLCOMS ocean model and the WAM wave model in a two-dimensional (depth-averaged), two-way mode and implemented several processes including wave refraction by currents, bottom friction due to combined currents and waves, and enhanced wind drag due

---

*Corresponding author. Email: r.hashemi@bangor.ac.uk

to waves. Further, they implemented three-dimensional interactions such as Stokes drift, radiation stress and Doppler velocity (Bolanos *et al.* 2011). The POLCOMS-WAM modelling system has been applied in a number of studies, including an investigation of surges in the Irish sea, and has been shown to predict well the surge and wave conditions (Brown *et al.* 2010).

Other three-dimensional ocean models have been developed to study wave-current interactions. For instance, Newberger and Allen (2007a) added wave forcing in the form of surface and body forces to the Princeton Ocean Model (POM) for applications in the surf zone. They incorporated a surface force proportional to wave energy dissipation, the effect of wave-current interactions on bottom stress calculations and body forces resulting from the wave radiation stress tensor into POM's new nearshore formulation. The nearshore version of POM was then applied to the nearshore surf zone off Duck, North Carolina, during the DUCK94 field experiment of October 1994 (Newberger and Allen 2007b).

The Coupled Ocean-Atmosphere-Wave-Sediment Transport (COAWST) modelling system comprises the ocean model ROMS, the atmospheric model WRF (Weather Research and Forecasting), the wave model SWAN and the sediment capabilities of the Community Sediment Transport Model. The data exchange between these modules is conducted by the Model Coupling Toolkit (Warner *et al.* 2010). The ocean, wave and atmospheric elements of COAWST are open source, and very popular amongst ocean and atmospheric modellers. ROMS, the Regional Ocean Modelling System, has been widely applied to a range of scales in shelf sea modelling for barotropic and baroclinic tides (e.g. Di Lorenzo *et al.* 2007, Haidvogel *et al.* 2008, MacCready *et al.* 2009). The ROMS code is highly flexible, and can be compiled assuming a diverse range of physics and solution algorithms, applied to the momentum equations, horizontal and vertical advection, pressure gradient, turbulence, open boundary forcing, sediment transport and wave–current interactions (Warner *et al.* 2010). SWAN, Simulating WAves Neashore, has been applied in many wave studies of this region (e.g. Neill and Hashemi 2013, Saruwatari *et al.* 2013), and includes the effect of ambient currents, water depth fluctuations and friction in its formulation. The COAWST modelling system has been used in various applications such as wave energy assessment and wave current interactions in the Adriatic Sea (Barbariol *et al.* 2013, Benetazzo *et al.* 2013) and surf zone dynamics using a new WEC (Wave Effects on Currents) vortex-force formalism (Uchiyama *et al.* 2010, Kumar *et al.* 2012).

Due to the attractive features of COAWST compared with other models, we, here, develop and present a COAWST model of the NW European shelf seas. Although many aspects of wave–current interaction can be investigated by this model, our main focus is on the interaction of barotropic tides and waves at shelf scale. Example applications such as the effect of tides on quantifying the wave energy resource, and the effect of waves on bottom stress are presented, and some issues and challenges discussed.

2. Theoretical background

Although various aspects of wave–current interactions in the SWAN and ROMS models have previously been discussed in detail in several papers, a brief yet comprehensive background of the wave–tide interaction formulation is presented here. This provides an overview of the processes that have been or can be modelled, and helps to understand the concept of the coupled model in relation to the COAWST switches for compilation (i.e. cpp flags which are C++ pre-compilation options).

2.1. *Wave modelling*

In the real sea state, the wave energy is distributed over a range of frequencies and directions, and can be represented by the directional wave energy density spectrum, $E(\sigma, \theta)$. The mathematical formulation of SWAN is based on the conservation of the action density rather than wave energy because in the presence of an ambient current, action density is conserved, as opposed to the energy density. The action density is defined as $N(\boldsymbol{x}, t; \sigma, \theta) = E/\sigma$ where σ is the relative angular wave frequency which is not affected by the Doppler shift. The SWAN formulation is based on the evolution of the wave action density in space and time, and can be expressed as

$$\frac{\mathrm{D}N}{\mathrm{D}t} = \frac{\partial N}{\partial t} + \nabla_\perp \cdot \left[(\boldsymbol{c}_g + \boldsymbol{u})N\right] + \frac{\partial(c_\sigma N)}{\partial \sigma} + \frac{\partial(c_\theta N)}{\partial \theta} = \frac{S}{\sigma}, \tag{1}$$

where $\nabla_\perp = (\partial/\partial x, \partial/\partial y)$ is the horizontal gradient operator; $\boldsymbol{u} = (\overline{u}, \overline{v})$ represents the depth averaged current velocities; $c_\sigma = \mathrm{d}\sigma/\mathrm{d}t$ and $c_\theta = \mathrm{d}\theta/\mathrm{d}t$ are propagation velocities in spectral space. S represents the source/sink term which represents all physical processes that generate (e.g. wind), dissipate (e.g. white capping, bottom friction and depth-induced wave breaking), or redistribute wave energy (wave–wave interactions). The group velocity is defined as

$$\boldsymbol{c}_g = \frac{\partial \sigma}{\partial \boldsymbol{k}} = \frac{1}{2}\left(1 + \frac{2kd}{\sinh(2kd)}\right)\frac{\sigma}{k^2}\,\boldsymbol{k}, \tag{2}$$

where $\boldsymbol{k} = (k_x, k_y)$ is the wave number and is related to the water depth, d, and wave frequency through the dispersion relation, $\sigma^2 = gk\tanh(kd)$. The absolute angular frequency of waves, ω which is observed in a stationary frame like a wave buoy or a wave energy device, is modified by the Doppler shift to $\omega = \sigma + \boldsymbol{k}\cdot\boldsymbol{u}$.

2.1.1. *Effect of tides on waves in the SWAN formulation*

Referring to SWAN's formulation, this model implicitly implements the effect of ambient currents and water elevation changes in its formulation. The water depth change (e.g. due to tides) and currents can either be provided through input files, or via model coupling. Further, the effect of currents on wave energy dissipation due to bottom friction is not taken into account in SWAN. However, it has been argued that the uncertainty in estimation of bottom roughness is larger than the actual impact on energy dissipation (Tolman 1992). In COAWST, additional formulations for computation of wave energy dissipation are available, based on the research of Reniers *et al.* (2004).

2.2. *Tidal modelling*

ROMS is a three-dimensional topographic following model which is based on the Reynolds averaged Navier-Stokes equations. The mathematical formulation of ROMS, with inclusion of WEC terms, consists of the continuity equation,

$$\nabla \cdot \boldsymbol{v} = 0, \tag{3}$$

the horizontal momentum equations,

$$\frac{\partial u}{\partial t} + (\boldsymbol{v}\cdot\nabla)u = fv - \frac{\partial(p/\rho_o)}{\partial x} - \frac{\partial}{\partial z}\left(\overline{u'w'} - \nu\frac{\partial u}{\partial z}\right) + S_u + D_u + F_u^{CW} + F_u^{NCW}, \tag{4a}$$

Table 1.   List of symbols in ROMS formulation.

Symbol	Description
$\boldsymbol{v}$	Time averaged velocity vector, (u, v, w)
$\boldsymbol{v_{st}}$	Stokes velocities, where $(u_{st}, v_{st}) = (2E/c)\left[\cosh\left(2k(z+d)\right)/\sinh\left(2kD\right)\right]\boldsymbol{k}$ and the vertical component, w_{st}, is computed based on the continuity. D is wave averaged thickness of water column and d is water depth
f	Coriolis parameter
S_u, S_v	Non-wave non-conservative forces
D_u, D_v	Optional horizontal diffusive terms
ϕ	Scalar quantity such as temperature, salinity, nutrient concentration or other tracers
S_ϕ	Tracer Sink/source term
F^{CW}	Sum of conservative wave related forces resulting from wave radiation forces
F^{NCW}	Sum of the non-conservative wave related forces resulting from wave energy dissipation
u', v', w'	Turbulent fluctuating velocities
p	Pressure
ρ_o, ρ	Reference density and density
ν	Kinematic viscosity
ν_θ	Molecular diffusivity
ε	Wave-induced tracer diffusivity
μ_t, D_t	Turbulent viscosity and diffusivity
K	Turbulent kinetic energy density, $K = \frac{1}{2}(u'^2 + v'^2 + w'^2)$
Ψ	Generic length scale. $\Psi = c^p K^m l^n$ where c is a constant and p, m and n are constants which are set for a particular turbulent scheme (e.g. $K - \epsilon$ model: $p = 3$, $m = 1.5$ and $n = -1$)
P_k, ϵ_k	Production and dissipation of turbulent kinetic energy
σ_k, σ_ψ	Turbulence Schmidt numbers
S_Ψ	Sink/Source terms of the general length scale
τ_{bx}, τ_{by}	Combined wave-current induced bottom stresses

$$\frac{\partial v}{\partial t} + (\boldsymbol{v} \cdot \boldsymbol{\nabla})v = -fu - \frac{\partial(p/\rho_o)}{\partial y} - \frac{\partial}{\partial z}\left(\overline{v'w'} - \nu\frac{\partial v}{\partial z}\right) + S_v + D_v + F_v^{CW} + F_v^{NCW},$$
(4b)

and the vertical momentum (hydrostatic relation) equation,

$$\frac{\partial(p/\rho_o)}{\partial z} + \frac{\rho}{\rho_o}g = F_w^{CW}.$$
(5)

Table 1 presents a list of symbols. In addition to the common terms in the horizontal momentum equations, which are local and convective accelerations, Coriolis force, pressure force, turbulent and fluid shear stresses, other terms (i.e. F^{CW} and F^{NCW}) have been added to the right-hand sides of (4a,b) to account for the wave forces.

The wave forces can generally be divided into conservative and non-conservative forces. The flux of momentum due to the wave hydrodynamic field is generally referred to as the wave radiation stress. The conservative wave forces arise from the gradient of the wave radiation stresses, which consist of a vortex force and a wave induced Bernoulli head. The non-conservative terms represent the wave dissipation induced forces, and can be further divided into the forces generated by bottom friction, surface friction, white capping and depth induced breaking. In COAWST, WEC-VF (Kumar *et al.* 2012) and WEC-MELLOR (Mellor 2008) are the alternative cpp switches to include these forces.

2.2.1. *Bottom stress calculations*

Many hydrodynamic field variables such as velocity, turbulent Reynolds stresses, turbulent energy dissipation and turbulent viscosity have a sharp gradient near the bed over a short

distance within bottom boundary layer (BBL). These processes cannot usually be resolved in the vertical discretization of an ocean model like ROMS and therefore need to be parameterised. The treatment of the BBL directly affects the hydrodynamic field through the implementation of the boundary conditions,

$$
\mu_t \left.\frac{\partial u}{\partial s}\right|_{s=-1} = \tau_{bx}, \qquad\qquad \mu_t \left.\frac{\partial v}{\partial s}\right|_{s=-1} = \tau_{by}, \qquad\qquad \text{(6a,b)}
$$

where s represents the vertical direction in the sigma coordinate. Further, sediment transport computations are directly affected by the formulation used for the BBL, which thereby quantifies the bed shear stress (Davies *et al.* 1988). Several methods for parameterising wave–current interactions in bed shear calculations can be selected (Warner *et al.* 2008) by the following switches: SG-BBL (Styles and Glenn 2002), MB-BBL (Soulsby and Clarke 2005) and SSW-BBL (Madsen 1994, Malarkey and Davies 2003). The local bed shear stress is calculated at each grid node from the near-bed wave velocity amplitude, the wave period and the equivalent bed roughness, through a series of conventional steps that have been presented by Warner *et al.* (2008).

2.2.2. *Tracer and turbulence transport formulation in the presence of waves*

An equation of state is required to compute the water density as a function of temperature and salinity ($\rho = f(T, S, p)$). The tracer equation which formulates the general transport of a scalar variable, including temperature and salinity, can be written as

$$
\frac{\partial \phi}{\partial t} + (\boldsymbol{v} + \boldsymbol{v}_{st})\cdot\nabla\phi = -\frac{\partial}{\partial z}\left(\overline{\phi'w'} - (\nu_\theta + 0.5\varepsilon)\frac{\partial\phi}{\partial z}\right) + S_\phi, \qquad\qquad \text{(7)}
$$

in which additional advection due to wave induced Stokes velocities and wave induced tracer diffusivity has been incorporated.

ROMS has several turbulence closure schemes to parameterise the turbulent shear stresses and turbulent tracer fluxes as follows (Warner *et al.* 2005):

$$
\overline{u'w'} = -\mu_t\frac{\partial u}{\partial z}, \qquad \overline{v'w'} = -\mu_t\frac{\partial v}{\partial z}, \qquad \overline{\phi'w'} = -D_t\frac{\partial\phi}{\partial z}. \qquad\qquad \text{(8a–c)}
$$

ROMS implements a general length scale (GLS) turbulence model in which turbulent viscosity and diffusivity are computed as a function of the turbulence kinetic energy and the length scale (i.e. $\mu_t, D_t \propto \sqrt{K}l$). The general two-equation transport model for turbulence kinetic energy and generic length scale can be formulated as

$$
\frac{\partial K}{\partial t} + u\frac{\partial K}{\partial x} + v\frac{\partial K}{\partial y} = \frac{\partial}{\partial z}\left(\frac{\mu_t}{\sigma_k}\frac{\partial K}{\partial z}\right) + P_k - \epsilon_k, \qquad\qquad \text{(9a)}
$$

$$
\frac{\partial\Psi}{\partial t} + u\frac{\partial\Psi}{\partial x} + v\frac{\partial\Psi}{\partial y} = \frac{\partial}{\partial z}\left(\frac{\mu_t}{\sigma_\psi}\frac{\partial\Psi}{\partial z}\right) + \frac{\Psi}{K}S_\Psi. \qquad\qquad \text{(9b)}
$$

The GLS formulation can be tuned to several classical turbulence models such as the Mellor-Yamada level 2.5 scheme, $K - \epsilon$, or $K - \omega$, by setting the ROMS input turbulent parameters. The effect of wave breaking in enhanced turbulent mixing has been implemented in the COAWST model (see for details Warner *et al.* 2005, Kumar *et al.* 2012).

3. Development of the COAWST Coupled tide-wave model

3.1. *Study area*

The study area extended from 14°W to 11°E, and from 42°N to 62°N (figure 1). A typical study period was selected in order to present the results of the coupled tide-wave model. Since the tidal regime is similar throughout the year, the wave regime provided the basis for the selection of a typical modelling period. Neill and Hashemi (2013) recently quantified temporal variability of the wave power resource over the same study area. Table 2 shows the monthly variability of the wave resource over the study region during 2005–2011 based on this research. According to this table, January 2005 and December 2006, with average monthly wave powers of 74.2 and 84.6 kW/m, respectively, may be considered as samples of highly energetic months. January 2005, as a typical stormy month, has been used here to highlight the importance of the wave-tide interactions. Nevertheless, even in this month, very low and even negligible wave energy regions occur in some parts of the domain, in addition to the high-energy regions.

3.2. *Model settings*

Although the COAWST system consists of several models, by setting cpp compilation options of the model, it is possible to choose the models which need to be coupled (e.g. ROMS + SWAN, SWAN + WRF or ROMS + SWAN + WRF). To meet the objectives of the present study, ROMS and SWAN were coupled in COAWST, and the wind forcing was provided by existing global data-sets as discussed later.

The ROMS model domain was discretised with a horizontal curvilinear grid, with a longitudinal resolution of $1/24°$ and variable latitudinal mesh size ($1/32° \sim 1/51°$ to ensure an approximately uniform cell aspect ratio. The model bathymetry was based on the ETOPO (www.ngdc.noaa.gov/mgg/global) global bathymetric data-set, which is available at a resolution of 1 arcminute. The vertical grid consisted of 11 layers distributed according to the ROMS topographic-following coordinate system. The open boundaries of the tidal model were forced by elevation (Chapman boundary condition) and tidal velocities (Flather boundary condition), generated using 10 tidal constituents (M_2, S_2, N_2, K_2, K_1, O_1, P_1, Q_1, M_f, M_m) obtained from TPXO7 global tide data which has $0.25° \times 0.25°$ resolution (volkov.oce.orst.edu/tides/). The COAWST compilation switches for ROMS (cpp flags) were: SSW-BBL for combined wave–current bottom friction, WEC-VF (using vortex formalism for inclusion of wave effects on currents), horizontal and vertical mixing of momentum, and Coriolis. Regarding the turbulence closure model, Warner *et al.* (2005) compared different ROMS turbulence schemes which are based on the generic scale method for a number of test cases, and concluded that they lead to very similar results, apart from one scheme ($k - kl$). In the present research, we used the generic length scale closure model for turbulence modelling, set to $K - \epsilon$ ($p = 3, m = 1.5$, and $n = -1$; see for details Warner *et al.* 2005).

SWAN was applied to the same curvilinear grid and bathymetry as the ROMS model. However, the open boundaries for the wave model may need further treatment. Figure 2 shows a sample from the ERA-Interim data-set of a wave field generated in the North Atlantic ocean which is approaching the study area. In SWAN, it is possible to run a larger model first, and provide the boundary information for the nested model (here, the NW European shelf model; for further details see Neill and Hashemi 2013). It should be mentioned that the lower energy swell waves are a more significant component affected by the boundary forcing compared with the higher energy wind waves which are usually developed by local winds. To enhance the
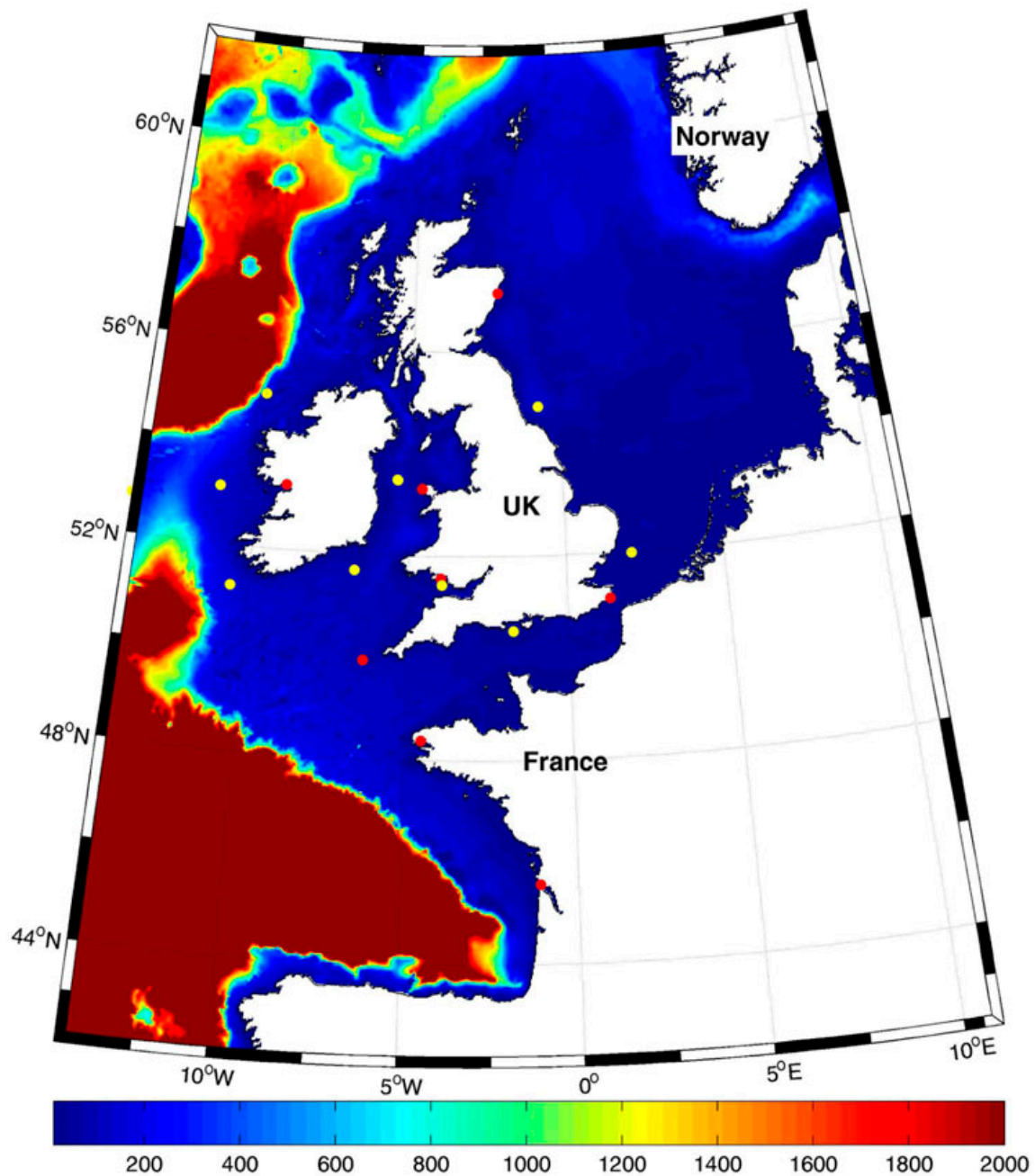
Figure 1.   The computational domain used for the coupled tide-wave model. The colour scale (refer to the web version) represents the bathymetry in metres, and the filled circles show the location of validation points (red represents a tidal, and yellow represents a wave point).

model performance, the wave model was nested inside a larger model of the North Atlantic Ocean. The parent model included the entire North Atlantic at a grid resolution of $1/6^{\circ} \times 1/6^{\circ}$, extending from 60°W to 15°E, and from 40°N to 70°N. Two-dimensional wave spectra were output hourly from the parent model and interpolated to the boundary of an inner nested model of the NW European shelf seas. Wind forcing was provided by European Centre for Medium-Range Weather Forecasts (ECMWF; www.ecmwf.int). ERA (Interim reanalysis) full resolution data, which are available three-hourly at a spatial resolution of $0.75^{\circ} \times 0.75^{\circ}$ were used. This wind data is based on model simulations that include data assimilation. SWAN was run in third-generation mode, with Komen linear wave growth and whitecapping, and quadruplet wave–wave interactions.

Table 2.   The inter-monthly variability of wave energy during 2005–2011 averaged over the NW European shelf seas (the same study area as Neill and Hashemi (2013)).

Year	Jan	Feb	Mar	Apr	May	Jun	Jul	Aug	Sep	Oct	Nov	Dec
2005	<u>74.2</u>	35.2	21.9	21.2	11.8	8.3	9.0	12.0	18.3	29.9	42.9	29.2
2006	32.6	37.2	29.2	20.4	15.5	8.1	9.2	8.2	17.5	24.0	67.6	84.6
2007	65.4	54.2	50.6	11.0	19.7	10.3	9.9	13.5	19.5	15.9	26.6	56.7
2008	54.1	46.1	54.5	20.9	7.2	10.2	12.0	15.0	18.7	39.5	35.1	44.9
2009	72.8	25.7	35.2	16.1	21.2	8.4	12.2	14.1	18.9	26.0	71.7	39.8
2010	30.7	31.1	25.9	18.6	9.4	10.5	17.0	9.0	19.6	32.1	50.5	25.4
2011	23.6	72.2	30.6	28.4	23.6	13.6	12.0	11.2	23.9	35.4	47.2	77.3
Avg.	50.5	43.1	35.4	19.5	15.5	9.9	11.6	11.9	19.5	29.0	48.8	51.1
SD.	21.3	15.9	12.5	5.3	6.3	1.9	2.8	2.6	2.1	7.8	16.3	22.9
Min.	23.6	25.7	21.9	11.0	7.2	8.1	9.0	8.2	17.5	15.9	26.6	25.4
Max.	<u>74.2</u>	72.2	54.5	28.4	23.6	13.6	17.0	15.0	23.9	39.5	71.7	<u>84.6</u>
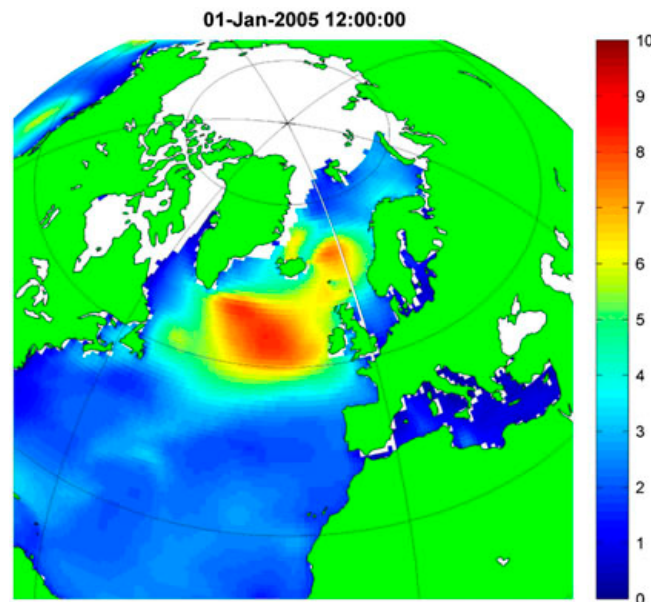
Figure 2.   An example of a wave field generated in the North Atlantic Ocean and approaching the UK shelf seas. The colour scale (refer to the web version) represents the significant wave height in metres. The global wave data is extracted from the ECMWF ERA-Interim dataset.

4. Results and discussion

4.1. *Validation*

The tide and wave results of the coupled COAWST model were first validated at a number of locations across the domain, listed in table 3. Following the validation, some results based on the coupled model are presented and discussed. Since most tidal models are forced by tidal constituents, it is a usual practice to validate model results against measured data in terms of the tidal constituents. The tidal energy of the NW European shelf seas is mainly distributed between the M_2 and S_2 components of the tide. Figure 3 shows the comparison of the model results and the measured data for these constituents. Based on these results, the relative error for amplitude and phase of M_2 were 13 cm and 8°, respectively, which is convincing. Also, good agreement was obtained for the S_2 component, as shown in this figure. Additionally, model results were compared with the global FES2012 dataset (Carrère *et al.* 2012). This
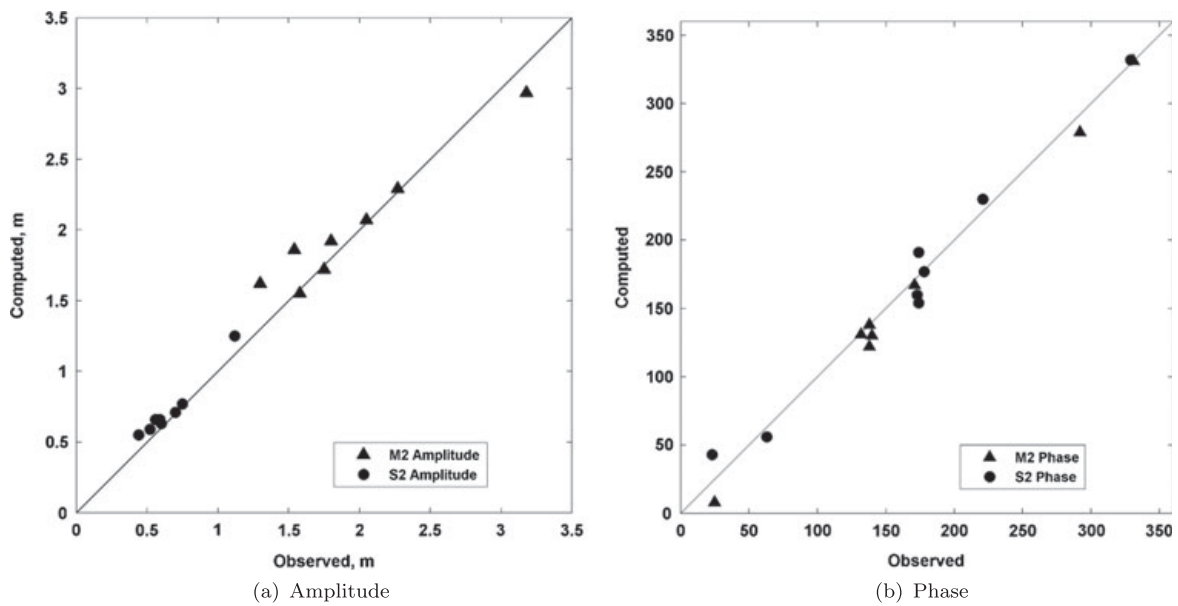
(a) Amplitude   (b) Phase

Figure 3. Validation of the ROMS results at a number of tidal gauges distributed across the domain. The absolute relative error for amplitude and phase of M_2 are 13 cm and 8$^\text{o}$, respectively. The corresponding values for S_2 amplitude and phase are 7 cm and 11$^\text{o}$. The locations of tidal gauges are reported in table 3.
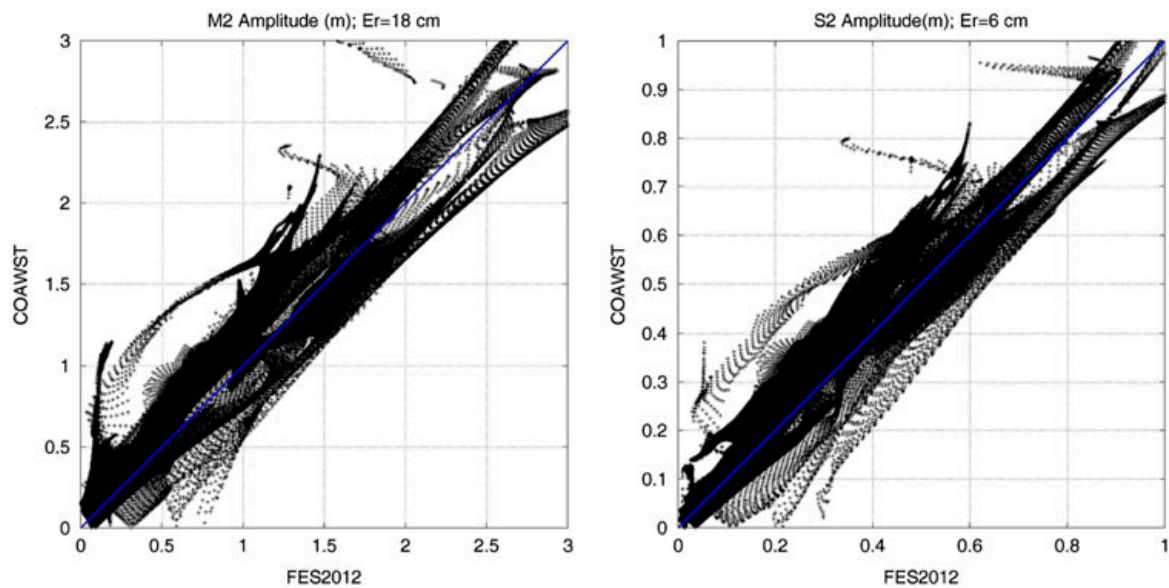

Figure 4. Comparison of the COAWST modelled amplitudes and FES2012 data. The axes units are metres.

data-set is based on hydrodynamic modelling, and data assimilation of altimetry data. The mean model performance over the entire model domain was good. For instance, figure 4 shows the comparisons for M_2 and S_2 amplitudes, which led to mean absolute errors of 18 cm and 6 cm, respectively.

Cotidal maps and tidal ellipses provide a more comprehensive basis for assessment of a tidal model. The computed $M2$ and S_2 cotidal charts based on the COAWST model are plotted in figure 5. These charts show the magnitude of tidal energy in terms of tidal range over the domain. Tidal ellipses, which reflect the magnitude and direction of the tidal currents, were also computed (figure 6), and these are in convincing agreement with the results of previous model studies (e.g. Pingree and Griffiths 1979, Neill *et al.* 2010).

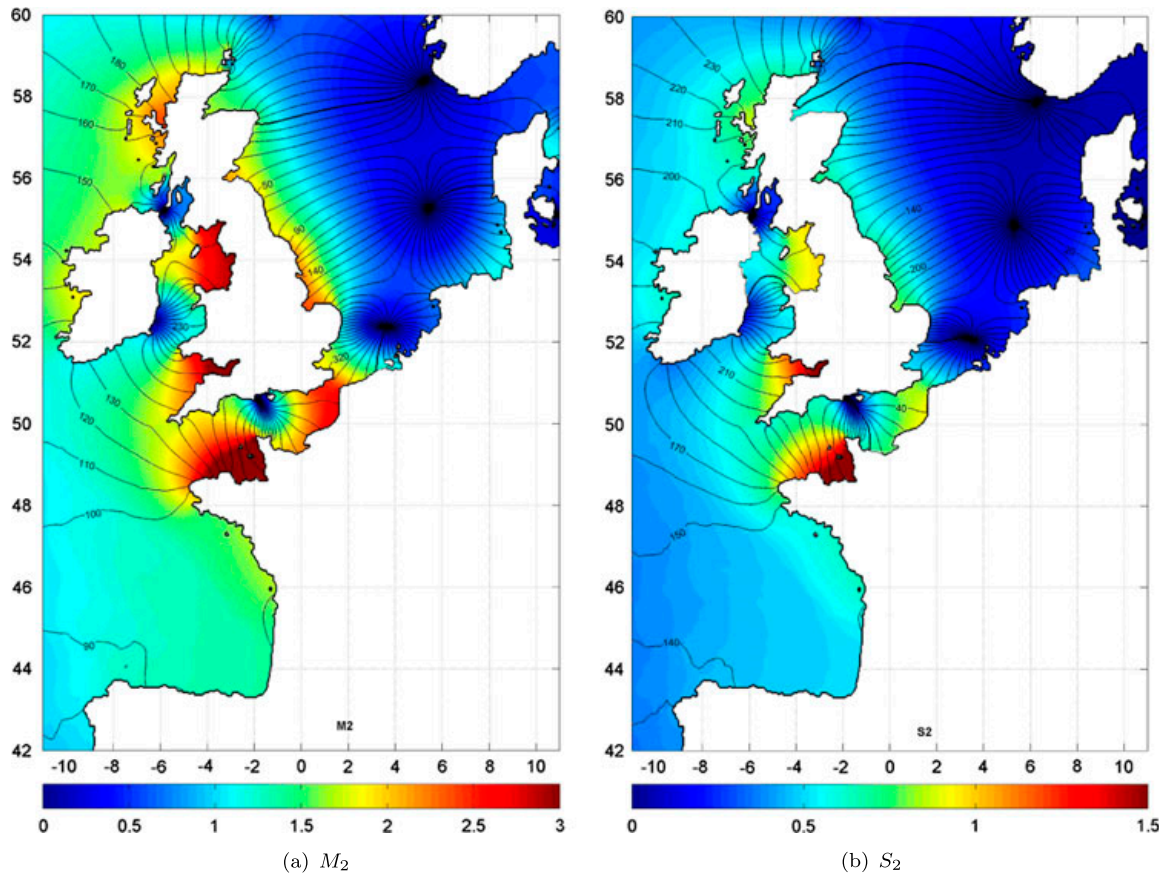(a) M_2 (b) S_2

Figure 5. Cotidal charts of the main tidal constituents over the study area based on the ROMS model output. The colour scale (refer to the web version) indicates the amplitude while the phases are represented by the contour lines.
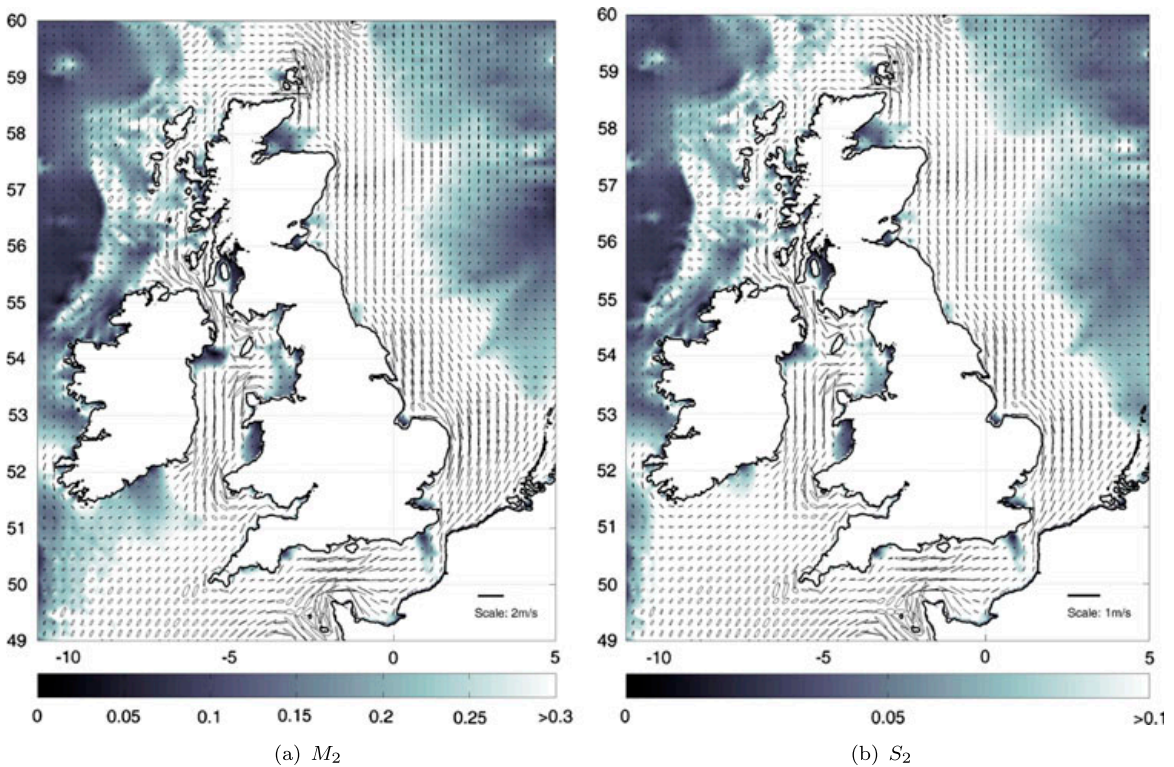

(a) M_2 (b) S_2

Figure 6. Tidal ellipses of the main tidal constituents representing the magnitude and direction of the tidal currents over the study area. The colour scale (refer to the web version) represents the velocity amplitude in m/s.
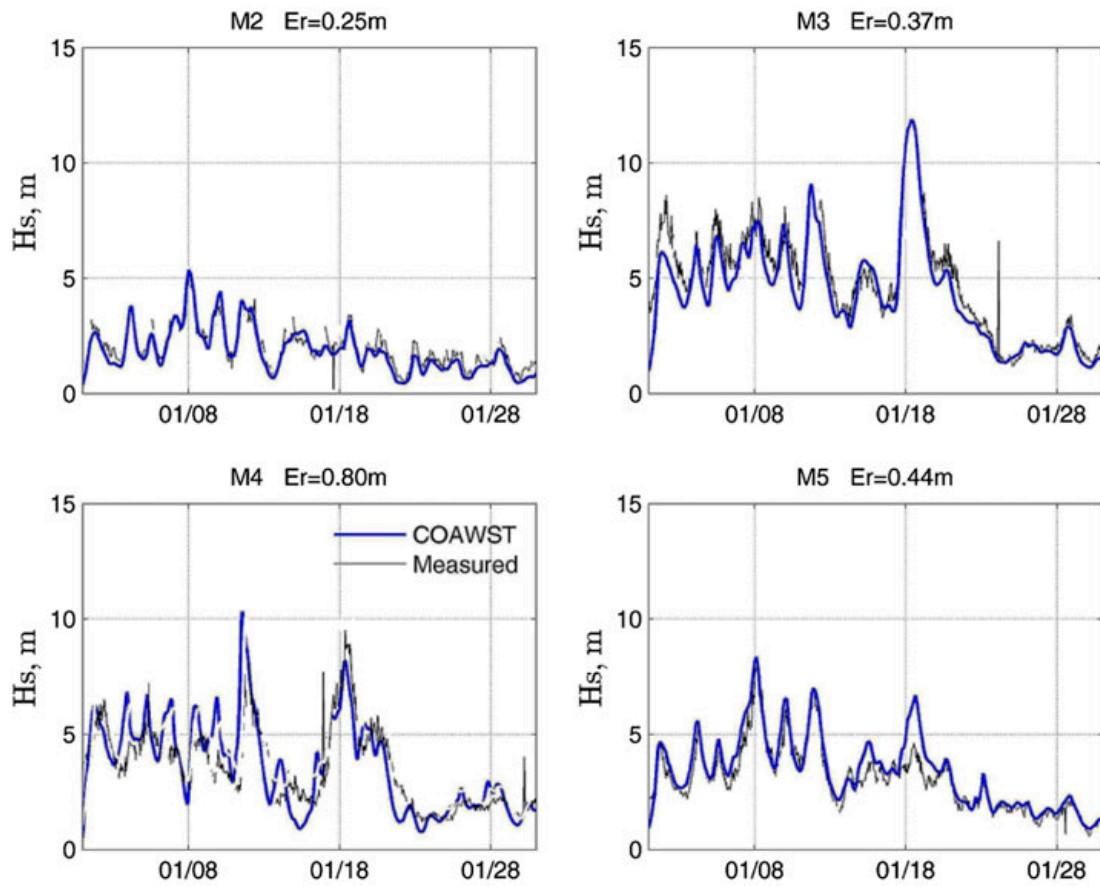
Figure 7.   Validation of the COAWST wave height results at a number of wave buoys (table 3) during January 2005.
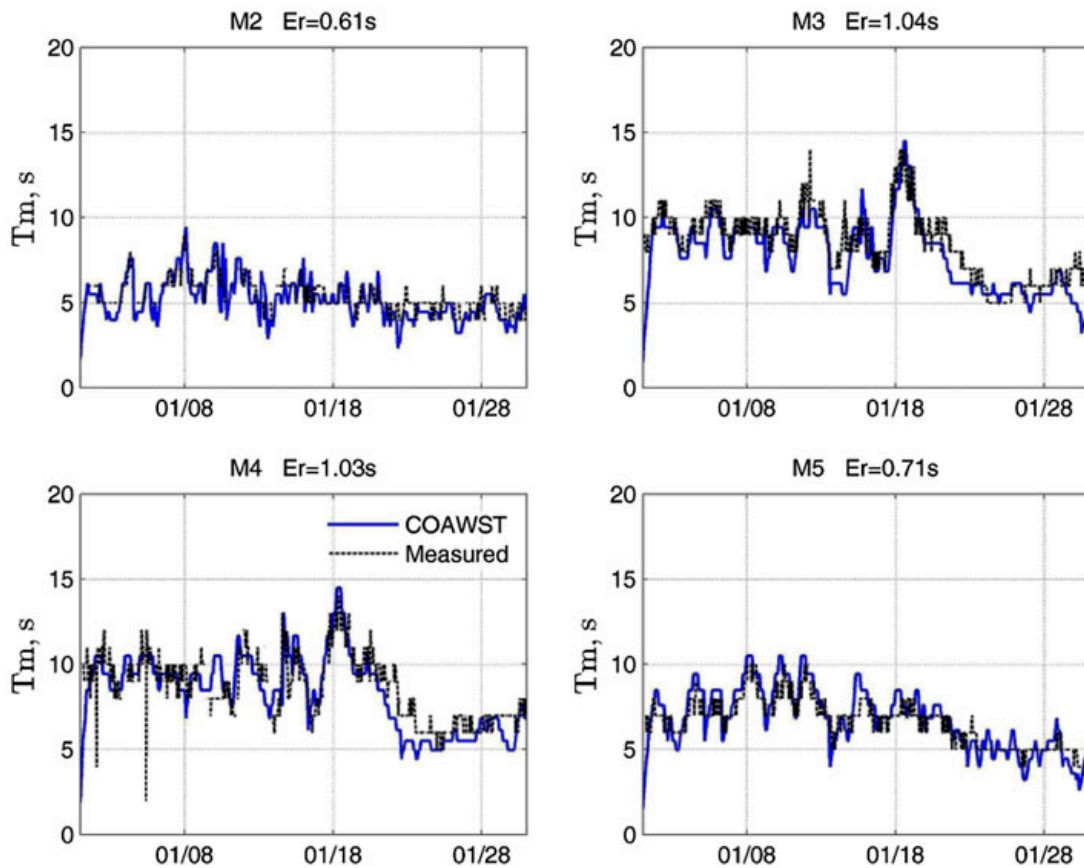

Figure 8.   Validation of the COAWST wave period results at a number of wave buoys (table 3) during January 2005.

Table 3.   Validation locations for COAWST tide and wave results.

Station	Coordinate	
Mumbles, TG[a]	3.97*W*	51.57 N
St Marys, TG	6.32*W*	49.93 N
Holyhead, TG	4.62*W*	53.51 N
Aberdeen, TG	2.67*W*	57.15 N
Dover, TG	1.32*E*	51.07 N
Galway, TG	9.04*W*	53.27 N
Pointe de Grave, TG	1.07*W*	45.56 N
Brest, TG	4.50*W*	48.38 N
M2, WB[b]	5.43*W*	53.48 N
M3, WB	10.55*W*	51.22 N
M4, WB	9.99*W*	54.99 N
M5, WB	6.70*W*	51.69 N
Scarweather, WB	3.93*W*	51.43 N
Poolebay, WB	1.72*W*	50.63 N
West Gabbard, WB	2.08*E*	51.98 N
Tynetees, WB	0.75*W*	54.92 N

[a]Tide Gauge
[b]Wave Buoy

In terms of the wave results, figures 7 and 8 show validation of the COAWST model at four wave buoys within the domain (table 3) during January 2005. The model was also validated using the other wave buoys based on data provided by the Cefas WaveNet (cefasmapping. defra.gov.uk/Map) for a period of three months during 2007, as shown in figures 9 and 10. The mean absolute errors have been computed and reported for each time series. The computed errors for the wave periods and significant wave heights are about, or less than, 1 s and 0.50 m (except for the M4 buoy), respectively, which is a convincing outcome. Further, although the wind forcing was three-hourly, the model was good at predicting the peaks.

Figure 11 shows the comparison of the COAWST and decoupled-SWAN model results at Scarweather wave buoy. This wave buoy is located in the Bristol Channel (see table 3) where significant wave–current interaction effects are expected (Jones 2000). Despite the relatively coarse resolution of the grid, the modulation of the tide in the wave parameters, and improved model performances by using the COAWST model can be observed in this figure. The improvement of the model performances was 25 and 23% for the significant wave height and the mean wave period, respectively. Nevertheless, the result at a specific location can be improved by employing higher resolution models. Obviously, there will be less difference when using the coupled model at locations where the tidal currents are weaker.

4.2. *Computational cost*

Although coupled models tend to produce more realistic results due to the additional processes that they simulate, the computational cost of coupling can be a major drawback, discouraging their use by ocean modellers. The HPC Wales Sandy Bridge system (www.hpcwales.co.uk) was used for the simulations in the present study. The computational cost of running SWAN, ROMS and COAWST (ROMS-SWAN) are reported in table 4, which is based on the use of 2.9 GHz Sandy Bridge processors. It should be mentioned that the reported costs are approximate, and vary depending on several factors such as the number of processors which are used in each simulation. Nevertheless, they give a general indication of the computational cost associated with running the coupled model, which is about five times the cost associated with running two decoupled models. Further, as table 4 shows, nesting of the model inside a larger wave model
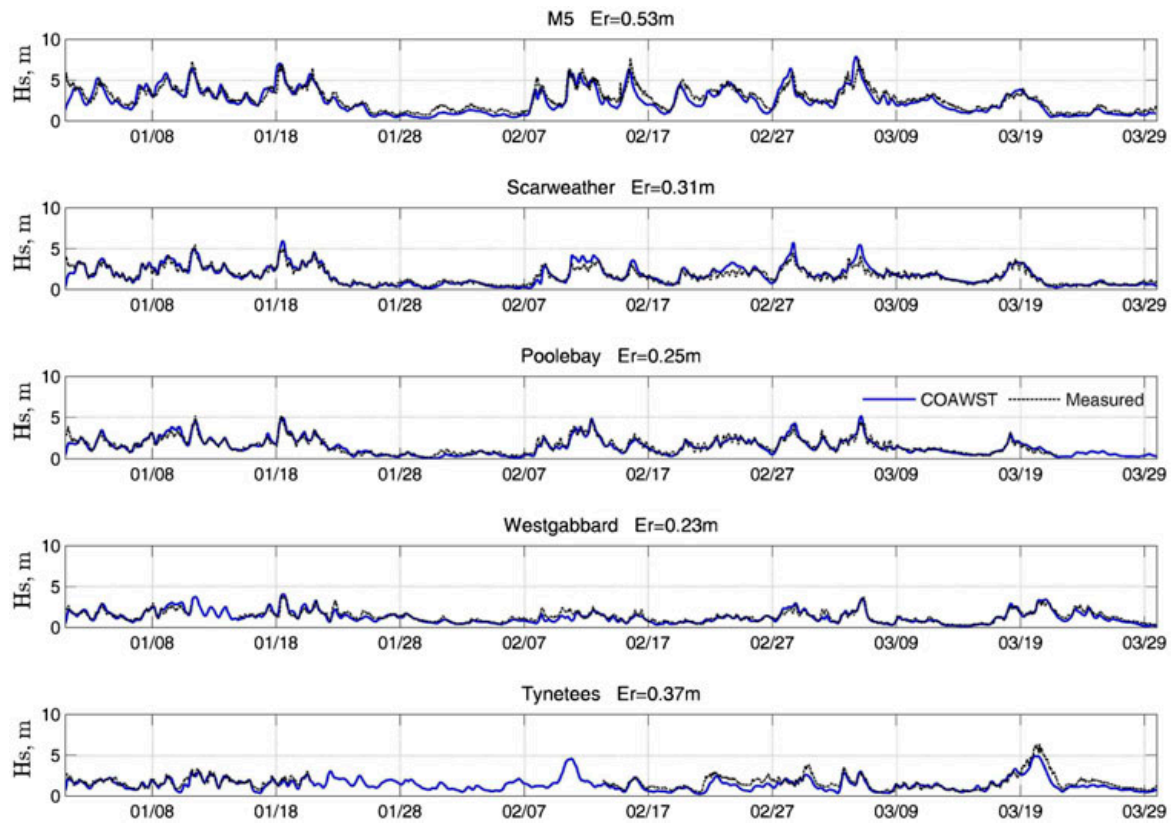
Figure 9.   Validation of the COAWST wave height results at a number of wave buoys (table 3) during January–March 2007.
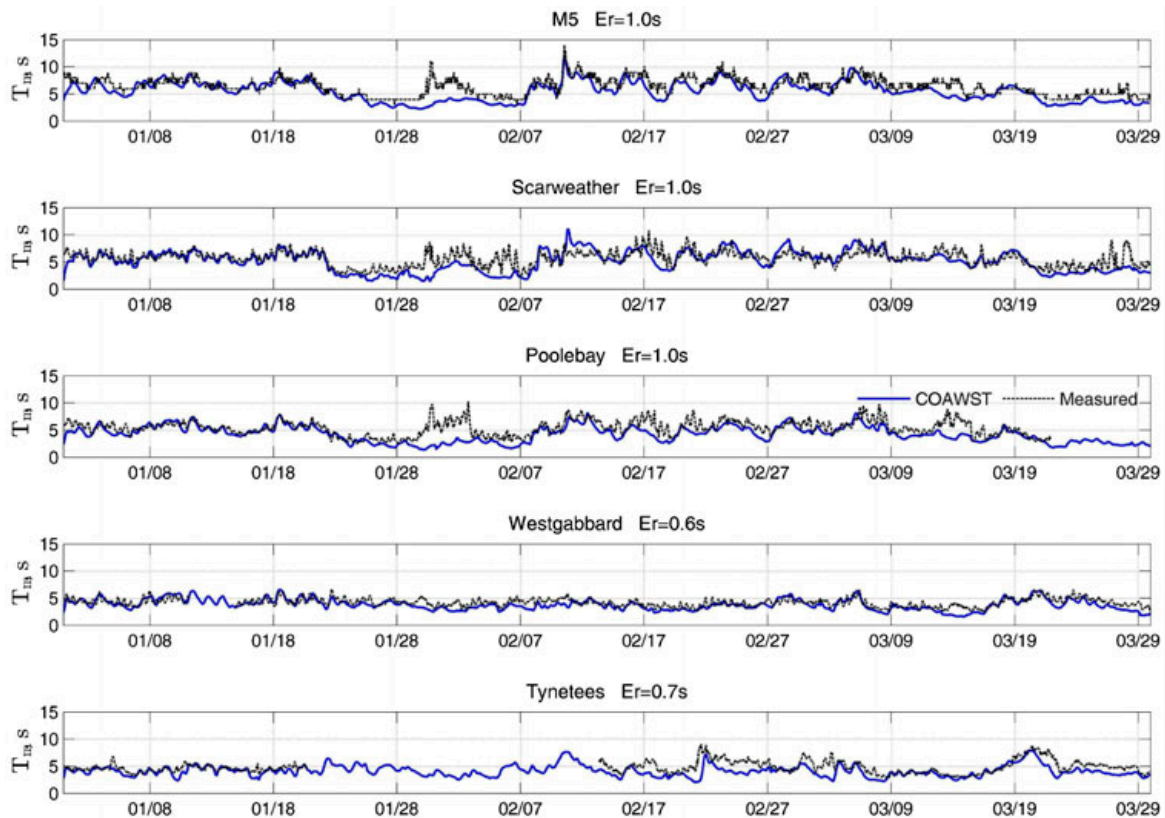

Figure 10.   Validation of the COAWST wave period results at a number of wave buoys (table 3) during January–March 2007.
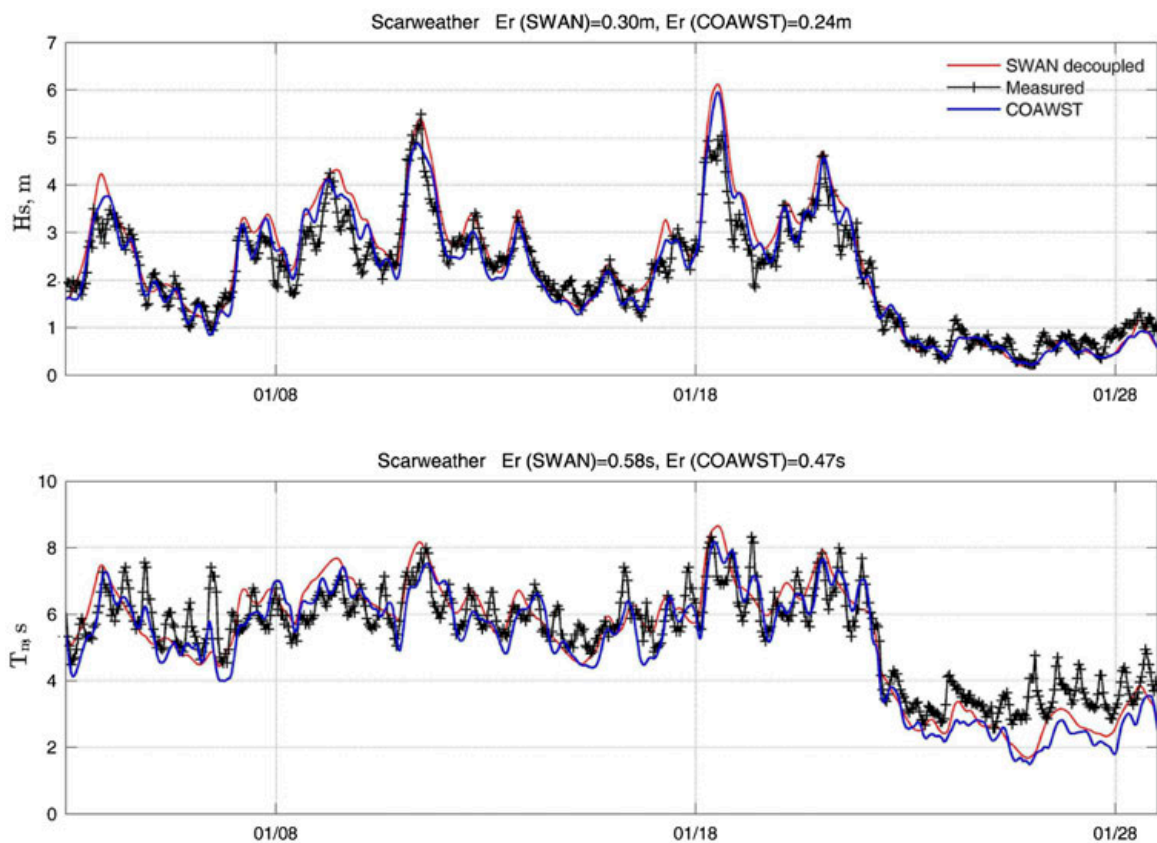
Figure 11.   Comparison of the COAWST and decoupled-SWAN model performances in January 2007, at Scarweather wave buoy (table 3).

(to enhance the model performance near the boundaries) did not change the computational cost associated with the COAWST model. However, additional time is required to run the parent SWAN model and provide the boundary information. One advantage of using the COAWST model is the ability to post-process all wave and tide data from a single (or a series of) NetCDF (Network Common Data Form) file. However, for three-hourly output data over a month of simulation, an 80 GB file was produced which, depending on the computer capacity, could be difficult to process.

4.3. *Effect of waves on bed shear stress*

For the first application of the coupled model, the wave induced and combined wave–current-induced average bed shear stresses are presented. As mentioned, accurate calculation of bed shear stress is essential in sediment transport and long-term morphodynamic studies. Recently, the environmental impact assessment of marine renewable energy devices has been the focus of several studies, especially in highly energetic regions of the NW European shelf seas (Neill *et al.* 2012). Many regions throughout this study area experience concurrently high waves and high tidal energy (e.g. Orkney in the north of Scotland; see also Neill *et al.* 2014). Therefore, coupled tide-wave models are useful for assessing the effect of wave energy and/or tidal energy extraction on sea-bed morphology and, in particular, the evolution of offshore sand banks (Neill *et al.* 2012).

Figure 12 shows the mean and peak wave height over the model domain during January 2005. The average and maximum computed wave heights follow a similar spatial pattern.

Table 4.   Computational cost of decoupled ROMS and SWAN compared with COAWST for one month of simulation.

Model	Number of CPUs	Simulation time, h	Total cost, CPU-h
ROMS, Decoupled	96	3.32	319
SWAN, Decoupled	96	2.81	270
COAWST (ROMS + SWAN)	96 + 96	12.01	2304
COAWST (ROMS + SWAN (Nested))	96 + 96	12.03	2310

(a)   (b)
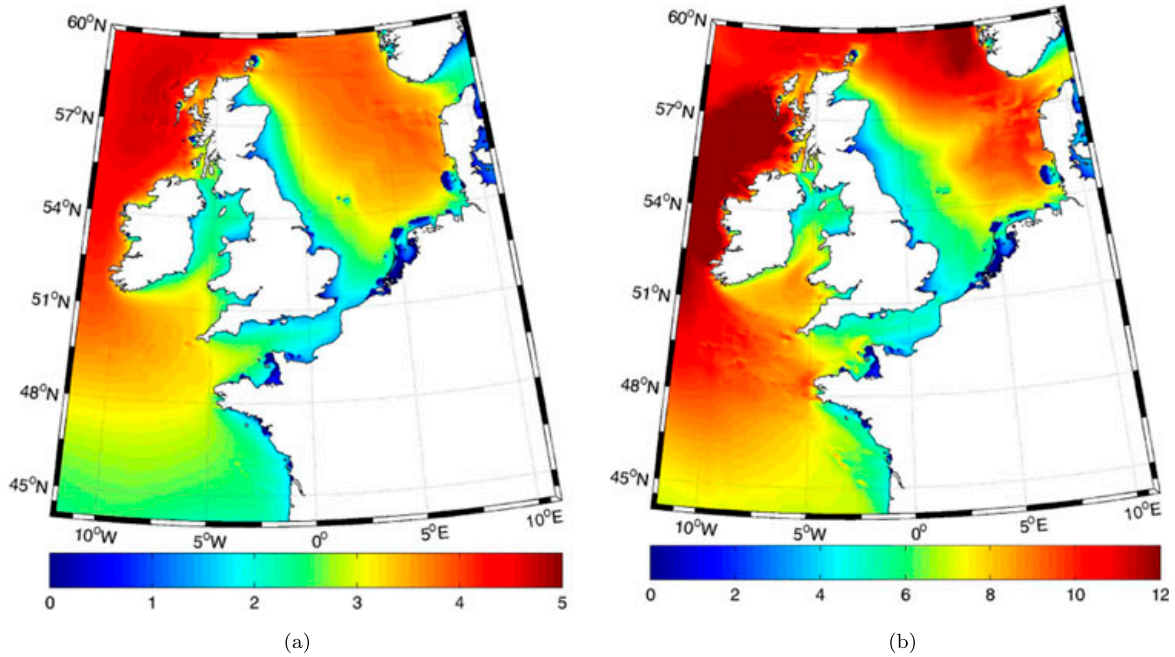
Figure 12.   Computed average and maximum wave heights during January 2005 over the domain. The colour scale (refer to the web version) shows significant wave height in metres; (a) average and (b) maximum.

The most energetic regions are NW of Scotland and west of Ireland as opposed to the more sheltered east coast of the UK, central parts of the Irish Sea and the English Channel.

The wave orbital velocity, estimated near the bed, is the basis for computation of the wave induced bed shear stresses and can be directly output from SWAN. Alternatively, it can be computed using the following equation,

$$u_b = \frac{\pi H_s}{T_w \sinh(kd)}, \tag{10}$$

where T_w is the wave period, H_s is the significant wave height and d is the water depth. Figure 13 shows the average wave induced bed shear stress, and the corresponding near-bed orbital velocities over the domain. As expected, exposed shallow regions are associated with higher wave induced bed shear stresses. In particular, western coasts of Scotland and Ireland, and the western coast of Denmark, are more affected by wave-induced bed shear stresses. Also, figure 14 shows the tide induced and combined wave–tide induced bed shear stresses over the domain. The spatial pattern of more active sediment transport regions based on the combined wave–tide effect can be inferred from this figure. It should be mentioned that the nearshore physics of the COAWST model, which includes wave breaking and surf zone parameterisation of wave–current interactions cannot be implemented in models at this scale and resolution. Therefore, regional models with higher grid resolution are necessary for detailed assessment of the bed shear stress, and the resulting sediment transport for a particular case study.
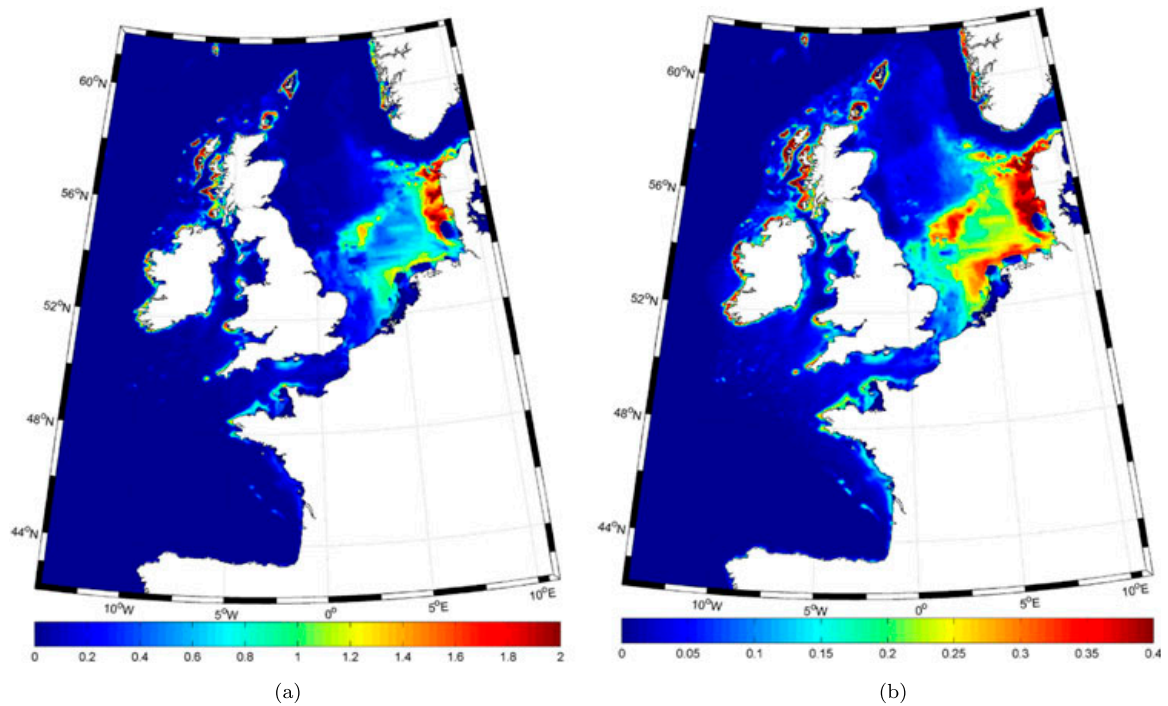
Figure 13. The average computed wave induced bottom stress (ignoring tide) and the average estimated bottom orbital velocities for January 2005 based on the COAWST results (refer to the web version for colour scales); (a) wave induced bottom stress (N/m^2) and (b) estimated orbital velocities at the bed (m/s).
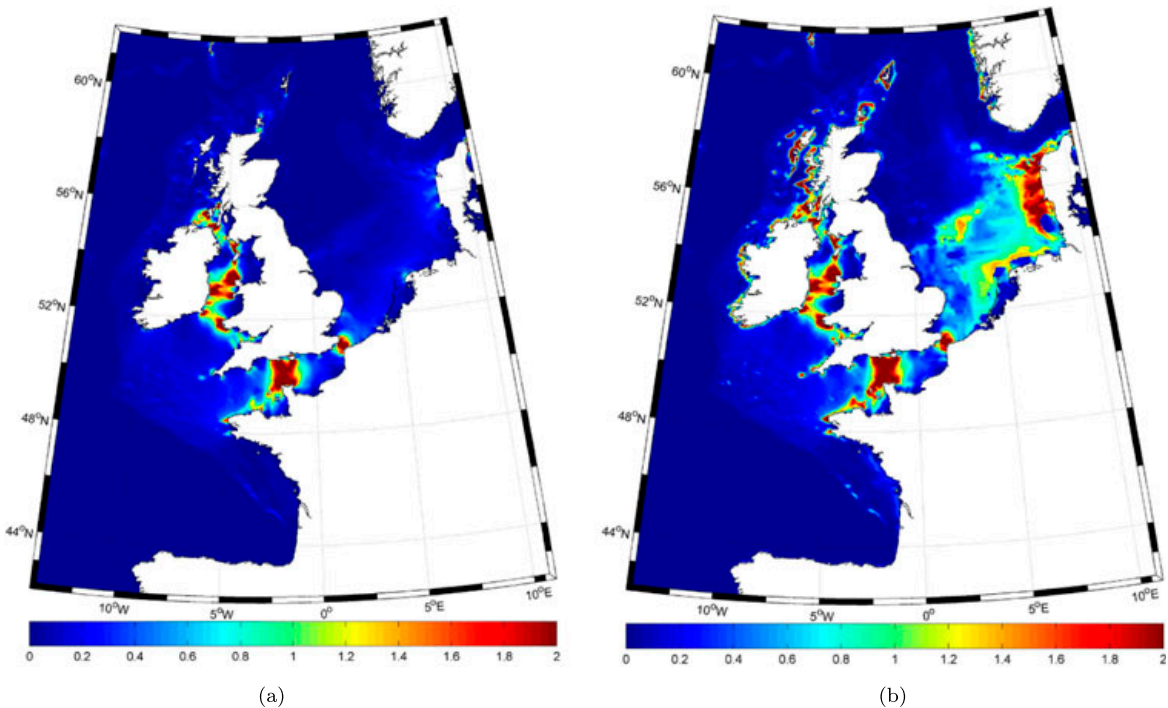

Figure 14. Average bed shear stress for January 2005, using the COAWST model for tidal current induced (ignoring waves) and combined wave-current induced cases. The colour scale (refer to the web version) is stress in N/m^2; (a) tide induced bottom stress (N/m^2) and (b) combined tide-wave induced bottom stress (N/m^2).
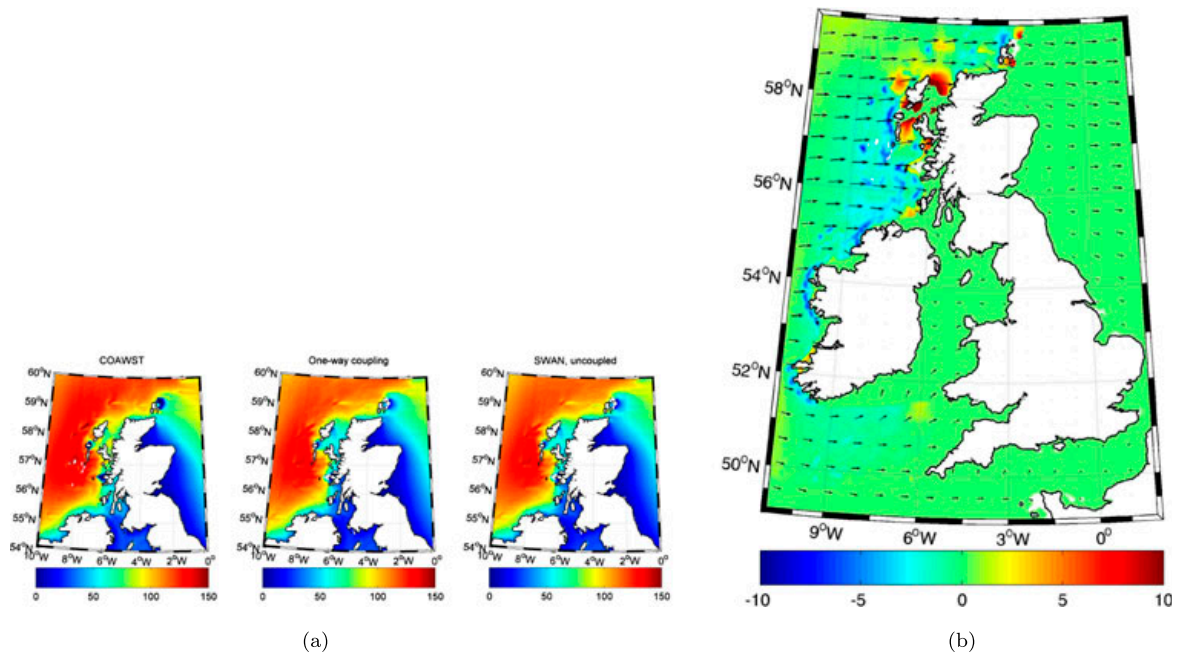
Figure 15. Effect of wave–tide interaction on the wave energy assessment for January 2005. The colour scale (refer to the web version) on the right hand plot represents the effect of tide on the wave power estimation in % which has been computed by subtracting the COAWST and decoupled SWAN model results. To avoid division by small numbers, the low-energy regions (less than 1/3 of the average) are filtered (set to green colour); (a) comparison of average wave power kW/m for January 2005, computed by different model configurations (fully coupled, one-way coupled, and uncoupled); and (b) effect of wave–tide interaction on the estimated wave power.
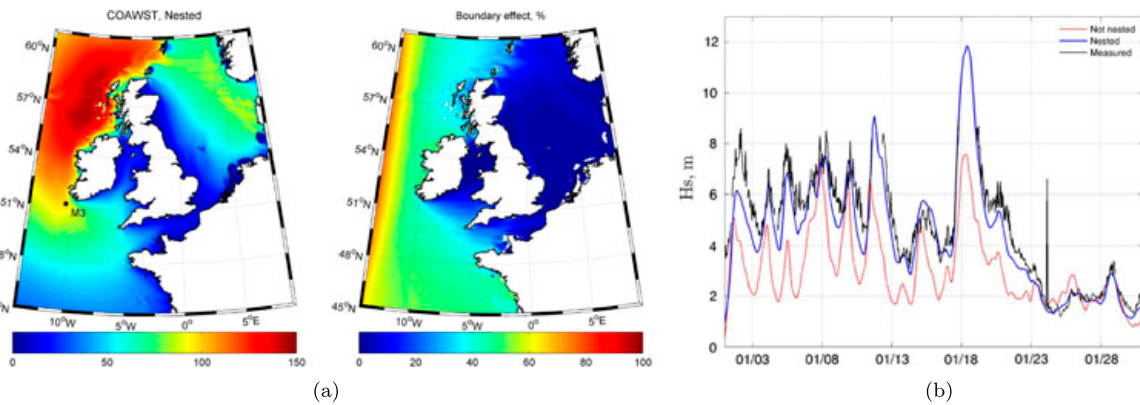

Figure 16. Effect of nesting on the computed wave parameters (refer to the web version for colour scales). The improvement of the model performance by nesting is significant, and over 30% in the west coasts of Ireland and Scotland. The effect is negligible in many parts of the Irish Sea and North Sea; (a) average wave power in January 2005 (left; kW/m) and effect of nesting on the results (right; %); and (b) effect of nesting on mode results at M3 wave buoy (see sub-figure a for location) in January 2005.

4.4. *Effect of tides on wave energy assessment*

As a second application, the effect of tides on wave energy assessment is presented here. In the majority of previous research on the assessment of wave energy over the NW European shelf seas, the effect of tides has not been included (e.g. the Atlas of UK marine renewable energy resources ABPmer 2008). There are two ways to include the effect of tides on the wave resource using SWAN. The first method (Hashemi and Neill 2014), which needs much less computational effort, is providing wave and current data files extracted from a ROMS simulation as input files for SWAN and running the decoupled SWAN model (one-way

coupling). The other method, which is more expensive, is to estimate the wave power by the fully coupled COAWST model. The advantage of the latter method lies in its flexibility and its more complete analysis of wave–current interaction, particularly when two-way interaction is important. Figure 15 shows the results for the three modelling approaches used to estimate the average wave energy resource for the most energetic part of the domain, and the effect of wave–tide interactions. As figure 15(a) shows, the decoupled SWAN model, one-way coupled model, and the COAWST model seem to produce very similar results. However, the wave–tide interaction effect becomes clearer when the differences between the model results are plotted. Referring to figure 15(b), although the impact is not significant when expressed as a percentage over the whole domain, in some specific regions (e.g. Orkney) it can reach 10% of the resource. Since the effect has been plotted as a percentage of the resource, only the regions with significant wave resources (higher than 1/3 of the average; to avoid division by small numbers) have been plotted. Further, the dominant wave climate of this region is southwesterly (Neill and Hashemi 2013), but the dominant waves for the simulation period were westerly. The temporal and spatial variability of this effect needs further research.

Figure 16 demonstrates how model performance and wave resource estimation are affected by the western boundary of the domain. Figure 16(b) shows the significant improvement of the model results for an exposed wave buoy which is relatively close to the boundary. Additionally, it can be concluded from figure 16(a) that in many potential wave energy development sites (e.g. Scotland), more than 30% of the wave energy resources are generated outside the region (i.e. swell waves), during the simulation period.

5. Conclusions

A COAWST coupled tide-wave model of the NW European shelf seas has been developed, and some applications of the model discussed. While the COAWST model can theoretically implement many wave-tide interaction processes, the application of the model for shelf scale simulations is highly constrained by computational costs (about five times the cost of decoupled simulations) and model resolution. The flexibility of the model, which allows the user to switch on/off a particular physical process, is a major advantage for this model. However, in large-scale applications of the model, the main challenge for the user is the selection of the appropriate model physics, through cpp switches, that are applicable over the entire domain. This becomes even more complicated when one tries to develop a model with a minimum number of physical processes for simplicity, and in order to reduce the computational cost for large scale simulations where in some parts of a region one physical process is dominant (e.g. wave induced stresses) as opposed to other regions (e.g. baroclinic currents). Further, although the computational cost of running the decoupled SWAN, using current and water elevation data provided by ROMS simulations (one-way coupling), is significantly less than that of the COAWST model, the pre/post-processing of the input and output data is much more convenient in COAWST, which reduces the user time and the corresponding cost.

The performance of the COAWST model in prediction of wave parameters was shown to improve by 25% in places where wave–current interaction is significant.

Application of the model in estimating the combined wave–tide-induced bed shear stress over the study area shows importance of the waves in sediment transport processes at shelf sea scale, and is consistent with the results of previous research. Application of the model in the assessment of wave energy resources has demonstrated the significance of tides in wave

resource assessment which in some regions can alter the estimated wave power by more than 10%. For accurate wave studies, the COAWST model of the NW European shelf seas should be nested inside a larger model covering the North Atlantic to account for swell waves which have been generated outside the domain. This effect exceeded 30% in many potential wave energy sites exposed to North Atlantic Ocean, for the selected period.

Acknowledgements

References

ABPmer, The Met Office and Proudman Oceanographic Laboratory; Atlas of UK marine renewable energy resources. Technical report, Department for Business Enterprise & Regulatory Reform, 2008.

Barbariol, F., Benetazzo, A., Carniel, S. and Sclavo, M., Improving the assessment of wave energy resources by means of coupled wave-ocean numerical modeling. *Renew. Energ.* 2013, **60**, 462–471.

Benetazzo, A., Carniel, S., Sclavo, M. and Bergamasco, A., Wave-current interaction: effect on the wave field in a semi-enclosed basin. *Ocean Model.* 2013, **70**, 152–165.

Bolanos, R., Osuna, P., Wolf, J., Monbaliu, J. and Sanchez-Arcilla, A., Development of the POLCOMS-WAM current-wave model. *Ocean Model.* 2011, **36**, 102–115.

Bolanos-Sanchez, R., Wolf, J., Brown, J., Osuna, P., Monbaliu, J. and Sanchez-Arcilla, A., Comparison of wave-current interaction formulation using POLCOMS-WAM wave-current model, in *Proceedings of the 31st International Conference on Coastal Engineering*, *Hamburg, Germany*, 2009.

Brown, J.M., Souza, A.J. and Wolf, J., An 11-year validation of wave-surge modelling in the Irish Sea, using a nested POLCOMS-WAM modelling system. *Ocean Model.* 2010, **33**, 118–128.

Carrère, L., Lyard, F., Cancet, M., Guillot, A. and Roblou, L., FES2012: a new global tidal model taking advantage of nearly 20 years of altimetry, in *Proceedings of meeting, 20 years of altimetry, Venice-Lido, Italy*, 2012.

Davies, A., Soulsby, R. and King, H., A numerical model of the combined wave and current bottom boundary layer. *J. Geophys. Res.-Oceans* 1988, **93**, 491–508.

Di Lorenzo, E., Moore, A.M., Arango, H.G., Cornuelle, B.D., Miller, A.J., Powell, B., Chua, B.S. and Bennett, A.F., Weak and strong constraint data assimilation in the inverse regional ocean modeling system (ROMS): development and application for a baroclinic coastal upwelling system. *Ocean Model.* 2007, **16**, 160–187.

Egbert, G.D. and Ray, R.D., Semi-diurnal and diurnal tidal dissipation from TOPEX/Poseidon altimetry. *Geophys. Res. Lett.* 2003, **30**, 1907, 9-1–9-4. doi:10.1029/2003GL017676.

Haidvogel, D.B., Arango, H., Budgell, W.P., Cornuelle, B.D., Curchitser, E., Di Lorenzo, E., Fennel, K., Geyer, W.R., Hermann, A.J., Lanerolle, L., Miller, A.J., Moore, A.M., Powell, T.M., Shchepetkin, A.F., Sherwood, C.R., Signell, R.P., Warner, J.C. and Wilkin, J., Ocean forecasting in terrain-following coordinates: Formulation and skill assessment of the Regional Ocean Modeling System. *J. Comput. Phys.* 2008, **227**, 3595–3624.

Hashemi, M.R. and Neill, S.P., The role of tides in shelf-scale simulations of the wave energy resource. *Renew. Energ.* 2014, **69**, 300–310.

Jones, B., A numerical study of wave refraction in shallow tidal waters. *Estuar. Coast. Shelf Sci.* 2000, **51**, 331–347.

Kumar, N., Voulgaris, G., Warner, J.C. and Olabarrieta, M., Implementation of the vortex force formalism in the coupled ocean-atmosphere-wave-sediment transport (COAWST) modeling system for inner shelf and surf zone applications. *Ocean Model.* 2012, **47**, 65–95.

MacCready, P., Banas, N.S., Hickey, B.M., Dever, E.P. and Liu, Y., A model study of tide-and wind-induced mixing in the Columbia River estuary and plume. *Cont. Shelf Res.* 2009, **29**, 278–291.

Madsen, O.S., Spectral wave-current bottom boundary layer flows. *Coastal Eng. Proc.* 1994, **1**, 384–398.

Malarkey, J. and Davies, A.G., A non-iterative procedure for the Wiberg and Harris (1994) oscillatory sand ripple predictor. *J. Coast. Res.* 2003, **19**, 738–739.

Mellor, G.L., The depth-dependent current and wave interaction equations: a revision. *J. Phy. Oceanogr.* 2008, **38**, 2587–2596.

Neill, S.P. and Hashemi, M.R., Wave power variability over the northwest European shelf seas. *App. Energ.* 2013, **106**, 31–46.

Neill, S.P., Hashemi, M.R. and Lewis, M.J., The role of tidal asymmetry in characterizing the tidal energy resource of Orkney. *Renew. Energ.* 2014, **68**, 337–350.

Neill, S.P., Jordan, J.R. and Couch, S.J., Impact of tidal energy converter (TEC) arrays on the dynamics of headland sand banks. *Renew. Energ.* 2012, **37**, 387–397.

Neill, S.P., Scourse, J.D. and Uehara, K., Evolution of bed shear stress distribution over the northwest European shelf seas during the last 12,000 years. *Ocean Dynam.* 2010, **60**, 1139–1156.

Newberger, P. and Allen, J.S., Forcing a three-dimensional, hydrostatic, primitive-equation model for application in the surf zone: 1. Formulation. *J. Geophys. Res.- Oceans* 2007a, **112**, C08018 1–12.

Newberger, P. and Allen, J.S., Forcing a three-dimensional, hydrostatic, primitive-equation model for application in the surf zone: 2. Application to DUCK94. *J. Geophys. Res.- Oceans* 2007b, **112**, C08019 1–21.

Pingree, R. and Griffiths, D., Sand transport paths around the British Isles resulting from M2 and M4 tidal interactions. *J. Mar. Biol. Assoc. UK* 1979, **59**, 497–513.

Reniers, A., Thornton, E., Stanton, T. and Roelvink, J., Vertical flow structure during Sandy Duck: observations and modeling. *Coast. Eng.* 2004, **51**, 237–260.

Saruwatari, A., Ingram, D.M. and Cradden, L., Wave-current interaction effects on marine energy converters. *Ocean Eng.* 2013, **73**, 106–118.

Soulsby, R. and Clarke, S., Bed shear-stresses under combined waves and currents on smooth and rough beds. HR Wallingford, Report TR137, 2005.

Styles, R. and Glenn, S.M., Modeling bottom roughness in the presence of wave-generated ripples. *J. Geophys. Res.-Oceans* 2002, **107**, 3110, 24-1–24-15.

Tolman, H., An evaluation of expressions for wave energy dissipation due to bottom friction in the presence of currents. *Coast. Eng.* 1992, **16**, 165–179.

Uchiyama, Y., McWilliams, J.C. and Shchepetkin, A.F., Wave-current interaction in an oceanic circulation model with a vortex-force formalism: Application to the surf zone. *Ocean Model.* 2010, **34**, 16–35.

Warner, J.C., Armstrong, B., He, R. and Zambon, J.B., Development of a coupled ocean-atmosphere-wave-sediment transport (COAWST) modeling system. *Ocean Model.* 2010, **35**, 230–244.

Warner, J.C., Sherwood, C.R., Arango, H.G. and Signell, R.P., Performance of four turbulence closure models implemented using a generic length scale method. *Ocean Model.* 2005, **8**, 81–113.

Warner, J.C., Sherwood, C.R., Signell, R.P., Harris, C.K. and Arango, H.G., Development of a three-dimensional, regional, coupled wave, current, and sediment-transport model. *Comput. Geosci.* 2008, **34**, 1284–1306.

Wolf, J., Coastal flooding: impacts of coupled wave-surge-tide models. *Nat. Hazards* 2009, **49**, 241–260.

Contribution statements

Contributions

Referring to Table 1.1 (Page 2), which is the list of publications submitted by M. Reza Hashemi to Bangor University, for the award of the degree of PhD by published works, the major contributions of the co-authors have been provided here[3].

Published work **P-I** : MRH initiated and led the research, developed the numerical models (SWAN and ROMS model of the NW European shelf seas), initiated and applied the analytical approach, presented/analysed the results; SPN, improved the presentation/writing of the paper, and provided data for model validation.

Published work **P-II** : SPN initiated and led the research, developed the SWAN model, extracted the observation data as well as the data used for comparison with Atlas of UK marine renewable energy resources. MRH suggested and quantified the statistical analysis of the results in terms of uncertainty, suggested the comparison with Atlas, expanded the results/discussion, performed a trend analysis on the time series, and helped in the revision.

Published work **P-III**: SPN initiated and led the research, developed the ROMS model, collected the observed data for model validation, and presented the results. MRH suggested

---

[3]**Abbreviations**: M. Reza Hashemi : MRH; Simon P. Neill: SPN; Alan G. Davies: AGD; Alan J. Elliott: AJE; Zahra Ghadampoor: ZG; Matt J. Lewis: MJL.

Published work **P-VII**: MRH initiated and led the research, developed the COAWST model - with the collaboration of researchers from the USGS department - on HPC systems, developed the COAWST model of the NW European shelf seas, and provided the results/analysis. SPN provided the dynamic boundary data through a North Atlantic wave model, improved the presentation/wrting of the paper, and helped in the version of the paper. AGD checked the theoretical part of the paper, in particular, regarding the wave current interaction, and improved the discussion/presentation of the paper.

Signatures

Reza Hashemi

TO WHOM IT MAY CONCERN,

This is to certify that Mr. Mohammad Reza Hashemi initiated and led the research article with title of "Using artificial neural network to model seasonal changes in beach profiles" that was published in Ocean Engineering Journal and I helped out in ANN simulations. Also, this research was not used as part of my PhD thesis.
Please do not hesitate to contact me should you require any further information

Yours sincerely
Zahra ghadampour
Civil PhD
Address: #12, Alley 2, Hor St. Baghe Takht
Shiraz Fars Iran
Mobile: +(98) 9177005440
Phone: +(98) 711 2284468
Fax: +(98) 711 2282701
Email: Zahra_ghadampour@yahoo.com

From:	Alan Elliott <alan.aj.elliott@gmail.com>
Sent:	21 July 2014 15:30
To:	Reza Hashemi
Subject:	Re: A request about published works

Reza:

Your comments look good. What are your plans for the future?

Regards

Alan

--
A J Elliott
32 Venus Street
Congresbury
Bristol
BS49 5EZ

01934 835 152
07800 637 497

Reza Hashemi

From:	Reza Hashemi
Sent:	21 July 2014 14:57
To:	'applied.ocean@googlemail.com'
Subject:	A request about published works

Dear Alan,

I hope that you are doing well and enjoying your time in this summer.

Since I started my collaboration with Bangor University- which was started by you – I have published more than 12 peer reviewed articles in collaboration of Bangor University. I am writing a "review of published works", and I have to mention my contribution, and other co-authors for each publication.

I have been the co-author of two papers with you. I have written a brief summary about each paper – Simon P. Neill (another co-author) is also happy about it and confirmed it. I would be grateful to you, if you confirm that the contributions are mentioned correctly. Otherwise, please feel free to revise them.

Neill, S. P., Hashemi, M. R., and Elliott,
A. J. (2007). An enhanced depthaveraged
tidal model for morphological
studies in the presence of rotary currents.
Continental shelf research, 27(1):82–102.

MRH initiated the idea of secondary flow in morphodynamic modelling;
SPN led the research. SPN developed the numerical models (POLCOMS, SWAN,
and sediment transport), and applied it to the case study. MRH developed the theoretical
and mathematical concepts of the secondary flows in rotary currents, applied it to some
idealised cases/river meanders which were included in the paper, developed a method for
morphodynamic simulation, and helped in results/discussion of the paper. AJE improved
the presentation/discussion of the paper, helped in collecting the measured data (ADCP),
and applied for the fund which supported the research

Neill, S. P., Elliott, A. J., and Hashemi,
M. R. (2008). A model of inter-annual
variability in beach levels. Continental
Shelf Research, 28(14):1769–1781.

SPN initiated and led the research, developed the numerical models,
and presented/dicussed the results. AJE improved the presentation/discussion of the paper,
helped in collecting the measured data, and applied for the fund which supported the project.
MRH initially analysed the storm and beach profile data and their relation, helped in longshore
transport modelling and results/discussion.

I have also added this to acknowledgements:

"I am also very grateful to Prof. Alan J. Elliott for his contribution and support. He was
the first one who introduced me to the ocean modelling in realistic conditions and was the
reason that I came to Bangor University."

I look forward to hear from you and see you in the near future
Best Wishes
Reza

Dr M. Reza Hashemi
Cymrawd Ymchwil/   Research Fellow
Canolfan Gwyddorau Morol Cymhwysol/   Centre for Applied Marine Sciences
Ysgol Gwyddorau Eigion/   School of Ocean Sciences
Prifysgol Bangor/   Bangor University
Porthaethwy, Ynys Môn/   Menai Bridge, Angelesey
DU/   UK
LL59 5AB/   LL59 5AB
Tfon: +44 1248 383872/   Tel: +44 1248 383872
Ffacs: +44 1248 716729/   Fax: +44 1248 716729

Hashemi,Reza   r.hashemi@bangor.ac.uk

Contributions

Hashemi, M. R., Neill, S. P., Robins, P. E., Davies, A. G., and Lewis, M. J. "Effect of waves on the tidal energy resource at a planned tidal stream array". Renewable Energy, Accepted.

MRH initiated and led the research, developed the coupled wave-tide model, and simulated the WCI; SPN improved the presentation of the paper, and suggested the inclusion of wind generated currents; PER developed the high resolution grid, and helped in modelling; AGD contributed in developing the method for inclusion of WCI in TELEMAC; MJL improved the discussion of the paper.